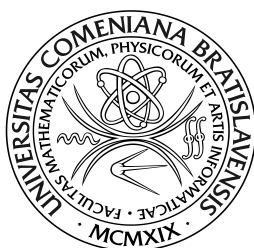


FACULTY OF MATHEMATICS, PHYSICS AND INFORMATICS
COMENIUS UNIVERSITY
BRATISLAVA, SLOVAKIA



Giga-seal solvent-free bilayer lipid membranes spanning arrays of through nanopores

RNDr. Slavoj Kresák


Dissertation
submitted in support of candidature for the degree of
Doctor of Philosophy (PhD.)

Advisors: **Prof. RNDr. Tibor Hianik, DrSc., FMPI CU, Bratislava**
Dr. Renate Naumann, MPIP, Mainz

BRATISLAVA 2009

Declaration of Originality

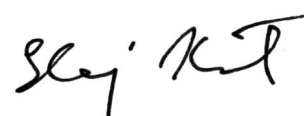
I declare that this dissertation is my own account of my research performed at the Faculty of mathematics, physics, and informatics, Comenius University, Bratislava, Slovakia, and the Max Planck Institute for Polymer Research, Mainz, Germany, and contains as its main content work which has not previously been submitted for a degree at any tertiary institution. Any uses made within it of the works of other authors in any form (e.g. ideas, equations, figures, text, tables, programs) are properly acknowledged at the point of their use. A full list of the references employed has been included.



Slavoj Kresák

Copyright

Attention is drawn to the fact that copyright of this thesis rests with its author. This copy of the thesis has been supplied on condition that anyone who consults it is understood to recognize that its copyright rests with its author and that no quotation from the thesis and no information derived from it may be published without the prior written consent of the author. This thesis may be made available for consultation within the University Library and may be photocopied or lent to other libraries for the purposes of consultation.



Slavoj Kresák

Acknowledgements

Dr. Naumann and Prof. Hianik, I am grateful for the valuable scientific guidance that you granted me with during my PhD. studies and that eventually evolved into this dissertation. Thank you also for the careful revising of the text and the suggestions for improvement.

Michael and Maren, thank you for giving me access to and training me with the FEI Nova 600 DualBeam FIB/SEM to mill my pores. I also thank you for your committed technical support.

Gunnar, thank you for helping me out with SEM imaging whenever needed and the constructive discussions of the FIB/SEM results.

Uwe and Rudiger, I greatly appreciate your training with the AFM, as well as your dedicated assistance whenever required.

Gabi, thanks for your help with all the thin film depositions and analyses.

Marcus, thank you for sharing the lab. You were a pleasant company, despite the occasional ‘interference’. And special thanks for the airbrush.

Andreas, I appreciate your time devoted to coding the simulations in MatLab for me.

Beate, thank you for acquainting me with and coordinating the EU MEST-CT-2004-513924 grant.

Mechanical workshop staff, I am very grateful for your fine craft and committed attitude to my countless cell revisions and additional designs.

Ingo and Uli, thank you for your equipment that you allowed me to adopt almost permanently.

Office mates, it has been an honor and a pleasure to work alongside you. Thanks for the relaxed atmosphere and the help with whatever came up.

Lunch buddies, thanks for helping me keep a natural biorhythm, for a bit of laid-back daily socializing, and for pulling me back up when work was bringing me down.

Coffee corner gang, thanks for the jolly atmosphere, the drug, and the enjoyable activities that your group produced.

Table of contents

Acknowledgements.....	5
Table of contents.....	i
List of abbreviations.....	v
1. Introduction	1
1.1. Biomembranes	1
1.2. Membrane proteins studied by electrical means.....	2
1.2.1. Classical methods of electrical studies of membrane proteins.....	2
1.2.2. Advanced methods of electrical studies of membrane proteins.....	3
1.3. An ideal system for electro-based investigations of TM proteins	5
2. Objectives	9
3. Methods and materials.....	11
3.1. Background and theory	11
3.1.1. Focused electron and ion beams ⁴⁸⁻⁵³	11
3.1.1.1. Electron and ion beam columns.....	12
3.1.1.2. Beam – sample interactions	14
3.1.1.3. Capabilities of focused electron and ion beams	15
3.1.1.4. Downsides related to focused electron and ion beams	19
3.1.2. Atomic force microscopy ⁵⁵⁻⁶⁰	20
3.1.2.1. AFM implementation	21
3.1.2.2. Light-lever force sensing.....	21
3.1.2.3. Probe-surface interactions.....	22
3.1.3. Photolithography ⁶¹	23
3.1.3.1. Photoresist	24
3.1.3.2. Steps of the photolithographic process	24
3.1.4. Optical microscopy ⁶²⁻⁶⁴	27
3.1.4.1. DIC optical microscopy	27
3.1.4.2. Fluorescence optical microscopy	28
3.1.5. AC impedance spectroscopy ⁶⁵⁻⁶⁷	31
3.1.5.1. The notion of electrical impedance.....	31
3.1.5.2. Impedance of AC circuits.....	33
3.1.6. Electrophysiological DC voltage clamp ^{23,68-71}	39
3.1.6.1. Voltage error.....	40
3.1.6.2. Temporal error	41
3.1.6.3. Compensation of series resistance and parallel capacitance.....	41
3.1.6.4. Minimization of series resistance.....	42
3.1.6.5. Noise	42
3.2. Experimental	44
3.2.1. Substrates of choice: Si ₃ N ₄ windows	44
3.2.2. Pore milling and characterization.....	45
3.2.2.1. FEI Nova 600 NanoLab DualBeam™-SEM/FIB.....	45
3.2.2.2. FIB milling.....	45

3.2.2.3.	Nanopore imaging.....	46
3.2.3.	Preparation of giant unilamellar vesicles.....	49
3.2.4.	Optical microscopy.....	50
3.2.5.	Formation of npsLBs on Si_3N_4 windows	51
3.2.6.	Simultaneous electrical measurements and micromanipulation under optical control.....	53
3.2.7.	AC impedance	55
3.2.8.	DC voltage clamp	55
3.2.9.	Passivation of Si_3N_4 windows	55
4.	Results and discussion	57
4.1.	Giant vesicles and supported lipid bilayers.....	57
4.1.1.	Giant unilamellar lipid vesicles.....	57
4.1.2.	Adhesion, spreading and rupture of GUVs on hydrophilic surfaces	59
4.1.3.	SLB fluidity	61
4.1.4.	Modulation of SLB fluorescence intensity by Si_3N_4 thickness.....	63
4.1.5.	Lipid domains in SLBs on glass.....	66
4.1.6.	SLBs on Si_3N_4 diaphragms irradiated with the e-beam and the i-beam	69
4.1.7.	Imaging of SLBs on Si_3N_4 diaphragms by plain bright-field reflected-light optical microscopy.....	75
4.1.8.	Conclusion	77
4.2.	Ion and electron beam irradiation of Si_3N_4 diaphragms: topographic and electrostatic effects	78
4.2.1.	Topographic changes detected by AFM	78
4.2.2.	Topographic changes – is it the e-beam, the i-beam, or both?.....	79
4.2.3.	Can charge be associated with the topography?	80
4.2.4.	Basis of i-beam effects	81
4.2.5.	Basis of e-beam effects.....	82
4.2.6.	Conclusion	84
4.3.	Pores in Si_3N_4 diaphragms	85
4.3.1.	Pore characterization	85
4.3.2.	SEM.....	87
4.3.3.	AFM	88
4.3.4.	Effect of patterning parameters on pore character	88
4.3.4.1.	Annular and hill-like elevations	89
4.3.4.2.	Determinant factors	91
4.3.4.3.	Non-determinant factors	92
4.3.5.	Elevated annulus vs. milling in the surroundings	95
4.3.6.	Minimum attainable pore size.....	97
4.3.7.	Arrays used for the formation of npsLBs	99
4.3.8.	Pore taper	101
4.3.9.	Conductance of unobstructed pores in Si_3N_4 diaphragms	102
4.3.10.	Conclusion	103
4.4.	Reduction of Si_3N_4 window capacitance.....	105
4.4.1.	The need of low capacitance.....	105
4.4.2.	Capacitance of a Si_3N_4 window	106

4.4.3.	<i>Implications on capacitance reduction strategies</i>	107
4.4.4.	<i>Requirements on coated chips</i>	108
4.4.5.	<i>Cross-linkable photoresist coating - the passivation strategy of choice</i>	109
4.4.6.	<i>Deposition parameters</i>	110
4.4.7.	<i>Assessment of coating and development quality</i>	112
4.4.7.1.	<i>Assessment by optical microscopy</i>	112
4.4.7.2.	<i>Assessment by AFM</i>	113
4.4.7.3.	<i>Assessment by EIS</i>	114
4.4.8.	<i>Conclusion</i>	115
4.5.	<i>Nanopore-spanning bilayer lipid membranes</i>	116
4.5.1.	<i>npsLB formation sequence</i>	116
4.5.2.	<i>Impedance changes upon npsLB formation</i>	117
4.5.3.	<i>Electrochemistry of TEM Si₃N₄ Windows</i>	119
4.5.3.1.	<i>Simple modeling approach</i>	119
4.5.3.2.	<i>Elaborate modeling approach</i>	120
4.5.4.	<i>npsLB breakdown voltage</i>	132
4.5.4.1.	<i>Successive collapse of npsLBs</i>	133
4.5.4.2.	<i>Simultaneous collapse of npsLBs</i>	135
4.5.4.3.	<i>Pore resealing</i>	135
4.5.5.	<i>Electrical manifestation of the GUV – SLB transition</i>	136
4.5.6.	<i>Conclusion</i>	139
4.6.	<i>Pore-forming peptides in npsLBs</i>	141
4.6.1.	<i>Gramicidin D</i>	141
4.6.1.1.	<i>Background</i>	141
4.6.1.2.	<i>gD in npsLBs – multi-channel conductance</i>	142
4.6.1.3.	<i>psLBs compared to tBLMs</i>	146
4.6.2.	<i>α-hemolysin</i>	147
4.6.2.1.	<i>Background</i>	147
4.6.2.2.	<i>αHL single-channel conductance</i>	148
4.6.3.	<i>Alamethicin</i>	159
4.6.3.1.	<i>Background</i>	159
4.6.3.2.	<i>Alm single-channel recordings</i>	160
4.6.3.3.	<i>Transmembrane voltage effects</i>	161
4.6.3.4.	<i>Alamethicin concentration effects</i>	162
4.6.3.5.	<i>Unique alamethicin behavior in npsLBs</i>	163
4.6.4.	<i>Conclusion</i>	171
5.	Conclusion and outlook	173
	References	177

List of abbreviations

AFM	atomic force microscope/microscopy
Alm	alamethicin
α HL	α -hemolysin
AMD	apparent milling depth
BLM	black (bilayer) lipid membrane
DIC	differential interference contrast
DPhPC	1,2-diphytanoyl- <i>sn</i> -glycero-3-phosphocholine
DPTL	2,3-diphytanyl- <i>sn</i> -glycerol-1-tetraethylene glycol-DL- α -lipoic acid ester
e-beam	electron beam
EBL	electron beam lithography
EIS	electrochemical impedance spectroscopy
EtOH	ethanol
FIB	focused ion beam
fsSi ₃ N ₄ (/fsSiN)	free-standing silicon nitride, same as Si ₃ N ₄ diaphragm
gA	gramicidin A
gD	gramicidin D
GL	giant liposome
GUV	giant unilamellar vesicle
i-beam	ion beam
IPA	isopropyl alcohol, also 2-propanol
ISE	ion-induced secondary electron
ITO	indium-titanium oxide
KSPM	Kelvin surface probe microscope/microscopy
LMIS	liquid metal ion source
npsLB	nanopore-spanning lipid bilayer
NBD-DMPE	1,2-dimyristoyl- <i>sn</i> -glycero-3-phosphoethanolamine-N-(7-nitro-2-1,3-benzoxadiazol-4-yl)
ND	nominal diameter
NLLS	non-linear least squares
OCP	open-circuit potential
PAC	photo-active compound
PC	phosphatidylcholine
PDMS	polydimethylsiloxane
psLB	nanopore-spanning lipid bilayer
px	pixel
PZT	piezoelectric ceramic transducer
SAM	self-assembled monolayer
sBLM	supported bilayer lipid membrane
SE	secondary electron
SEM	scanning electron microscope/microscopy
SPM	Surface probe microscope/microscopy
SLB	supported lipid bilayer
SUT	surface under test
tBLM	tethered bilayer lipid membrane
TM	transmembrane
TMA ⁽⁺⁾ /OH/Cl	tetramethylammonium (cation/hydroxide/chloride)

1. Introduction

1.1. Biomembranes

A *bio(logical)membrane* is an enclosing or separating amphipathic layer that acts as a barrier within or around a cell. A key feature of a biomembrane is the selective permeability, i.e. the ability to allow or block the traversal of a specific substance based on its physical and chemical properties. The biomembrane between the interior of a eukaryotic cell and the outside environment, the so called *cell membrane*, regulates what enters and exits the cell, thus aiding the transport of substances needed for survival. The cell membrane also plays a role in anchoring the cytoskeleton to provide shape to the cell, and in attaching to the extracellular matrix. Furthermore, the cell membrane facilitates communication by signal transduction between the inside and the outside of the cell, and allows for immunological recognition. Within the cell, on the other hand, semi-permeable biomembranes separate the specific contents of various organelles (e.g. the nucleus, the endoplasmic reticulum, the Golgi apparatus, mitochondria, lysosomes, etc.) from the cytoplasm.¹ Similar to the cell membrane, the *endomembranes* help define the structure and location of cell organelles and allow for recognition processes within the cell interior. Some organelle-specific functions are tightly bound to the membranes, too. Mitochondria, for example, contain two biomembranes, an inner and an outer one, the particular alignment of which allows for the highly efficient conversion of nutrients into ATP.²

Biomembranes consist of a double layer of various (phospho-)lipid and sterol molecules, and an assortment of proteins. The outer cell membrane additionally contains carbohydrates. According to the fluid-mosaic model³ of the biomembrane all constituents diffuse freely within the planar structure. Recently, the model has been adjusted to allow for higher degrees of order such as lipid-protein microdomains (rafts)^{4,5} and superlattice structures⁶. Membrane proteins can be classified as *integral* and *amphitropic*.⁷ Integral proteins are permanently bound to the membrane. Usually they are transmembrane, i.e. they span the entire membrane and exhibit intra- and extra-membrane domains. The amphitropic are proteins that can exist in two alternative states: a water-soluble and a lipid bilayer-bound state. The amphitropic protein category includes water-soluble channel-forming polypeptide toxins, which associate irreversibly with membranes. The various functions and activities of a biomembrane are primarily carried out by membrane proteins. The significance of the protein constituent in biomembrane functioning is apparent simply from the content: they usually make up ~50% of the total membrane weight.¹ ~30% of all open reading frames of the *H. sapiens* genome encode integral membrane proteins.⁸ Mutations or changes in membrane proteins cause a vast array of inherited or acquired conditions including cystic fibrosis, multi-drug

resistance, diabetes, Alzheimer's, kidney and digestive diseases, hypertension, and heart failure. Membrane proteins are also the major targets for pharmaceuticals.⁹

1.2. Membrane proteins studied by electrical means

A considerable portion of protein-facilitated biomembrane activity involves movement of charge across the membrane. A plethora of pumps and exchangers exist that transport specific ionic species from one side of a biomembrane to the other, commonly giving rise to a distinct electrochemical gradient. Transfer of protons across a membrane can also be coupled to transfer of electrons, such as in the case of electron transport chains in chloroplasts and mitochondria. Thanks to the excellent intrinsic resistance of the lipid bilayer, electrical means can be employed to detect the currents and potentials associated with such electrogenic activity. Potential energy of the transported ions can be released by opening of selective ion channels in the membrane and a consequent flow of the ions down the thermodynamic gradient, which too is well detectable as electric current or change of transmembrane (TM) potential. Non-electrogenic membrane proteins the function of which is not directly related to ion transport or conduction, yet which are capable thereof, can also be studied by means of electro methods. Porins as well as bacterial and fungal polypeptide toxins forming lytic TM pores can thus be investigated.

1.2.1. Classical methods of electrical studies of membrane proteins

The advances in physiological research of TM structures that transport or are permeable to charge have been mediated almost exclusively by planar bilayer lipid membrane (BLM)¹⁰ and patch clamp experiments.¹¹ Although similar in the results they deliver, the methodological difference between the two approaches allowed them to coexist in parallel for over 30 years, while neither managed to outscore the other. BLMs are superior to the patch clamp technique in the following: the composition of the membrane can be defined precisely, artifacts arising from species other than the one under study are absent, ion channels expressed in bacteria or internal organelles of eukaryotic cells can be explored, and the access to both sides of the membrane is straight-forward. On the other hand, patch clamp beats classical BLMs in aspects like noise, environment nativeness, and protein purification and reconstitution limitations. Common to both is that the duration of an experiment is rather limited: the BLMs rupture unpredictably, while the patched cells die. Furthermore, classical patch-clamp and BLM both suffer from shortcomings that disqualify them in the light of novel requirements on a high-throughput drug screening or biosensing platform posed by pharmacology and medicine. Considerable effort has thus been devoted to improving the classical techniques. Artificial BLMs evolved into (electrode-)supported BLMs (sBLM) and BLMs

on small apertures, whereas pipette-based patch-clamp has recently progressed towards its planar alternative.

1.2.2. Advanced methods of electrical studies of membrane proteins

(Electrode-)supported BLM (sBLM). sBLMs are lipid bilayers that are supported by a solid surface. Should electrical measurements across the bilayer be possible, the surface must be of conductive nature, i.e. an electrode. sBLMs may adhere to the electrode based on physical intermolecular interactions between the lipid and the support,¹² or they are coupled to the surface chemically.¹³ Unlike classical BLMs, sBLMs, and particularly those covalently bound to a flat metallic surface, exhibit a notably high stability and resistance. Besides electrical investigations, they allow for an (simultaneous) employment of various techniques of surface analysis (e.g. SPR, ellipsometry, AFM, etc.). We have shown previously that the quality of an sBLM derived from a self-assembled monolayer (SAM) of alkanethiols on a gold electrode can be enhanced if a positive DC potential is applied to the electrode during SAM formation.¹⁴ Sadly, there are some significant negative features associated with an sBLM, namely no or a very thin gap between the bilayer and the electrode, and limited fluidity of the proximal bilayer leaflet. These aspects of the sBLM prevent correct insertion of larger TM proteins into the bilayer. There have been several attempts to expand the sub-membrane space by placing a hydrophilic polymer cushion between membrane and substrate. In general, however, these systems did not show enough electrical sealing.¹³ A further development of sBLMs, the tethered BLM (tBLM), has been considerably more successful. Similar to the most resistive sBLMs, tBLMs are chemically anchored to electrode surface. Sufficient decoupling between bilayer and electrode is provided by a spacer group that is covalently linked to both.¹³ Although tBLM offers to TM proteins an environment more native than the sBLM, the packing density in the spacer region and the still rather low fluidity of the proximal bilayer leaflet hinders functional reconstitution of complex TM proteins.¹⁵ Our results on the interaction of a model α -peptide with a tBLM based on DPTL showed, for example, that this relatively simple and small helix binds to the surface of the tBLM only, and does not insert in the membrane in a trans-bilayer fashion.¹⁶

BLMs on small apertures. Over the past two decades, a number of approaches have been adapted to enhance the classical technique of a free-standing BLM on an aperture. Procedures have been developed to minimize the presence of organic solvents in the BLMs and to reconstitute membrane proteins with preserved functionality.¹⁷⁻¹⁹ Moreover, successful attempts at automated BLM formation have been reported.²⁰ A robustness improvement has been achieved by supporting¹² or encapsulating²¹ a BLM by a hydrogel matrix. Supporting a BLM with a free-standing crystallized

monolayer of bacterial S-protein has also provided for better sturdiness.²² Stability and noise performance have been further targeted primarily via reduction of BLM area. Several strategies on fabrication of microapertures have been developed.²³⁻²⁵ Recently, multiporous materials with submicrometer pore width have been employed. Stable BLMs were spread over anodized porous silicon^{26,27} and alumina^{28,29}. Similarly, porous silicon nitride³⁰ and polymer³¹ substrates fabricated by means of microdevices technology yielded robust well-sealing BLMs.

Patch clamp advances. With respect to patch clamp, on the other hand, a demand has emerged for a high-throughput drug screening assay. The focus has thus moved from the patch pipette towards the planar patch clamp geometry. In addition to the potential applicability for pharmacology, the planar concept offers lower background noise and facilitates concomitant application of complementary investigation techniques.³² Successful whole-cell³³ and single-channel³² planar patch clamp measurements on cells were delivered by single microapertures in glass substrates. Recordings from ion channel proteins from cells patched at single apertures in silicon substrates have also been achieved, although an overall low yield of ‘gigaseals’ has been reported in parallel.³⁴ Arrays of microapertures in planar PDMS apertures have been used with success to patch frog oocytes.³⁵ As anticipated, planar patch clamp has pioneered automation in electrophysiology and opened the possibility for parallel drug screening targeted at membrane proteins.³⁶ To our knowledge, only the ‘whole-cell’ and ‘cell-attached’ configurations have been achieved by means of planar patch clamp to date, however. The benefits of the ‘excised’ patch clamp modes have thus far not been made use of.

Solvent-free lipid bilayers. Lately, direct formation of solvent-free pore-spanning lipid bilayers (psLB) via spreading/fusion of (proteo)lipid vesicles has become of major interest. As opposed to any variety of painted BLMs, a vesicle-derived psLB is completely free of organic solvents which, if present in the membrane, may affect the character of the lipid environment and thus alter the behavior of proteins or peptides under study. Unlike patch clamp of cells, it allows for precise control of the lipid composition of the bilayer, and elimination of artifacts related to the presence of other channel/pore species in the patch. In addition, it offers an elegant way to form a free-standing bilayer and simultaneously reconstitute TM proteins, thus avoiding the most critical step of membrane protein research in artificial matrices. Functional reconstitution of complex proteins into BLMs after they had been spanned over an orifice has proved to be challenging.³⁷ Native tissue preparations where protein activity is fully preserved are, however, oftentimes predominantly composed of proteovesicles that might be directly employed in formation of psLBs. In addition,

numerous protocols for functional reconstitution of delicate proteins into liposomes of a desired lipid composition have been developed.³⁸

Vesicle-derived psLBs. psLBs from vesicles on surfaces with ordered cylindrical *blind* pores were formed and investigated previously.³⁹⁻⁴² Unfortunately, low-resistance electrical access to the bilayer is possible only if the challenge of introducing a suitable electrode inside the pore is resolved.³¹ In addition, the contents of the medium filling the cavity cannot be reached without disrupting the BLM. Unlike blind pores, *through* pores do not suffer from such access limitations. Fluorescence and atomic force microscopy showed that psLBs can be spanned over through nanopores in multiporous substrates by fusion/rupture of vesicles^{40, 41} or adhesion of cell membrane fragments.⁴³ Spanning all of the pores of such a multiporous substrate can be a problem. Full coverage is a prerequisite for DC electrical measurements at low noise and low background currents, however. Good sealing resistances were obtained for psLBs from giant unilamellar vesicles (GUVs) over single pores in silicon nitride diaphragms⁴⁴ and glass cover-slips.⁴⁵ In both cases, though, the pore size was in the micrometer range, and there was little control over the process of bilayer formation. Moreover, the presence of charged lipids in the GUV lamella was required in the work of Schmidt et al.⁴⁴ Sealing npsLBs derived from large unilamellar vesicles (LUVs) were formed recently over through nanopores in Si₃N₄ diaphragms.⁴⁶ Again, however, only diaphragms with single pores were used for current measurements, and the peculiarities of the setup (e.g. a non-faradaic AFM tip holder as an electrode) did not allow for standard electrophysiological recordings. Most recently, formation of npsLBs from LUVs over functionalized porous alumina has been explored.⁴⁷ Although a substantial increase of substrate resistance was observed, the GΩ range has not been attained on these multiporous substrates. As pointed out by the authors, the remaining conductance was most likely due to incomplete pore coverage with bilayers.

1.3. An ideal system for electro-based investigations of TM proteins

Some general characteristics can be identified that an ideal platform intended for electrical studies of TM transporters, carriers, channels, and pores should exhibit:

1. **Robustness and stability.** The (lipid) matrix should remain in a steady state and exhibit constant electrical properties over prolonged (~ tens of hours) periods of time. Duration of an experiment should in no case be constrained by a limited lifetime of the platform. Steadiness should not be affected by TM DC potentials up to ~300 mV. The platform should also be robust to slight mechanical disturbances arising from perfusion/manipulation/mechanical noise.

1. Introduction

2. **Bilateral electrical and chemical accessibility.** Independent electrical access to both sides of the membrane is a must if closed-circuit electrical measurements across the membrane are to be conducted. The ability to reach both sides of the membrane chemically is of great benefit if change of content of the bathing medium on either side of the entity under study is required.
3. **Low background.** The intrinsic electrical resistance of the platform matrix should be high enough ($> 1 \text{ G}\Omega$) so as not to induce substantial background currents and leaks.
4. **Control over environment.** Functionality of TM proteins is often very sensitive to subtle changes in the character of the lipid environment they are reconstituted in. The chemical composition and the physical state of the matrix should thus be well tunable. Primarily, conditions equivalent to or comparable with the natural surroundings of the protein should be attainable. Conversely, if relationships are to be explored between environment character on one side and protein structure and functionality on the other side, the ability to easily alter matrix properties is crucial.
5. **Unrestricted hydrophilic extramembrane space.** Correct folding of the extramembrane (EM) portions of a TM protein is as essential for unaltered functionality as the folding of the TM domains. No structures should thus exist on either side of the membrane that would restrict the EM domains sterically.
6. **Target signal purity.** Presence of protein moieties other than the one of interest in the supporting matrix may give rise to artifacts in the measured signals. A possibility to deactivate or eliminate the potentially interfering structures would therefore be welcome.
7. **Adequate number of functional units.** Conductance per transmembrane functional unit ranges from $\sim 10^{-17} \text{ nS}$ for active ion transporters to $\sim 10^{-8} \text{ nS}$ for large protein or polypeptide pores. Measurements of currents of magnitudes below $\sim 1 \text{ pA}$ generally lack the required precision. Apparently, a single large pore present in the supporting matrix may conduct currents of sufficient magnitudes, whereas hundreds of thousands of transporter units functioning in unison may be needed to generate a signal of acceptable magnitude. Even at very high protein packing densities, the total area occupied by such numbers of units becomes substantial. The platform should be able to accommodate protein at a quantity sufficient to produce a signal of satisfactory quality.
8. **Versatility in measured signal.** DC current or voltage recordings can provide excellent temporal resolutions of fast events. AC measurements, on the other hand, can be informative of a broader spectrum of electrical properties of a system (e.g. parallel capacitance, series

resistance, etc.). Compatibility of the platform with both AC and DC measurement techniques would therefore be favorable.

2. Objectives

It follows from the above that methods of straight-forward formation of solvent-free BLMs from vesicles remain restricted to single pores. The attempt of Schmitt et al.⁴⁷ to seal vastly multiporous functionalized AlO_x with LUVs failed. Sondermann et al.⁴⁵ succeeded in forming GUV-derived npsLBs over single pores in thin glass slides, which, however, do not allow for the fabrication of arrays of densely packed narrow pores. The substrates of Schmidt et al.⁴⁴, on the other hand, were well suited for such arrays, yet the authors did not extend their single-pore endeavors to pore clusters. Moreover, their approach to spanning the npsLBs was restricted to charged vesicles and functionalized surfaces.

The objective of this thesis has been to establish a platform exhibiting *solvent-free* bilayer lipid membranes spanning over *arrays of through* nanopores. High temporal stability and total resistance in the GΩ range have been targeted so as to make recordings of ionic currents through single channel proteins possible. The project proceeded through the following stages (not necessarily in the listed order):

1. selection of an appropriate substrate allowing for fabrication of arrays of through nanopores and exhibiting sufficient mechanical sturdiness to manipulation and fluidic perfusion; design of a suitable cell for the particular substrate with bilateral perfusion and electrical access by low-impedance electrodes
2. formation of planar SLBs from vesicles on non-porous surfaces of the substrate of choice, with the option to functionalize the surface of the substrate and alter the ionic composition of the aqueous medium and the lipid composition of vesicular envelopes, if necessary
3. fabrication of arrays of through nanopores of limited size and pore count; characterization of the pores in terms of size, shape, topography, pore-to-pore distance, etc.
4. spanning of npsLBs over pores and arrays of pores followed electrically by AC impedance measurements; assessment of seal resistance and membrane stability in view of recording of ionic currents through channel protein; adjustment of platform parameters to comply with the former

2. Objectives

5. delivery and insertion of microbial channel*-forming peptides in the npsLBs; assessment of assembly of transmembrane conductive channels by AC impedance; DC voltage clamp recordings of ionic currents through peptide-formed channels with single-channel resolution

* To avoid confusion, the term ‘channel’ will be used throughout this work to address a transmembrane conductive assembly of microbial peptide monomers. The term ‘pore’, on the other hand, will be reserved to a hole in a substrate (mostly in an Si₃N₄ diaphragm) that the npsLBs are suspended over.

3. Methods and materials

3.1. Background and theory

3.1.1. Focused electron and ion beams⁴⁸⁻⁵³

A high degree of analogy exists between a focused ion beam system (FIB) and an electron beam system, the scanning electron microscope (SEM). In these systems, the beam of particles is directed towards the sample, and upon interaction it generates signals that are used to create high magnification images of the sample. As the beam is well controlled in size and position and the signals are strong enough to be detected without excessive noise, these kinds of tools are very powerful to analyze samples in great detail over a wide range of magnifications.

In an SEM, electrons are accelerated and focused onto the sample surface. The beam can be scanned over the sample surface to create an image, or can be controlled by a patterning function to locally expose the sample to the beam, as for example used in e-beam lithography. These same basic functionalities are found in an FIB system. The most fundamental difference between SEM/TEM and FIB is the use of ions instead of electrons to create the primary beam. This has major consequences for the interactions that occur at the sample surface. The characteristics of typical focused ion and electron beams are summarized in Table 3-1.

Table 3-1. A comparison between FIB and SEM including particles, beams and signals.⁴⁸

		FIB	SEM	Ratio
Particle	type	Ga ⁺ ion	electron	
	elementary charge	+1	-1	
	particle size	0.2 nm	0.00001 nm	20000
	mass	1.2×10^{-25} kg	9.1×10^{-31} kg	130000
	velocity at 30 kV	2.8×10^5 m/s	1.0×10^8 m/s	0.0028
	velocity at 2 kV	7.3×10^4 m/s	2.6×10^7 m/s	0.0028
	momentum at 30 kV	3.4×10^{-20} kgm/s	9.1×10^{-23} kgm/s	370
	momentum at 2 kV	8.8×10^{-21} kgm/s	2.4×10^{-23} kgm/s	370
Beam	size	nm range	nm range	
	energy	up to 30 kV	up to 40 kV	
	current	pA to nA range	pA to uA range	
Penetration depth	in polymer at 30 kV	60 nm	12000 nm	
	in polymer at 2 kV	12 nm	100 nm	
	in iron at 30 kV	20 nm	1800 nm	
	in iron at 2 kV	4 nm	25 nm	
Signal* (average number of sputtered particles per 100 incident particles at 20 kV)	secondary electrons	100 - 200	50 - 75	
	back scattered electron	0	30 - 50	
	substrate atom	500	0	
	secondary ion	30	0	
	x-ray	0	0.7	

* Some of the figures are averages due to dependence on the particular material involved.

3.1.1.1. Electron and ion beam columns

A. Electron beam column

In a typical SEM, an electron beam (e-beam) is thermionically emitted from an electron gun fitted with a tungsten filament cathode. Tungsten is normally used in thermionic electron guns because it has the highest melting point and lowest vapor pressure of all metals, thereby allowing it to be heated for electron emission, and because of its low cost. Other types of electron emitters include lanthanum hexaboride (LaB_6) cathodes, which can be used in a standard tungsten filament SEM if the vacuum system is upgraded and field emission guns, which may be of the cold-cathode type using tungsten single crystal emitters or the thermally-assisted Schottky type, using emitters of zirconium oxide. The electron beam, which typically has an energy ranging from a few hundred eV to 40 keV, is focused by one or two *electromagnetic* condenser lenses to a spot about 0.4 nm to 5 nm in diameter (Figure 3-1). The beam passes through pairs of scanning coils or pairs of deflector plates in the electron column, typically in the final lens, which deflect the beam in the x and y axes so that it scans in a raster fashion over a rectangular area of the sample surface. Magnification in an SEM can be controlled over a range of up to 6 orders of magnitude from about $25\times$ to $250000\times$. Unlike optical and transmission electron microscopes, image magnification in the SEM is not a function of the power of the objective lens. SEMs may have condenser and objective lenses, but their function is to focus the beam to a spot, and not to image the specimen. Provided the electron gun can generate a beam with sufficiently small diameter, an SEM could in principle work entirely without condenser or objective lenses, although it might not be very versatile or achieve very high

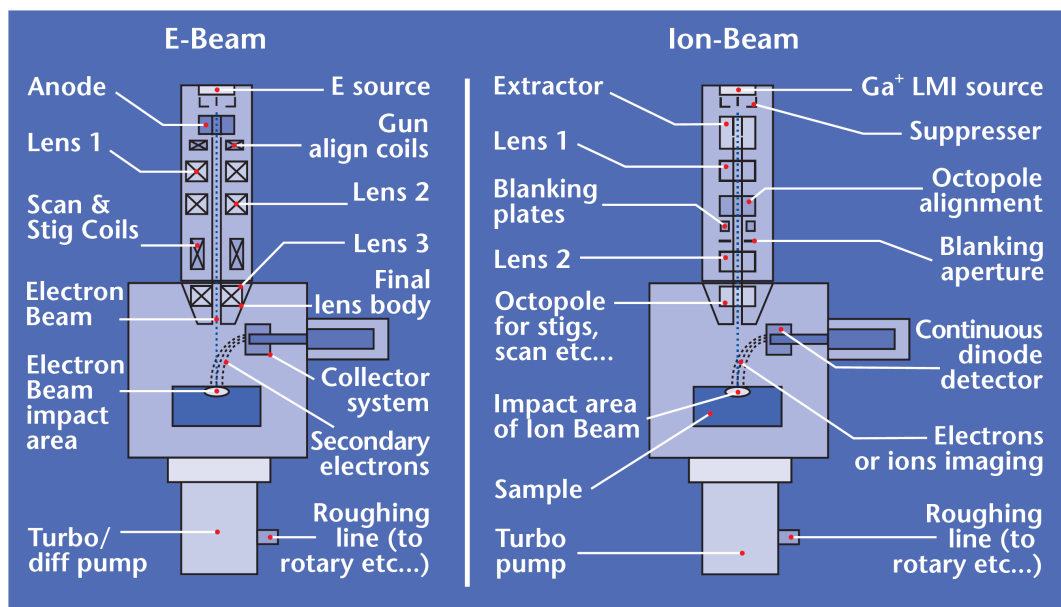


Figure 3-1. Schematic presentation of the SEM and FIB instruments (adopted from ref. [48]). Noteworthy are the many design similarities between the instruments.

resolution. In an SEM, as in scanning probe microscopy, magnification results from the ratio of the dimensions of the raster on the specimen and the raster on the display device. Assuming that the display screen has a fixed size, higher magnification results from reducing the size of the raster on the specimen, and vice versa. Magnification is therefore controlled by the current supplied to the x,y-scanning coils, and not by objective lens power.

B. Ion beam column

The most common ion source type used in FIB instruments is the liquid metal ion source (LMIS), for it provides the brightest and most highly focused beam of the existing ion source types. There are a number of different types of LMIS sources, the most widely used being a Ga-based blunt needle source. Ga has decided advantages over other LMIS metals such as In, Bi, Sn, and Au because of its combination of low melting temperature (30°C), low volatility, and low vapor pressure. The low melting temperature makes the source easy to design and operate, and because Ga does not react with the material defining the needle (typically W) and evaporation is negligible, Ga-based LMISs are typically more stable than other LMIS metals. During operation, Ga flows from a reservoir to the needle tip (with an end radius of about 10 μm), where it is extracted by field emission. A large negative potential between the needle and an extraction electrode generates an electric field of magnitude 10^{10} V/m at the needle tip. The balance between the electrostatic forces and the Ga surface tension wetting the tapered W needle geometry results in the formation of a single Taylor cone at the needle tip. For typical emission currents used in FIB microscopes (~ 2 μA), a cusp forms at the tip of the Taylor cone with a tip radius of approximately 5 nm.

The simplest and the most widely used ion beam (i-beam) columns consist of two lenses (a condenser and objective lens) to define the beam and then focus it on the sample, beam-defining apertures to select the beam diameter and current, deflection plates to raster the beam over the sample surface, stigmation poles to ensure a spherical beam profile, and a high-speed beam blanker to quickly deflect the beam off the sample and onto a beam stop such as a Faraday cup (Figure 3-1). Because the focusing strength of an electromagnetic lens is directly related to the charge/mass ratio of a particle, it is impractical to build electromagnetic lenses for ions (which would weigh thousands of kilograms); thus, focusing and steering are performed using *electrostatic* components rather than the electromagnetic components used for electrons. The size and shape of the beam intensity profile on the sample determines the basic imaging resolution and micromachining precision. Generally, the smaller the beam diameter, the better the achievable resolution and milling precision. However, the ultimate spatial resolution for FIB imaging is, in fact, limited by

sputtering and is thus sample-dependent. In modern FIB systems, the imaging resolution determined by the sputter-limited signal/noise usually is about 10 nm.

3.1.1.2. Beam – sample interactions

A. Interactions between electron beam and sample

When the primary electron beam interacts with the sample, the electrons lose energy by repeated random scattering and absorption within a teardrop-shaped volume of the specimen known as the interaction volume, which extends from less than 100 nm to around 5 μm into the surface. The size of the interaction volume depends on the electron's landing energy, the atomic number of the specimen and the specimen's density. The energy exchange between the electron beam and the sample has both an elastic and an inelastic contribution (Figure 3-2A). Secondary electrons (SE) are created by inelastic collisions between the high-energy electrons in the illuminating beam (so-called "primary" electrons) and outer shell electrons of the atoms in the sample. Such collisions knock the low-energy electrons out of their orbits. Backscattered electrons (BSE) are created by elastic reflections of the primary beam electrons from the nuclei of the target atoms. Finally, emission of X-ray radiation is induced upon collisions of primary electrons with inner shell electrons of the sample.

B. Interactions between ion beam and sample

Ion kinetic energy and momentum are transferred to the solid through both inelastic and elastic interactions. In inelastic interactions (called electronic energy loss), ion energy is lost to the electrons in the sample and results in ionization and the emission of ion-induced secondary electrons (ISEs) and electromagnetic radiation from the sample. In elastic interactions (called nuclear energy loss), ion energy is transferred as translational energy to target atoms and can result

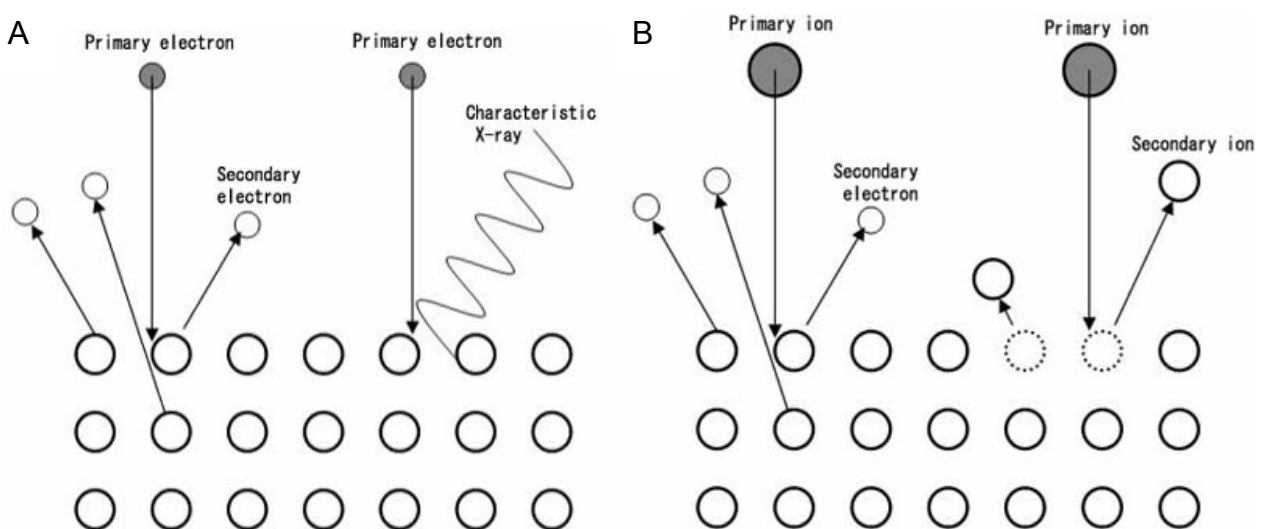


Figure 3-2. Irradiation of a solid surface with an electron (A) and an ion (B) beam (adopted from ref. [51]).

in displacement of sample atoms from their initial sites and sputtering of (ionized) atoms from the sample surface (Figure 3-2B). The most widely accepted concept for ion–solid interactions is the collision cascade model.^{49,52} For the case of 5–30 keV Ga impinging on most solids, the collision cascade involves a series of independent binary collisions (the linear collision cascade regime). If the translational energy transferred to a target atom during a collision exceeds a critical value called the displacement energy, the atom will be knocked out of its original site, for example, creating an interstitial–vacancy pair in a crystalline sample. This primary recoil atom may have sufficient energy to displace further sample atoms (secondary recoils), thus generating a volume where large numbers of atoms have excess kinetic energy. If a displacement collision occurs near the surface, the recoil atom may be emitted from the solid and lead to sputtering. The displacement energy (typically on the order of 20 eV) is much larger than the binding energy for the atoms (of the order of 1 eV), reflecting the fact that the collisions are nonadiabatic, because of the very short time scale. After approximately 10^{-11} s, the 5-30 keV Ga ion comes to rest in the solid, and the energies of all particles participating in the cascade have decreased below the displacement energy. At this point, the collision cascade has ended. What remains are the emitted particles and radiation, and ion beam damage such as lattice defects, incorporated Ga, and heat, all of which may continue to interact and evolve. Monte Carlo molecular dynamics calculations are well suited to simulating ion–solid interactions. Such calculations for 30 keV Ga into elements from Li to Bi show that roughly two times as much of the ion energy is lost to nuclear energy losses than to ionization energy losses (the former from interactions with the nucleus of an atom and the latter from interactions with the electrons).⁵² Of the nuclear energy losses, the majority is lost through sample atom vibrations or heating rather than through vacancy formation. The projected and lateral ranges of the 30 keV Ga scale inversely with the sample density and are between 10 nm and 100 nm (projected) and between 5 nm and 50 nm (lateral).

3.1.1.3. Capabilities of focused electron and ion beams

A. Imaging

Imaging by means of a focused e- or i-beam is done by rastering the beam over a sample surface and collecting the emitted particles and electromagnetic radiation by dedicated detectors (Figure 3-3). The SEM takes advantage of the fact that two distinct types of electrons are generated (low-energy SE and high-energy BSE) to provide different imaging modes. Through the use of a variably biased detector entry mesh the behavior of the low-energy secondary electrons can be manipulated. A positive charge on the mesh attracts the SEs to the detector. Images obtained in the SE mode of operation show extremely high edge definition and emphasize the small detail on the

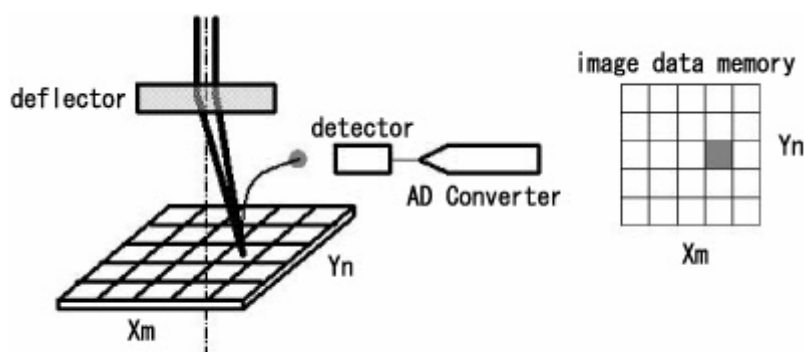


Figure 3-3. Schematic of a scanning microscope. The focused beam scans the sample surface. A detector acquires the secondary signal generated from the sample surface through beam irradiation. The detected intensity is saved in image data memory with respect to pixel coordinate.

surface of the samples. On the other hand, applying a negative bias to the detector mesh will cause SEs to be repelled from the detector. Images acquired in this BSE mode are derived from backscattered signal only, as the high-energy BSEs are unaffected by the small negative bias on the cage and strike the detector anyway. Since BSEs move in line-of-sight paths, the shadows caused by high areas blocking BSEs from lower areas are much accentuated, emphasizing the overall topography of the sample surface. In addition to electrons, an alternative image can be constructed based on capture of emitted X-rays by a specialized detector. In analogy to SE detection with the SEM, imaging in an FIB is based on detecting the ISEs. Typically, 1–10 electrons with energies below 10 eV are generated per incoming 5–30 keV Ga ion. These electrons are created by both kinetic and potential emission from the top few atomic layers where the primary ion impacts the solid as well as where backscattered or sputtered particles exit the sample. The total low-energy electron yield depends strongly on surface oxidation and contamination and thus will change as the surface is sputter-cleaned and Ga is incorporated. Ion beams are not as finely focused as electron beams and, partly for this reason, they generally offer lower resolution. However, the contrast mechanisms for ISE generation are different from those for SE generation and can offer complementary information about a sample surface. Both SE and ISE images show contrast due to surface topography and material differences. However, ISE imaging typically delivers stronger channeling contrast from crystals than SE imaging. The contrast due to crystal orientation is easily distinguished from material contrast, because crystal contrast changes with the incidence angle of the ion beam and material contrast does not. In ideal samples such as Cu or Au, ISE channeling contrast can reveal twin lamellae as narrow as 20 nm and grains as small as 50 nm. The SE and ISE images are also often distinguished by the amount of charging generated in insulating samples. Presumably because of differences in the low-energy/secondary electron yields and the fact that the Ga implantation creates a thin conducting layer at the sample surface, the FIB can often be used to image uncoated samples that are difficult to image even with low-voltage SEM. It is also possible

to use the (secondary) ion signal itself to create an image and in, for example, crystalline materials such as metals it will produce an excellent additional contrast that shows the different grains of the material. The contrast of the ion signal can be different from the SE contrast (channeling, voltage contrast) and therefore ion imaging can give additional information. On the other hand, ion beam imaging always results in some Ga implantation and sputtering of the sample surface.

B. Patterning

i. E-beam lithography

Electron beam lithography (EBL) is the practice of scanning a beam of electrons in a patterned fashion across a surface covered with a film of resist (irradiation-sensitive organic material) and of selectively removing either exposed or non-exposed regions of the resist ('developing'). The purpose is to create very small structures in the resist that can subsequently be transferred into another material for a number of purposes, for example for the creation of very small electronic devices. EBL has found wide usage in mask-making used in photolithography, low-volume production of semiconductor components, and research and development. The primary advantage of EBL is that it is one of the ways to beat the diffraction limit of light and make features in the nanometer regime. The reason for this is the short wavelengths (0.2-0.5 Å) exhibited by the electrons in the energy range that they are being used by EBL systems. However, the resolution of an electron lithography system may be constrained by other factors, such as electron scattering in the resist and by various aberrations in its electron optics. Just like optical lithography, electron lithography also uses positive and negative resists, which in this case are referred to as electron beam resists (or e-beam resists). E-beam resists are e-beam-sensitive materials that are used to cover the wafer according to the defined pattern. The major difference to optical lithography is the lack of need for a mask, as an EBL system simply 'draws' the pattern in the resist layer using the electron beam as its drawing pen. On the other hand, the key limitation of electron beam lithography is throughput, i.e. the very long time it takes to expose an entire silicon wafer or glass substrate. A long exposure time leaves the user vulnerable to beam drift or instability which may occur during the exposure.

ii. FIB milling

Because of the sputtering action of the ion beam, the FIB can be used to locally remove or 'mill' away material. The milling process as such is a process of elastic atomic collisions. The milling rate ($\mu\text{m}^3/\text{s}$) is (linearly) proportional to the beam current and high amounts of material are removed with high beam currents. In addition, precise control is possible by the use of smaller spot sizes and therefore smaller currents. As the ion beam position is well controlled, milling in the material of

not only simple structures such as squares or round holes, but also more complex patterns is possible. Milling is the most powerful capability of the focused ion beam and directly related to the choice of ion, its energy range and the momentum of the particle. Milling allows the freedom to manipulate the sample, open it up in the third dimension and create a cross-section, or to create any possible shape as ‘carved in stone’. Not only the lateral position, but also the local depth can be controlled. For direct milling, the limiting feature size is typically about 10 nm. Quantitative aspects of sputtering are complicated and depend on the material, ion beam incidence angle, crystal orientation, and the extent of redeposition. As the incidence angle of the ion beam is increased, the intersection of the collision cascade with the sample surface increases, and the number of sputtered atoms per collision cascade increases. However, at the same time, the fraction of reflected or backscattered Ga ions increases. The combination of these two effects leads for amorphous or polycrystalline materials to a maximum in sputtering yield at an incidence angle of approximately 75–80°. The behavior is more complicated in crystalline material where both incident angle and channeling effects are present. The sputtering yield at a given incidence angle can vary by as much as a factor of 10 for strongly channeling crystal orientations. This is because for easy channeling orientations, the ion experiences only inelastic glancing-angle collisions with the atoms lying in a crystal plane and travels deeper into the crystal before causing elastic collisions, so that fewer atoms are sputtered from the surface. Finally, redeposition of material decreases the effective sputter yield and changes sputter profiles. The decreased yield comes about because redeposited material lands in the area being sputtered and must be sputtered a second time. Redeposition, along with the intensity tails of an ion beam profile and the decrease in sputter yield at high incidence angles, is given as a reason why completely vertical sidewalls cannot be cut with the FIB without over-tilting the sample.^{49,50,52}

Removal of atoms from the surface can be enhanced by the addition of local chemistry in the form of a gas delivery system. The delivery system locally supplies a chemical compound close to the surface impact point. This supply of gas can, for example, change the oxidation of released particles and may substantially speed up the milling process. In general, it will also reduce the local re-deposition of atoms released from the surface. Examples of gases that are used to enhance milling are I₂ and XeF₂.

C. FIB deposition

As FIB technology is frequently used for milling, an additional technique can convert the ion beam system into a deposition system allowing the addition of material instead of removing material. This is realized by means of the same gas delivery system introduced above. In this case, the

chemical gas compound often consists of an organic-metallic molecule such as methylcyclopentadienyl-Pt-(IV)-trimethyl. When this compound is exposed to the ion beam it will decompose locally and deposit Pt onto the surface. As the cracking of the molecule is not 100% efficient, some additional matrix molecules such as organic residues are always deposited. The purity of the deposit is therefore generally lower compared to, for example, chemical vapor deposits. The main advantage in comparison to chemical or physical vapor deposition is the high localization, and the capability to create different heights of the deposit in one exposure. In addition the direct deposition capability is flexible and does not require complex mask structures. Molecules are absorbed on the irradiated area, and by using the patterning capability of the system 3D structures can be grown at selected positions, with full control of size, position and height. The material deposited depends on the gas chemistry used and various options are possible. Most commonly available gas chemistry allows the deposition of Pt, W, SiO₂, C. Important characteristics for the depositions are the minimum size (typically around 50 nm), the purity of the material, and its conductivity (usually lower than for pure metal).

3.1.1.4. Downsides related to focused electron and ion beams

A. Specimen charging

Charging is the condition when a material cannot effectively conduct the beam energy imparted to it. Upon e-beam irradiation of a thick material, a large fraction of the probe current remains in the specimen as the beam electrons lose all of their initial energy and are captured by the specimen. This charge flows to ground if the specimen is a conductor and a suitable connection exists. If the ground path is broken, even a conducting specimen quickly accumulates charge and its surface potential rises. Non-conducting specimens will obviously accumulate charge. The ensuing image will ‘glow’ or cause streaks or general distortion in the image as electron production is artificially enhanced and the beam is unintentionally deflected.

Excess charge accumulates on the surfaces of substrates made of insulators when a primary FIB is being scanned across them. This charging is usually positive, since it results from the deposition of positive charge in ionic gallium delivered to the sample by FIB and the subsequent generation of secondary electrons that leave the sample. In the worst case, the image completely disappears (since the secondary electron cannot escape from the sample), and the milling and deposition process become unmanageable. The charging of insulators can be prevented (in part) by electron-irradiation, UV irradiation, conductive-film evaporation, a conductive-membrane cover, or a conductive-paste coating for charge neutralization.

B. Carbon contamination

Contamination can be a serious limitation to low voltage microscopy.⁵⁴ Contamination results from the interaction of the electron beam with residual gases and hydrocarbons on the specimen surface. SE imaging in particular is vulnerable to contamination given the low energy level of SEs. The electron source, the chamber vacuum pump, or the conductive tapes and paints that are used to attach samples to their holders can all be sources of contamination. Carbon-based surface layers are particularly prevalent in samples that have been imaged in the SEM after FIB milling.

C. Specimen damage

A major drawback of FIB imaging and machining, particularly for TEM samples, is the damage created by the ion beam. As the ion dose increases, the individual disordered cascade regions overlap and a damaged surface layer is formed. Depending in particular on the sample material and temperature, the ion beam damage can take the form of sample surface amorphization, point defect creation, dislocation formation, phase formation, grain modification, or other unusual effects. The loss of electron beam energy in the specimen occurs mostly in the form of heat generation at the irradiated point. Polymer materials and biological specimens, which are generally not resistant to heat, are easily damaged by the electron beam, because of their low heat conductivity.

D. Ga incorporation

Imaging and milling with Ga ions always result in the incorporation of Ga near the sample surface. As the sample surface is sputtered away at a rate proportional to the sputtering yield and the ion flux (ions per area per time), the Ga is implanted further into the sample, and a steady-state profile of Ga is reached. The maximum Ga concentration occurs at steady state after the removal of target material to a depth roughly equal to the ion range and is constant over a depth also roughly equal to the ion range.

3.1.2. Atomic force microscopy⁵⁵⁻⁶⁰

The atomic force microscope (AFM) is a scanning probe imaging and sensing device useful for physical and chemical studies. In its basic configuration, it measures the microscopic surface profile of a near-planar target by mechanically scanning a tiny probe across it in a raster pattern. The probe rises and falls in accordance with the surface profile. As it does so, its position is sensed and captured digitally. That captured topogram can then be rendered as a photograph-like image, reminiscent of an optical micrograph. The three dimensional profile of a surface is measured with the AFM by monitoring the position of the probe in three dimensions as it scans. A feedback control system maintains the force between the probe and the surface sensibly constant during the

scan. The probe tip thus follows the surface profile, as one might do with a finger tip at a more macroscopic scale.

3.1.2.1. AFM implementation

Figure 3-4A shows the elements of a basic atomic force microscope. The probe tip is positioned in three dimensions by three mutually orthogonal actuators. Each actuator is a piezoelectric ceramic transducer (PZT). PZTs are well suited to the small motions required by the AFM. Their travel is approximately linear in the applied voltage when used in the AFMs. X and Y are coordinate axes nominally parallel to the surface under test (SUT), and the Z axis completes a right handed Cartesian coordinate system. The Z-axis positioner thus moves the probe toward (negative Z) or away (positive Z) from the SUT, while the X and Y positioners move the probe in a nominal object image plane. In normal operation, the X and Y position is programmed in a raster scanning path, while the Z position is tightly controlled relative to the SUT by a feedback control loop. The Z-axis error signal is derived from a force transducer that measures the force on the probe tip. The transducer output is differenced against a fixed voltage, which corresponds to a setpoint (target) force. The error signal is amplified and drives the Z-axis PZT. This control loop acts to reduce the error signal, and hence the probe-to-SUT distance, near to zero. The feedback loop thus causes the probe to closely follow the undulations of the SUT while the X-Y PZTs scan the probe over a rectangular image area. Meanwhile, the control voltage applied to the Z-PZT provides a convenient representation of the elevation of the probe and surface is used to generate an image or topogram of the surface.

3.1.2.2. Light-lever force sensing

High sensitivity in the force transducer of an AFM is typically achieved by a simple geometric optical device known as the light lever (Figure 3-4B). A low-power laser diode beam is reflected

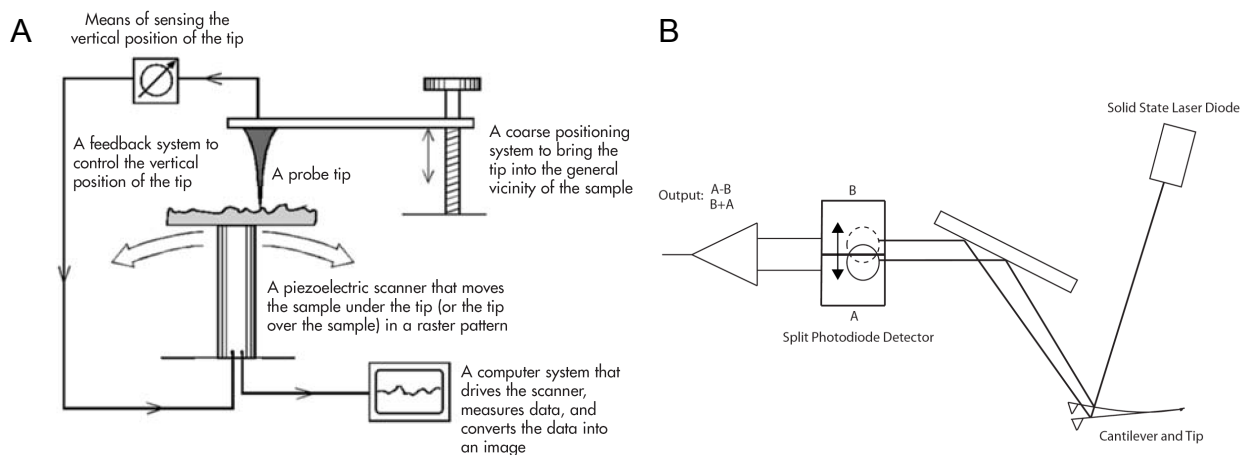


Figure 3-4. The atomic force microscope. Schematic of the operation principle (A) and AFM beam deflection detection – the “light-lever” (B). Images were adopted from refs. [55] and [57], respectively.

from the top of the cantilever to a distant position-sensitive photo detector. The detector consists of two closely spaced photodiodes whose output signal is collected by a differential amplifier. Angular displacement of cantilever results in one photodiode collecting more light than the other photodiode, producing an output signal (the difference between the photodiode signals normalized by their sum) which is proportional to the deflection of the cantilever. It is capable of detecting cantilever deflections lower than 1 Å (thermal noise limited). A long beam path (several cm) amplifies changes in beam angle.

3.1.2.3. Probe-surface interactions

At the nanoscopic scale, the force between an AFM probe and a hard surface does not have an abrupt brick wall character. Not only are fundamental interatomic forces finite in extent, there is also the problem of surface contamination. AFMs are usually operated in ambient environmental conditions (room temperature, atmospheric pressure, ambient air). As a result, there is invariably a surface layer comprising water and miscellaneous hydrocarbons. This layer is thick enough relative to the nominal probe operating height that the probe tip is almost always immersed in it (Figure 3-5A). The forces between probe and surface, to the extent that they are position-dependent only, i.e. are lossless, can be represented by an effective potential energy. As apparent in Figure 3-5B, the interaction between the probe and the surface falls into one of three zones:

- Large separations, where the probe experiences no significant influence from the surface.
- An attractive zone, caused by capillary attraction between the probe and the contaminant layer, which is thick compared to the range of the interatomic forces from the surface. This zone is usually associated with the formation of a meniscus.
- A ‘hard’ repulsive region, where the interatomic forces from the surface dominate those from the contaminant layer.

Topographic AFM modes. There are two primary methods for measuring the force between a probe and a sample: contact mode and vibrating mode. Contact mode entails a direct quasi-static

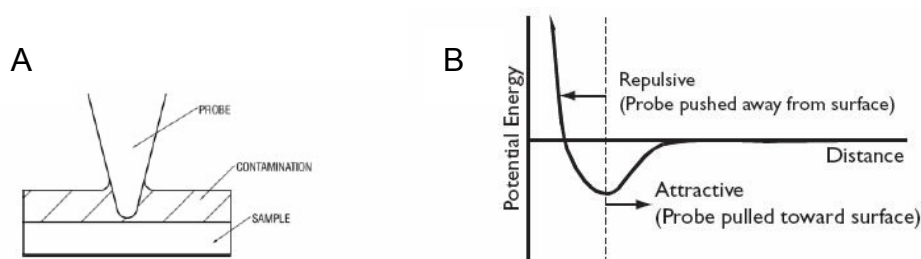


Figure 3-5. (A) In ambient, the AFM probe must pass through surface contamination before touching the surface under test. (B) An example of a potential energy diagram of a probe and a sample. The attractive regime is due to capillary forces from the surface contamination layer (images adopted from ref. [56]).

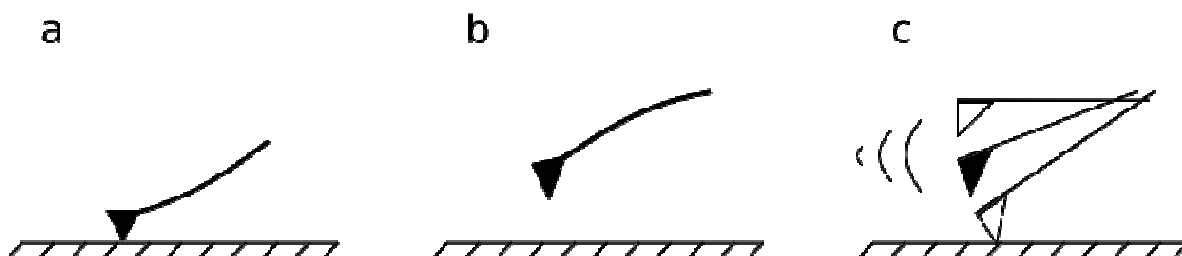


Figure 3-6. A schematic of the contact (a), non-contact (b) and tapping (c) AFM scanning modes.

force versus distance measurement, that is, a rather intimate contact between probe and surface. While producing accurate results, it tends to rapidly damage both probe and surface. Vibrating mode may be either large amplitude, in which the probe contacts the surface on every cycle (tapping), or small amplitude (non-contact). The individual topographical AFM modes are depicted in Figure 3-6 and their characteristics are summarized in Table 3-2.

Table 3-2. Comparison of the most common AFM topographical scanning modes.

AFM mode	Advantages	Disadvantages
Contact	<ul style="list-style-type: none"> • high scan speeds (throughput) • contact mode AFM is the only AFM technique which can obtain “atomic resolution” images • rough samples with extreme changes in vertical topography can sometimes be scanned more easily in contact mode 	<ul style="list-style-type: none"> • lateral (shear) forces can distort features in the image • forces normal to the tip-sample interaction can be high in air due to capillary forces from the adsorbed fluid layer on the sample surface • combination of lateral forces and high normal forces can result in reduced spatial resolution and may damage soft samples (i.e., biological samples, polymers, silicon) due to scraping between the tip and sample
Non-contact	<ul style="list-style-type: none"> • no force exerted on the sample surface 	<ul style="list-style-type: none"> • lower lateral resolution, limited by the tip-sample separation • slower scan speed than tapping and contact modes to avoid contacting the adsorbed fluid layer • non-contact usually only works on extremely hydrophobic samples, where the adsorbed fluid layer is at a minimum
Tapping	<ul style="list-style-type: none"> • higher lateral resolution on most samples (1 nm to 5 nm) • lower forces and less damage to soft samples imaged in air • lateral forces are virtually eliminated, so there is no scraping 	<ul style="list-style-type: none"> • slightly slower scan speed than contact mode AFM

3.1.3. Photolithography⁶¹

Photolithography is a process of patterning the surface of a material that makes use of a film of an organic photosensitive compound, the so-called photoresist. Typically, a pattern of features is induced in the photosensitive film by irradiation by UV-blue light through a lithographic mask. A

solubility difference is thus produced between the exposed and the unexposed regions of the film. ‘Development’ of the irradiated film removes its soluble parts and selectively exposes the underlying surface of the substrate. Conversely, the insoluble parts of the film remain in place, protecting the rest of the substrate. The features produced in the photoresist film are subsequently transferred onto the material by an etching process.

3.1.3.1. Photoresist

The photoresist is a viscous organic photosensitive compound. The major constituent is a polymeric resin (e.g. novolak, polymethylmethacrylate, polymethylglutarimide, polyimide, epoxy-based polymers, etc.) that defines the physical and chemical properties of the resist. Sensitivity of the resist to light is given by the presence a photo-active compound (PAC). The chemical interaction between the PAC and the resin is crucial for the desired change of solubility upon irradiation. A resin is thus always coupled to a specific PAC (e.g. novolak to diazoquinone or diazonaphthoquinone). To facilitate deposition and handling, the resin and the PAC are dissolved in an appropriate solvent. The photoresist may contain additional ingredients, such as adhesion promoters, stabilizing agents, etc.

3.1.3.2. Steps of the photolithographic process

Photoresist deposition (Figure 3-7, step a). The goals of a photoresist deposition procedure are 1) full coverage of the coated surface, 2) homogeneous thickness, and 3) smoothness of the resulting film. The photoresist is usually spin-coated or sprayed on the surface to be patterned. Thickness of a spin-coated resist film can be controlled elegantly by spin speed, whereby a fast spin generates a thin film and a slow spin gives rise to a thick film. Optionally, film thickness can be further reduced by photoresist dilution. Thickness of a spin-coated resist film is typically in the 1-5 μm range. Thick resist films can be produced by several repeated coating steps. In general, spraying yields thicker and rougher films than spin-coating. If minimization of resist losses is crucial, however, spraying may be a more efficient approach.

Softbake. After coating, the resist film still contains a (strongly resist-film dependent) remaining amount of solvent. Soft-baking increases the rate of solvent evaporation and thus reduces its content in the film. Thereby, sticking of the film to and/or contamination of lithographic masks is avoided, foaming of the resist due to generation of N_2 upon exposure is prevented, adhesion of the resist to the substrate is improved, etc. Softbake is typically done on a hot plate at $\sim 90^\circ$ and, depending on film thickness, lasts one to a few minutes.

Exposure (step b). The selective change of solubility of the desired parts of the photoresist film is induced by irradiation of the film through a lithographic mask. A standard lithographic mask is a plate of glass coated on one side with a Cr layer of several hundreds of nm in thickness. The features (down to ~ 500 nm in size) to be transferred onto the substrate had been etched into the Cr layer at mask production. Upon exposure, the Cr layer is in physical contact with the photoresist film. Due to diffraction, a gap between the mask and the resist may reduce the lateral resolution of the image. Common PACs exhibit absorption maxima in the near UV and blue region of light wavelength. A Hg light source, which is typically used to activate a photoresist film, exhibits three characteristic peaks in this range of wavelengths (Figure 3-8): the i-line (365 nm), the h-line (405 nm), and the g-line (436 nm). Some resists are broadband-sensitive (spectral sensitivity overlapping with all three lines), whereas other ones exhibit absorption spectra more narrow (i- and h-line, or purely i-line sensitive). Exposure dose has to be sufficient to induce complete photoreaction and hence maximum development rate. On the other hand, overexposure must be avoided to prevent artifacts due to possible irregularities in the mask or interference phenomena in the resist.

Development (step c). The parts of the photoresist film with high solubility (the exposed regions of

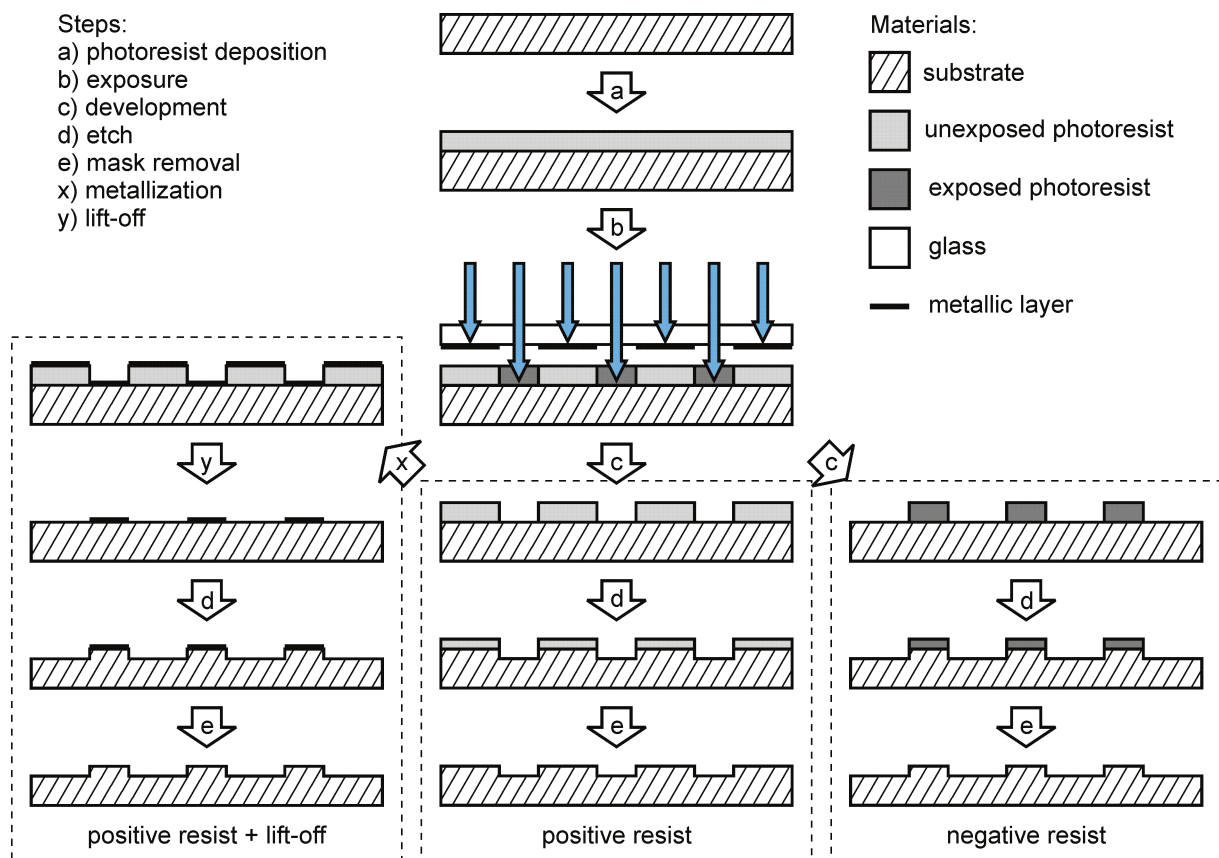


Figure 3-7. Schematic of the photolithographic process.

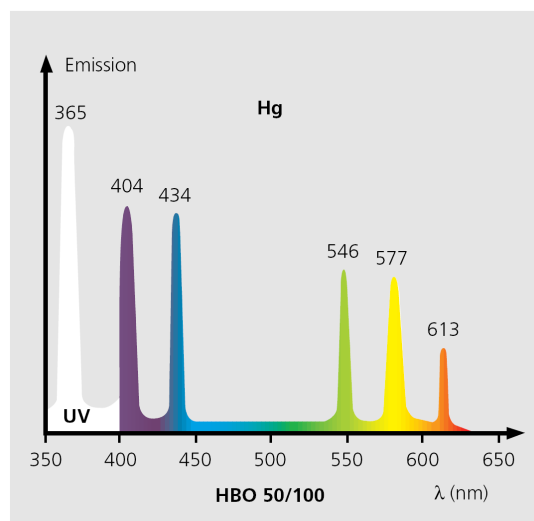


Figure 3-8. Schematic of an emission spectrum of a Hg discharge bulb, the typical source of light for irradiation of photoresist films in photolithography and for fluorescent microscopy.

a positive resist film or the unexposed regions of a negative photoresist film) are dissolved in an appropriate developer. For diazo-Novolak resins, for example, the developer is a simple alkaline aqueous solution, typically 0.05-0.3 M, of TMAOH, NaOH, or KOH. Development time must be sufficiently long to completely remove the highly-soluble resist, yet short enough not to induce substantial dissolution of the parts of the film that are meant to remain on the substrate (dark erosion). Another critical value is developer concentration, as the ratio of development and dark-erosion rates is a function thereof.

Hardbake. An optional final step of the process may be a bake of the substrate with the patterned photoresist film at temperatures $>130^{\circ}$. The hardbake is performed to increase the thermal, physical, and chemical stability of the developed resist structures for subsequent processes.

Transfer of pattern onto substrate (step d). In the final step, the pattern produced in the photoresist film is etched onto the substrate. The structured photoresist film remaining on the surface of the substrate after the preceding steps may be utilized directly as a mask for the (wet or dry) etching process. After etching, the remains of the resist are removed using acetone, the original resist solvent, or a dedicated remover (step e). Alternatively, the entire surface of the substrate, including the resist structures as well as the bare developed regions, is (evaporation- or sputter-) coated with a thin metallic layer (step x). The resist structures are then dissolved, or “lifted off”, and the underlying surface areas are uncovered (step y). Conversely, the previously developed regions of the surface remain coated with the metallic film. A robust metallic mask is thus produced on the surface that can be used in harsh and/or deep-penetrating etching processes. It should be noted that the mask generated by metallization and lift-off is inverse with respect to the structured resist film.

3.1.4. Optical microscopy⁶²⁻⁶⁴

3.1.4.1. DIC optical microscopy

Differential interference contrast (DIC), also known as Nomarski interference contrast, is a highly efficient microscopic contrasting technique that allows visualization of minute elevation differences in surfaces of unstained, transparent samples. DIC works on the principle of interferometry to gain information about the optical density of the sample. Features otherwise invisible can thus be well resolved. DIC works by separating a polarized light source into two beams which take slightly different paths through the sample. Where the length of each optical path (i.e. the product of refractive index and geometric path length) differs, the beams interfere when they are recombined. This gives the appearance of a three-dimensional physical relief corresponding to the variation of optical density of the sample, emphasizing lines and edges. DIC configurations in the transmitted and the reflected light are different, and are therefore described separately. Figure 3-9 shows a schematic of an upright optical microscope with both transmitted and reflected light modes.

DIC in transmitted light. Figure 3-10A shows the beam path of a DIC configuration in the transmitted light mode. The polarizer (1) on the condenser – near the aperture diaphragm – transmits only linearly polarized light. The birefringent prism (2) performs a vectorial decomposition of the previously linearly polarized light into two vibration directions which are perpendicular to each other, and laterally shifts these partial beams in such a way that a lateral displacement of $\Delta x = k\lambda$ occurs in the specimen (λ is the wavelength of the light used and k is a factor which normally is smaller than 1). The beams are focused on the sample (4) via condenser optics (3). If the two partial beams pass through exactly the same structures, no further path difference will occur in the specimen (cases A and C in Figure 3-10C). However, if the two partial

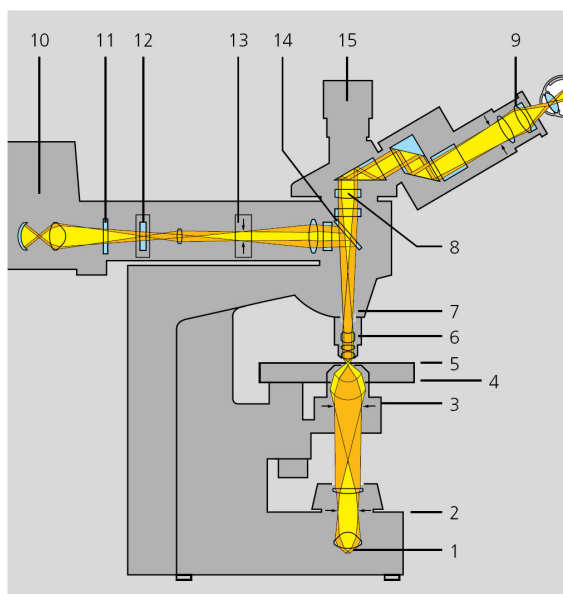


Figure 3-9. Schematic of a bimodal upright transmitted/reflected light optical microscope. 1 Built-in illuminator with collector, 2 Luminous-field diaphragm for transmitted light, 3 Aperture diaphragm in the transmitted-light condenser, 4 Transmitted-light condenser (front optics), 5 Specimen plane (focal plane), 6 Objective, 7 Pupil plane of the objective, 8 Tube lens, 9 Eyepiece, 10 High-pressure lamp with collector, 11 Heat-protection filter, 12 Filter slider / Beam stop, 13 Luminous-field diaphragm for epifluorescence, 14 Filter combination with beam splitter for epifluorescence, 15 Camera/TV adapter.

beams ‘see’ slightly different conditions, each of them will ‘experience’ its own path difference which accompanies it on the remaining path to the intermediate image (case B in Figure 3-10C). The light transmitting through the specimen is collected by the objective (5, Figure 3-10A). The second birefringent prism (6) cancels the splitting process again behind the objective, and analyzer (7) selects those components from the now phase-shifted wave trains which lie in its vibration direction. It is only now – with a common vibration plane – that the two partial beams can interfere with each other and therefore convert path differences to intensity differences which can be seen by the eye. A λ -plate (7a, λ) permits additional color contrast to be produced. The resulting images look like reliefs because this method displays only ‘lateral’ changes.

DIC in reflected light. In reflected light, DIC is simplified by the use of a single birefringent prism that both splits the beam on the way to the sample and combines it again on its way to the tube lens. The light arriving from the reflected-light illuminator (1) hits a polarizer (2,P) and is reflected, linearly polarized, of the beam splitter (3) towards the objective (5). A birefringent prism (4) is used in the path, which splits the polarized light beam into two partial beams on its way to the sample. These partial beams hit the sample (6) with lateral displacement from each other. As with transmitted light, if the surface is completely flat, nothing will happen. However, if there is a small step between the two partial beams, one of the two beams must travel a path which is $2\Delta h$ longer and is assigned this path difference. The reflected partial beams are combined again in the *same* DIC prism (4). They are further transmitted by the beam splitter (3) towards the analyzer (7), which is in fact a second polarizer rotated at 90° with respect to the first one (2). Beyond the analyzer, the beams feature the same vibration direction again, and can interfere with each other in the intermediate image. The path difference assigned on the surface then changes into grey values which can be seen by the eye: steps become visible as a relief. As an auxiliary object, the lambda plate (7a) changes the grey values into colors again.

3.1.4.2. Fluorescence optical microscopy

Fluorescence microscopy is designed to study properties of organic or inorganic substances using the phenomenon of fluorescence. Fluorescence is a luminescence (light emitted at low temperatures), in which the molecular absorption of a photon triggers the emission of a photon with a longer wavelength. The energy difference between the absorbed and emitted photons ends up as molecular rotations, vibrations or heat.

Photochemistry of fluorescence. Fluorescence occurs when a molecule, atom or nanostructure relaxes to its ground state after being electrically excited.

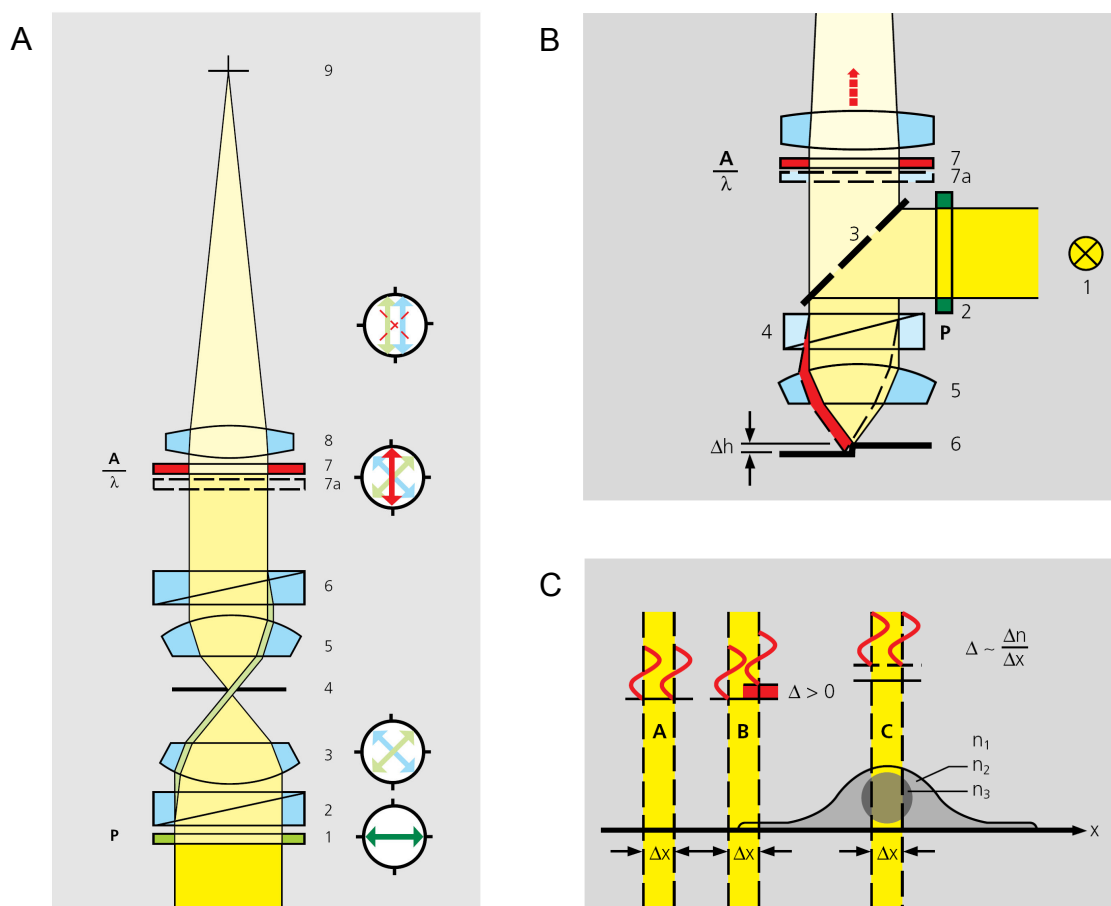


Figure 3-10. The DIC contrasting technique: light path in the transmitted (A) and reflected (B) light mode (see text for details). C – beam interference due to a difference in optical paths between neighboring regions of the sample.

$$\text{Excitation: } S_0 + h\nu_{ex} \rightarrow S_1 \quad \text{Eq. 3-1}$$

$$\text{Emission: } S_1 \rightarrow S_0 + h\nu_{em} \quad \text{Eq. 3-2}$$

Here, h is the Planck's constant, ν is the frequency of light, state S_0 is the ground state of the fluorophore (fluorescent molecule), and S_1 is its first (electronically) excited state. A molecule in its excited state, S_1 , can relax by various competing pathways. In addition to the (fluorescent) radiative relaxation, it can undergo 'non-radiative relaxation' in which the excitation energy is dissipated as heat (vibrations) to the solvent. Excited organic molecules can also relax via conversion to a triplet state which may subsequently relax radiatively via phosphorescence or by a secondary non-radiative relaxation step. Relaxation of an S_1 state can also occur through interaction with a second molecule through fluorescence quenching.

Quantum yield. The quantum yield of a fluorophore gives the efficiency of the fluorescence process. It is defined as the ratio of the number of photons emitted to the number of photons absorbed. The maximum fluorescence quantum yield is 1.0 (100%); every photon absorbed results in a photon emitted. Compounds with quantum yields of 0.10 are still considered rather fluorescent.

Lifetime. The fluorescence lifetime refers to the average time the molecule stays in its excited state before emitting a photon. Fluorescence typically follows a first-order exponential decay:

$$[S_1] = [S_1]_0 e^{-\Gamma t} \quad \text{Eq. 3-3}$$

where $[S_1]$ is the concentration of excited fluorophores at time t , $[S_1]_0$ is the initial concentration of excited fluorophores, and Γ is the decay rate, i.e. the reverse of fluorescence lifetime. Various radiative and non-radiative processes can de-populate the excited state. In such case the total decay rate is the sum over all rates. For commonly used fluorescent compounds typical excited state decay times are within the range of 0.5 to 20 nanoseconds.

Benefit of the Stokes shift. Fluorescence molecules can only absorb light of a certain wavelength. Each fluorophore exhibits its own, very specific absorption spectrum, depending on its internal structure and sometimes also on the surroundings. The (Stokes) shift of an emitted photon relative to an absorbed photon is ~20-50 nm. The excitation light can thus be completely filtered from the output signal using a combination of barrier filters and a dichroic mirror with a cutoff between the excitation and emission wavelength.

The fluorescence microscope. The beam path of an upright epifluorescence microscope is identical to that of the reflected light beam path in Figure 3-9. The light travels from a powerful mercury light source (10) via additional optical components to the fluorescence filter/beam splitter set (14, see also Figure 3-11A for a detailed schematic). The exciting light transmitted by the excitation filter is reflected at the dichroic beam splitter into the specimen (5) via the objective (6). The resulting emission is gathered by the objective (6) and transmitted by the dichroic beam splitter. The rays then pass through the emission (barrier) filter, where the remaining excitation light is filtered out. The tube lens (8) and the eyepiece (9) form the microscope image, which only consists of fluorescence light.

Light source. Fluorescence requires intensive short-wave light, therefore filament lamps are not suitable as light sources in fluorescence microscopy. Instead, a high-pressure mercury lamp is typically the light source of choice. Unlike the filament lamp, it uses the gas discharge principle and does not feature a continuous, but a discrete light spectrum (Figure 3-8). The ability to change between intensive lines and weak spectral ranges is a major benefit of this line emitter and is very helpful in fluorescence. Excitation is usually made with a single “line” and the fluorescence is viewed at a wavelength at which the light of the illuminator causes practically no disturbance.

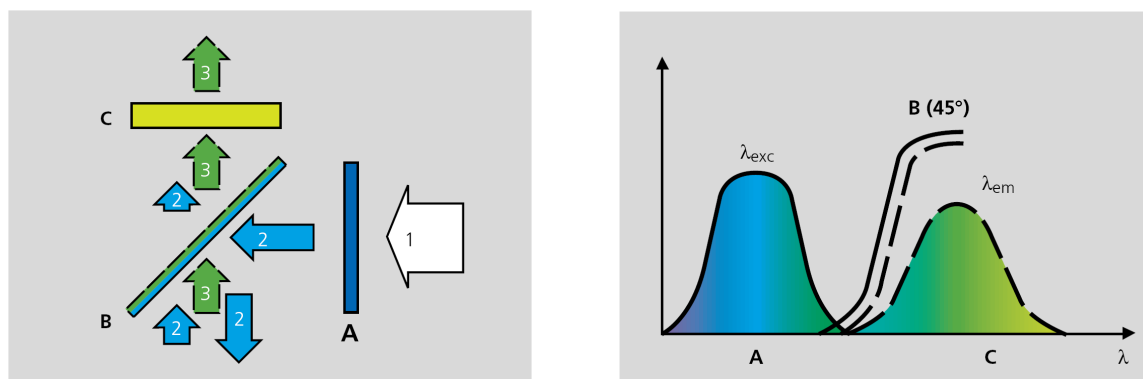


Figure 3-11. A - function of the filter combinations (see text). B – Typical individual spectral curves for the components of the filter combination: A – exciter filter, B – beam splitter, C – emission filter.

Filter/beam splitter set. The specific combination of filters and the beam splitter is crucial for the functioning of the fluorescence microscope. Filter combinations are arranged in the reflector area between the objective and the tube lens. These combinations determine the beam path of the excitation and emission light. The exciter filter (A, Figure 3-11A) filters almost monochromatic light (2) out of the light source radiation (1). The dichroic beam splitter (B) reflects the short-wave excitation light to the objective almost without any loss, but allows the fluorescence light (3) returning from the specimen via the objective to pass through almost completely. At the same time, most of the excitation light is reflected again and can therefore no longer affect the formation of the intermediate image. Above the beam splitter, the emission light and the remainder of the excitation light hit the emission (barrier) filter (C). Only the fluorescence light can pass the filter almost unhindered because its wavelengths are longer than those of the excitation light. In most cases, fluorescence filters are combinations of color lenses and interference filters. The interference filters have been given coatings precisely adapted to the wavelengths of the light. Such filters can be “tailor-made” and exactly meet the spectral requirements made on a fluorescence dye (Figure 3-11B).

3.1.5. AC impedance spectroscopy⁶⁵⁻⁶⁷

3.1.5.1. The notion of electrical impedance

Electrical *impedance*, defined as

$$\bar{Z}(\omega) = \frac{\dot{E}}{\dot{I}} \quad \text{Eq. 3-4}$$

is a measure of the ability of a circuit to resist the flow of electrical current. Electrochemical impedance is usually measured by applying an AC potential to an electrochemical cell and measuring the current through the cell. The response to an AC potential excitation is an AC current

signal. This current signal is usually analyzed as a sum of sinusoidal functions in and out of phase with the potential perturbation.

The excitation signal, expressed as a function of time, has the form

$$E(t) = E_0 \sin(\omega t) \quad \text{Eq. 3-5}$$

$E(t)$ is the potential at time t , E_0 is the amplitude of the signal, and ω is the radial frequency (rad/s), related to frequency f (Hz) as

$$\omega = 2\pi f \quad \text{Eq. 3-6}$$

In a linear system, the response signal, $I(t)$, is shifted in phase, φ , and has a different amplitude, I_0 :

$$I(t) = I_0 \sin(\omega t + \varphi) \quad \text{Eq. 3-7}$$

An expression analogous to Ohm's Law allows one to calculate the impedance of the system as:

$$Z(\omega) = \frac{E(t)}{I(t)} = \frac{E_0 \sin(\omega t)}{I_0 \sin(\omega t + \varphi)} = Z_0 \frac{\sin(\omega t)}{\sin(\omega t + \varphi)} \quad \text{Eq. 3-8}$$

The impedance is therefore expressed in terms of a magnitude, Z_0 , and a phase shift, φ .

With Euler's relationship,

$$e^{i\varphi} = \cos \varphi + i \sin \varphi, \quad \text{Eq. 3-9}$$

it is possible to express the impedance as a complex function. The potential is described as

$$E(t) = E_0 e^{i\omega t} \quad \text{Eq. 3-10}$$

and the current response as

$$I(t) = I_0 e^{i(\omega t - \varphi)} \quad \text{Eq. 3-11}$$

The impedance can then be represented as a complex number in the polar and the Cartesian form, respectively:

$$\bar{Z}(\omega) = \frac{E(t)}{I(t)} = \frac{E_0}{I_0} e^{i\varphi} = Z_0 e^{i\varphi} = Z_0 (\cos \varphi + i \sin \varphi) = Z_{\text{Re}} + iZ_{\text{Im}} \quad \text{Eq. 3-12}$$

Z_{Re} and Z_{Im} can also be denoted as Z' and Z'' , respectively. The polar and the Cartesian forms can be converted from one to another using the following relationships:

$$Z_0 = \sqrt{Z_{\text{Re}}^2 + Z_{\text{Im}}^2} \quad \text{Eq. 3-13}$$

$$\varphi = \arctan\left(\frac{Z_{\text{Im}}}{Z_{\text{Re}}}\right) \quad \text{Eq. 3-14}$$

$$Z_{\text{Re}} = Z_0 \cos \varphi, \quad Z_{\text{Im}} = Z_0 \sin \varphi \quad \text{Eq. 3-15}$$

It may be useful to introduce the concept of *admittance*, \bar{Y} . Admittance is the inverse of impedance, $1/\bar{Z}$, and therefore represents a kind of conductance. Similar to impedance, admittance can be expressed in polar terms as

$$\bar{Y}(\omega) = \frac{1}{Z} e^{-i\varphi} \quad \text{Eq. 3-16}$$

and in Cartesian terms as

$$\bar{Y} = \frac{1}{\bar{Z}} = \frac{1}{Z_{\text{Re}} + iZ_{\text{Im}}} = \frac{Z_{\text{Re}} - iZ_{\text{Im}}}{Z_{\text{Re}}^2 + Z_{\text{Im}}^2} = Y_{\text{Re}} + iY_{\text{Im}} \quad \text{Eq. 3-17}$$

3.1.5.2. Impedance of AC circuits

In electrochemistry, impedance analysis of a system of interest typically involves measurement of its current response to an applied AC potential at a spectrum of frequencies. The system can be envisioned as a set of (simple) circuit elements. The resulting spectrum can thus be analyzed in terms of an equivalent circuit. Impedance of individual circuit components relevant to this work and combinations thereof will be analyzed below.

Resistance. A basic component of an electrochemical equivalent circuit is a simple resistor. As Ohm's law holds in the case of an AC perturbation, too, it follows for the resistor that

$$I = \frac{E_0 \sin \omega t}{R} \quad \text{Eq. 3-18}$$

$$\bar{Z} = R \quad \text{Eq. 3-19}$$

$$Z_{\text{Re}} = R, \quad Z_{\text{Im}} = 0 \quad \text{Eq. 3-20}$$

$$Z_0 = R, \quad \varphi = \arctan\left(\frac{Z_{\text{Im}}}{Z_{\text{Re}}}\right) = 0 \quad \text{Eq. 3-21}$$

Capacitance. A capacitor is another key element of an electrochemical equivalent circuit. The fundamental relationship, $Q = CE$, yields

$$I = \frac{dQ}{dt} = C \frac{dE}{dt} = \omega CE_0 \cos \omega t = \omega CE_0 \sin\left(\omega t + \frac{\pi}{2}\right) \quad \text{Eq. 3-22}$$

$$\bar{Z} = -\frac{i}{\omega C} \quad \text{Eq. 3-23}$$

$$Z_{\text{Re}} = 0, Z_{\text{Im}} = -\frac{1}{\omega C} \quad \text{Eq. 3-24}$$

$$Z_0 = \frac{1}{\omega C}, \varphi = \arctan\left(\frac{Z_{\text{Im}}}{Z_{\text{Re}}}\right) = -\frac{\pi}{2} \quad \text{Eq. 3-25}$$

Resistance and capacitance in series. Impedance of multi-element circuits can be analyzed by combining component impedances according to rules analogous to those applicable to resistors. It holds for the impedance of the simplest combination, a resistor and a capacitor in series, that

$$\bar{Z} = \bar{Z}_1 + \bar{Z}_2 = R - \frac{i}{\omega C} \quad \text{Eq. 3-26}$$

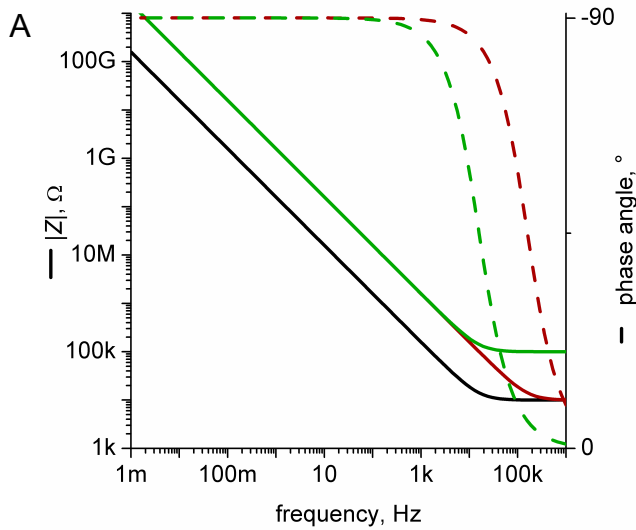
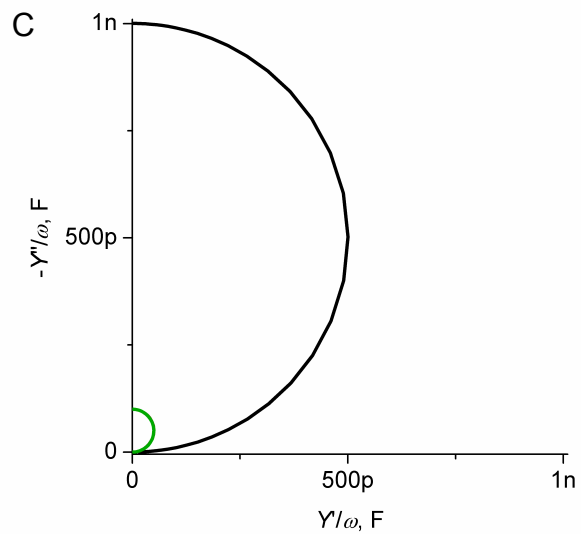
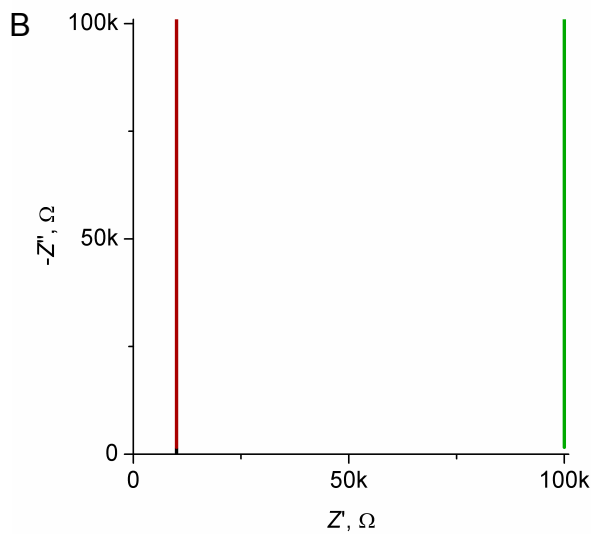
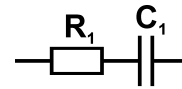


Figure 3-12. Bode (A), complex plane impedance (B), and complex plane capacitance (C) plots for a series RC circuit.

R_1	C_1
1 k Ω	1 nF
1 k Ω	100 pF
10 k Ω	100 pF



$$Z_{\text{Re}} = R, Z_{\text{Im}} = -\frac{1}{\omega C} \quad \text{Eq. 3-27}$$

$$Z_0 = \sqrt{R^2 + \frac{1}{(\omega C)^2}}, \varphi = \arctan\left(\frac{1}{\omega RC}\right) \quad \text{Eq. 3-28}$$

Most commonly, impedance data are represented graphically by means of a *Bode plot*, whereby $\log |Z|$ and φ are both plotted against frequency. Alternatively, plot in the complex impedance plane that displays Z_{Im} vs. Z_{Re} for different values of ω , the so-called *Nyquist plot*, can be used. Data can be plotted in the complex admittance plane, too, or as Y_{Im}/ω vs. Y_{Re}/ω , i.e. in the complex capacitance plane. While the global informative value of a Bode plot is superior to plots in the complex planes, the latter may be more useful if, for example, subtle differences between datasets are to be discerned or specific circuit parameters are to be emphasized.

Figure 3-12 shows the three different plots for series *RC* circuits of several parameter combinations. At frequencies whereby the resistor is the dominant element of the circuit ($f > 100$ kHz) the $|Z|$ curves of the Bode plot (plot A) are flat and equal to R_1 , and the phase shift is 0° . In the region of frequencies where the capacitor prevails ($f < 1$ kHz) the $|Z|$ curves exhibit a slope of -45° and the phase shift is constant at -90° . The slope of $|Z|$ and the value of φ fall between these limiting values at frequencies whereby both elements contribute to the impedance. The plots in the complex impedance plane (B) are strictly vertical, as given by eq. 3-27. Noteworthy are the plots in the complex capacitance plane. Here, semicircles are produced that converge to C_1 at the y -axis at low frequencies. The value of C_1 , which was irresolvable in either of the previous plots, can be clearly discerned here.

In the scope of this work, a plain series combination of a resistor and a capacitor is sufficient to model the electric behavior of a thin continuous *dielectric* partition (i.e. a foil of Teflon or a Si_3N_4 diaphragm) bathed on both sides by electrolyte. The partition is represented by the capacitor, whereas the finite conductance of the electrolyte is accounted for by the resistor.

Resistance and capacitance in parallel. The inverse of impedance of a parallel combination of elements is the sum of reciprocals of the individual element impedances. For a resistor and a capacitor in parallel one obtains

$$\frac{1}{\bar{Z}} = \frac{1}{\bar{Z}_1} + \frac{1}{\bar{Z}_2} = \frac{1}{R} - i\omega C, \quad \text{Eq. 3-29}$$

$$\bar{Z} = \frac{R}{1 + i\omega RC} = \frac{R(1 - i\omega RC)}{1 + (\omega RC)^2} \quad \text{Eq. 3-30}$$

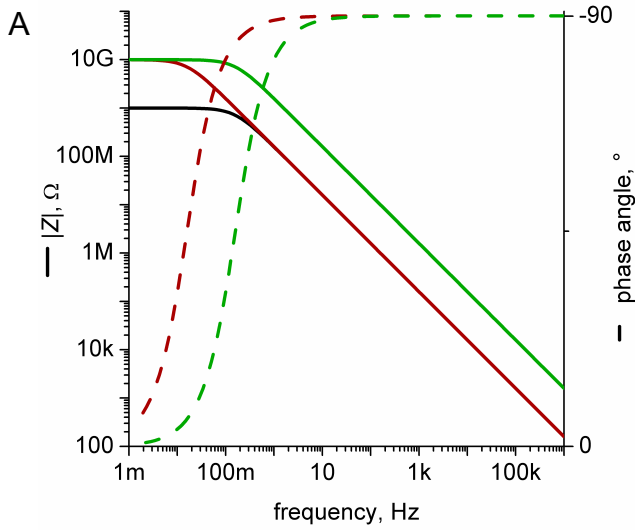
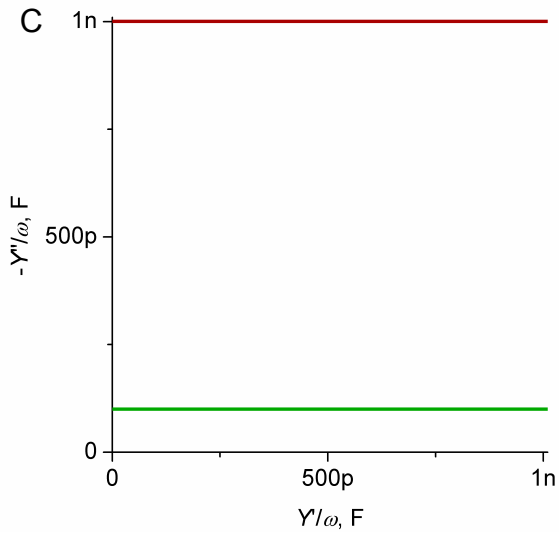
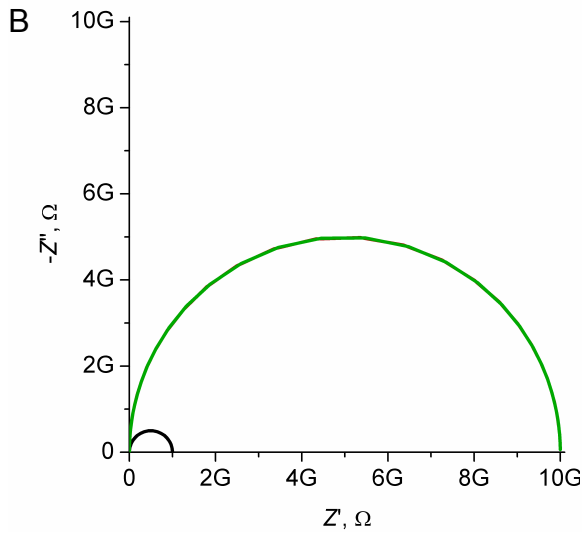
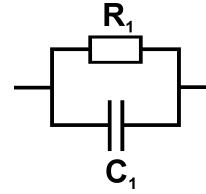


Figure 3-13. Bode (A), complex plane impedance (B), and complex plane capacitance (C) plots for a parallel RC circuit.

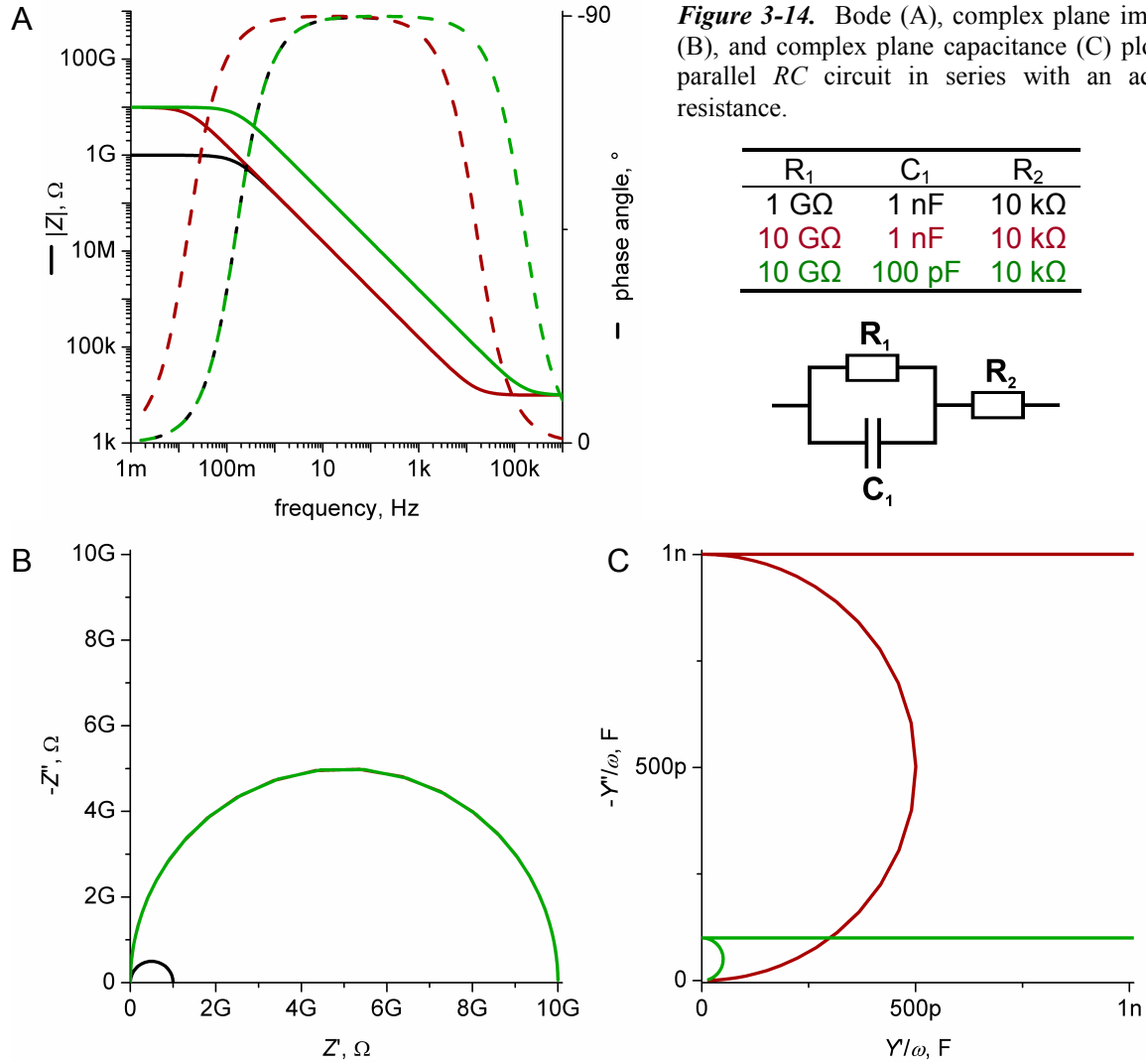
R_1	C_1
1 G Ω	1 nF
10 G Ω	1 nF
10 G Ω	100 pF



$$Z_{\text{Re}} = \frac{R}{1 + (\omega RC)^2}, \quad Z_{\text{Im}} = \frac{-\omega R^2 C}{1 + (\omega RC)^2} \quad \text{Eq. 3-31}$$

$$Z_0 = \frac{R\sqrt{1 + (\omega RC)^2}}{1 + (\omega RC)^2}, \quad \varphi = \arctan(\omega RC) \quad \text{Eq. 3-32}$$

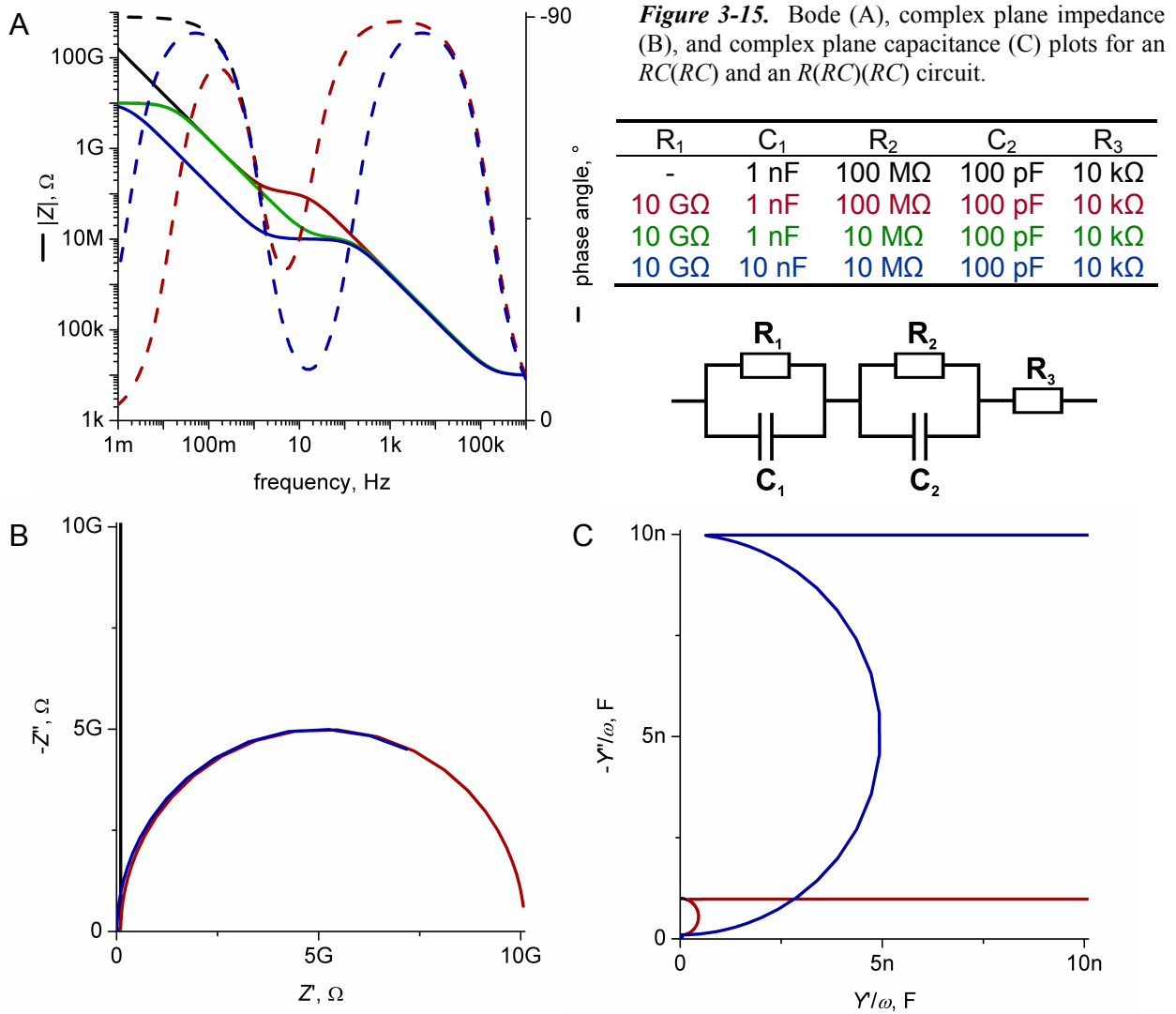
The three common spectral plots for several parametric variations of a parallel RC circuit are displayed in Figure 3-13. As in the Bode plot of the previous figure, the resistance-dominated parts of the $|Z|$ curves are flat at R_1 and the phase shift is 0° (A). Similarly, capacitance-dominated parts of $|Z|$ are inclined at -45° and the phase is shifted by -90° . Conversely, the resistor prevails at low frequencies, and the capacitor is dominant in the high-frequency range of the spectrum. The plots in the complex impedance (B) and capacitance (C) planes are quasi-reversed: semicircles are induced in the $-Z_{\text{Im}}$ vs. Z_{Re} plot that converge to R_1 at low frequencies, while horizontal lines appear in the $-Y_{\text{Im}}/\omega$ vs. Y_{Re}/ω plot.



Resistance in series with a parallel RC circuit. Spectra of several variations of the $R(RC)^*$ scenario are plotted in Figure 3-14. Intuitively, the plots display a fusion of the preceding two scenarios. R_2 is dominant in the high-frequency regime, C_1 prevails in the middle range of frequencies, and R_1 stands out at the lowest frequencies (A). The semicircles in the complex impedance plane (B) now converge to $R_1 + R_2$ at low frequencies, which is, however, indiscernible due to $R_1 \gg R_2$. In the capacitance plane (C), plots transform from horizontal lines due to $(R_1 C_1)$ to semicircles given by $[R_2 C_1]$.

Electrical behavior of a porous dielectric partition (e.g. a porous Teflon foil or a Si_3N_4 diaphragm), whereby both sides are bathed by and the pores are filled with electrolyte, can be modeled effectively by an $R(RC)$ circuit. The components can be indexed as $R_S(R_P C)$ and associated with the

* The in-line notation for electrical circuits is as follows: elements or sub-circuits enclosed by round brackets are in a parallel combination, elements or sub-circuits enclosed in square brackets or not enclosed at all are in a series combination. For example, $R(RC)$ and $[R(RC)]$ are two equivalent notations for an R in series with a parallel RC loop.



resistance of the electrolyte (R_S), resistance of the pores in the partition (R_P) and capacitance of the partition (C). Similarly, a lipid bilayer spanning one or more apertures in a dielectric partition and containing transmembrane conductive channels or transporters can typically be modeled using the same equivalent circuit. C would then stand for the sum of capacitances of the bilayer and the partition, whereas R_P would be a reciprocal of ionic conductance through the bilayer.²⁸

More complex circuits. More complex circuits can be solved in analogy to the simple combinations presented above. Figure 3-15 displays impedance spectral plots of an $RC(RC)$ and three $R(RC)(RC)$ circuits. Obviously, further expansion of a circuit introduces additional time constants in the dynamic response that manifest themselves as inflections in the $|Z|$ and ϕ curves of the Bode plot (A). In the complex planes (B and C), the plots exhibit multiple (incomplete) semicircles. These are, however, not discernible in the linearly-scaled axes due to the differences in the parameter values that span orders of magnitude.

3.1.6. Electrophysiological DC voltage clamp^{23,68-71}

DC ‘voltage clamp’ is a recording of transmembrane current in time while holding transmembrane voltage at a constant value. It is one of the two approaches generally available to an electrophysiologist, the other being the ‘current clamp’. Typically, the current measured under a voltage clamp is due to the presence of (particular) ion channels, charge carriers, or charge transporters in the biomembrane. The character of current traces thus recorded is informative of the functionality of the entity that induced them.

Electrophysiological voltage clamp was devised in the late 1940’s and employed in the breakthrough studies of Hodgkin and Huxley on biophysics of ion channels of squid giant axons.^{72,73} Later, it became associated with the development of the famous patch clamp technique that involves the use of micropipettes to form high-resistance seals on tiny patches of cell membrane.¹¹ Despite its tight bond to the classical patch clamp setup, voltage clamp is a measurement approach applicable to any other electrophysiological platform, be it the painted BLM, appositioned (Montal or Schiller) BLM, planar patch clamp, or any other BLM design.

An ideal voltage clamp setup would consist of a voltage source, a wire, a biomembrane, and an ammeter of zero internal resistance. In reality, voltage clamp measurements* are typically performed in a closed circuit comprising the biomembrane bathed on both sides with electrolyte, a high fidelity current amplifier, and two electrodes each in direct access to one side of the membrane via the electrolyte. A schematic of an equivalent electrical circuit of the scenario is depicted in Figure 3-16A. The element that the voltage clamp experiment is to address is the membrane resistance, R_m . The value of R_m is modulated in time by the activity of the entity conducting or transporting charge across the membrane. In the case of a perfectly-sealing membrane and in the absence of a functional conductive/electrogenic protein therein, R_m should be near-to-infinite. Unfortunately, due to an imperfect lateral seal of the membrane, a finite background current is usually present in voltage clamp experiments. If infinite R_m is considered for a plain membrane, the lateral leakage current is represented by R_{seal} . The famous ‘gigaseal’ refers to a patch-clamp experiment with R_{seal} being in the $G\Omega$ range. Values of R_{seal} in planar BLMs painted or appositioned on hydrophobic apertures are usually higher than those associated with micropipette seals, primarily due to the contrary interaction of the lipids with the partition. The parallel capacitors C_m and C_{stray} stand for the capacitance of the membrane and the additional stray capacitance of the setup (comprised by the pipette and the holder, or the partition), respectively. In

* Low-current measurements are assumed, hence the continuous single-electrode voltage clamp mode is described only.

patch clamp experiments, C_m is insignificant and C_{stray} is rather low, typically in the range of 3-15 pF. In planar bilayer setups, on the other hand, C_m can be as high as hundreds of pF, and C_{stray} of a thin foil partition can easily extend beyond ~ 100 pF. As C_m and C_{stray} are in parallel they act as a single capacitor of capacitance given by the sum of the two. The resistance in series to the membrane, R_s , known also as the access resistance, accounts for the resistance of the electrodes and the electrolyte in the particular setup geometry. Micropipette resistance (up to 10 M Ω) is the major contributor to R_s in the case of patch clamp, whereas R_s is generally below $10^5 \Omega$ in planar BLM configurations. In addition to the elements related to the membrane and the partition, there is also an intrinsic capacitance and resistance of the amplifier. Obviously, the equivalent circuit of a real voltage clamp setup is substantially more complex than the ideal case. Consequences of the presence of the additional elements in the circuit on the current measurements will be discussed below.

3.1.6.1. Voltage error

R_s and R_m in series (assuming infinite R_{seal}) act as a voltage divider. If larger currents flow through the circuit (in response to reduced R_m , presumably due to channel activity in the membrane), the voltage drop across R_s grows at the expense of the voltage drop across R_m ($V_x = IR_x / (R_x + R_y)$). Therefore, current measured for a particular voltage applied across the whole circuit corresponds in actuality to a lower transmembrane voltage (Figure 3-16B).

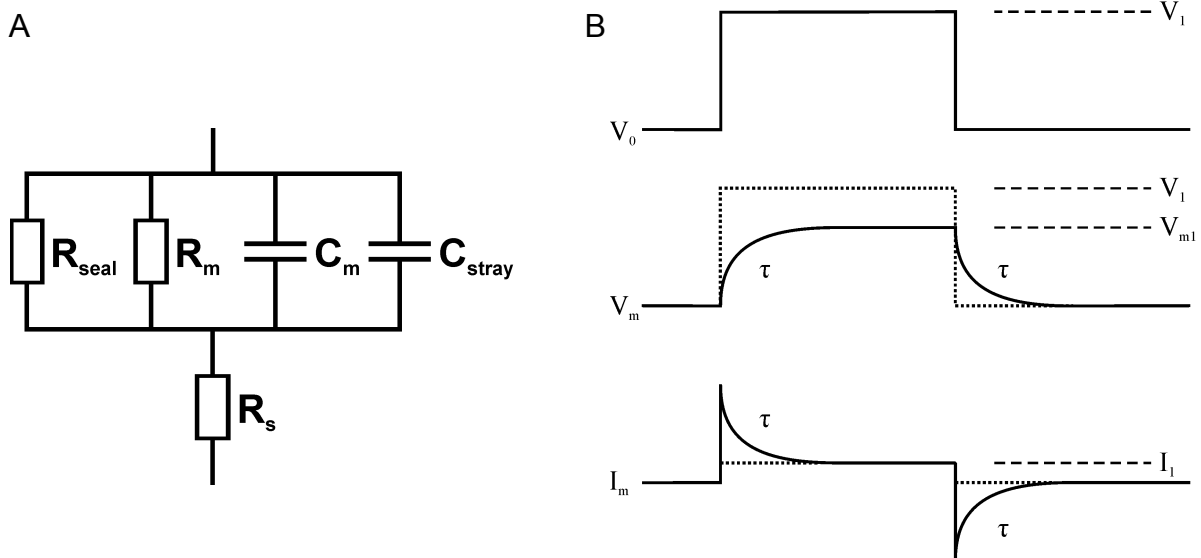


Figure 3-16. Voltage and temporal errors caused by the presence of R_s . A – schematic of an equivalent circuit (excluding the instrument) of a voltage-clamp setup. R_s – series resistance, R_m – lipid membrane resistance, R_{seal} – seal resistance, C_m – lipid membrane capacitance, C_{stray} – stray capacitance. B – voltage across the membrane, V_m (center), and current through the circuit, I_m (bottom), upon a command voltage step from V_0 to V_1 and back (top). Voltage error: V_m does not reach V_1 due to the voltage drop across R_s . Temporal error: Both current and voltage across the membrane settle to their steady-state values exponentially with $\tau = R_s(C_m + C_{\text{stray}})$.

3.1.6.2. Temporal error

The current response of an ion channel to electric potential is typically studied by series of short-termed voltage pulses (see Figure 3-16B for an example). This is especially so if modulation due to transmembrane potential, i.e. voltage gating, is associated with the channel. Unfortunately, the capacitance parallel to R_m , namely $C_m + C_{\text{stray}}$, must be charged or discharged upon a voltage step. After the step change, I_m and V_m settle exponentially to their steady state values with $\tau = R_s(C_m + C_{\text{stray}})$. One negative consequence of the transient is that no meaningful data can be recorded while it lasts. Second, current due to membrane conductance changes is filtered by the same time constant, i.e. events with dynamics faster than the dynamic response of the circuit cannot be resolved. Finally, the course of the transient in a real setup is different from that depicted in the figure. Typically, a feedback resistor of 500 M Ω or more is used to monitor the current. In an instrument driven from ± 15 V power supplies, the maximum current that can be passed through the resistor is limited to ~ 30 nA. Upon a typical voltage step, however, the circuit is required to pass a current much higher than the maximum current of the resistor. Since this is impossible, the system would saturate and the time to effect a step would be prolonged significantly.

3.1.6.3. Compensation of series resistance and parallel capacitance

The problems presented above can partly be resolved by incorporation of compensation circuitry in the voltage clamp instrument.

Capacitance compensation. In order to prevent saturation of the system due to charging transients, for example, the transient current can effectively be injected through a capacitor. Since the current monitor output on voltage clamp amplifiers is only proportional to the current through the feedback resistor, the transient current is not seen, even though in reality it is still being passed through the electrodes into the cell. Parameters of the injection circuit, namely the capacitance and the time constant, are controlled.

R_s compensation. Compensation of series resistance is somewhat less effective. Two approaches are possible: 1) ‘correction’ – the applied voltage is increased in proportion to the measured current to compensate for the potential drop across the series resistance, and 2) ‘prediction’ – supercharging is induced at the start and the end of a voltage pulse by adding a brief charging pulse. Unfortunately, the compensation level of the former approach is limited due to electronic circuit saturation at high potentials. Moreover, the circuit is driven by a positive feedback, and hence prone to instability. The latter approach offers faster response to a potential step yet does not correct the voltage error nor improve the dynamic response of the circuit. Apparently, good reasons exist for minimization of series resistance by choice and/or adjustment of setup components.

3.1.6.4. Minimization of series resistance

Electrodes. Current must be transformed smoothly from a flow of electrons in the circuitry to a flow of ions in solution at the electrode-electrolyte interface. Needless to say, the process occurring at the electrode should interfere with neither the entity under study nor the membrane itself. The most common electrodes used in electrophysiological measurements are those of the Ag/AgCl type. A reversible reaction between the Ag atoms of the wire core on one side and the Ag^+ ions (in equilibrium with the AgCl pellet) and wire electrons on the other side transduces the current across the interface. As long as the AgCl is not exhausted, Ag/AgCl electrodes meet the above requirements.

Access geometry and electrolyte concentration. The resistance of a conductor specimen of a uniform cross-section is given by

$$R = \frac{\rho l}{A}, \quad \text{Eq. 3-33}$$

where ρ is the electrical resistivity of the material, l is the length, and A is the cross-sectional area of the specimen. Equation 3-33 also holds for the resistance of an electrolyte in a confined geometry. Apparently, long narrow access channels filled with electrolyte will exhibit a significant resistance. This is an inherent problem of techniques that make use of electrodes confined to micropipettes, such as any of the conventional patch-clamp configurations, and one of the primary incentives for planar patch-clamp. Conversely, high access resistance due to confined geometry usually does not occur in planar BLM setups. In novel BLM designs that employ microfluidic perfusion, however, careful placement of electrodes relative to the lipid bilayers will be crucial.

3.1.6.5. Noise

A. Sources of noise

Several setup-specific sources of background noise are present in a voltage clamp experiment. Due to the random nature of noise, uncorrelated noise sources add in an rms fashion. Thus, if E_1 , E_2 , and E_3 are the rms values of three uncorrelated noise sources, the total rms noise, E_T , of these sources together is given by

$$E_T = \sqrt{E_1^2 + E_2^2 + E_3^2} \quad \text{Eq. 3-34}$$

Thermal noise. First, there is the ubiquitous Johnson (thermal) noise, which arises from random motion of thermally excited charge carriers in a conductor. The current rms value of thermal noise is described by

$$I_{th} = \sqrt{4kTB Y_{Re}(\omega)}, \quad \text{Eq. 3-35}$$

where k is the Boltzmann constant, T is the absolute temperature, B is the bandwidth (in Hz), and Y_{Re} is the real part of admittance, which depends, in general, on angular frequency, ω . For a parallel RC circuit

$$Y_{Re}(\omega) = 1/R, \quad \text{Eq. 3-36}$$

and for a series RC circuit

$$Y_{Re}(\omega) = \frac{R(\omega C)^2}{1 + (\omega RC)^2} \quad \text{Eq. 3-37}$$

In the high frequency limit eq. 3-37 approaches $1/R$, in the low frequency limit $Y_{Re} \approx R(\omega C)^2$. Since all real dielectric materials display some loss, dielectric thermal noise is generated in dielectrics. For a bandwidth extending from DC to an uppermost cut-off frequency B , the rms thermal noise current I_D resulting from a lossy dielectric can be described in terms of the dissipation factor D and the capacitance C_D of the dielectric:

$$I_D = \sqrt{4kTDC_D\pi B^2} \quad \text{Eq. 3-38}$$

Shot noise. Shot noise arises when current flows across a potential barrier. Rms current due to shot noise is given by

$$I_{sh} = \sqrt{2qIB}, \quad \text{Eq. 3-39}$$

where q is the elementary charge, I is the DC current, and B is the bandwidth. Sources of shot noise in voltage clamp experiments are, for example, p - n junctions of operational amplifiers, or ions crossing the membrane through leakage channels or pumps.

Excess noise. Excess noise can broadly be defined as any noise that is present in a circuit element in addition to the fundamental noise mechanisms already described. For example, in the presence of direct current all resistors exhibit low-frequency noise whose power spectral density varies inversely with frequency. This noise is present in addition to the thermal noise of the resistor and is usually referred to as ‘ $1/f$ noise.’ Its magnitude is directly proportional to the DC current flowing through the resistor. Semiconductor devices also exhibit $1/f$ noise.

Amplifier noise. Apart from the thermal and shot noise arising in the instrument, there is also the voltage noise of the operational amplifier itself. The spectral density of the current noise produced by clamping a noise voltage of the amplifier across $C_m + C_{stray}$ (Figure 3-16A) is

$$S_i^2(f) = e_n^2 \omega^2 (C_m + C_{stray})^2, \quad \text{Eq. 3-40}$$

where e_n is the rms noise voltage (in V/ $\sqrt{\text{Hz}}$).

B. Effective noise in DC voltage clamp

Because the micro-patch single-channel patch-clamp arrangement is not relevant to this work, effective noise of the whole-cell and the analogous planar bilayer voltage-clamp configurations will be assessed only. The noise associated with these configurations at moderate to high bandwidths is dominated by 1) thermal noise from the series resistance, and 2) voltage noise of the amplifier input. Both noise sources act in conjunction with the series capacitance ($C = C_m + C_{stray}$) ((1) via equations 3-35 and 3-37 and (2) via equation 3-40). Minimization of noise by reduction of both R_s and C is favorable. In the whole-cell voltage clamp configuration, R_s , typically in the order of $\sim 10 \text{ M}\Omega$, is primarily given by the pipette which does not allow much room for alterations. C can be kept low by patching small cells ($C_m \propto \text{cell area}$). Compared to whole-cell patch clamp, R_s is much lower and C , on the other hand, much higher in the planar BLM configuration. C_m can be minimized by using small apertures, C_{stray} by using thick septa with low dielectric constant and reduction of area on the septum wetted with electrolyte. If this is accomplished, further prominent sources of noise become the feedback resistor of the current monitor (thermal and $1/f$ noise) and the seal resistance (thermal noise). The thermal noise of the feedback resistor can be reduced by cooling the headstage. The noise due to the seal can be limited by establishing conditions that generate near-to-infinite seal resistances.

3.2. Experimental

3.2.1. Substrates of choice: Si_3N_4 windows

Silicon nitride transmission electron microscopy (TEM) windows, further referred to as Si_3N_4 windows, with free-standing Si_3N_4 diaphragms were used as substrates for spanning npsLBs. A Si_3N_4 window is a square-shaped piece of a silicon wafer coated on both sides with a thin layer of silicon nitride (Figure 3-17). A pyramidal pit has been etched through the Si_3N_4 film and the entire thickness of the chip from one side. The exposed unsupported square-shaped part of the Si_3N_4 film on the other side will further be referred to as the ‘free-standing Si_3N_4 ’ (fs Si_3N_4) or the ‘ Si_3N_4 diaphragm’. The windows are commercially available and can be purchased at various configurations at reasonable prices. Si_3N_4 windows of the following nominal parameters were purchased from Silson Ltd. (Northampton, England): Si frame thickness $525 \mu\text{m}$, Si frame width $5 \times 5 \text{ mm}$, Si_3N_4 membrane width $250 \mu\text{m}$, Si_3N_4 diaphragm thickness 50, 75, 100, 150, 200 and 500 nm . The actual Si_3N_4 membrane width was $330 \mu\text{m}$, as determined by both SEM and light

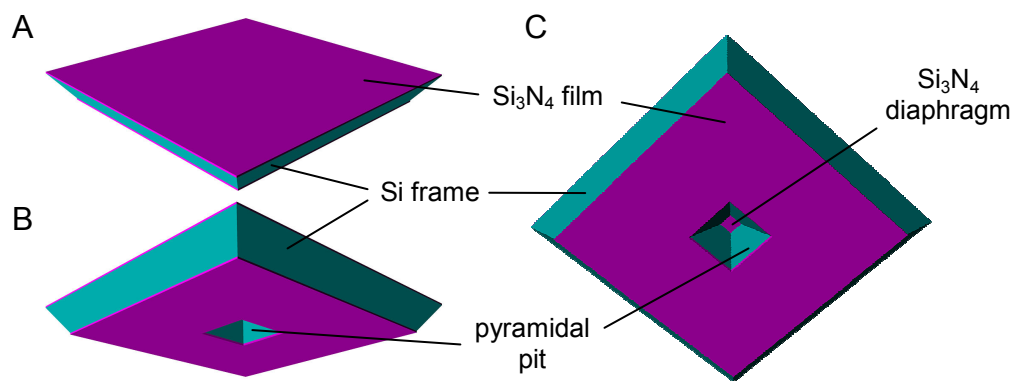


Figure 3-17. Schematic of an Si_3N_4 window. The square-shaped Si_3N_4 diaphragm is located in the center of the silicon frame (turquoise). The (bottom) side where a pyramidal pitch has been etched is denoted the ‘pit’ side (B and C). The (top) side where continuity of the Si_3N_4 film (magenta) has been preserved is denoted the ‘flat’ side. Although the Si_3N_4 diaphragm is optically transparent, it has been drawn opaque here in order to emphasize the complete absence of topographical features at the flat side of the window.

microscopy. Though not exactly rugged, the Si_3N_4 diaphragms exhibit acceptable mechanical stability. The low thickness of the diaphragms was determinant for fabrication of multiple pores at short pore-to-pore distances.

3.2.2. Pore milling and characterization

3.2.2.1. FEI Nova 600 NanoLab DualBeam™-SEM/FIB

Focused scanning Ga^+ and electron beams of the Nova 600 NanoLab DualBeam™-SEM/FIB (FEI Company, Hillsboro, OR, USA) were used to fabricate and image nanopores in Si_3N_4 diaphragms, respectively. The instrument consists of an evacuated sample chamber with a motorized stage, an electron and an ion beam column, a set of detectors, an optical camera, a precursor-gas delivery system, and an external control unit. The stage exhibits three-axis translation, rotation, and tilt capabilities. The stage is designed to have a eucentric point (i.e., a well-centered point such that the field of view is maintained when tilting the specimen) at the location where the two beams cross (Figure 3-18).

3.2.2.2. FIB milling

Pretreatment. Prior to pore machining, a 10-nm layer of Au was evaporated over the pit side of the Si_3N_4 window to avoid local charge accumulation upon FIB machining and SEM imaging. After pore fabrication, the Au layer was dissolved in *aqua regia* (a 3:1 mixture of 37% HCl and 68% HNO_3).

Milling. A Si_3N_4 window was mounted horizontally on the NanoLab stage by stripes of conductive double-sided adhesive tape with the pit side facing up. The chamber was evacuated to $\sim 10^{-6}$ Pa. The electron beam, operated in a ‘field-free’ mode (5 kV accelerating voltage, 98 pA probe current,

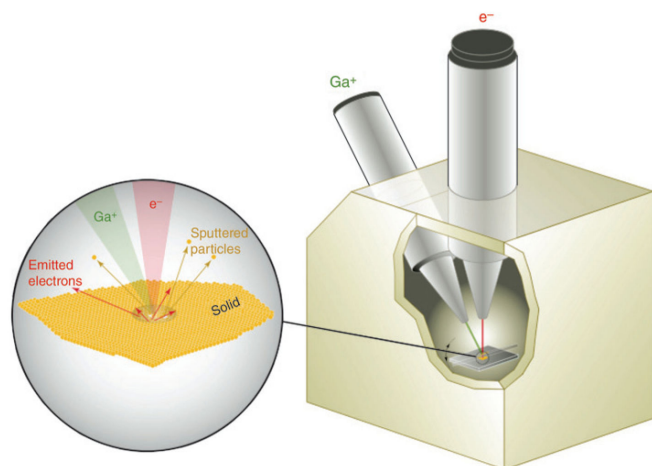


Figure 3-18. Schematic illustration of a dual-beam FIB-SEM instrument. The expanded view shows the e-beam/i-beam/sample interaction (image adopted from ref. [52]).

Everhart Thornley SE detector, low magnification), was focused and aligned. Subsequently, the pore fabrication site, typically the diaphragm corner opposite to the ion beam, was located on the sample and brought to eucentric height. The stage was tilted by 52° to position the Si_3N_4 diaphragm perpendicular to the ion beam. Next, the ion beam (30 kV accelerating voltage, 1 pA probe current) was focused and aligned in the vicinity of but not directly at the milling site so as not to induce excessive sputtering and implantation at the spot where the pores were to be milled. The planar patterning function employed to produce a pore was a simple filled circle. Typically, the pattern comprised an array of 1-12 circles of 50-800 nm in diameter (constant for all circles of the array) in a hexagonal arrangement with a nearest center-to-center distance in the range of 0.25-2 μm . The ion beam was scanned repeatedly over the area covered by the pattern. The lowest available beam current, namely 1 pA, was used exclusively, since the membranes were very thin and minimum sputtering was desired upon beam focusing and alignment at the diaphragm plane.

Recurrent rastering by an i-beam over a 2D circular pattern on a solid surface mills a conical cavity. If the target is a thin diaphragm and the beam has been scanned over the pattern a sufficient number of times, a through hole is produced. The most straight-forward method to determine whether the bottom of the cavity has reached the opposite side of the diaphragm would be to measure the intensity of the beam behind the sample. The event of beam penetration through the diaphragm can be detected as a sharp increase of the monitored signal intensity.⁷⁴ Unfortunately, the specific configuration of the FEI Nova 600 Dual-beam used to mill the pores did not offer a detector capable of monitoring emission of particles behind the diaphragm. Therefore, cavity break-through could only be determined post-process by the AFM.

3.2.2.3. Nanopore imaging

A. SEM

SEM images of the milling site were acquired using the electron beam of the Nova 600 Nanolab. The instrument was operated in the ‘immersion’ mode (5 kV accelerating voltage, 98 pA probe current, thru-the-lens SE detector, magnification >2000×) to obtain high-resolution images. The heterogeneous thin film of gold on the side of e-beam incidence facilitated focusing of the beam to the diaphragm surface that was otherwise completely free of features. Furthermore, it helped dissipate charge that would otherwise accumulate at the interface and deteriorate imaging quality. The images were used to evaluate the size, shape, and in the case of arrays, planar distribution of the pores.

B. AFM

The topography of nanopore openings in Si₃N₄ diaphragms was examined by means of the Dimension 3100 atomic force microscope (Veeco Metrology Inc./Digital Instruments, Santa Barbara, CA, USA) featuring a scanned-tip design. The system was operated from the NanoScope software (v7.20) coupled to the NanoScope V controller.

i. Cantilevers

Unless stated otherwise, samples were probed in the tapping topographical mode using OMCL-AC160TS micro cantilevers (Olympus Corp., Tokyo, Japan). The OMCL-AC160TS cantilevers feature a tetrahedral tip and are designed for standard applications using oscillating cantilever AFM techniques like tapping or non-contact mode. The tetrahedral tip exhibits almost symmetrical side angles with respect to the substrate, which yields comparable aspect ratio in all directions of the image. This makes special orientation of the sample with respect to the cantilever unnecessary. Tip is located exactly at the cantilever end allowing for precise optical positioning of the tip with respect to features of interest on the sample. Aluminum reflex coating on the cantilevers’ back side increases laser reflectivity and minimizes optical interferences on reflective samples. SEM images and schematics of the cantilever are displayed in Figure 3-19 and its characteristics are summarized in Table 3-3.

ii. Lateral resolution issues due to tip shape

Tip curvature radius. The radius of curvature of the end of the tip determines the highest lateral resolution obtainable with a specific tip. The smaller the radius of curvature, the smaller the feature that can be resolved. A sharper tip is able to laterally resolve smaller features than a dull tip with a larger radius of curvature. The radius of curvature of OMCL-AC160TS is specified as <10 nm (typically ~7 nm), whereas the imaged pore radii were mostly >25 nm. Therefore, tip curvature radius did not substantially deteriorate the lateral resolution of nanopore openings. Some detrimental effect might have occurred when breakthrough of very narrow pores was being

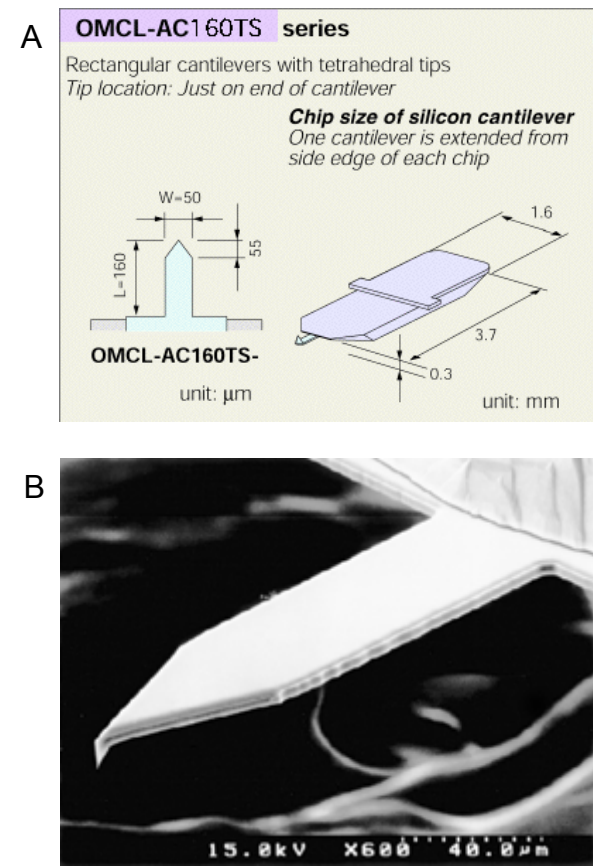


Table 3-3. Olympus OMCL-AC160TS AFM microcantilever specifications.

	Parameter	OMCL-AC160TS
Cantilever	shape	rectangular
	stiffness	42 N/m
	res. freq.	300 kHz
Lever-arm	thickness	4.6 μm
	width	50 μm
	length	160 μm
Tip	shape	tetrahedral
	height	14 μm
	radius	<10 nm
	tip/lever	Si/Si
Material Coating	tip side/reflex	none/Al

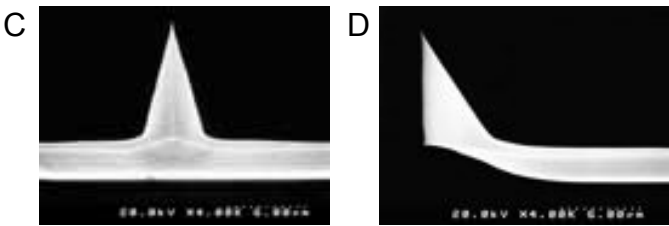


Figure 3-19. SEM images of an OMCL-AC160TS AFM probe. Schematic of the microcantilever body and lever (A) and SEM images of the lever (B), tip front (C) and tip side (D).

examined (Chapter4.3).

Tip sidewall angles. The ability to image steep sidewalls on a sample surface is determined by the sidewall angles of the tip. The tip is not able to profile sides of surfaces steeper than the sidewall angle of the tip. When scanning across features which are steeper than the sidewall angle of the tip, the sidewall angle in the images will reflect the sidewall angle of the tip. The OMCL-AC160TS tip exhibits an angle of 35° , whereby the axis of symmetry is normal to the lever at the front view and tilted by $\sim 18^\circ$ at the side view (Figure 3-19c and d, Figure 3-20). When mounted in the scanner head of the microscope, the cantilever is tilted at an angle of about 10° . The angles measured with the front and back sides of the tip should be skewed accordingly. The effective scan line profiles

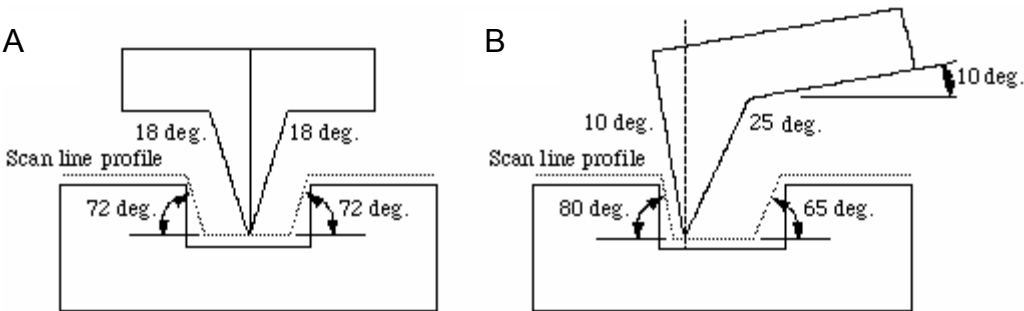


Figure 3-20. Scan line profile given by the OMCL-AC160TS tip shape in the side-to-side (A) and front-to-back (B) directions.

parallel (front-to-back) and perpendicular (side-to-side) to the long lever axis are illustrated in Figure 3-20. The side-to-side scan is expected to yield a symmetric profile with a maximum sidewall slope of 72° . The front-to-back line scan over vertical sidewalls should, on the contrary, result in an asymmetric profile with maximum angles of 80° for features probed by the front side and 65° for features probed by the back side of the tip.

iii. AFM image analysis

Pore dimensions and topography were mostly extracted from high-magnification height images of single pores. Figure 3-21 illustrates the image analysis process. Primary processing of raw data (leveling and scaling) was done using the AFM control software (Nanoscope v7.20). The resulting 2D matrix of height values (A) was then imported into an image processing application such as ImageJ. Note the presence of an elevated annulus at the circumference of the pore. Similar elevated rims were oftentimes observed to have formed around the pores (Chapter 4.3). If present, the outer circumference and the maximum height of the rim were extracted in addition to pore size. In the 2nd step, the mean height value of the region in the near vicinity of the pore was determined (B). A threshold of 2σ below the mean was taken as the boundary of the pore mouth (C). Similarly, if an annular elevation was found, the height threshold of its outer circumference was defined as 2σ above the mean (D). The binary image was fed to a particle analysis routine. Thereby, an ellipse was fitted to the spot masking the pore mouth or the elevated annulus. The resulting major and minor diameters of the ellipse were used to describe the feature size (E, F).

3.2.3. Preparation of giant unilamellar vesicles

Giant unilamellar vesicles (GUVs) were prepared by the electroformation technique.^{75,76} ~50 μl of 1 mg/ml solution of lipid (pure DPhPC, or 99:1 w/w DPhPC/NBD-DMPE, see Figure 3-22 for structures) in chloroform were spread dropwise over an area of ~5 cm^2 of a glass plate coated with In/Ti oxide (ITO) and dried in vacuum overnight. After drying, two lipid-coated glass plates were clamped against each other with a 1-mm-thick PDMS spacer in between. The gap between the glass plates was filled with a 180-mM sucrose solution in water. An electrical contact was made from a signal generator (Pulse-/Function Generator PGS201) to the lipid-coated ITO surfaces. Sinusoidal voltage of 1 V rms at 10 Hz was applied between the glass plates to induce lipid swelling and GUV formation. After two hours, the suspension of GUVs in sucrose was extracted from the cell and transferred to a plastic vial. GUV suspensions were stored at 4°C for up to two weeks. Polydisperse suspensions of GUVs of diameters ranging from a few up to ~100 μm were obtained repeatedly using this procedure.

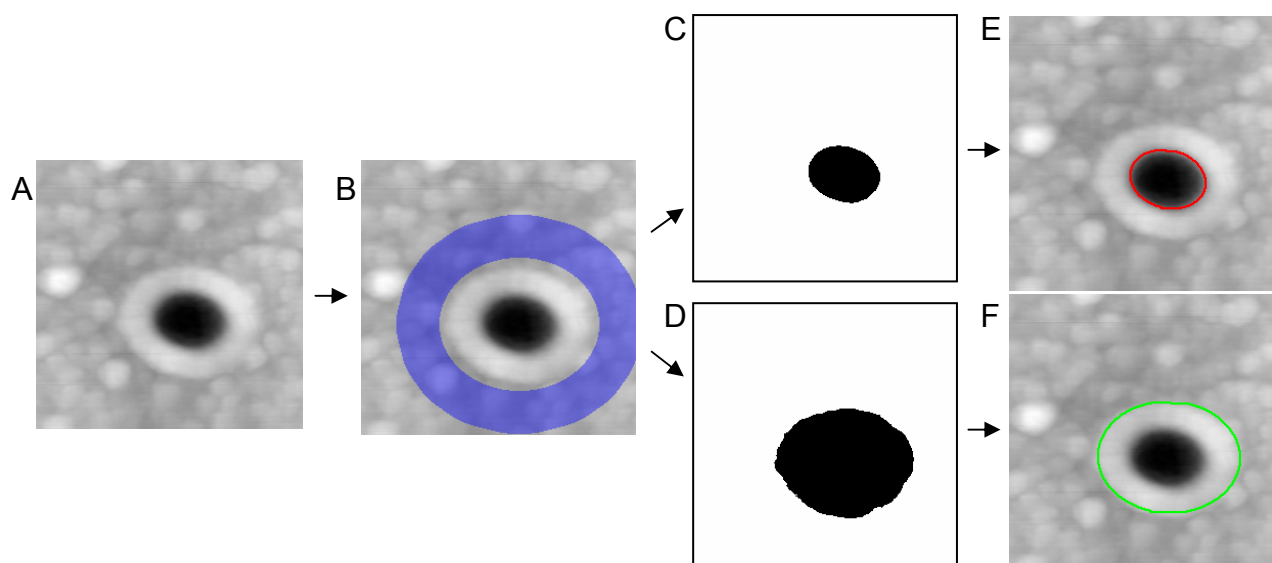


Figure 3-21. Analysis of pore size and topography. A – a 500×500 nm/256×256 px AFM height image of a single pore (nominal diameter 200 nm, apparent depth 110 nm). B – the blue annulus marks the area that statistics was performed on to determine the mean height of the surface in the proximity of the pore. C, D – binary images containing the masks of the pore mouth and the elevated annulus, respectively. E, F – ellipses fitted to the corresponding masks. Resulting dimensions of the pore mouth and the elevated annulus are 139×104 nm and 254×205 nm, respectively.

DPhPC is a standard phospholipid used extensively to span painted BLMs with enhanced stability. We chose this lipid so as not to introduce unnecessary mismatch in parameters to inter-platform comparisons of conductance of peptide channels observed on painted BLMs and npsLBs. Furthermore, DPhPC is known not to show the gel-to-liquid crystalline phase transition which is characteristic of straight-chain phosphatidylcholines.⁷⁷ Change of npsLB properties upon bilayer gel-to-liquid transitions would be an additional unknown parameter. Bilayers in the liquid-crystalline phase at room temperatures formed of alternative PC lipids, e.g. POPC and DOPC, exhibit longer hydrophobic thickness than DPhPC bilayers. A mismatch between the thickness of the hydrophobic core of such a bilayer and the length of some shorter oligomeric peptide TM channels (e.g. gramicidin) shortens open channel lifetimes and thereby decreases macroscopic channel conductance.⁷⁸

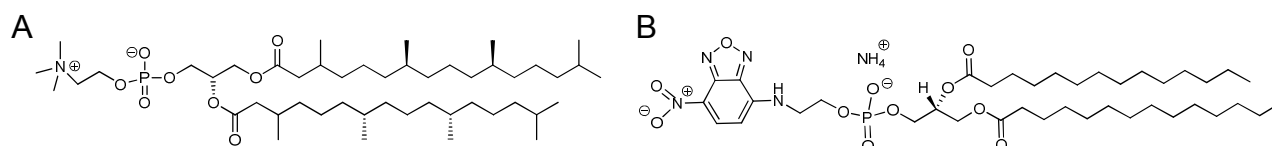


Figure 3-22. Chemical structures of the phospholipids used in this study. A – DPhPC, B – NBD-DMPE.

3.2.4. Optical microscopy

An Axioskop upright optical microscope (Carl Zeiss GmbH, Oberkochen, Germany) was utilized throughout the study to accomplish versatile observation and imaging tasks (Figure 3-23A). A

50 W HBO mercury discharge lamp was used as a source of light in the fluorescence and reflected light modes. Zeiss Achroplan water-immersion objectives 440091 (40 \times , 0.8NA) and 440049 (20 \times , 0.5NA) were employed to observe GUV and SLB behavior on Si-based surfaces, as well as maneuver GUVs over Si₃N₄ diaphragms with a micromanipulator. Zeiss Epiplan-Neofluar HD-DIC objectives of various magnifications were used for imaging in air. Fluorescence imaging of GUVs and SLBs was done by exciting the NBD-DMPE (headgroup-labeled) green lipid dye incorporated in the envelope of the vesicles. Zeiss fluorescence filter-set 09 was used to filter the exciting and emitted light (Figure 3-23B).

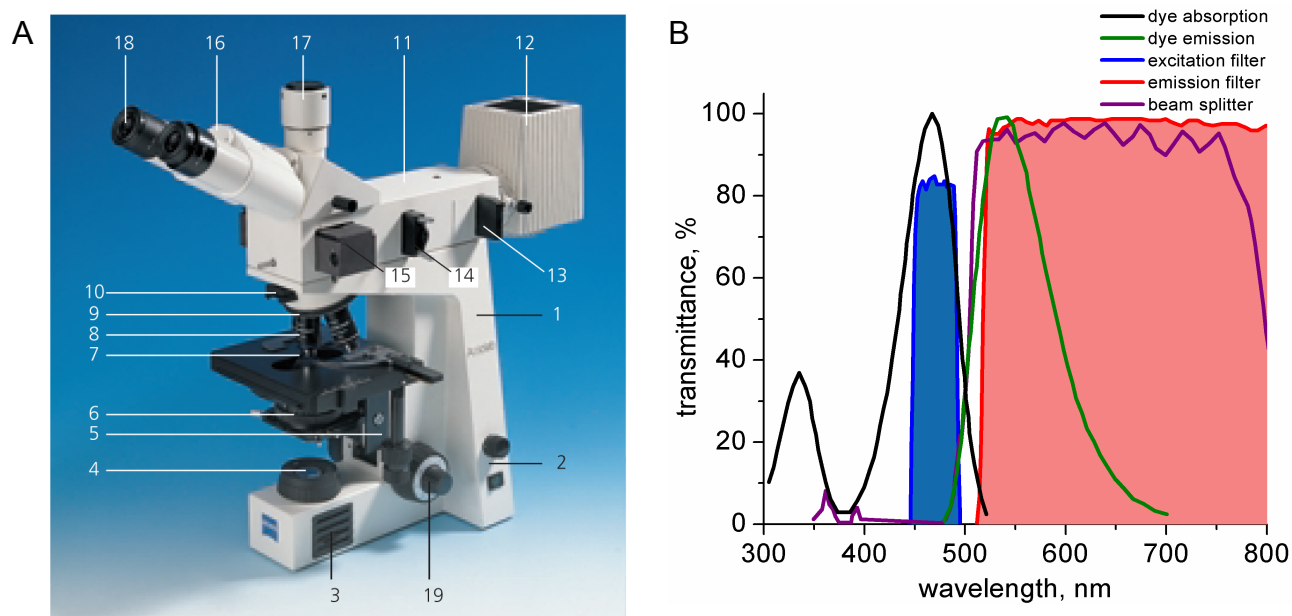


Figure 3-23. A - photograph of the Zeiss Axioskop microscope. The Microscope consists of the following components: 1 microscope stand, 2 power switch and light control, 3 built-in illuminator, 4 variable luminous-field diaphragm, 5 condenser mount with height adjustment, 6 transmitted-light condenser, with variable aperture diaphragm, 7 specimen stage with object guide, 8 objectives, 9 nosepiece, 10 filter mounts, in transmitted light on the observation side, 11 illumination equipment for epifluorescence, 12 lamp for epi-fluorescence, 13 filter slider for reflected-light fluorescence, 14 luminous-field diaphragm for epi-fluorescence, 15 reflector slider for epi-fluorescence, 16 binocular tube, 17 camera/TV port (switchable), 18 eyepieces, 19 focusing drive. B – excitation and emission spectra of the NBD dye, together with transmittance spectra of the individual components of Zeiss fluorescence filter-set 09.

3.2.5. Formation of npsLBs on Si₃N₄ windows

Procedure. A pore-bearing Si₃N₄ window was typically cleaned for 10 minutes in a fresh piranha solution prior to npsLB formation. Next, the Si₃N₄ window was mounted horizontally in the measurement cell (Figure 3-25B and C) with the flat side facing upwards. Electrolyte was introduced into both compartments via perfusion channels. The cell was mounted on a microscope stage, an objective was immersed in the top compartment, and the pore-bearing region of the Si₃N₄ diaphragm was localized. The stage was lowered and a micromanipulator tip was brought into view, focused, centered, and raised slightly so as not to collide with the free-standing Si₃N₄

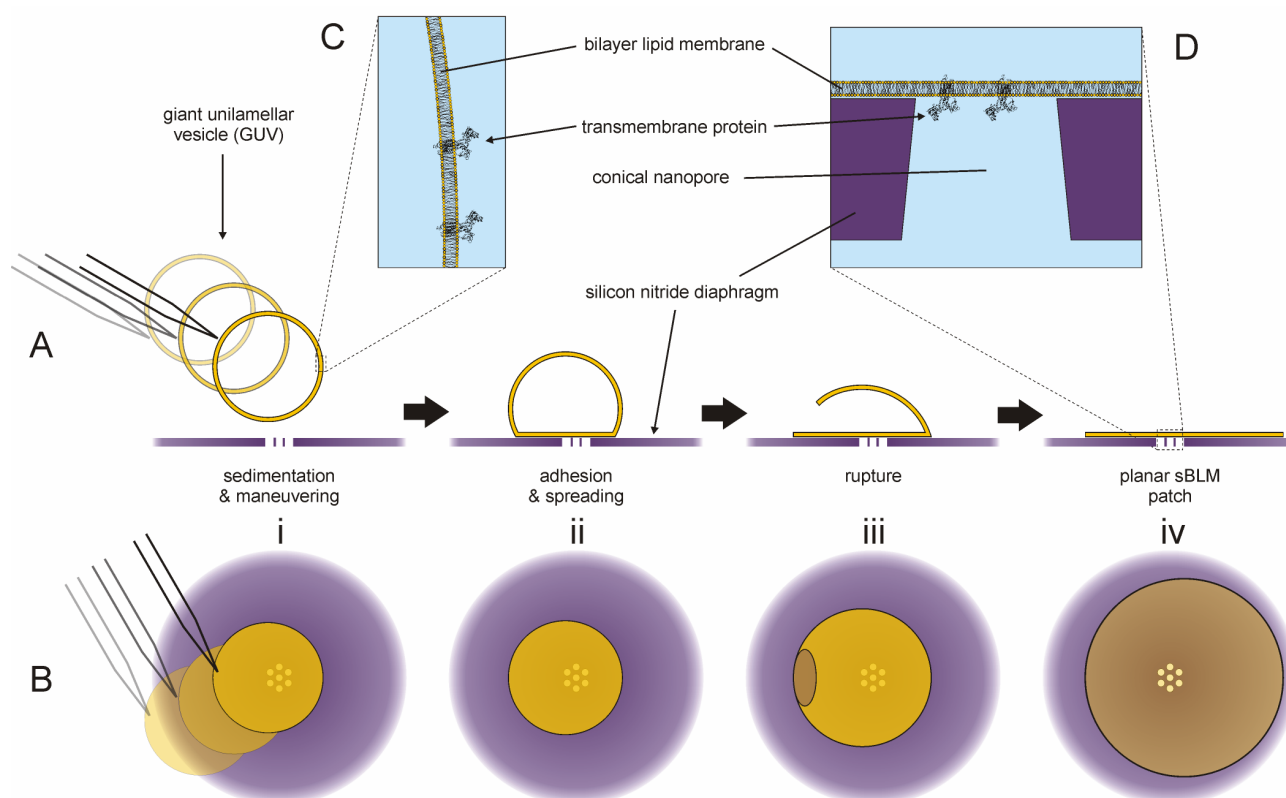


Figure 3-24. Schematic of npsLB formation by directed fusion of a GUV to a Si_3N_4 diaphragm containing an array of pores (not drawn to scale, except for D). (A) and (B) are side and bird's-eye views of the formation process, respectively. (i) GUV suspension is injected in the bathing electrolyte and GUVs sediment to the Si_3N_4 diaphragm. One of the GUVs sinking at the pore-bearing location is maneuvered to directly above the pore array by horizontal movements of a patch pipette tip attached to a micromanipulator. (ii) Upon contact with the Si_3N_4 diaphragm, the GUV adheres to the surface and spreads into a pancake-like shape, spanning over all pores of the array. (iii) A spontaneous local loss of integrity, i.e. rupture, of the lipid bilayer occurs at the rim of the GUV as it flattens on the surface. The defect widens progressively as the vesicle unfolds. (iv) The GUV unfolds completely, forming a large planar SLB patch spanning over all pores of the array. (C) A zoom-in at the GUV lamella, displaying in detail the lipid bilayer with reconstituted transmembrane protein. (D) A zoom-in at an npsLB spanning a slightly conical nanopore 50 nm wide and 50 nm long (drawn to scale).

diaphragm. The objective was withdrawn and 0.5 - 2 μl of a GUV suspension were injected into the top compartment above the diaphragm by a micropipette. The objective was re-immersed and the pore-bearing region brought into focus. The micromanipulator tip was lowered to $\sim 10\text{-}20\ \mu\text{m}$ above the surface. One of several GUVs that typically sank to the vicinity of the pore array was maneuvered to and centered over the array by lateral movements of the manipulator tip (Figure 3-24). The GUV was then allowed to adhere, spread and unfold into a unilamellar patch over the pore-bearing location. A supported bilayer lipid membrane (SLB) formed at the Si_3N_4 -electrolyte interface, whereas free-standing npsLBs formed over the pores. The top compartment was flushed with base electrolyte to remove sucrose and lipid debris suspended in the solution, and to verify npsLB stability. If desired, electrolyte was exchanged and pore-forming peptides were introduced by perfusion of one or both chambers manually via tubing connected to disposable syringes, or via a Reglo ISM834 peristaltic pump (Ismatec SA, Glattbrugg, Switzerland).

Micromanipulation. GUVs were pushed around under the microscope by finely-tipped glass micropipettes. The micropipettes with tip diameters of $\sim 3\ \mu\text{m}$ were pulled thermally of 1-mm-OD thin-wall glass capillaries (TW100F-4, WPI, USA) using a dedicated micropipette puller (P-97, Sutter Instrument Company, USA). The micropipettes were immersed at a static angle of 30° with respect to the horizontal plane and maneuvered by a 3D motorized micromanipulator (MP-225, Sutter Inst. Co.).

Reflected vs. transmitted light microscopic mode. Even though the 100-nm thick diaphragms of the Si_3N_4 windows are optically transparent, the reflected light microscopic mode was used to direct GUVs to the pore-bearing location in the diaphragm. The pores were typically milled in the vicinity ($\sim 50\ \mu\text{m}$) of a diaphragm corner to ease their optical localization. When the pore-bearing location was centered under the microscope, only a quarter of the field of view was comprised by the diaphragm, while the Si-supported Si_3N_4 surface occupied the rest. Only the Si_3N_4 diaphragm portion of the field of view would be illuminated in a transmitted-light mode. Therefore, the micromanipulator tip and the sinking GUVs would be visible above the diaphragm, but not in the remaining portion of the field of view. This reduced the number of large GUVs available for spanning of npsLBs by a factor of four. Moreover, it was preferable to limit manipulation of GUVs above the diaphragm to a minimum so as to reduce the risk of diaphragm destruction upon collision with the manipulator tip. The tip was not visible elsewhere but above the diaphragm in transmitted light, however. In the reflected-light mode, the complete field of view was illuminated and could serve as a source of adequate GUVs. In addition, the chip could be positioned so that manipulation occurred predominantly over the Si-supported regions of the Si_3N_4 film. Thereby, a (rare) collision between the tip and the surface resulted in a destruction of the tip, but not in a destruction of the Si_3N_4 diaphragm.

3.2.6. Simultaneous electrical measurements and micromanipulation under optical control

A cell allowing for simultaneous observation of the diaphragms under a microscope, maneuvering of GUVs, and electrical measurements with the following features was used (Figure 3-25C):

- horizontal set-up allowing for sedimentation of GUVs to the surface of the substrate and straight-forward observation through upright or inverted microscopes
- narrow channels and small compartment size, giving rise to a small working volume and thus reducing significantly analyte amounts required

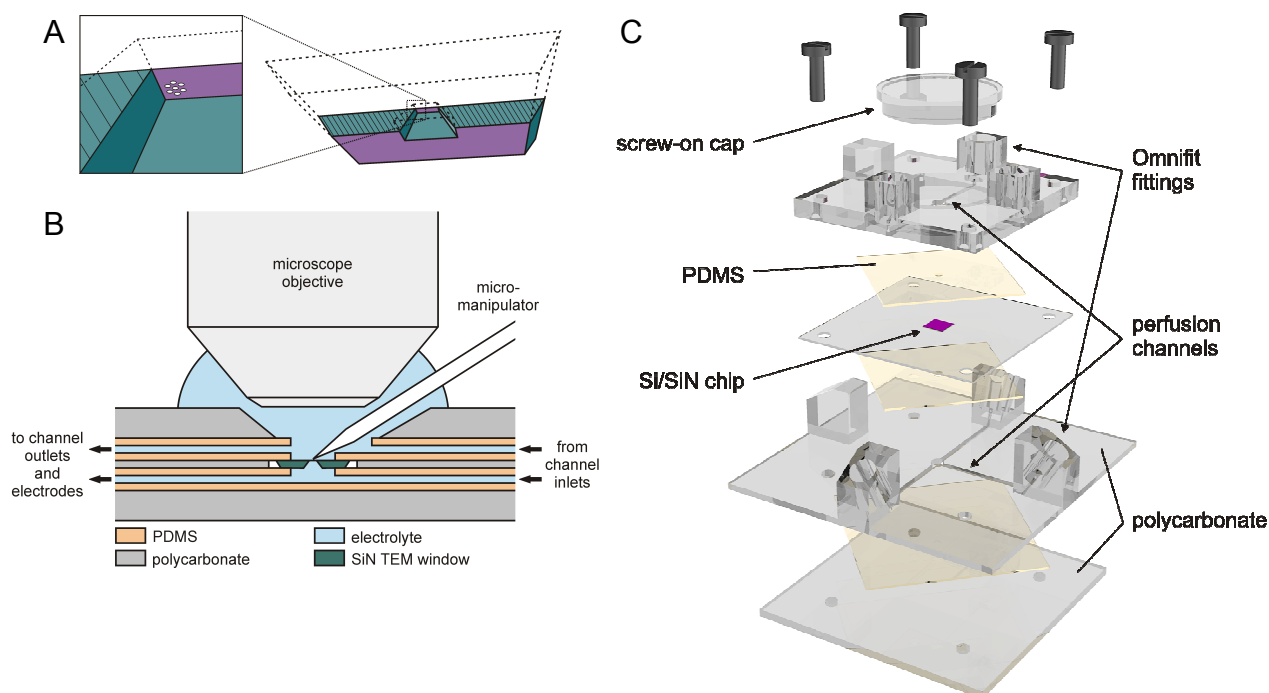


Figure 3-25. A - 3D section view of an Si₃N₄ window with a single pore array milled in the corner of the diaphragm. B – section view of the cell used for formation and electrical investigation of npsLBs on porous Si₃N₄ windows (drawn to scale, Si₃N₄ window width is 5 mm). The Si₃N₄ TEM window is mounted in the center. Both sides of the window are accessible to perfusion by inlet and outlet channels, as indicated by the arrows. The top side can additionally be accessed optically by the immersed microscope objective and mechanically by the micromanipulator tip. C - schematic of the perfusion cell for simultaneous electrical and microscopic studies of npsLBs. The cell is assembled of polycarbonate (*grey*) and polydimethylsiloxane (*beige*) components.

- thread-terminated channels to accept the tight-sealing Omnifit 1/16" fittings for easy solution exchange
- individual perfusion of and electrical access to both the upper and the lower compartment via separate channels
- top screw-on cap allowing microscopic observation through a water-immersion objective and solution exchange via perfusion while off and on, respectively
- transparent polycarbonate main body and polydimethylsiloxane (PDMS) sealing pads for microscopic observation of events at the substrate and macroscopic inspection for bubbles and perfusion failures
- moderate (polycarbonate) to high (PDMS) chemical robustness
- well-sealing PDMS pads for reliable electrolyte confinement to channels and compartments communicating with the substrate

3.2.7. AC impedance

Impedance measurements *across* the Si_3N_4 windows were carried out by means of two AgCl-coated Ag wires. The electrodes were sealed in the PDMS matrix of the measurement cell and communicated with the electrolyte in the respective compartments by perfusion channels. Impedance spectra of free pores and npsLBs and AC current vs. time traces at constant frequency were recorded using an Autolab PGSTAT302 (Eco Chemie B.V., Utrecht, The Netherlands) expanded with a FRA2 frequency analysis module and controlled from the FRA 4.9.007 software (Eco Chemie). Impedance spectra were measured at frequencies ranging from 2 mHz to 20 kHz, at no DC potential difference between the electrodes, and with an rms AC modulation amplitude of 10 mV. 200 mHz, a compromise between sufficient time resolution and npsLB resistance sensitivity, was typically used for the AC current vs. time recordings at a constant frequency. Impedance investigations *of* the Si_3N_4 windows were done in a classical 3-electrode configuration, the working electrode being the Si_3N_4 window itself, the reference electrode being an Ag/AgCl wire, and the counter electrode being a Pt wire. Equivalent circuit parameters were identified by fitting theoretical impedance curves to experimental data in ZView 2.8 software (Scribner Associates, Southern Pines, NC, USA) using a non-linear least squares algorithm.

3.2.8. DC voltage clamp

Breakdown of npsLBs at elevated DC potentials was examined by means of cyclic voltammetry. The same setup and instrument as for impedance was used, the only difference being the operating software, namely the GPES 4.7.009. Currents through single channel proteins incorporated in npsLBs were recorded by means of an EPC10 patch-clamp amplifier (HEKA Elektronik Dr. Schulze GmbH, Lambrecht/Pfalz, Germany). The signals were filtered at 3 kHz by a built-in low-pass Bessel filter. The EPC10 amplifier was controlled by Patchmaster 2.1 software (HEKA). Data were analyzed and plotted in Origin 8 software (OriginLab Corp., Northampton, MA, USA). Classical BLMs for verification single-channel recordings were painted of 10 mg/ml solutions of DPhPC in *n*-decane on apertures in 200- μm -thick Teflon septa. Apertures of $\sim 400\ \mu\text{m}$ in diameter were made by perforating the septa with sharpened hypodermic needles.

3.2.9. Passivation of Si_3N_4 windows

To enhance the dielectric properties of Si_3N_4 windows in accordance with the requirements of ionic current recordings through TM channel proteins with single-channel resolution, the pit side of a Si_3N_4 window was spray-coated with a layer of the AZ 5214E positive image-reversal photoresist. The resist was of the novolak-diazonaphthoquinone type with extra ingredients that induced thermal polymerization of exposed resist at temperatures above 110° and complete polymerization

regardless of exposure at temperatures above 130°. Spraying turned out to be the best strategy of depositing the resist on the windows (see also Chapter 4.4.6). For coatings of optimum parameters, the resist was sprayed downwards using a vertically-mounted airbrush at a distance of about 10 cm above a Si_3N_4 window. Gas pressure was set to 1 bar and resist flow-rate into the nozzle was adjusted so that a deposition rate of $\sim 2 \mu\text{m}/\text{minute}$ was achieved. A circular region of the photoresist film centered at the pore-bearing spot was exposed to blue light and dissolved in an alkaline developer. The exposure was done using the HBO bulb of the Axioskop microscope. Small diameters ($\sim 50 \mu\text{m}$) of the developed spots were achieved by minimizing the field of view by the luminous-field diaphragm and by exposure through a 100 \times objective. The window was further treated with UV-ozone and/or O_2 -plasma and/or fresh piranha solution to completely remove the photoresist from the pores. The photoresist film was then polymerized on a hotplate at 170°C for ~ 2 hours.

4. Results and discussion

4.1. Giant vesicles and supported lipid bilayers

Giant lipid vesicles were the medium of choice to form nanopore-spanning bilayer lipid membranes in this study. A primary requirement for the controlled formation of npsLBs was an abundance of large solitary GUVs. In addition, unilamellarity of vesicle envelope was demanded. The first section of this chapter thus presents and discusses the results of the GUV formation protocol.

Next, to obtain npsLBs from vesicles it is essential that the vesicles exhibit physical affinity for the surface. In particular, the vesicles should be able to adhere to and rupture/unfold at the interface. The result of the transition from a vesicular structure to a planar one should preferably be a well-defined continuous single-leaflet SLB. The presence of additional structures in the SLB, such as multilayer regions, local lipid agglomerates, holes, or adsorbed closed vesicles, might have a detrimental effect on the npsLBs. Therefore, conditions were sought that would allow for reproducible formation of good-quality SLBs from GUVs. Only at such conditions a satisfactory level of certainty could be attained that the structure suspended over a pore after GUV rupture truly was a bilayer. Adhesion and rupture of GUVs at hydrophilic interfaces is discussed in the second part of this chapter.

The ability to resolve fluorescent GUV-derived SLBs directly on the Si_3N_4 windows was another step in the sequence to successful npsLB formation. As the thicknesses of Si_3N_4 films on the windows were in the range of the wavelengths of visible light, interesting optical phenomena related to thin-film interference were observed. These findings, as well as their consequences on the optimum Si_3N_4 window parameters, are discussed in the final sections of this chapter.

4.1.1. Giant unilamellar lipid vesicles

Giant lipid vesicle yields generated by electroformation were assessed by means of fluorescence microscopy. Figure 4-1 shows a set of microscopy images of GUVs that were produced this way. The GUVs were imaged as circles of higher intensity relative to the background. The signal is most intense at the contours of the circles and minimum in the centers. This is a typical outcome of imaging surface-labeled transparent spheres via a conventional fluorescent microscope. Several facts can be pointed out with respect to our GUV populations based on these images:

Size distribution. The size distribution of the GUVs was heterogeneous, ranging from a few μm (e.g. images B or E of Figure 4-1) to above 50 μm (image C). Variation of vesicle size in one sample was welcome, as the relationship between npsLB resistance and the surrounding SLB patch (i.e. GUV) size could be investigated easily. As apparent from the figure, the mean vesicle

diameter was roughly 20 μm . Localization and manipulation of GUVs of such size under the optical microscope in order to form npsLBs was facile. A significant fraction of small vesicles and undefined lipid debris was obtained in the GUV suspension at times. The large GUVs could be cleaned of the small lipid agglomerates by dialysis through thin filter membranes.

Unilamellarity. The fluorescence intensity from vesicle to vesicle in the scope of a single image is almost equal. A variation of the number of lamellae in the GUV envelope among vesicles would induce a (discrete) variation of signal intensity. Hence it appears that the vesicles displayed in

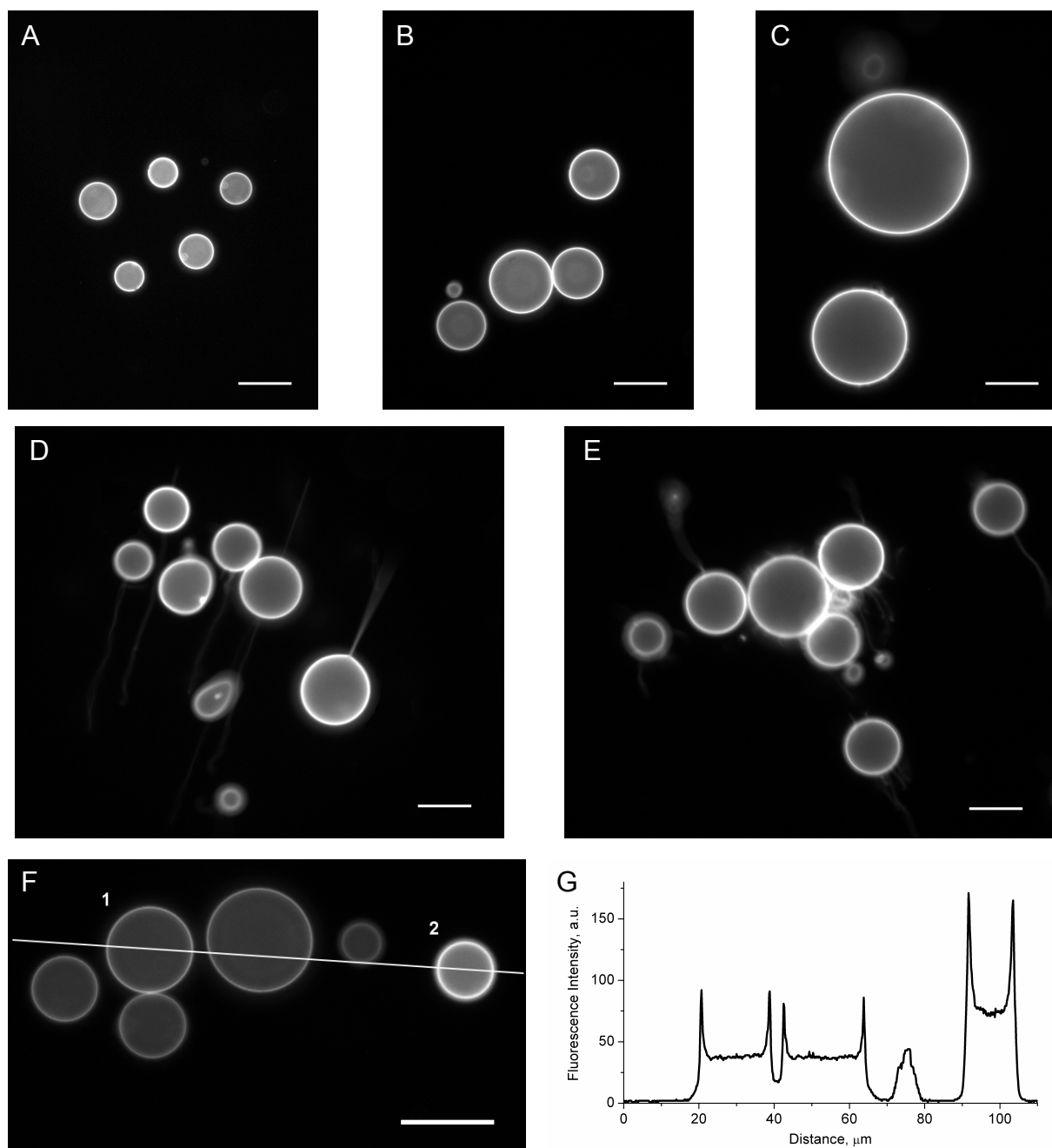


Figure 4-1. A-F – fluorescence microscopy images of intact DPhyPC(99%)/NBD-DMPE(1%) GUVs sunk, but not adhered, to a surface. The GUVs contained 0.2 M sucrose, the external medium was 0.2 M glucose. Images were adjusted to yield normalized histograms. The scale-bars correspond to 20 μm . G – intensity profile along the line depicted in F.

images A-E all have envelopes of equivalent structure. Vesicles giving a signal of intensity roughly double to that of the rest of the vesicles were observed at times. Image F shows an example of a relatively brighter vesicle (GUV 2) next to a group of (common) darker vesicles. A profile along the white line (section G) reveals for the center of GUV 2 an intensity approximately twice as large as that for the center of GUV 1. The actual (background-corrected) mean intensity values derived from areas of $25\ \mu\text{m}^2$ around the centers of GUV 1 and GUV 2 are 35.5 and 72.4, respectively. Given the signal intensity ratio of 2.04, it appears that GUV 2 exhibits double the lamellarity of the common vesicles. As revealed by comparisons between GUV size and the area of the corresponding planar SLBs formed by the rupture thereof, the common GUVs were unilamellar (*vide infra*). Although the occurrence of brighter (i.e. bilamellar) vesicles in our GUV populations could not be completely avoided, the total ratio of brighter to darker GUVs was negligible. Our GUV suspensions thus comprised predominantly unilamellar vesicles.

Envelope homogeneity. The fluorescence intensity profile (Figure 4-1G) across an imaged GUV complies with the profile of an imaged surface-labeled transparent sphere. No additional signal variation is apparent inside the GUVs in the images of Figure 4-1. This observation implies that the lipid dye has distributed evenly over the vesicle envelope. No domains of altered dye surface density with dimensions above the resolution limit of the imaging system were found.

Tubular structures. Peculiar single or multiple thread-like fluorescent structures were observed to extend from the GUVs frequently (images D and E). It appears the threads were in fact continuous extensions of the GUV lamellae that bound the vesicles to the surface or to each other. Their appearance gave the impression to the observer of looking at a group of wobbling microscopical balloons. The threads tended to extend indefinitely upon GUV displacement by a micromanipulator. After displacement, the GUVs would be pulled back near to the original location.

4.1.2. Adhesion, spreading and rupture of GUVs on hydrophilic surfaces

An assortment of factors is known to be associated with the formation of SLBs from liposomes on Si-derived hydrophilic surfaces such as glass, mica, SiO_2 , or Si_3N_4 .⁷⁹ The behavior (adhesion and rupture) of fluorescently-labeled GUVs was hence first followed *in-situ* on plain hydrophilic surfaces without pores. Glass, SiO_2 , and Si_3N_4 surfaces were used.

Due to the density difference between the inside and the outside of the GUVs, the vesicles were observed to sink to the Si_3N_4 surface after injection into the aqueous medium. Their behavior at the interface was strongly dependent on the ionic content of the electrolyte. Unless the concentration of

cations in the medium was very low, the vesicles followed a sequence of adsorption, spreading, and spontaneous rupture at the surface, forming patches of planar supported lipid bilayers, as observed previously.⁸⁰⁻⁸² Low pH, small, or divalent cations all enhanced the rate at which the transition from vesicular to planar form occurred.⁸³

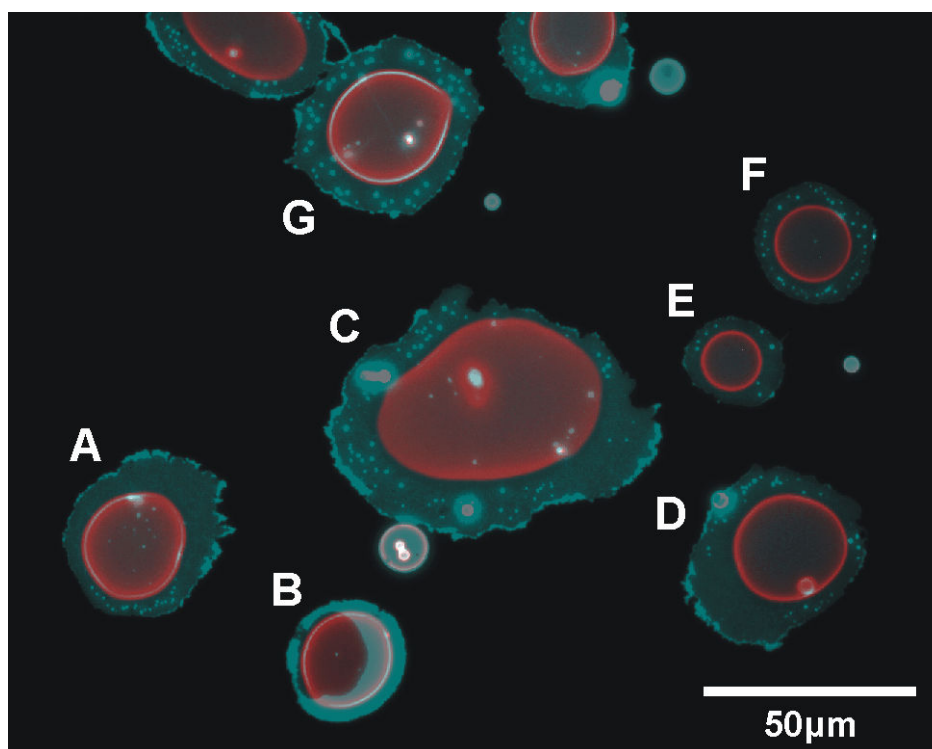


Figure 4-2. Fluorescence images of GUVs (red) adsorbed to glass, and patches of SLBs (cyan) formed by the rupture thereof.

Table 4-1. Comparison of area (in px²) of the GUVs and the respective SLB patches displayed in Figure 4-2.

GUV/SLB	vesicle area	SLB area	ratio
A	18689	40835	2.13
B	15262	21776	2.23
C	56814	109190	1.92
D	20281	46365	2.29
E	6479	14459	2.23
F	10192	22207	2.18
G	23286	49174	2.11

Figure 4-2 is an overlay of two fluorescence microscopy images. The red layer depicts a group of GUVs adhered and partly spread over a Si₃N₄ surface. Although the planar projections of most of the vesicles in the figure are near to circular (e.g. GUVs A, B, D-F) distortions of shape upon spreading, such as that of vesicle C, were commonly observed. Intensity of the fluorescent signal is minimum in the central area and peaks at the edge of every adsorbed vesicle. This is a typical

outcome of imaging transparent surface-labeled 3D objects via a conventional fluorescent microscope. The *cyan* layer of Figure 4-2 shows planar SLB patches formed by rupture of the corresponding GUVs. Area of the patches complied well with the surface area of the vesicles Table 4-1), as estimated from their diameter before the transition. This result gave strong evidence that the patches bear predominantly a single bilayer structure and can indeed be referred to as SLBs.

The two superimposed images had been taken to provide for a clear comparison of adsorbed GUVs and the corresponding SLB patches formed by the rupture thereof. For the sake of acquiring the image of GUVs in the adsorbed state, the transition sequence had been deliberately slowed down by fine-tuning the electrolyte composition. This essentially means a reduction of the affinity of the phospholipids for the surface. While in the presence of cations the two-dimensional lamellar configuration seems to be energetically most favorable, in their (relative) absence the occurrence of other structural lipid assemblies, such as small adsorbed vesicles, buds, or simply double bilayer regions, might be enhanced. In general, a higher concentration of lipid per unit area can be associated with the alternative assemblies. Under the assumption that the fluorescently dyed lipid moiety distributes evenly over such structures, their existence should manifest itself by raised intensities of the fluorescence signal relative to that induced in a plain bilayer. The obvious regions of locally increased fluorescence intensity in the patches in Figure 4-2 are presumed to be attributable to non-bilayer structures. The features occurring predominantly along the contours are regarded as folded edges, i.e. double bilayers, due to their irregular shape, homogeneous fluorescence intensity, and continuity along the periphery. The small round spots scattered throughout the patches are assumed to be either of vesicular or double-bilayer character. GUV A seems to have undergone a particularly incomplete opening, with more than a half of the patch area being comprised by a folded-edge double bilayer. It should be emphasized that planar SLB patches formed by GUV adhesion and rupture under the conditions typically adapted for npsLB formation showed very limited presence of non-SLB assemblies. In addition, even under these non-standard conditions most of the non-SLB assemblies appear in the peripheral regions of the patches. In contrast, in the central regions where the GUV lamella adhered to the surface before GUV rupture, the non-SLB assemblies are scarce. Since the npsLB would normally be located in this segment of the patch, the probability that a non-bilayer structure extended over the pore(s) was low.

4.1.3. SLB fluidity

As a side-effect of fluorescence studies aimed at the behavior of GUVs at hydrophilic surfaces, an interesting and previously unreported way to observe lateral diffusion of lipid molecules in SLBs was discovered. Two populations of GUV were used: one with a fluorescently-labeled lipid

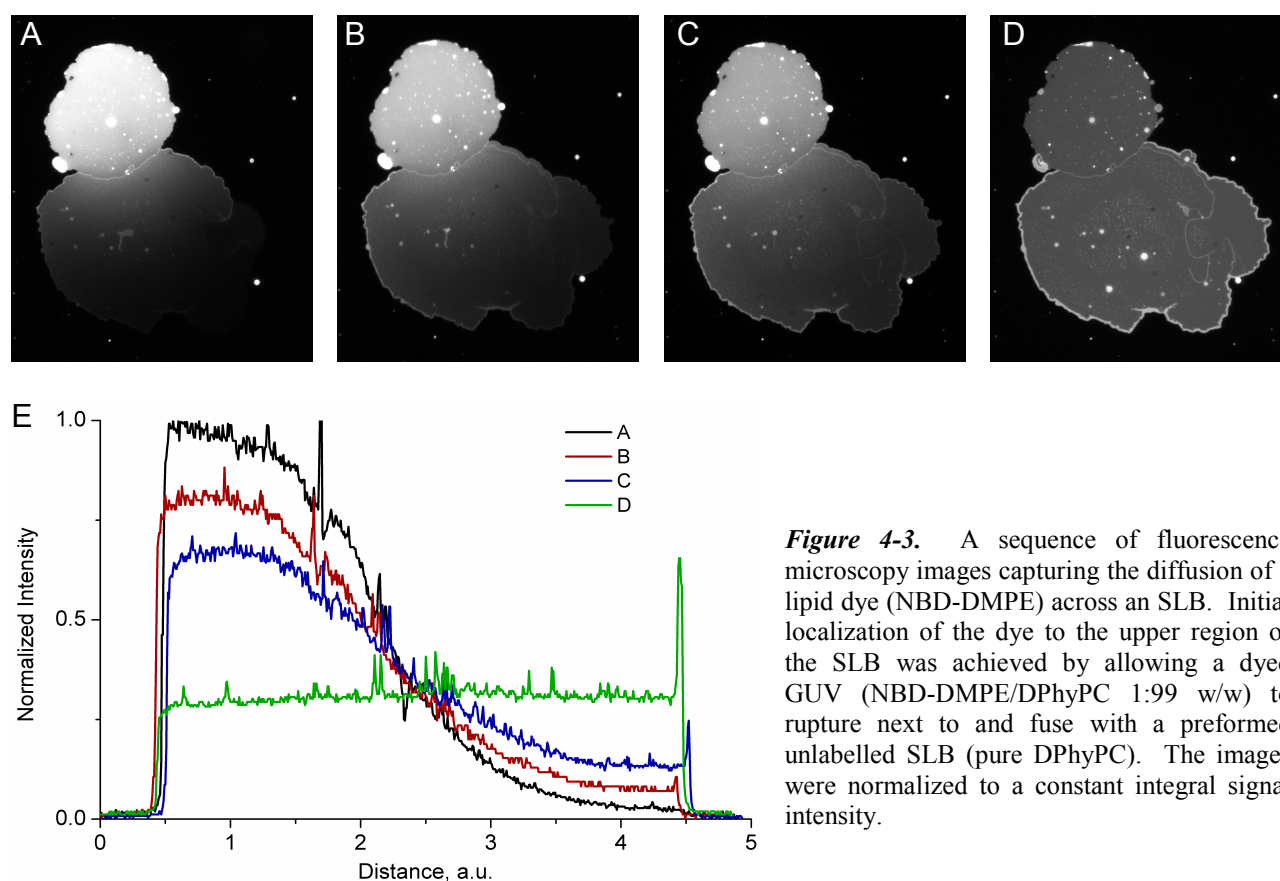


Figure 4-3. A sequence of fluorescence microscopy images capturing the diffusion of a lipid dye (NBD-DMPE) across an SLB. Initial localization of the dye to the upper region of the SLB was achieved by allowing a dyed GUV (NBD-DMPE/DPhyPC 1:99 w/w) to rupture next to and fuse with a preformed unlabelled SLB (pure DPhyPC). The images were normalized to a constant integral signal intensity.

incorporated in the lamella, and one free of the dye. Unlabelled GUVs were first allowed to form isolated SLBs free of the dye lipid. Subsequently, labeled GUVs were injected and allowed to transform into SLBs. Because the surface available to observation was partly covered with unlabelled SLBs, several instances occurred whereby a labeled GUV sank, spread, and ruptured in the vicinity of an unlabelled SLB patch. If a GUV unfolding on a surface encounters an SLB patch, the new SLB patch being formed accommodates to the presence of the original SLB patch and unfolds tightly alongside its edge without bilayer overlap. A ‘fusion’ of the opening GUV with the original SLB occurs and a completely fluid suture is established between the two SLB patches. Due to planar Brownian motion, the lipid molecules corresponding to the labeled and dye-free regions of the now-unified SLB start mixing immediately. Figure 4-3, a sequence of fluorescence images, captures the mixing of lipid between two such SLBs. An initially steep signal intensity gradient between the two regions relaxes over time as the diffusion of the dyed lipid into the unlabeled part of the SLB progresses. An even distribution of the dye over the entire SLB area is achieved eventually (Figure 4-3D). Theory on the determination of lateral mobility of dyed lipid in an SLB in a comparable scenario has been developed⁸⁴.

4.1.4. Modulation of SLB fluorescence intensity by Si_3N_4 thickness

Reproducible formation of well-defined SLBs by rupture of GUVs on Si_3N_4 was of primary importance with respect to the goals of this study. A pronounced variation of SLB fluorescence intensity was observed as a function of Si_3N_4 thickness during these investigations. Similarly, a significant difference in signal intensity was observed at times between SLBs formed on Si-supported Si_3N_4 and free-standing Si_3N_4 of the same thickness. Images A and B in Figure 4-4 demonstrate this variation. The contour of the Si_3N_4 diaphragm is clearly noticeable in both images. SLBs on 75-nm-thick Si_3N_4 (image A) supported by Si yielded a significantly stronger signal than SLBs from the unsupported section of the Si_3N_4 film. On 100-nm-thick Si_3N_4 , on the contrary, SLB fluorescence intensity from the two sections of the film was far less different. The signal from the diaphragm was slightly more intense than the signal from the supported film in this case. A plot of average fluorescence intensity relative to Si_3N_4 thickness for SLBs on both supported and unsupported Si_3N_4 is plotted in section C of the figure. The variation is considerably higher on Si-supported Si_3N_4 . Of the five Si_3N_4 thicknesses tested, fluorescence from the 75-nm film is most intense, while at 150 nm of nitride the intensity is at minimum. Conversely, the unsupported 150-nm-thick film (bathed on both sides with electrolyte) generated twice as strong a signal, surpassed minutely only by the 100-nm-thick film. Although the quantitative value of the plot in Figure 4-4 is ambiguous due to the experimental difficulties that accompany the attempts to relate intensity values among images (drift of light source intensity, uneven planar illumination over the field of view, dye bleaching, etc.), the qualitative message is clear. Furthermore, evaluation of data extracted from multiple non-distant spots in a single image is not burdened by such errors. Figure 4-4D, a plot of SLB fluorescence intensity on the supported relative to the free-standing Si_3N_4 , was constructed that way. The contrast is as high as 7.5 on 75-nm-thick Si_3N_4 , whereas at 100 nm the intensities are almost equal.

Light absorption and light emission of dye molecules depend on the distance and on the orientation with respect to a mirror.⁸⁵ Due to its considerable reflectivity, modulation of dye fluorescence intensity occurs at a smooth silicon surface, too. An extensive theory on fluorescence variation of SLBs in the interference field generated by thin films of SiO_2 on Si has been developed by Lambacher and Fromherz.⁸⁶⁻⁸⁸ An analogous theoretical approach to the detected intensity could be applied to this scenario while taking the following into account: Si_3N_4 as the optical ‘spacer’, diminished reflectivity of the electrolyte in the case of free-standing Si_3N_4 , and the quantum yield and lifetime of the dye. As the case is further complicated by non-monochromatic excitation, integration over the excitation spectrum in addition to the emission spectrum (the former given

4. Results and discussion

jointly by the source, the dye, and the optics, the latter given by the dye and the optics, i.e. the objective, mirrors, and filters) would be necessary. Full adaptation of the theory to the specific scenario is out of the scope of this study.

Some key points derived from the simulations on SiO_2 can be discussed here without elaborating on the details of the theory, however. The intensity modulation with respect to thickness of the spacer layer (SiO_2 , Si_3N_4) after all factors have been taken into account is a damped almost-periodic oscillation.^{88,89} The function is at minimum for zero displacement of the dye from the reflective surface. The period of the oscillation is roughly a half of the dye excitation wavelength corrected for the refractive index of the spacer. Damping of the oscillation amplitude with growing thickness is due to the wavelength shift between excitation and emission, broadband detection, and large aperture of illumination and detection. Large aperture also increases the period of oscillation (by $\sim 5\%$ at $\text{NA} = 0.4$ ⁸⁹ and $>15\%$ at $\text{NA} = 1.0$ ⁸⁸). If some degree of order exists for the dye on the

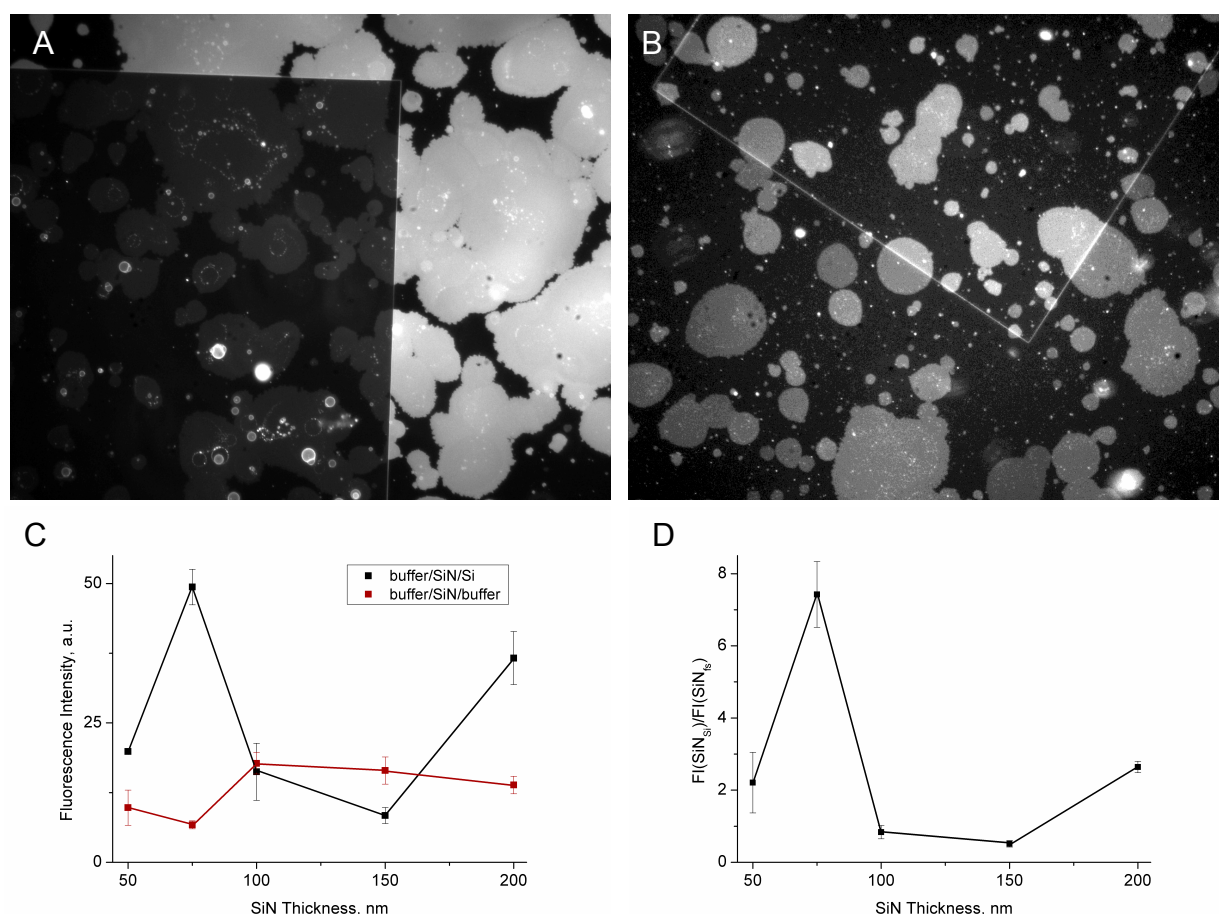


Figure 4-4. Fluorescence microscopy images of DPhyPC/NBD-DMPE (99:1 w/w) SLBs on silicon nitride of 75 nm (A) and 100 nm (B) in thickness. Sections of both Si-supported Si_3N_4 and the square-shaped Si_3N_4 diaphragm are depicted. Fluorescence intensity is significantly higher on the Si-supported film relative to the free-standing film in A and slightly weaker in B. Contrast of the images was enhanced, the intensities of A vs. B thus do not compare realistically. (C) SLB fluorescence intensity with respect to Si_3N_4 film thickness on Si-supported (*black*) and free-standing (*red*) Si_3N_4 . (D) Ratio of SLB fluorescence intensity from Si-supported and free-standing Si_3N_4 with respect to Si_3N_4 film thickness.

surface, then the average polar angle of the dye transition dipole tends to invert the fluorescence intensity pattern as it converges to zero with respect to the surface normal (Figure 4-5).

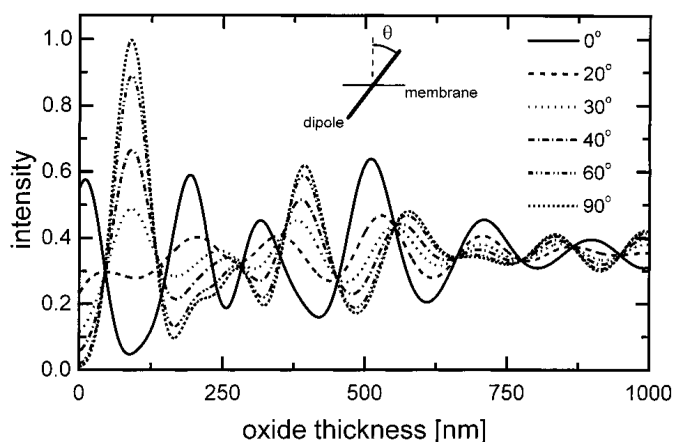


Figure 4-5. Theoretical fluorescence intensity of Di8ANEPPS in lipid bilayer on silicon versus thickness of silicon dioxide. The polar angle of the transition dipole at random azimuthal angle is indicated. Numerical aperture $NA = 0.9$, monochromatic excitation is at 434 nm, broadband detection is at 630 nm. The intensities are scaled with respect to the intensity at infinite thickness of silicon dioxide. Figure was adopted from ref. [88].

At normal incidence, the thickness of Si_3N_4 at the first maximum of the specific fluorescence modulation curve is given by $d_{\text{max}} = \lambda_{\text{ex}}/4n_{\text{SiN}}$, where λ_{ex} is the excitation wavelength of the fluorophore (~ 470 nm) and n_{SiN} is the refractive index of the material. Refractive index in the range of 2-2.5 has been reported for LPCVD SiN_x of varying N/Si ratio⁹⁰. It is assumed that the LPCVD Si_3N_4 films used in this study comprise stoichiometric Si_3N_4 . At $n_{\text{SiN}} = 2.00$, $d_{\text{max}} = 58.8$ nm. This first approximation appears not to comply with the experimental data too well, as in our case the maximum seems to be near to 75 nm of Si_3N_4 , whereas at 50 nm the intensity is rather low. Taking the numerical aperture of the objective into account, however, the first maximum can be expected to appear at Si_3N_4 thickness of ~ 63 nm. Moreover, the (rather unrealistic) assumption that the fluorophore dipoles are ordered parallel to the membrane may be reconsidered. Data on preferential inclination of transition dipole moment in lipid bilayers are not available. It is known, however, that the absorption and emission transition dipole moments of the NBD dye are inclined by 25° with respect to each other.⁹¹ In the model, Lambacher and Fromherz assume parallel transition dipole moments for their fluorophore. Taking these differences into account, a good match between the collected data on SLB fluorescence on Si-supported Si_3N_4 films and the theory may be attained. The pattern of fluorescence modulation at the free-standing Si_3N_4 diaphragm should be inverted, because the $\lambda/2$ phase shift does not occur at beam reflection from an optically thinner medium. Furthermore, a less pronounced intensity pattern magnitude can be expected due to lower reflection at the Si_3N_4 /buffer interface relative to the Si_3N_4 /Si interface ($\Delta n_{\text{SiN/Si}} \approx -2.0$, whereas $\Delta n_{\text{SiN/water}} \approx 0.65$). The experimental data (Figure 4-4C) seem to comply with these deductions.

The experimental analysis of NBD-labeled SLB fluorescence modulation on Si-supported and free-standing Si_3N_4 films made 100 nm the preferred thickness of Si_3N_4 diaphragms for the next phases

of the study. Of the five Si_3N_4 film thicknesses offered by the supplier, 100-nm one yields the best signal intensity of an SLB on the Si_3N_4 diaphragm. This was a key argument with respect to observation of SLBs on porous Si_3N_4 diaphragms at good S/N ratios. Although 150 and 200 nm of Si_3N_4 are not substantially worse in this aspect, thicker Si_3N_4 films require 1) longer pore milling times that can induce shape and spacing distortions, and 2) give rise to pores with potentially limited diffusion characteristics due to higher aspect ratios. A major benefit of thicker Si_3N_4 diaphragms might be better mechanical robustness. 100, 150, and 200-nm-thick Si_3N_4 diaphragms all appeared to be equally sturdy, however.

4.1.5. Lipid domains in SLBs on glass

Interesting fluorescence microscopy images of SLBs derived from GUVs were acquired on borosilicate glass of Lab-tek cell culture wells (Figure 4-6). The experiments were performed with 0.2 M non-buffered glucose as the external medium. Adhesion of GUVs to the surface and transition to SLBs was induced by addition of CaCl_2 to a final concentration of 1 mM. The planar lipid structure displayed in the image exhibits regional variation of fluorescence intensity at three discrete levels (denoted below as I_0 , I_1 , and I_2). Two sorts of large-scale regions can be noticed easily that exhibit small-scale signal variation between levels I_0 and I_1 , and I_1 and I_2 , respectively. It appears there are two contributors to this phenomenon: 1) planar domains of varying lipid character and composition, and 2) lipid bilayer overlay.

A key *a priori* assumption for the following discussion is that planar *monolayer* structures were not formed. The assumption is derived from the following facts: first, the cell culture wells that the experiment was performed in were denoted as ‘sterile’, i.e. the supporting glass surface was clean hence hydrophilic. Phospholipids are known to interact with a hydrophilic surface via their headgroups and assemble in bilayers to minimize the free energy.⁷⁹ Second, the planar structures were formed from vesicle envelopes, i.e. bilayers. Given the former argument, the transition from a bilayer to a monolayer structure upon vesicle opening was very unlikely.

Let us first focus on the circular regions of lowest fluorescence intensity (I_0). The dark regions are all surrounded with structures (presumably bilayers) of signal intensity I_1 . Since no form of fluorophore quenching is expected on a glass surface, low signal must correspond to a low dye surface density. This can be due to complete absence of a planar lipid structure, or to local exclusion of the dye from the dark regions. The former option would imply the existence of holes scattered all over the SLB of signal intensity I_1 . A steady-state scenario of this kind would be energetically very unfavorable, however. Moreover, it is difficult to imagine why upon GUV unfolding on a hydrophilic surface the continuous vesicular lamella would lose integrity in such an

extent. It is thus more likely that the dark regions are caused by local exclusion of the dye, i.e. planar domain formation. As DPhPC and NBD-DMPE are the only components of the lipid mixture, the domains seem to be composed primarily of DPhPC. A value of ~ 8 a.u. (arbitrary units) has been assigned to I_0 via raw image analysis (Figure 4-7A). This non-zero signal intensity of the domains can be due to noise, but it can also reflect the presence of NBD-DMPE in the domains, albeit at a significantly reduced concentration as compared to the surrounding SLB regions. It is peculiar that the domains seem to agglomerate, yet tend not to coalesce to form circular domains of larger diameters (Figure 4-6).

No domains were observed in the GUV lamellae that gave rise to the SLB. Domain appearance in the SLB is thus obviously a consequence of an interaction between the bilayer and the glass surface, presumably mediated by the presence of CaCl_2 . A question arises whether the character of both leaflets of the SLB is equal in the domains, or the character of the proximal leaflet (the leaflet adjacent to the surface) is different to that of the distal leaflet. It has been found, for example, that the lateral mobility of phospholipids is significantly reduced in an SLB relative to an unsupported BLM, and this holds true for both leaflets of the SLB.^{68,69} Apparently, in the case of lateral diffusibility the interaction of the proximal leaflet with the surface propagates onto the distal leaflet. Formation of domains in lipid bilayers made of lipid mixtures is a well-known phenomenon.⁹²

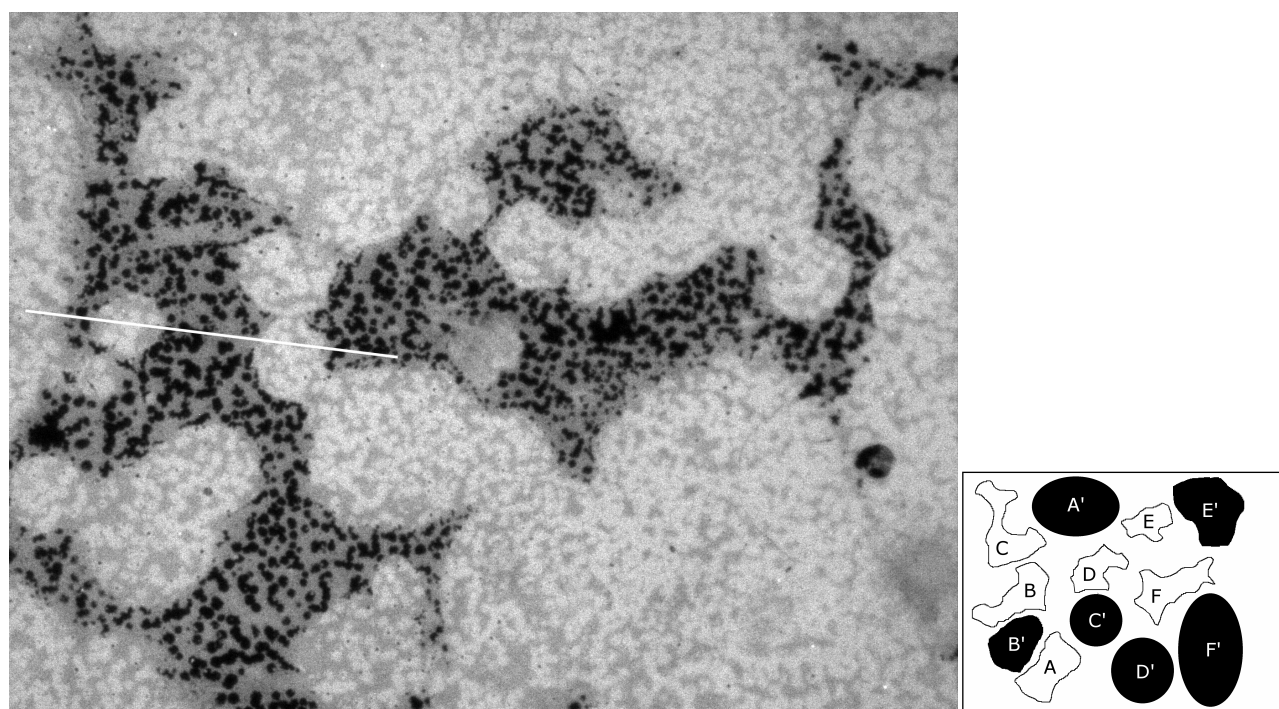


Figure 4-6. A - fluorescence image of an SLB formed from GUVs on borosilicate glass of a Lab-tek cell-culture well. Noteworthy is the presence of regions with large-scale and small-scale variation of signal intensity. Image brightness and contrast were adjusted to give a normalized histogram. B - regions used to evaluate the mean signal intensity of the single and double bilayer (A-F and A'-F', respectively).

The large-scale regions whereby signal intensity varies between I_1 and I_2 probably correspond to the presence of a second lipid bilayer on top of the domain-bearing SLB (further denoted as the top and the bottom SLB, respectively). As the overlaid bilayers originate from the homogeneous GUV lamellae, it can be expected that the density of the fluorescent dye is the same in both. Although a short-range variation of signal intensity exists in the SLBs, signal averaging should yield values that correspond to the mean surface density of the dye in the individual large-scale regions. Mean signal intensity from the regions where the top SLB is present should be twice as high as the mean intensity from the bottom SLB alone. Averaging of raw image intensity over the total area of the regions outlined in Figure 4-6B gives values of 24.9 a.u. (\bar{I}_{bottom}) and 51.1 a.u. (\bar{I}_{both}) for the bottom and for both SLBs, respectively.* The resulting ratio of 2.05 implies a double dye surface density in the brighter large-scale regions, and hence an overlaying continuous bilayer.

Did domains equivalent to those in the bottom SLB form in the top bilayer, too? If they did, spots of intensity given by the three possible overlay combinations should be observable: $I_0 + I_0$ for a domain/domain overlay, $I_0 + I_1$ for a domain/non-domain overlay, and $I_1 + I_1 (=I_2)$ for an overlay of two non-domain bilayer structures. The absence of intensity of $2I_0$ in the double-bilayer regions allows one to deduce that domains comparable to those in the bottom SLB did not form in the top bilayer.

The intensity histogram in Figure 4-7A comprises data of four independent histograms each constructed for a spot ($\sim 2000 \text{ px}^2$) of constant signal intensity: a dark and a bright spot from region B, and analogously from region A' (Figure 4-6B). Gaussian fits to the data yield signal intensity values of $8.2 \pm 1.3 \text{ a.u.}$ and $36.0 \pm 3.5 \text{ a.u.}$ for the dark (domain) and the bright spots of the SLB without overlay, respectively. It holds for the mean signal intensity of the top bilayer that $\bar{I}_{top} = \bar{I}_{both} - \bar{I}_{bottom} = 26.2 \text{ a.u.}$ If the domain pattern of the bottom SLB is retained even when overlaid with the top bilayer, and the distribution of the dye throughout the top bilayer is homogeneous, an intensity histogram of the double bilayer should be analogous to that of the single bilayer. Namely, both peaks should be shifted rightward by \bar{I}_{top} to 34.5 a.u. and 62 a.u., respectively. The actual mean intensity values for the dark and the bright spots of the double bilayer are $44.9 \pm 3.4 \text{ a.u.}$ and $58.3 \pm 4.0 \text{ a.u.}$. The dark spots are 30% brighter than what would be expected for domain regions equivalent to those in the bottom SLB alone, but overlaid by an additional homogeneously-fluorescing bilayer. Conversely, the bright spots are 6% darker than expected. The difference can

* Quantitative analysis was done on raw image data rather than the normalized version presented in the figure.

be due to a more homogeneous dye distribution in the bottom bilayer, possibly due to domain restructuring induced by the presence of the top layer, and/or heterogeneous dye distribution in the top layer. Should the latter scheme act on its own, the dye in the top bilayer would in fact have to favor the underlying domain regions. Figure 4-7B, a profile plot along the line displayed in Figure 4-6A, displays clearly the variation of signal intensity with respect to distance.

Obviously, experimental conditions could be attained rather easily whereby 1) partitioning of lipids of the given mixture within SLBs into heterogeneous domains, and 2) formation of double bilayers was observed. Both phenomena were undesirable with respect to spanning of npsLBs over nanopores. The key factors inducing the effect seemed to be the specific type of glass surface, the presence of Ca^{2+} in the medium, and the availability of lipid bilayer on the surface in excess to a saturated single SLB. Even though analogous effects were not detected in SLBs on Si_3N_4 surfaces, Ca^{2+} and excessive amounts of GUVs on the surface were generally avoided in npsLB experiments.

4.1.6. SLBs on Si_3N_4 diaphragms irradiated with the e-beam and the i-beam

The procedure of milling of nanopores through Si_3N_4 diaphragms by the FIB involved local exposure of the pit side of the diaphragm to focused electron and ion beams (see Chapter 3.2.2 for details on the milling procedure). The 5 keV electron (imaging) beam was used to select the location on the diaphragm where the pores were to be milled, adjust the height of the stage so that this location was placed in the eucentric point, and image the pores after milling had been finished. Apart from the milling itself, exposure to the 30 keV ion beam occurred upon alignment and focusing of the beam at the diaphragm. In other words, excess areas of the Si_3N_4 diaphragm in the vicinity of the pore-bearing location were exposed to the electron and/or the ion beam.

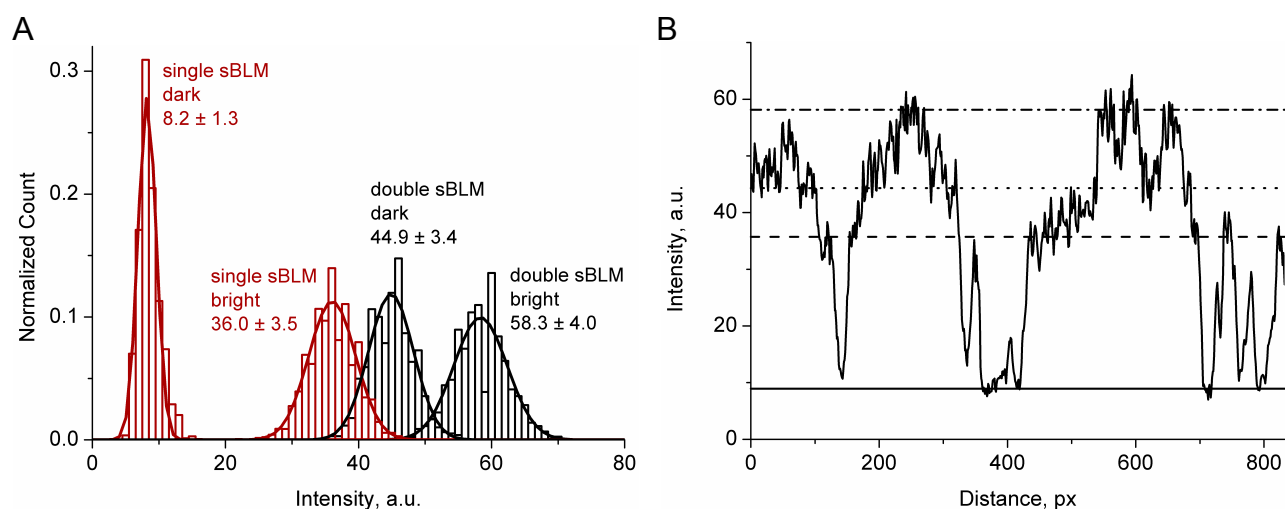


Figure 4-7. A – fluorescence intensity histograms derived from $\sim 2000 \text{ px}^2$ spots in Figure 4-6 each corresponding to one of the four discrete intensity levels. The spots were located in regions B (red) and A' (black). B – profile scan along the white line plotted in Figure 4-6A.

Surprisingly, fluorescence microscopy imaging of GUV-derived SLBs over these areas revealed significant reduction or complete absence of signal intensity and some interesting SLB behavior.

Fluorescence images of SLBs captured during an attempt to form an npsLB over a single pore in a Si_3N_4 diaphragm are displayed in Figure 4-8. In image A, a solitary SLB patch can be seen that, as deduced from its shape, location, and previous observations of such patches on Si_3N_4 surfaces, would be expected to typically span over the corner of the diaphragm. Contrary to this expectation, no signal can be detected from the diaphragm corner that would indicate the presence of a continuous SLB. Image B was taken after additional GUVs ruptured at the pore-bearing corner and fused with the existing solitary patch. The character of the fluorescence signal indicates that a nearly continuous SLB spans all over the free-standing and the Si-supported Si_3N_4 surface. The surroundings of the pore-bearing location remain dark, however. The shape of the dark region is of a well-defined triangle and shows a sharp intensity transition towards the center of the diaphragm. These facts and the absence of the phenomenon on diaphragms that were not exposed to accelerated charged particles suggest that it is the irradiation of the diaphragm with the ion and/or the electron beam that induces the effect. The phenomenon was observed repeatedly on different samples where pores were produced using the same protocol. The shape of the dark corner area varied from sample to sample, but remained unchanged for multiple tries on the same sample.

What could have been the cause of attenuated fluorescence in this region? Strictly speaking, it is the absence of photon emission by the fluorophores that translates into the lack of fluorescence. Obviously, emission occurs only, but not necessarily, if the fluorophores are excited. Several alternatives can be considered that would give rise to attenuated emission. First, the concentration

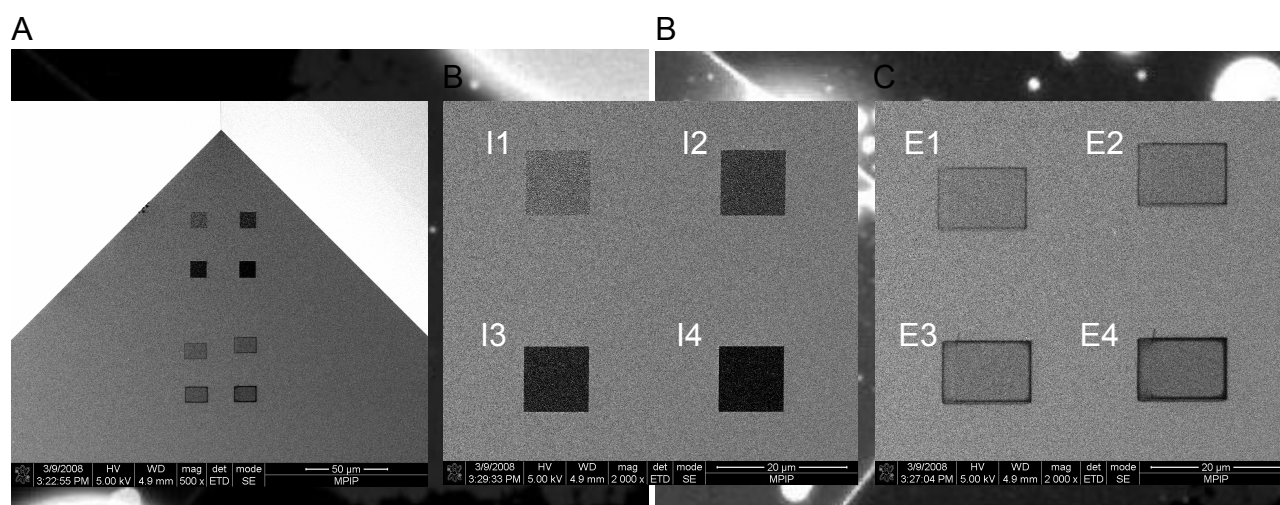


Figure 4-9. SEM images of the pit side of a gold-coated Si_3N_4 diaphragm with two groups of rectangular regions exposed to the ion or the electron beam over varying periods of time. (A) – 500× magnification, with ion-irradiated squares near and electron-irradiated rectangles far from the corner of the diaphragm. (B) and (C) – SEM images of the ion- and the electron-beam treated regions, respectively, at 2000× magnification.

of the dye molecule in the irradiated region could be significantly lower as compared to the non-irradiated regions of the diaphragm. Two scenarios are possible: either the SLB does not form there at all, or the SLB forms, yet with locally altered composition, i.e. with the NBD-DMPE fraction considerably reduced. Second, if unaltered spreading and composition of the SLB is assumed, attenuated excitation of the dye due to physical changes of the diaphragm induced by irradiation can be considered. Third, if unaltered spreading and composition of the SLB as well as dye excitation is assumed, subsided fluorescence could be a consequence of non-radiative dye relaxation (quenching), again due to physical changes of the diaphragm induced by irradiation.

As simultaneous AC measurements of ionic currents through the pores did not indicate npsLB formation, the thesis that no SLB existed over the dark corner region seemed most plausible. This, however, was in contrary to the notion of npsLB spanning that this project aimed for. To eliminate the problem, it was crucial to first identify which of the two beams was responsible for the effect. We thus prepared Si_3N_4 TEM windows with well-defined regions that were exposed to the electron or the ion beam at controlled doses and observed SLB formation over these.

SEM images of the Si_3N_4 diaphragm of the test sample are shown in Figure 4-9. At the top part (nearer to the corner) of image A, four square-shaped regions can be seen that the ion beam was rastered over. Similarly, the four rectangular regions at the bottom were exposed to the electron beam. Images B and C are close-ups of the ion and electron beam irradiated areas, respectively. In both cases, the exposure dose was minimum for the top-left rectangle and maximum for the

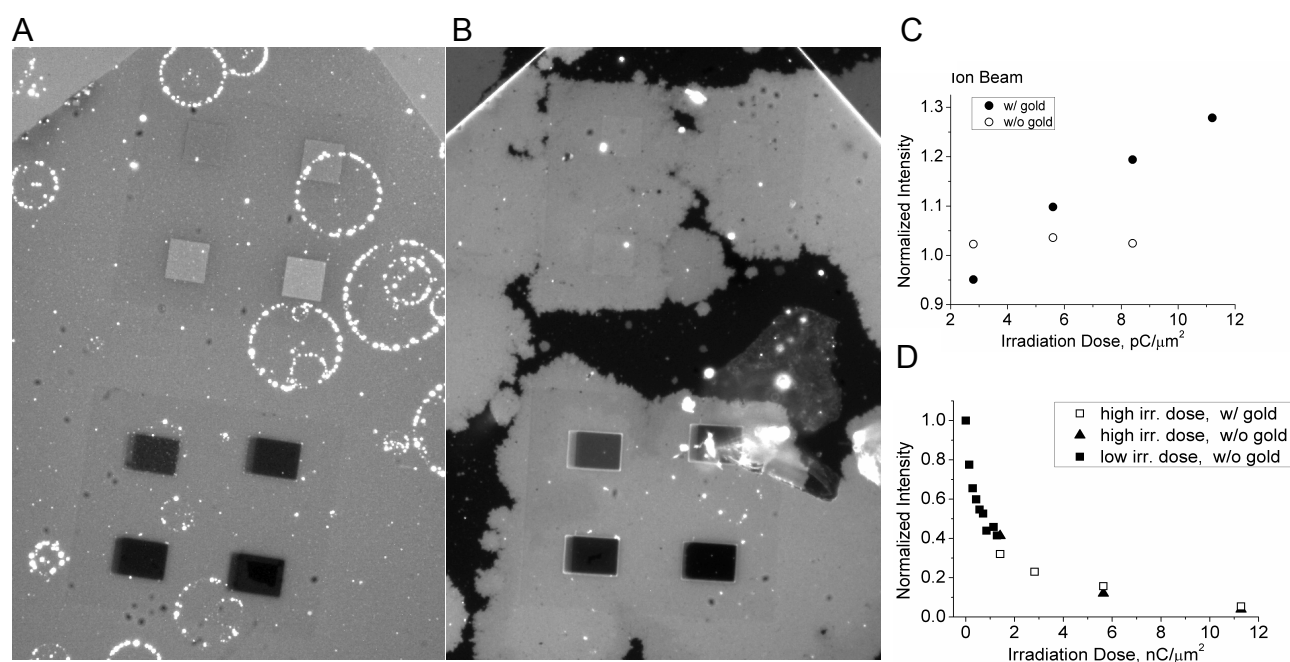


Figure 4-10. Ion-irradiated regions are $10 \times 10 \mu\text{m}$ wide and $30 \mu\text{m}$ apart, while the electron-irradiated rectangles have the dimensions of $12.6 \times 9 \mu\text{m}$ and analogous separation.

bottom-right one. The trend of rising exposure dose is clearly reflected by the shade of the rectangles. While in the case of the ion beam the shade can undoubtedly be correlated to the thickness of gold sputtered off the diaphragm, in the case of the electron beam the darkening upon prolonged exposure is most likely due to build-up of carbon contamination on the surface or charge accumulation in the diaphragm. Exposure of I4 to the ion beam has been calculated to just remove the assisting gold layer without significantly attacking the Si_3N_4 diaphragm.

Figure 4-10 shows two images of NBD-DMPE-labeled SLBs formed on the flat side of the test sample by rupture of GUVs. The SLBs in image A and B were formed before and after removal of the gold layer from the pit side, respectively. Let us first examine the group of squares irradiated with the ion beam. An obvious trend of growing signal intensity from square I1 to I4 can be noted in image A. The intensity values normalized to the surrounding SLB fluorescence are quantified in plot C of Figure 4-10. Signal from the SLB on non-irradiated regions of the Si_3N_4 diaphragm exhibits an intensity comparable to that of I1. The SLBs look significantly different after gold had been removed from the pit side, however (image B). Although I4 is not utterly covered by an SLB, a comparison among I1-I3 reveals negligible difference in signal intensity (plot C of Figure 4-10). Similarly, the SLB surrounding the irradiated squares shows comparable fluorescence. Apparently, the thin gold layer on the pit side of the Si_3N_4 diaphragm alters the electromagnetic interference field at the interface with a net negative effect on final fluorescence intensity of the fluorophores. The longer the exposure to the ion beam, the thinner the reflecting gold layer, and hence the stronger the signal. Dissolution of the remaining gold in aqua regia equalizes the fluorescence intensity in all i-beam irradiated squares with respect to each other as well as the surroundings. Irrespective of the presence of the gold layer, signal intensity is homogeneous over the complete area of each irradiated square. No hindrance to the spreading of SLBs has been observed due to treatment with the i-beam. Exposure of the pit side of the diaphragm to the i-beam thus obviously is not responsible for the lack of fluorescence from around the pore-bearing site.

SLBs covering the electron-irradiated rectangles are considerably different. Regardless of whether the gold film is present or absent on the pit side of the diaphragm (Figure 3, image A vs. B), the SLBs over the electron-irradiated rectangles show notably weaker fluorescence than the surrounding bulk SLB. A trend of decreasing signal intensity is apparent from E1 to E4 in both cases. Plot D shows normalized SLB fluorescence intensity from spots E1-E4 of the sample depicted in Figure 4-10, as well as from regions E1-E9 of the sample depicted in Figure 4-11. Data acquired in both the presence and the absence of the gold layer on the pit side of the diaphragm is presented for the former, and solely in the absence of the gold layer for the latter. The fluorescence

intensity of the SLB over E4 in image B of Figure 4-10 is comparable to the background intensity. A peculiar dark spot of size roughly a quarter of that of the whole rectangle can be noted near the center of E4 in image A. On all the other irradiated spots in both images the signal is uniform and continuous. This finding implies that an SLB *does* span the electron-irradiated regions, yet its fluorescence is inversely proportional to irradiation dose. Apparently, it is the exposure of the Si_3N_4 diaphragm to the electron beam (i.e. SEM imaging before and after milling) that induces loss of fluorescence intensity around the site of pore milling.

To obtain a better understanding of the attenuated fluorescence of SLBs on diaphragms exposed to the e-beam, an additional sample has been prepared with features irradiated at lower doses than

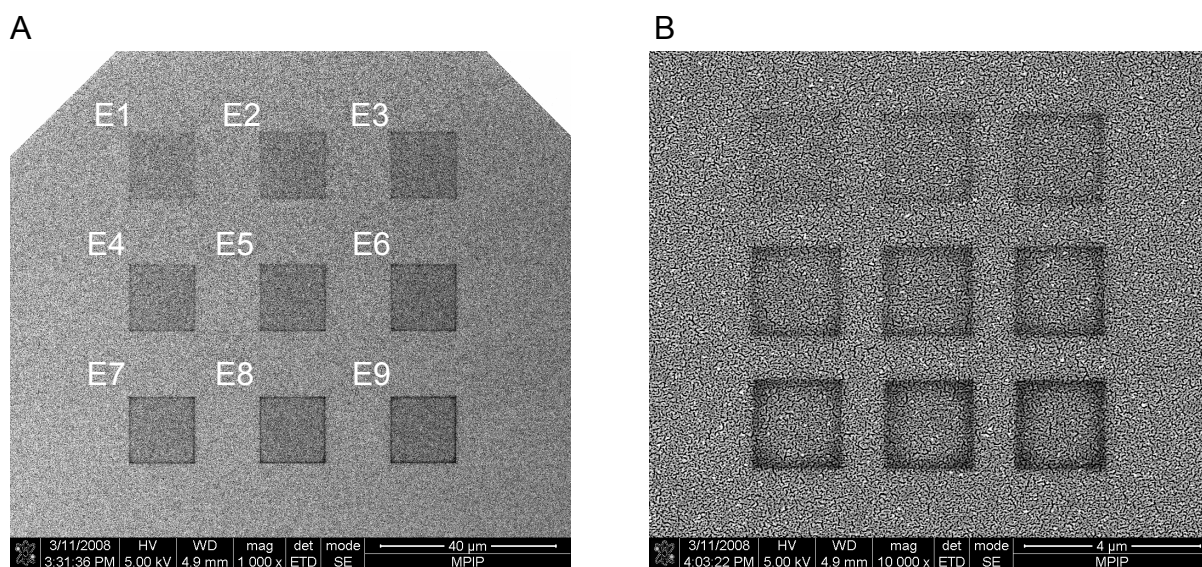


Figure 4-11. SEM images of feature patterns on the pit side of the SIN diaphragm irradiated by the electron beam. Features optimized for fluorescence microscopy studies (A): size - $15 \times 15 \mu\text{m}$, pitch - $30 \mu\text{m}$, charge dose increment - $0.142 \text{ nC}/\mu\text{m}^2$. Features optimized for AFM studies (B): size - $2 \times 2 \mu\text{m}$, pitch - $3 \mu\text{m}$, charge dose increment - $0.142 \text{ nC}/\mu\text{m}^2$. Charge dose was minimum in the top-left and maximum in the bottom-right corner of either pattern.

previously. Squares of two different sizes, $15 \mu\text{m}$ and $2 \mu\text{m}$, in 3×3 patterns were irradiated for fluorescence microscopy and AFM investigations, respectively (Figure 4-11). The dose per unit area was increased from square to square in $0.142 \text{ nC}/\mu\text{m}^2$ increments.

Fluorescently-labeled SLBs formed on the flat side of the corner of the diaphragm depicted in Figure 4-11A are shown in Figure 4-12. As before, fluorescence intensity of SLBs spanning over the irradiated squares scales inversely with irradiation dose in image A. Their normalized intensities are plotted as *black squares* in Figure 4-10D. A smooth continuation exists between the data points obtained from the sample with features irradiated at higher (Figure 4-9C) and lower charge doses (Figure 4-11A). Interesting SLB behavior can be noticed in squares 2, 6, and particularly 8 of image A. The SLB seems to have preferred spreading over the irradiated squares, as if a higher affinity existed of the lipid for the irradiated regions as compared to the untreated

bulk. Similar behavior is apparent in image B, here in the most pronounced extent in squares 4 and 6. The squares barely communicate with SLB patches that are located on the bulk diaphragm, yet in both cases a continuous SLB clearly extends along the full perimeter of their rims. Intriguingly, the central parts of all irradiated squares in image B seem not to be covered by an SLB. The extent to which the inner part of a given square is covered seems to be related to the abundance of an SLB around the square. This is a surprising change with respect to the situation in image A, where all squares are covered continuously. Image B comes from an experiment performed one day after the experiment that image A is related to. Between the two images were taken, the diaphragm was rinsed with ethanol and water, and incubated in a suspension of GUVs in water for several hours.

How could irradiation of the pit side of a 100-nm-thick Si_3N_4 diaphragm with a 5 keV e-beam have such a pronounced effect on the character of SLB fluorescence on the flat side? Primarily, it is important to realize that the penetration depth of 5 keV electrons through silicon nitride is in the order of 300–400 nm⁹³. The 10 nm of gold on the pit side does not hinder electron penetration significantly. A portion of the electrons impinging on the diaphragm traverse the complete thickness without collision, while a fraction of the electrons collide with the atoms of the material.

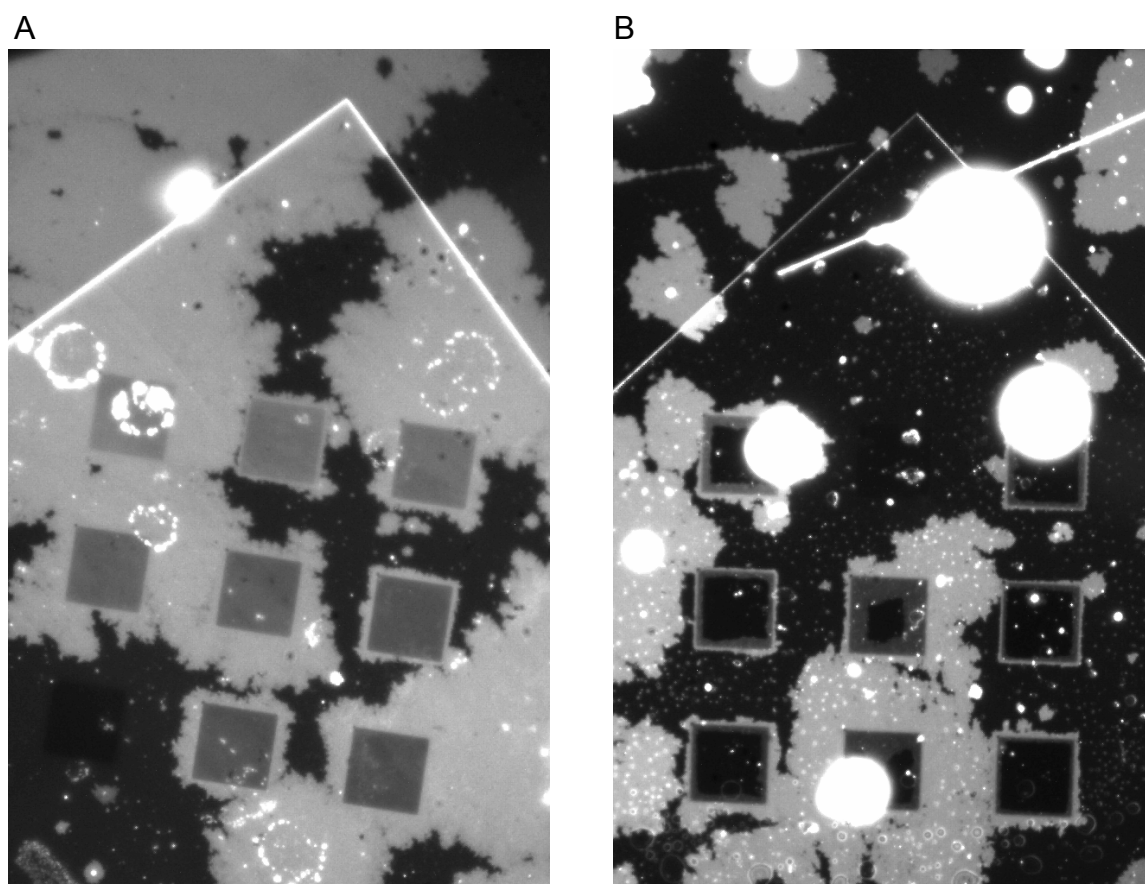


Figure 4-12. Two instances of fluorescently-labeled SLBs formed on the flat side of the Si_3N_4 diaphragm depicted in Figure 4-11A.

The collisions lead to electron backscattering and release of secondary electrons from the electron shells of the atoms. As Si_3N_4 is an insulator, a net negative charge builds up in the diaphragm as more and more electrons are trapped within the material. For the thickness of the membrane is lower than the maximum penetration depth of the electrons, charge accumulates over the entire thickness of the diaphragm. Charge build-up is a likely candidate to cause the interesting effect of attenuated fluorescence, either by inducing a locally decreased dye concentration, or by facilitating non-radiative relaxation, i.e. quenching. The thesis is supported by detection of charge in the irradiated regions by scanning Kelvin probe microscopy (Chapter 4.2). Another effect induced by e-beam irradiation that could contribute to the reduced fluorescence intensity is the accumulation of carbonous material at the exposed surface. Positively charged hydrocarbons ionized by the e-beam may be attracted to the surface that is being imaged and thereby negatively charged. Carbon build-up usually manifests as gradual blackening of the edges, or the complete imaged area, upon prolonged exposure. Very little contamination in the chamber is sufficient to cause this problem. Moreover, if any residual carbon is adsorbed on the surface exposed to the beam, it will be polymerized by the electron beam. The fact that the e-beam-irradiated features in Figure 4-9 and Figure 4-11 show a contrast with respect to the untreated surroundings indeed seems to be a consequence of carbon contamination, albeit on the pit side of the diaphragm. As mentioned above, since the diaphragm is thinner than the electron penetration depth, carbon may pile-up on the back side, too. A charged surface coated by a thin layer of amorphous carbon is likely to induce efficient quenching of excited fluorophores, just as observed in the stained SLB patches that extend over the irradiated regions. AFM of the flat side reveals elevated topography at the irradiated regions, which can be well correlated with accumulation of amorphous carbon (Chapter 4.2).

4.1.7. Imaging of SLBs on Si_3N_4 diaphragms by plain bright-field reflected-light optical microscopy

It has been realized in the course of the study that GUV-derived SLBs on 100-nm-thick Si_3N_4 films can be visualized by simple bright-field reflected-light microscopy. As discussed above, a ~100-nm thick Si_3N_4 film on flat Si is an optical system that generates standing waves with wavelengths in the range of visible light. Apparently, a contrast is generated due to the interference phenomena between regions of the surface covered and not covered by a lipid bilayer. This effect is similar to the one exploited by the reflection interference contrast microscopy (RICM) technique.⁹⁴ Although primary contrast is poor, background subtraction yields images with good resolution (Figure 4-13). Non-adhered vesicles appear above the Si frame as darker round spots, whereas adhered vesicles

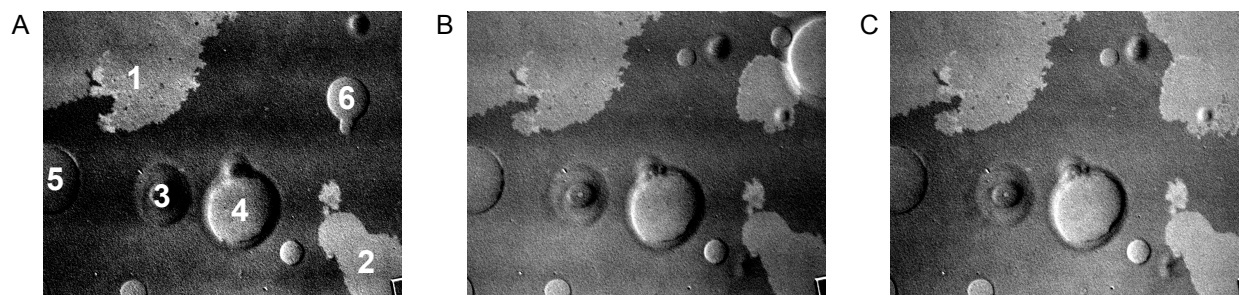


Figure 4-13. A sequence of bright-field microscope images of GUVs on the surface of a 100-nm-thick Si_3N_4 film on Si (scenarios 1 and 2 of Figure 4-14A). The images shown are contrast-enhanced residuals after background subtraction. Figures 1 and 2 in image A denote separate SLB patches brought about by unfolding of GUVs before image A was captured. Spot 3 is a GUV that communicates with but does not adhere to the surface, whereas spots marked by 4 and 5 are GUVs adhered to and stable on the surface during the entire sequence. Spot 6 is another adhered GUV, which, however, has unfolded into an SLB by the time image B was taken. Another GUV can be noticed in B that has descended and adhered right next to patch 6. This GUV, too, has unfolded into an SLB patch by

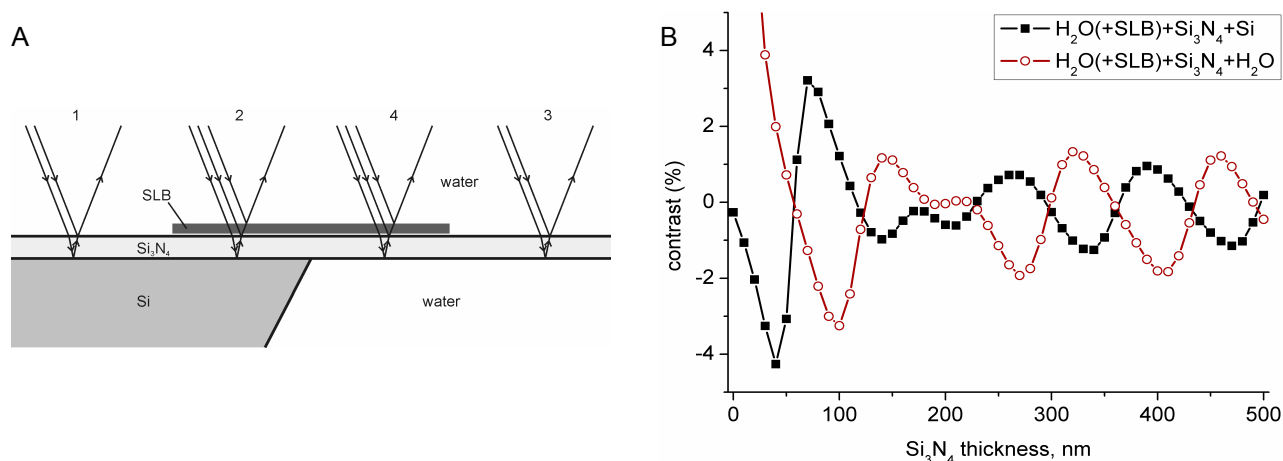


Figure 4-14. A – schematic of the different possibilities of reflective light beam interference at the flat side of a Si_3N_4 window: 1 – Si-supported Si_3N_4 w/o an SLB, 2 – Si-supported Si_3N_4 w/ an SLB, 3 – free-standing Si_3N_4 diaphragm w/ an SLB, 4 – free-standing Si_3N_4 diaphragm w/o an SLB. Both sides of the window are bathed with aqueous electrolyte. B – simulation of Weber contrast ($(I - I_{bg})/I_{bg}$) versus Si_3N_4 thickness between regions coated and not coated with an SLB of the Si-supported (*full black*) and free-standing (*empty red*) Si_3N_4 film.

are brighter than the background and show distinct dark contours. Planar SLB patches are about as bright as adhered GUVs, yet they exhibit no contours.

The two different scenarios of SLB visualization, i.e. above the Si frame and on the free-standing diaphragm, are drawn schematically in Figure 4-14A. Figure 4-14B displays a simulation of contrast intensity of the SLB patch against the background vs. Si_3N_4 thickness for a Si-supported and a free-standing Si_3N_4 film. Radial wave symmetry has been assumed for the calculation. Reflected light intensity per arbitrary angle and unpolarized incident light has been expressed based on Fresnel equations and corrected for multilayer thin film interference. The expression has been integrated over the angular aperture of the particular objective, the intensity spectrum of the illuminating light source, and the sensitivity spectrum of the detector. The contrast is modulated within $\sim \pm 3\%$ of the background intensity over most of the thickness interval. At 100 nm, the

absolute contrast of an SLB on a free-standing and a Si-supported Si_3N_4 film is right at and just next to a local maximum, respectively. The model seems to be qualitatively valid, as SLBs on the Si_3N_4 diaphragm indeed appear darker than the background (e.g. Figure 4-46). Apparently, the TEM windows with 100 nm of Si_3N_4 are very well suited for a simple bright-field microscopic observation of SLB patches.

4.1.8. Conclusion

Electroformation generated high yields of GUVs 1-50 μm large, with a good proportion of vesicles at the higher limit of the range. The GUVs showed a high affinity for clean hydrophilic Si-based surfaces, where they adsorbed, spread, ruptured, and unfolded into planar SLB patches. Unfolding of multiple GUVs next to each other gave rise to mutually interconnected supra-patches with full fluidic continuity. Modulation of fluorescence intensity with respect to thickness of the Si_3N_4 film was observed on fluorescently-dyed SLBs. Of several available diaphragm thicknesses, the ones 100 nm thick gave the best signal intensity and became the diaphragms of choice for the following phases of the project. A surprising lack of fluorescent signal was detected in SLBs from regions of Si_3N_4 diaphragms the reverse sides of which had previously been exposed to the e- and i-beam of the FIB device in the course of pore milling. Extensive irradiation by the e-beam has been found responsible for the phenomenon. The extent to which fluorescence was attenuated scaled inversely with irradiation dose. SLBs showed an increased affinity for the irradiated regions with an interesting preference for the edges, i.e. transitions between the irradiated and the intact fsSi_3N_4 . The effect has been associated with accumulation of ionized carbonous material at the charged surface of the diaphragm. The lack of fluorescence seems to be a consequence of quenching of radiative relaxation of the lipid dye by the carbonous material.

4.2. Ion and electron beam irradiation of Si_3N_4 diaphragms: topographic and electrostatic effects

It has been found upon AFM examination of pore opening shape and size on the flat side of the Si_3N_4 diaphragms that interesting topographical features appear in the region of milling. These topographical features were not observed in regions of the diaphragms that were not exposed to the particle beams. The following chapter reveals the cause and the nature of the effects.

4.2.1. Topographic changes detected by AFM

An SEM image (A) of the pit side of a diaphragm taken immediately after pore milling and a topographical AFM image of the flat side (B) of the same diaphragm are shown in Figure 4-15. The SEM image has been taken at a tilt of 52° to the normal of the diaphragm plane (i.e. the sample was aligned perpendicular to the ion beam). The corner of the diaphragm and the two contiguous pit walls are clearly resolvable. A single milled pore can be noticed at a distance of $\sim 2\ \mu\text{m}$ from either diaphragm edge. The diaphragm has been deliberately etched by the 30 keV/1 pA i-beam at multiple locations along the edges so as to identify the i-beam's association with the interesting topography. These spots appear darker than the surroundings due to the partial etch of the assisting gold layer upon i-beam irradiation. An additional rectangular spot just below the pore has been exposed to the ion beam, too (marked by an arrow). The corner of the diaphragm has also been exposed to the 5 keV/98 pA e-beam at higher magnifications rather excessively during sample alignment. An obvious elevation at the very corner can be noticed in the AFM scan of the flat side

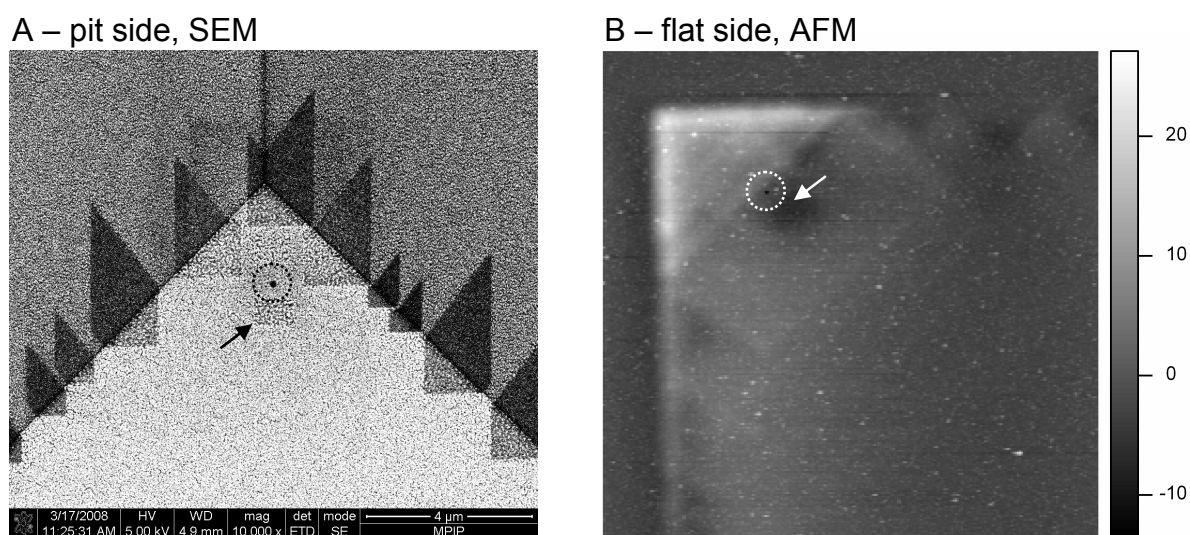
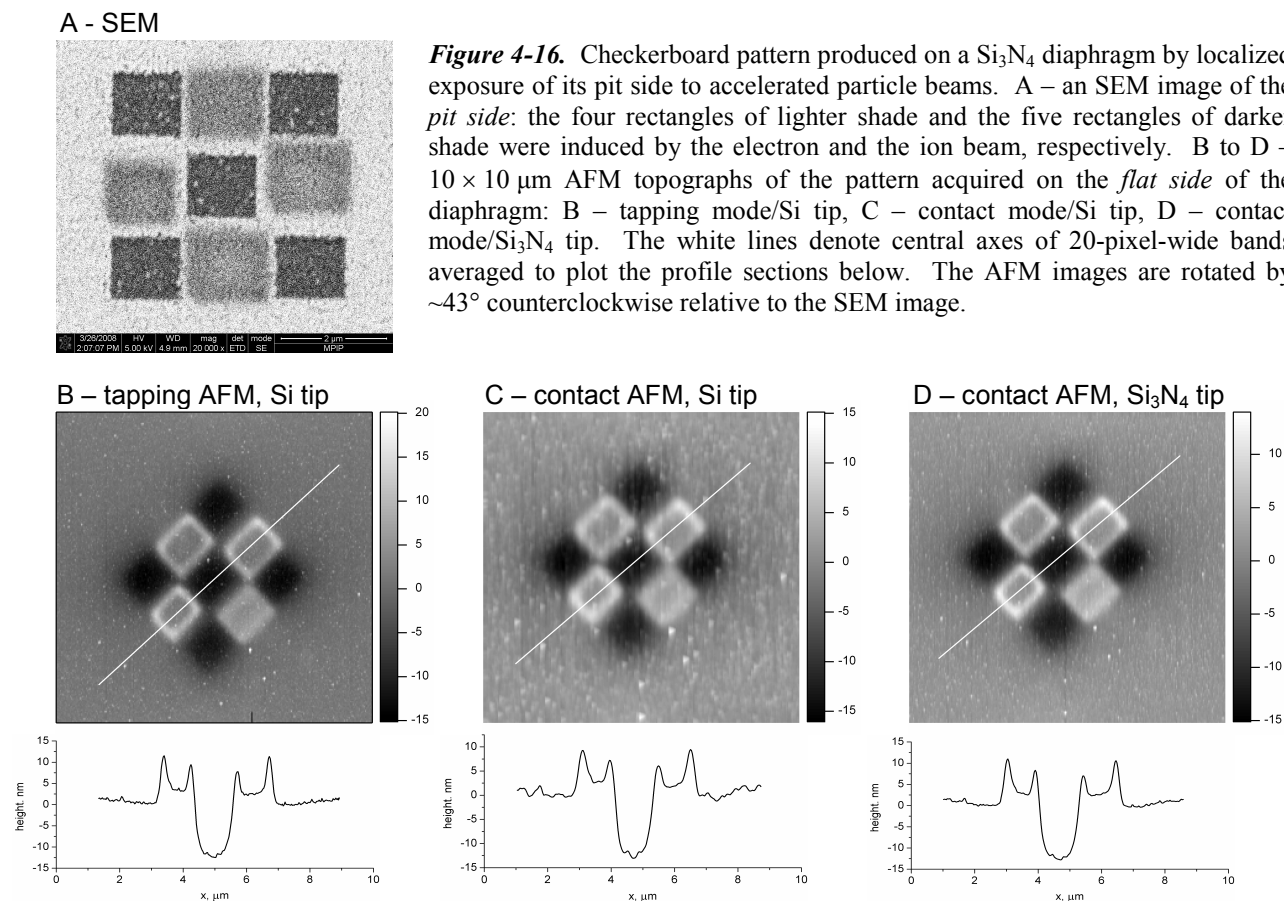


Figure 4-15. An SEM image of the pit side (A) and an AFM height image of the flat side (B) of the same corner of a Si_3N_4 diaphragm. As the two images correspond to opposite sides of the diaphragm, image B has been flipped to ease the comparison. B is rotated by $\sim 45^\circ$ CCW relative to A. A single pore has been milled through the diaphragm $\sim 2\ \mu\text{m}$ from either edge (*dashed circle*). Sections of the diaphragm have been exposed to the ion and electron beam extensively. The *arrow* marks a particular rectangle irradiated by the ion beam and discussed in the text.

of the diaphragm. The elevated region corresponds to the area that was irradiated with the highest doses of electrons. On the contrary, the spots treated with the ion beam appear as depressions with respect to the diaphragm bulk (triangles of darker shade along the edge of the diaphragm). The rectangle south-east of the pore (the same as the one in image A, marked with an arrow again) shows a particularly pronounced depth.

4.2.2. Topographic changes – is it the e-beam, the i-beam, or both?

The shape and size of the topographical elevations on the flat side of the diaphragm seemed to correlate with regions where attenuated SLB fluorescence was observed (Chapter 4.1.6). It was suspected that a relationship exists between the initial failures to form robust npsLBs and the lack of fluorescence from the pore-bearing locations. Therefore, motivation emerged to gain a better understanding of the topographical changes generated on the flat side of the Si_3N_4 diaphragms. The primary effort was targeted at determining whether the observed diaphragm elevations and depressions induced by the beams were real topographical features or artifacts (e.g. due to electrostatics). A small 3×3 checkerboard pattern with spots exposed to either one or the other beam was thus produced on a diaphragm and examined in different modes of scanning probe microscopy.



An SEM image (A) as well as three independent topographical AFM scans (B-D) of the pattern are shown in Figure 4-16. The five dark squares positioned diagonally were treated with the i-beam at equal doses of $8.7\text{pC}/\mu\text{m}^2$. The lighter four rectangles were irradiated by the e-beam, whereby the rectangle on the left was given a dose of $6.2\text{nC}/\mu\text{m}^2$ and the remaining three rectangles were given doses of $4.8\text{nC}/\mu\text{m}^2$. The topographical AFM scans were taken in different operating modes and with different tips: B – tapping mode/Si tip; C – contact mode/Si tip; D – contact mode/ Si_3N_4 tip. All of the resulting images as well as the line profiles are essentially the same. Given the different modes and tip materials the three scans were acquired with, the evident similarity between the images suggests that the observed elevations and depressions are indeed genuine topography. The e-beam-irradiated features are elevated with respect to the plane of the unexposed surface. Rather than being homogeneous over the complete feature area, the elevations are most pronounced at the rims, reaching up to 10 nm. On the contrary, the central regions of the irradiated features exhibit heights of only $\sim 2\text{-}3$ nm above the plane of the unexposed surface.

4.2.3. Can charge be associated with the topography?

An additional experiment was designed to establish whether excess accumulated charge can be detected at the flat side of the diaphragm in addition to the topographical features. Kelvin scanning probe microscopy (KSPM), a surface microscopy technique capable of measuring the DC potential offset between a probe tip and a surface, was used.⁵⁹ 3×3 arrays of $2\text{-}\mu\text{m}$ -wide squares were irradiated by either the electron or the ion beam at linearly-increasing doses on the pit sides of the diaphragms (see Figure 4-11B for an SEM image of the e-beam-irradiated array). The arrays were examined at the flat side by SPM using a Pt-coated Si tip in a combined height-electrical potential mode.

Topographical features analogous to those described above were observed: the i-beam induced depressions, whereas the e-beam generated elevations relative to the surface of the intact diaphragm (Figure 4-17, images A and C, respectively). In addition to the increase of depth, the square-shaped depressions brought on by the i-beam show lateral broadening with respect to exposure time. Moreover, the unexposed regions between the squares, as well as along the outer boundary of the array, are also lower than the bulk diaphragm surface. Overall, the impact of the i-beam on the flat side of the diaphragm seems to have had a rather diffuse character. The elevations induced by the e-beam are, on the other hand, very well defined and no impact of the beam on the areas around the exposed regions can be observed. Again, the rims and the corners, in particular, of the exposed features are pronounced relative to the central parts. Proportionality appears to exist between irradiation dose and elevation height.

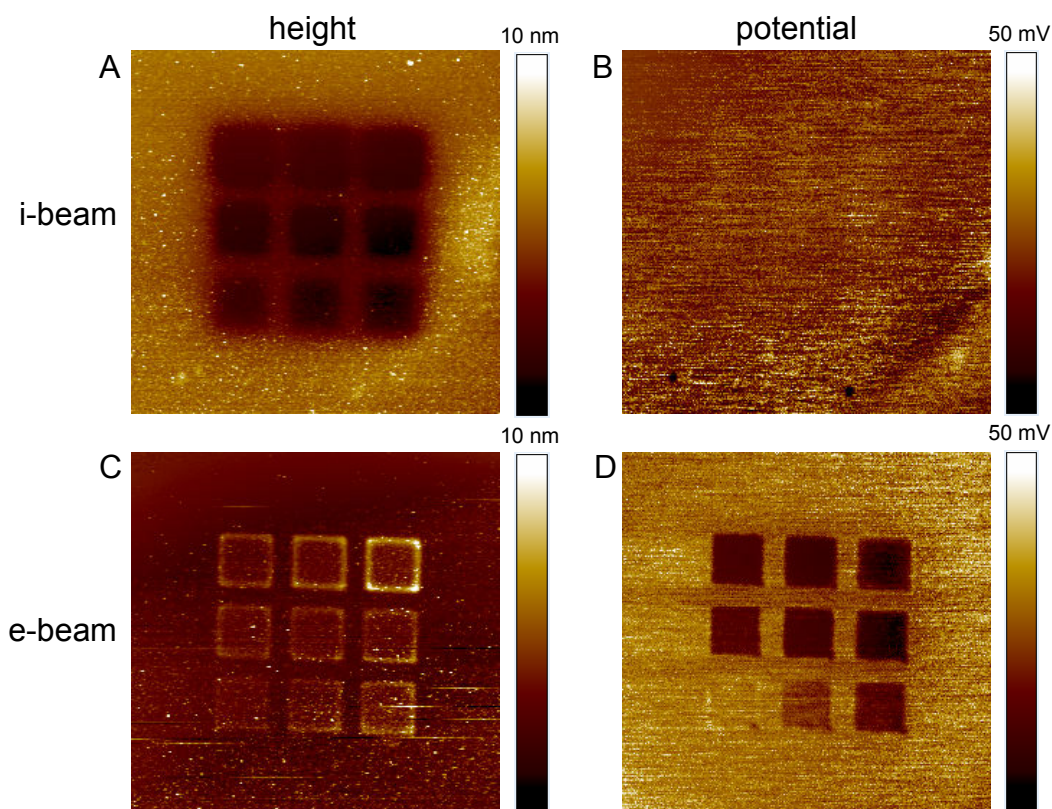


Figure 4-17. Kelvin SPM images of 3×3 arrays of $2\text{-}\mu\text{m}$ -wide squares on an Si_3N_4 diaphragm irradiated by an electron (A, B) and an ion (C, D) beam. The images were acquired at the side of the diaphragm retrograde to the side of beam incidence. (A, C) – topography, (B, D) – electrostatic potential.

Similar to the topographical scans, the electrostatic potential images reveal a remarkable difference between the two types of arrays: equal electrostatic potential has been detected at the i-beam-irradiated features and the rest of the diaphragm, whereas the squares treated by the e-beam have been found to exhibit electrostatic potentials evidently different from those at the diaphragm bulk (Figure 4-17B and D, respectively). The surface potential of the e-beam squares seems to be proportional to irradiation dose at short exposure times and saturate at prolonged irradiation. The potential of the irradiated features is negative relative to that of the bulk diaphragm.

4.2.4. Basis of i-beam effects

The topographic depressions induced by the i-beam are puzzling. Forward sputtering (ejection of atoms from the back side of the diaphragm in the direction of the incident ion vector) might offer a feasible interpretation of the effect. The diffuse character of the impact of the i-beam (Figure 4-17A) would also comply with the forward-sputtering hypothesis, as multiple recoil incidents along the path of an accelerated ion through the diaphragm are expected to deflect the ion off its original vector of incidence. The occurrence of forward sputtering may be expected at material thicknesses comparable to the projection range of the incident ions in the material. It follows from numerical simulations as well as experimental results, however, that 30 keV Ga^+ ions penetrate

through Si_3N_4 up to ~ 35 nm only.⁷⁴ This value makes it unlikely that forward sputtering was induced by the i-beam on the other side of a 100-nm thick Si_3N_4 membrane. Besides, the width of the depressed region along the boundary of the array in Figure 4-17A is much wider than the expected lateral radius of 30 keV Ga^+ in Si_3N_4 . Finally, no charge accumulation has been detected on the flat side of the i-beam squares by KSPM (Figure 4-17B). Irradiation of a dielectric material by an ion beam is known to result in a build-up of positive charge at the surface.⁴⁹ Two processes can be identified that contribute to this effect. First, it is the entrapment of the impinging positively charged ions in the material. Second, negative charges are depleted off the material via emission of SEs. In a dielectric, such charging should be restricted to the volume the incident ions can reach. Again, the key question is whether a fraction of the 30 keV Ga^+ can penetrate the full thickness of the diaphragm. No potential difference relative to the diaphragm bulk has been found at the flat side of the i-beam-irradiated features for the given interval of exposure doses. If the incident ions really do not penetrate beyond ~ 35 nm, this implies that the electric field due to accumulation of excess positive charge at the beam impact side of the diaphragm is of negligible intensity at its flat side. If some of the incident ions do penetrate the full thickness of the diaphragm, as could be deduced from the topographical depressions of the features exposed to the i-beam, some accumulation of positive charge should be expected at the back surface of the diaphragm, too. The lack thereof could perhaps be accounted for if ionization of residual carbonous gas behind the diaphragm and neutralization of the surface charge by electrostatic accumulation of the ionized species is considered (see below). Further speculations regarding the grounds of the depressions may relate to alterations of topography without material loss, such as localized shrinking or bending, or radial diffusion of the material, yet none appears to have the potential to yield a reasonable explanation of the phenomenon.

4.2.5. Basis of e-beam effects

The most likely cause of the positive topographic change on the flat side of the diaphragm due to irradiation of the pit side by the e-beam is accumulation of carbonous contamination. Even high-vacuum specimen chambers of e- and i-beam devices are known to contain residual carbonous gases.^{54,95} Such gases can come from the instrument (e.g. rotary pump oils) as well as the specimen (directly or indirectly, e.g. via adhesive tapes or paints used to mount the specimen in the chamber). The diaphragm is about 3-4 times thinner than the mean penetration depth of the incident electrons in Si_3N_4 .⁹³ Therefore, accumulation of charge across the full thickness of the diaphragm is expected. Organic residues dispersed in the vicinity of the sample are ionized by the primary electrons that penetrate through the diaphragm as well as secondary electrons (SEs) induced in the

diaphragm by the primary electrons. Under such conditions, the ionized species are likely to build up at the charged surface of the diaphragm due to electrostatic attraction, giving rise to topographical elevations. The peculiar profile of the elevations, i.e. pronounced edges (Figure 4-16) and, even more particularly, corners (Figure 4-16), correlates with the premise. The penetrating e-beam becomes considerably diffracted by inelastic interactions of the electrons with the diaphragm.⁵³ Therefore, a section parallel to the diaphragm plane some distance beyond the back side of the diaphragm across the space accessible to the beam yields an area larger than the original irradiated area. Moreover, collisions of electrons with the carbonous gas induce still further diffraction of the beam. Obviously, then, the space behind the diaphragm where the density of ionized carbonous molecules is near to homogeneous should exhibit a dome-like shape centered over the irradiated region. If a homogeneous surface density of charge over the back side of the irradiated region is assumed, the electric field in the space behind the diaphragm shows a shape similar to that of the density of ionized carbon. Lateral availability of the ionized molecules in conjunction with the shape of the electric field result in accumulation of carbonous material that is more extensive at the periphery relative to the inner parts of the irradiated regions.

KSPM revealed a significant impact of e-beam irradiation on the electrostatic potential at the flat side of the Si_3N_4 diaphragm (Figure 4-17D). Charging phenomena in non-conducting materials due to build-up of charge at the surface of a target upon e-beam irradiation are well known.⁵³ A single accelerated electron impinging on a target is known to generate ~ 0.5 -2 secondary electrons (SEs) that escape the target. The so-called SE yield depends on the character of the material and the energy of the primary electrons. SE yields for a 5 keV beam are < 1 for most materials. If the total flux of electrons (penetrating, backscattered, secondary) out of the diaphragm is lower than the flux of electrons into the diaphragm (probe current), the net charging will have a negative character, as is the case here. It is known that negatively charged regions of a surface imaged in the SE-mode of an SEM appear brighter in the SE image than the surroundings.⁹⁶ SEM imaging of the flat side (i.e. the side not coated with gold) of pore arrays was attempted at the initial stages of this work. Apart from pore shrinking (Chapter 4.3.2), an obvious increase of brightness of the areas scanned by the e-beam at high magnifications relative to the rest of the diaphragm was detected upon SE imaging (results not shown). Based on the presented observations and arguments it can be concluded that irradiation of a Si_3N_4 diaphragm by 5 keV electrons induces an accumulation of negative charge in the exposed spot. The penetrating e-beam further ionizes carbonous molecules dispersed in the space behind the diaphragm. Positively-ionized carbon-based material piles up at the negatively-charged regions of the flat side of the diaphragm due to electrostatic attraction. The carbonous

layer thus formed is topographically elevated with respect to the surrounding diaphragm, while its net charge is not sufficient to screen the negative charge of the diaphragm.

4.2.6. Conclusion

Irradiation of the pit side of Si_3N_4 diaphragms with the e-beam and the i-beam induced in both cases topographical changes on the flat side. The e-beam gave rise to elevations with pronounced edges and corners, and with accumulated negative charge. Both effects were dependent on irradiation dose. The phenomena seem to be related to the same grounds as the attenuation of SLB fluorescence described in the previous chapter – diaphragm charging and build-up of ionized carbonous material. Irradiation with the i-beam, on the contrary, generated fairly regular depressions without accumulated charge respective to the surrounding intact fs Si_3N_4 . Forward sputtering would provide a feasible explanation, were it not inconsistent with the much shorter penetration depth of 30 keV Ga^+ in Si_3N_4 . These findings resulted in optimization of the pore milling protocol so that unnecessary diaphragm exposure to either of the beams was minimized.

4.3. Pores in Si₃N₄ diaphragms

A crucial step on the way towards the ultimate goal of the thesis was to fabricate substrates with well-defined through pores. Control over parameters such as pore size, length, shape, location, topography, and pore-to-pore distance in the case of arrays, was required. The pores were milled through Si₃N₄ diaphragms by a focused ion beam and characterized by scanning electron and atomic force microscopes. This chapter begins with an assessment of the two microscopy methods in terms of accuracy and interference with the pores being examined. The effects of several FIB patterning parameters on pore character are discussed further on. Examples of pore arrays that the npsLBs were actually spun over are presented next. Finally, results of electrolyte conductance through unblocked pores are described.

4.3.1. Pore characterization

Figure 4-18 displays an example of images acquired by the SEM (A) and the AFM (B) of an array of seven pores in a 100-nm-thick Si₃N₄ diaphragm. Section C of the figure is a profile scan along the white line depicted in B.

All pores in the SEM image (front/pit side of the diaphragm) are clearly resolved as circles of low signal intensity (no secondary electrons induced) against the gray continuous Si₃N₄ membrane (some secondary electrons induced). The white islets scattered over the surface are regions of the diaphragm covered with gold (high secondary electron yield). Gold films are known to coagulate during the growth on silicon-derived substrates.⁹⁷ At an average layer thickness of ~10 nm, the islets are interconnected in a partly-closed layer, as visible at the periphery of the image. In the vicinity of the pores, however, the white patches are scarce, small and isolated. Apparently, a considerable portion of the Au layer has been etched off this region during the pore milling process. For the specific array, particle analysis after image processing yields for the pore openings an average diameter of 183.7 ± 2.2 nm (200 nm nominal) and the nearest center-to-center distance of 497.5 ± 2.2 nm (500 nm nominal).

In the AFM height image (back/flat side of the diaphragm), the pores appear as regular depressions against the flat continuous Si₃N₄ membrane. Apart from a few round elevated spots, the Si₃N₄ membrane itself is considerably smooth. Average roughness, R_a , of ~0.8 nm has been determined for analogous Si₃N₄ surfaces free of pores (images not shown). Similar to the SEM image, the pores captured by the AFM have a well-defined circular shape.

Three sorts of features that deserve further discussion are apparent in the section profile plot (C). First, the section generates a quasi-conical pore profile with the lateral surface sloping inversely to

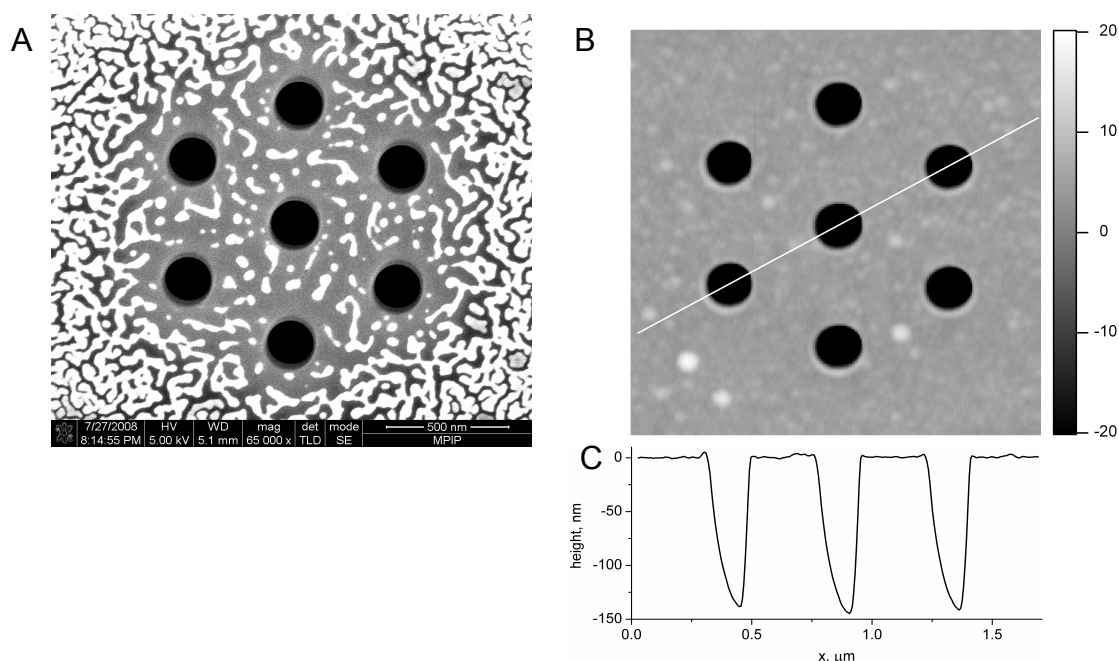


Figure 4-18. Secondary electron SEM (A) and height AFM (B) images of an array of seven pores in a 100-nm-thick Si_3N_4 diaphragm. A – 65k \times magnification; B – scan size 1.7 μm , height color scale in nm. C - section profile plot along the white line depicted in B.

what is expected given the fabrication procedure. Second, a finite maximum pore depth of ~ 150 nm is obtained for the pores that are ‘through’ in reality. Third, an asymmetry is yielded in the cone shape with the slopes on the right being steeper than the slopes on the left. All of these features are artifacts that can be attributed to the limitations of the AFM. The former two observations arise from the conical geometry of an AFM tip. Given a specific slanting angle of the lateral tip plane, a critical angle from the vertical direction exists below which the slope of a feature cannot be resolved. Similarly, a depression of an aspect ratio higher than that of the tip will prevent the tip from reaching the bottom, and a lower than actual depth will be rendered. Thus an AFM image acquired via a conical probe of a cylindrical or a negatively conical through nanopore will inevitably be a projection of the tip geometry, i.e. a cone. Two possible reasons exist for the third artifact - the apparent slope asymmetry of the cone. First, the tip cone axis can simply be tilted away from the Si_3N_4 membrane surface normal. Second, the asymmetry can be given by the difference in response of an AFM tip in the tapping mode to positive and negative slopes. The accommodation of the vertical position of the stage piezo to a smaller tip oscillation amplitude (a positive slope) is slower than that to a bigger tip oscillation amplitude (a negative slope). In effect, the probe descends into the pore more slowly than it ascends back up. This is a scan-direction dependent phenomenon, i.e. the slope asymmetry is reversed upon a scan in the opposite direction.

4.3.2. SEM

A set of valuable information with respect to pore character can be obtained conveniently from a good SEM image. The convenience dwells in the fact that with a dual ion/electron beam device the SEM image can be taken immediately after pore fabrication. A tilt of the stage is all that is required - no hassle of sample transfer to a specialized SEM device, mounting on the stage, and lengthy vacuum pumping exists. Even more importantly, both beams of a dual-beam device are always aligned at the spot where fabrication takes place. Thus, the location of the features needs not to be sought for. An attempt to localize a small array of pores of ~50 nm in diameter on a surface coated with a heterogeneous layer of Au such as the one in Figure 4-18A without any guiding features may oftentimes prove very challenging. On the contrary, a ‘zoomed-out’ and scaled SEM image centered at the pore location and including an additional reliable feature (usually the nearest diaphragm corner) in the scope of the frame can be extremely helpful in finding the location under an optical or a scanning probe microscope.

Unfortunately, prolonged rastering of a focused electron beam over a pore-bearing location has been found to induce shrinking of the pores. The effect was particularly pronounced at high magnifications, such as required for close-up images of individual pores (Figure 4-19A and B). We briefly examined the influence of particle speed and found that the rate of pore shrinking scales inversely with the energy of the accelerated electrons (Figure 4-19E). Two theories have been presented in the literature to account for the phenomenon: one attributes the closing to e-beam-

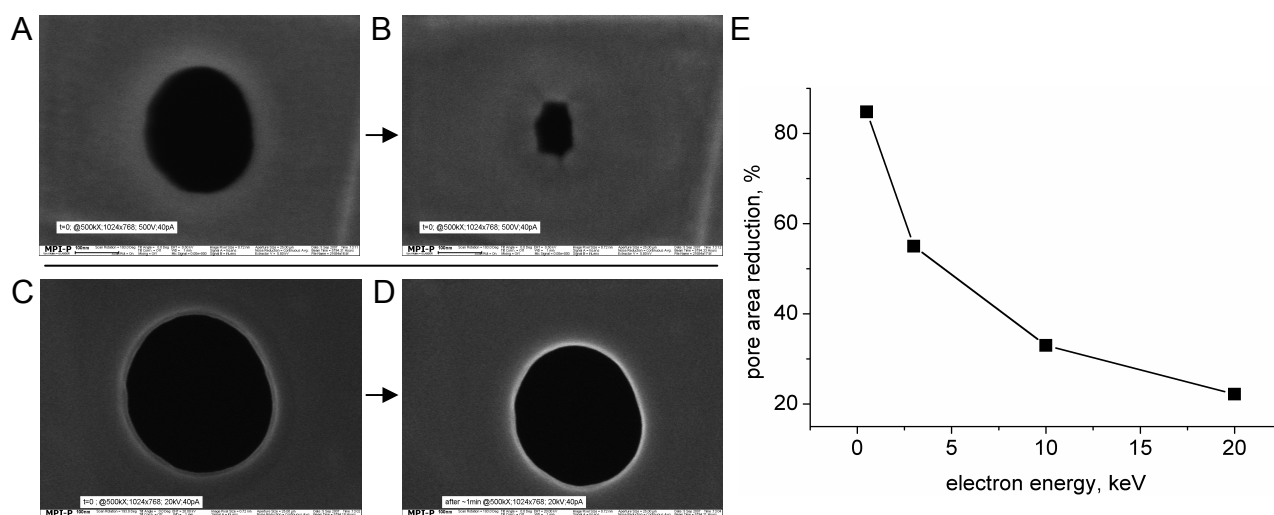


Figure 4-19. Shrinkage of pores in an Si₃N₄ diaphragm upon irradiation by the e-beam. SEM images of a single pore were acquired before (A, C) and after (B, D) the exposure to the scanning 40 pA E-beam for 1 minute at 500000× magnification. The difference in shrinking rate induced by 0.5 keV (A, B) versus 20 keV (C, D) electrons is illustrated. E – a plot of pore area reduction relative to incident electron energy. The data was derived from pairs of images captured under the same conditions as A-D.

induced diffusion of matter at the surface,⁹⁸ whereas the other associates the effect with build-up of carbonous contamination.⁹⁹

Although potentially useful for post-milling reduction of pore diameter to very small values, the pore-shrinking effect was disturbing with respect to our attempts to correlate the FIB patterning parameters with the resulting pore specifications. Along with the electrostatic and topographical effects of SEM irradiation on the diaphragm (Chapter 4.2) and the altered SLB behavior on e-beam-irradiated regions (Chapter 4.1.6), the method had a significant impairing overall impact on the porous Si₃N₄ diaphragms. The alterations of PC affinity for the diaphragm due to e-beam irradiation might be utilized later to enhance npsLB properties. At this stage of the work, however, e-beam treatment of the diaphragms was expanding the number of variables intolerably. Measures were thus adopted to minimize the irradiation dose at the pore-bearing location to limit the undesired disturbances due to the e-beam. First, coarse focusing and alignment of the beam has never been performed at the milling site directly, neither before nor after milling. Second, image quality has been compromised to shorten the duration of exposure. Third, acquisition of high-magnification images of single pores was avoided.

4.3.3. AFM

Unlike with the SEM, it takes a long time to acquire an AFM image (~5-20 minutes at a resolution of 256-512 px and scan frequency of 0.5-1 Hz). Lateral drift of the sample with respect to the scanner was often observed during the capture period. The consequence was a distortion of the image with skewed pore shapes and altered inter-pore distances. Besides, as the pit side of the diaphragm is located deep in the pyramidal pit, only the flat side was available for AFM imaging. On the other hand, although prone to imaging artifacts, slow, and less accurate than the SEM, tapping-mode AFM was considered completely undisruptive to the samples. The diaphragms could thus be examined repeatedly without any adverse effects on pore size or diaphragm surface character. Moreover, the topography of the surroundings of the pore mouth at the flat side of the diaphragm, potentially a determinant factor behind successful or failing attempts of npsLB formation, was revealed via the AFM. All in all, the complementary information provided by the SEM and the AFM about the respective sides of the diaphragm fused conveniently to yield a solid picture of pore and diaphragm character.

4.3.4. Effect of patterning parameters on pore character

The FIB, being a complex and versatile device, offered a plethora of variable parameters that could affect the result of the process of pore milling. The primary questions associated with the parameters of the milling process were as follows:

1. How does the interplay between irradiation dose and nominal pore diameter project onto the resulting pore size and shape?
2. Does scan speed and scan direction play a role?
3. Is any topography, apart from the pore opening, induced at the back side of the diaphragm by the milling process?
4. What is the minimum attainable pore diameter?

The outcome of investigations meant to gain an understanding of the relationship between FIB patterning parameters and the character of the milled pores is compiled in Figure 4-20 and Figure 4-21.

Figure 4-20 displays the results of an experiment targeted at the effect of pore nominal diameter (ND) and apparent milling depth (AMD) on pore properties. The test array comprised a rectangular matrix of pores, whereby AMD and ND were varied in the X and Y dimension, respectively. AMDs from 80 to 150 nm and NDs of 50, 100, and 200 nm were tested. Topographical AFM images of some of the individual pores are displayed in sections A-C of the figure. Rows of nominally 100-nm-wide pores with altered patterning direction and magnification were milled in the scope of the same array, too (images not shown). In addition to pore openings, elevated annular features have been detected around each pore. Pore diameters, elevation diameters, and elevation heights were extracted of the AFM topography images using the routine described in Chapter 3.2.2.3. The resulting values have been plotted with respect to AMD in sections D and E of the figure.

Figure 4-21 shows AFM images at lower magnification of additional test arrays and pore specifications derived from these. The arrays were all milled through the same diaphragm, albeit in two separate sessions (Section 1 and 2 of the figure). For all arrays of Section 1, AMD was raised from 70 to 140 nm in 10-nm increments (left to right, top to bottom) and ND was set to either 100 (A and B) or 200 nm (C). Arrays A and B differ by pore-to-pore distance. In Section 2 of Figure 4-21, AMD was varied between 100 and 260 nm for NDs of 50 and 100 nm. Additionally, possible effects of altered magnification and dwell time were probed here.

4.3.4.1. Annular and hill-like elevations

Obvious annular elevations with respect to the bulk diaphragm surface have often formed around the pore openings (all pores of Figure 4-20 and pores of Section 1 of Figure 4-21). Similarly, hill-like elevations could frequently be found at the expected locations of pores milled to an apparent depth below the break-through threshold (Figure 4-20A, pore 100; Figure 4-21A, B, and C). The

size and the height of the elevations scale logarithmically or convergently with the AMD. In Figure 4-21, the elevations of array A seem to be more pronounced in comparison to those of array B. As inter-pore distance was the only objective difference between the milling settings for the two arrays, this particular parameter seems to be involved in determining the size of the elevations. Furthermore, a relationship between elevation character and previous/subsequent milling in the nearby area has been identified, and is discussed below. Most importantly, however, the presence or absence of the elevations followed an all-or-none principle. If the elevations formed, then they did so for every pore of an array at all AMDs above the break-through threshold and up to 50 nm below the threshold (Figure 4-20 and Sec. 1 of Figure 4-21). In analogy, if the elevations did not form, then they did not form around any pore of an array nor at locations where pores were milled to below threshold AMDs (Section 2 of Figure 4-21). Despite considerable efforts, we were unable to reveal the nature of the phenomenon decisively. Intriguingly, the effect has been found not to follow any of the patterning parameters that could be objectively controlled, but rather to be tightly session-dependent. In other words, milling of analogous pores through the same diaphragm at two separate sessions could give rise to the elevated features in one case, but not in the other case (e.g. Sec. 1 vs. Sec. 2 of Figure 4-21). Subjective parameters, such as 1) quality of focus and alignment of the beam, 2) substrate contamination, 3) modification of the diaphragm via reckless exposure to the e-/i-beam upon focusing and alignment, or 4) vacuum quality in terms of pressure and carbonous contamination have to be considered.

Beam focus and alignment. Beam focusing and alignment has always been done to the best possible degree. Emergence of the elevations would thus have to be sensitive to very subtle differences in focus quality. Pores milled with a beam that had been partly defocused did not differ from pores milled with a perfectly (as far as the subjective judgment allowed) focused beam, however. Unfortunately, at the particular test pronounced elevations appeared around the pores milled with the focused beam, too. A result whereby elevations did not form at both no and a partial defocus would have been more valuable.

Substrate contamination. The process of manufacture of Si_3N_4 TEM windows is presumed not to leave behind any carbonous contaminants on the diaphragm surface. Apart from physical vapor deposition of the thin gold layer on the pit side, the Si_3N_4 diaphragms were not subject to contact with anything but the ambient atmosphere before milling. Besides, the fact that elevations were able to appear or not to appear on the same diaphragm at separate milling sessions implies the contamination would have to be rather local, which is hard to account for.

Diaphragm modification by beam irradiation. The locations of milling might have been irradiated by the ion and electron beams rather excessively at the initial stages of the work. After the effects on diaphragm topography and SLB spreading behavior had been recognized, however, exposure of the locations of milling to the beams was minimized. Despite, pore-related elevations continued to form or not to form ‘randomly’.

Vacuum quality. Vacuum quality was not recognized as a potential cause of the phenomenon until a significant failure in the vacuum system of the FIB device occurred, which effectively obstructed any attempts to mill pores under the usual settings. Chamber pressure was reduced to below the critical value at any milling session, nevertheless the actual pressure values that might have varied from session to session were not noted. Volatile carbonous residues are known to be often present in the atmosphere of analogous vacuum chambers. It may be that at specific sessions the chamber pressures did not fall far below the minimum required pressure and the vacuum atmosphere was contaminated. Further indices that volatile carbonous material might be responsible for the formation of elevated features above and around the pores are presented below.

4.3.4.2. Determinant factors

A. Nominal pore diameter

As expected, ND is the most determinant factor of the resulting pore size. At NDs at and above 120 nm, the actual diameter of the pore mouth at the back side of the diaphragm is fairly consistent with the nominal value (Figure 4-20D). The nominally 50- and 100-nm pores are slightly elliptical (lowest minor to major axis ratio of ~0.8, pores not shown), the 200-nm pores are almost perfectly circular. This could have been due to a slight drift of the sample with respect to the patterning coordinates. More pronounced pore ellipticity and diameters considerably exceeding the preset NDs have been observed for high AMDs (e.g. Figure 4-21, Sec. 2). This could possibly be related to the absence of elevations and significant lateral drift at that particular milling session.

B. Apparent milling depth

Quite intuitively, a threshold value must exist for the apparent milling depth at which the back side of the diaphragm is reached and a through pore is produced. The break-through depth turned out to scale inversely with the nominal pore diameter. For the arrays of Figure 4-20, the break-through occurred at an AMD of 110 nm for ND of 50 nm, whereas for NDs of 100 and 200 nm the threshold value was below the lowest AMD tested, i.e. lower than 70 nm. For a 100-nm-thick diaphragm, the observed threshold depths at higher NDs are surprisingly low. Milling depth is one of the input parameters of the patterning function. Alongside other parameters and via several constants, the milling depth effectively translates into the size of a single pixel and the number of times each pixel

is passed over by the beam. The constants used in the conversion are presumed to be appropriate for the particular device and material and thus considered correct. What other factors could bring about the low break-through AMDs? Although discrepancies between the nominal and the actual diaphragm thickness may exist, they would hardly exceed the range of $\sim 5\%$ and therefore cannot account for a difference of ~ 30 nm. It seems more likely that the real beam current, which there was no fine control over, exceeded the nominal value of 1 pA. The break-through thresholds for the arrays of Figure 4-21 are higher: 130 and (ambiguous) 140 nm for the 100-nm-ND arrays B and A, respectively, and 90 nm for the 200-nm-ND array C. This could be a consequence of lower beam intensity due to beam current fluctuations and/or a thicker atmosphere of the chamber (formation of elevations implies presence of volatile contaminants, i.e. low vacuum quality). Interestingly, break-through thresholds for the arrays in Sec. 2 of Figure 4-21 are higher than for those in Figure 4-20, too: above 120 nm at NDs of 50 nm and ~ 100 nm at NDs of 100 nm. As the absence of elevations suggests good vacuum had been attained during the particular milling session, a beam of augmented intensity seems to be the only plausible explanation here.

Let us next look at the way the pore mouth behaved at AMDs just below, at, and far above the break-through depth. At AMDs just below the threshold, an elevated dome-like feature has formed (AMD 100 nm of line 50). At AMDs above the threshold, pore and annulus diameters seem to grow in a logarithmic manner, i.e. at a faster rate just above the threshold (AMD range of ~ 80 -100 nm for NDs of 100 and 200 nm and ~ 110 -120 nm for the ND of 50 nm) and at a slower rate at larger AMDs. This is consistent with the notion that milling proceeds slower at the edges due to redeposition of sputtered material at the walls of the feature being milled.^{49,52}

4.3.4.3. Non-determinant factors

A. Magnification

The size of the pattern to be milled by the FEI Nova 600 was constrained by the magnification: the smaller the magnification, the larger the area accessible to the beam, and thus the larger the maximum pattern dimensions. The pores of an array could either be milled all at once at lower magnifications as a pre-designed array of multiple circles (e.g. $\sim 20k\times$ for a 7-circle hexagonal array of a pitch of 2 μm), or one by one at higher magnifications (e.g. $1M\times$ for a 100-nm-wide circle) via milling a single-circle pattern successively at multiple locations defined by stage movements. The red traces of Figure 4-20D&E represent the characteristics of pores analogous to those of B, but milled at a magnification of $20k\times$ rather than $1M\times$. The FEI Nova 600 operator's manual recommends to mill patterns at a magnification such that ~ 35 -50% of the frame area is occupied by the pattern features. Patterning a single 100-nm circle at $1M\times$ complies with the advice. On the

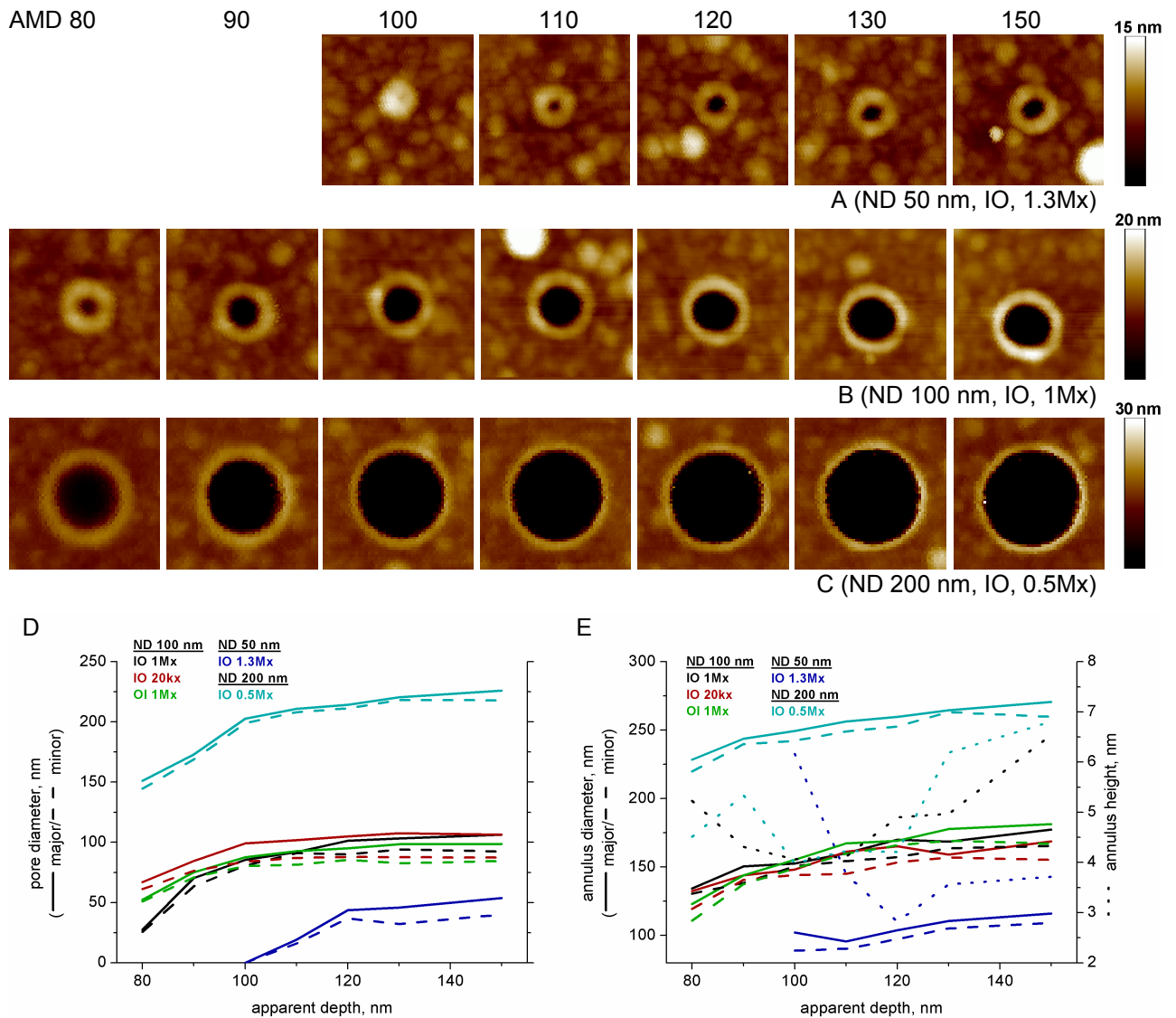
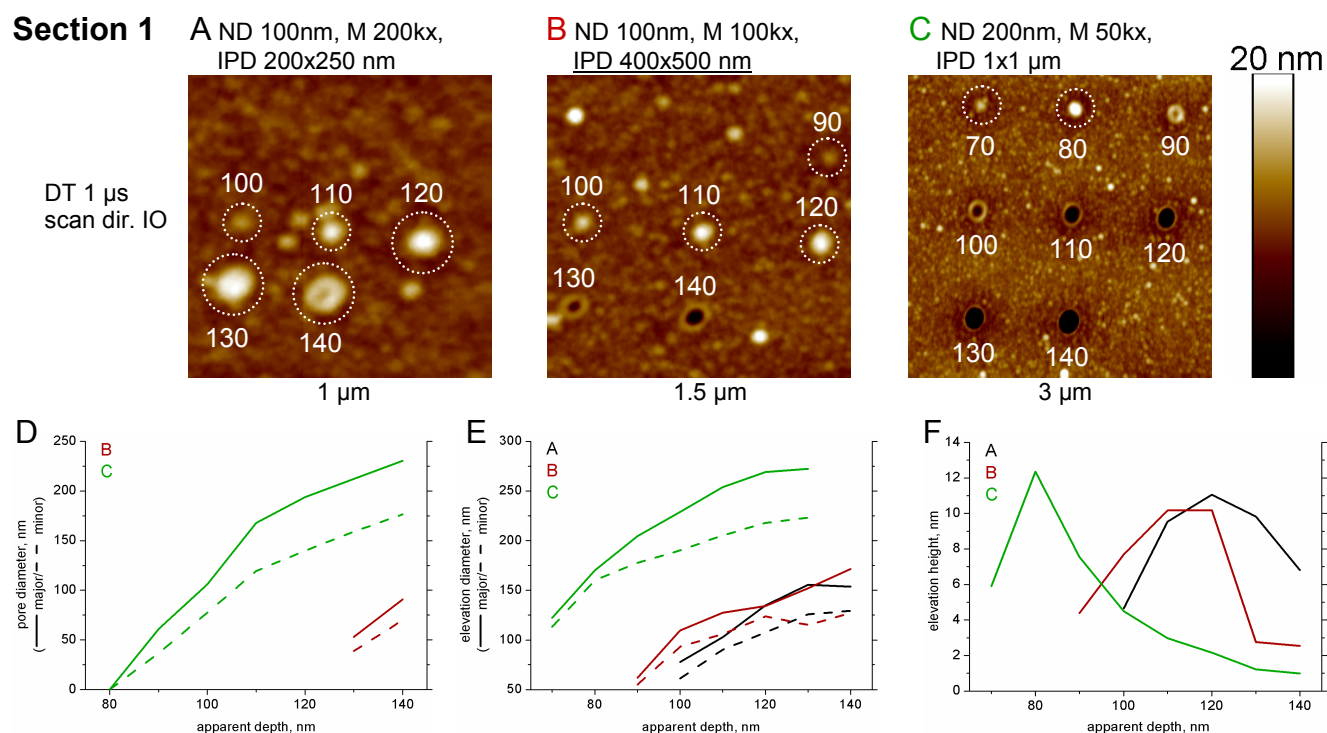


Figure 4-20. AFM analysis of individual pores of an array milled by the FIB with varied nominal diameter (ND), apparent milling depth (AMD), magnification, and scan direction (inner-to-outer, IO, vs. outer-to-inner, OI). The images are aligned left to right according to the AMD and top to bottom according to the ND (A – 50 nm, B – 100 nm, C – 200 nm). AFM scan size was 350 nm. FIB scan direction and magnification are included in the legend. D – plots of major and minor diameters of ellipses that were fit to the pore openings. The blue, black, and cyan traces correspond to image sets A, B, and C, respectively, whereas the red and green traces refer to additional pore sets in the scope of the same test array. E – as D, but respective to outer edges of the annular elevations around the pores, and including plots of mean elevation heights.

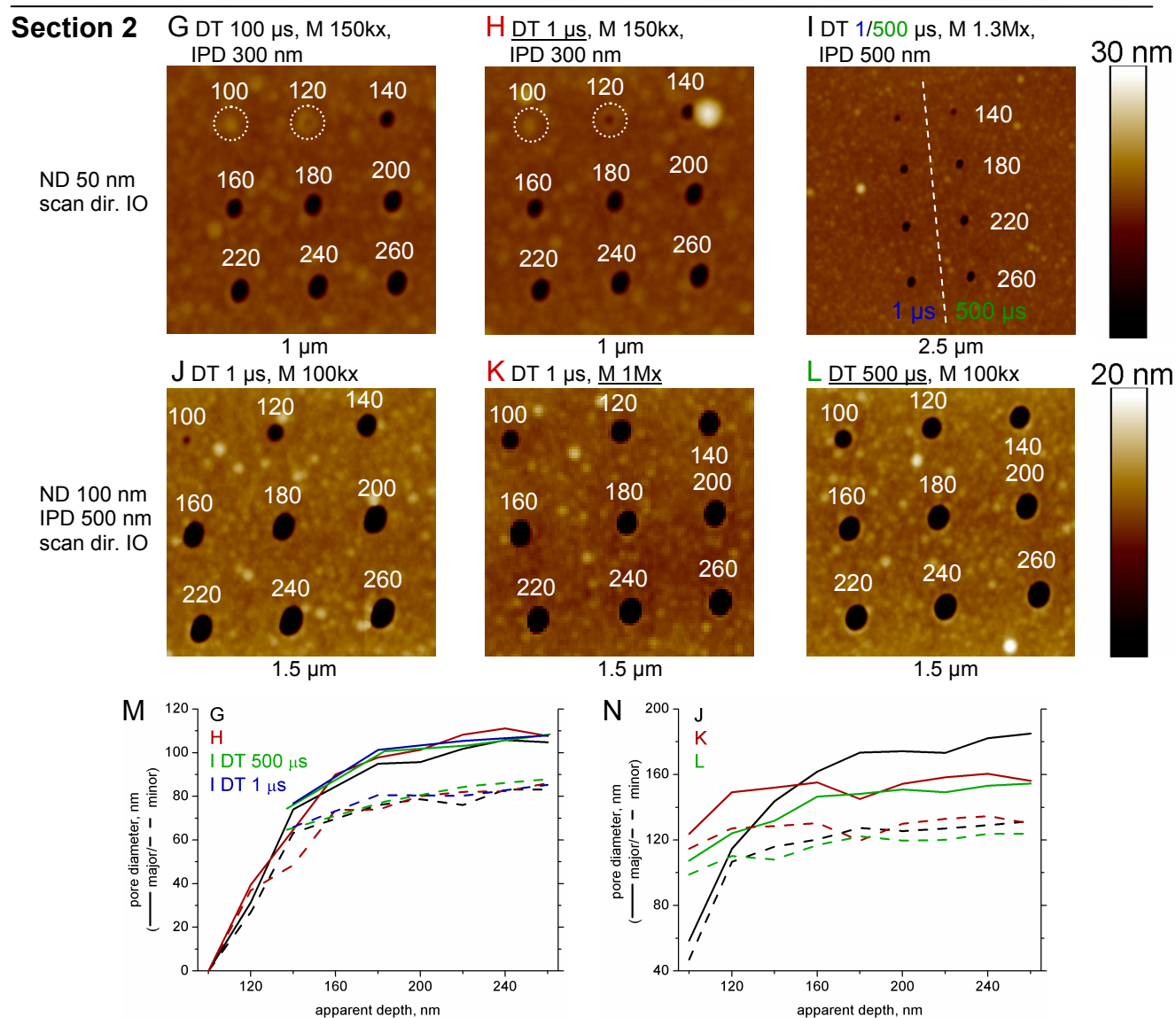
Figure 4-21 (next page). AFM analysis of additional square-shaped test arrays of FIB-milled pores. Milling parameters specific for the individual arrays and groups of arrays are listed above and to the left of the images, respectively: nominal diameter (ND), inter-pore distance (IPD), dwell time (DT), scan direction (inner-to-outer, IO/outer-to-inner, OI). Locations of pores that are not through but reveal as hill-like elevations are emphasized by white dotted circles. The value of the apparent milling depth (AMD) setting is provided next to each distinguishable milling spot. Section 1: AMD was stepped from 70 to 140 nm (left to right and top to bottom) in 10-nm increments. Section 2: AMD was stepped from 100 to 260 nm (left to right and top to bottom) in 20-nm increments. Plots E, F and G correspond to images A, B and C; plot M corresponds to images G, H and I; plot N corresponds to images J, K and L.

4. Results and discussion

Section 1



Section 2



contrary, milling a full line of pores as one pattern at 20k \times was far from the recommended setting, yet the pores produced thereby were very similar to the ones of B. At AMDs of 80-110 nm, the 20k \times pores were in fact somewhat bigger, as if the sputtering at lower magnification was more efficient. Interestingly, an inverse effect is apparent when images J (100k \times) and K (1M \times) of Figure 4-21 are compared. Here, the pores are *smaller* at lower AMDs if milled at *lower* magnification, whereas at AMDs that exceed the diaphragm thickness considerably the pores milled at lower magnification became markedly elliptical and hence larger than the ones milled at 1M \times .

B. Spiraling direction (inner-to-outer vs. outer-to-inner)

Values corresponding to a line of pores equivalent to those of Figure 4-20B, but milled in the outer-to-inner direction, are plotted as green lines in Figure 4-20D&E. No significant difference with respect to pore character has been introduced by reversing the direction the pattern circle has been spiraled over by the beam.

C. Dwell time

Several of the presented AFM images of pore arrays allow for an assessment of the effect of beam dwell time (DT) per patterning pixel on pore character. The 50-nm-pore arrays G and H of Figure 4-21, for example, were milled under identical parameters but the beam dwell time: G - 100 μ s, H - 1 μ s. Only insignificant differences between pores of corresponding AMDs were found (plot M). A slightly more obvious dissimilarity has been induced upon milling 100-nm-wide pores at DTs of 1 μ s and 500 μ s (Figure 4-21 J and L, respectively). In particular, the first pore (100 nm AMD) of array L has turned out considerably larger than its counterpart in array J. As mentioned above, however, this could also be due to lateral sample drift and a consequent reduction of irradiation dose per pixel during the milling of array J. Finally, the two lines of 50-nm pores milled at high magnification (1M \times) in the scope of array I of Figure 4-21 allow for yet another evaluation of the effect of beam DTs of 1 μ s vs. 500 μ s. Despite the fact that the lines were milled at substantially different DTs, the plots of ellipse diameters that model the pore openings are virtually equal (green vs. blue traces of N).

4.3.5. Elevated annulus vs. milling in the surroundings

A relationship between the size of an elevated annulus around the pore mouth and the extent of milling in the vicinity of the particular pore was suspected. The following experiment was designed to confirm the linkage: two arrays of 7 identical pores were prepared equally in terms of all parameters but the order the pores were milled in (Figure 4-22). The six peripheral pores of both array A and array B were milled in a parallel fashion, i.e. simultaneously. The central pore of array

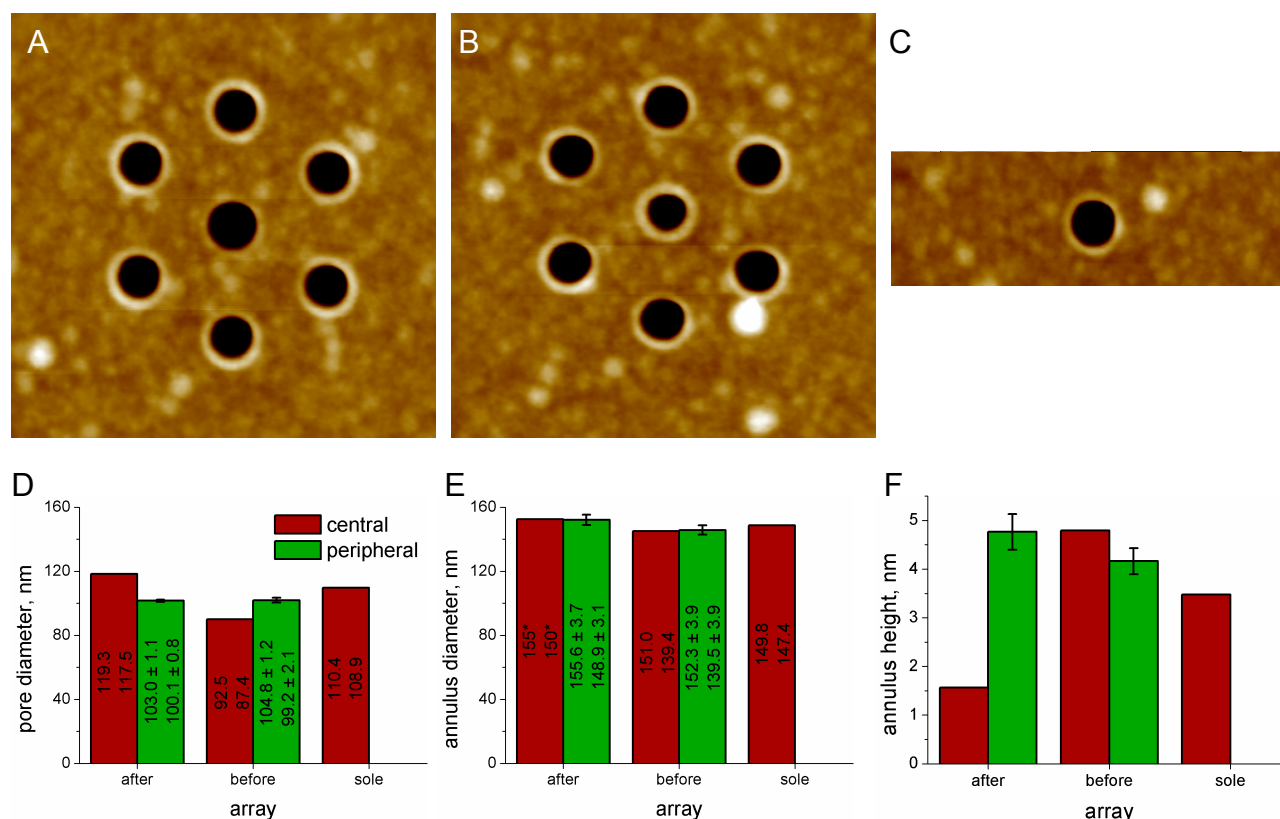


Figure 4-22. AFM height images of arrays of seven pores (A and B) and a sole pore (C) milled at identical settings but different order. A – peripheral pores milled first, central pore milled afterwards. B – central pore milled first, peripheral pores milled afterwards. In both cases, the peripheral pores were milled in parallel. Patterning settings: nominal pore diameter 100 nm, pore center-to-center distance 250 nm, magnification 150k \times , beam dwell time 10 μ s, scan direction inner-to-outer. * typical analysis routine not feasible due to very low elevation height, the values listed are estimates.

A was milled after the peripheral pores, whereas the central pore of array B was milled before the peripheral pores (see figure caption for specific patterning parameters). Array C comprises a single pore milled at the same parameters as the pores in arrays A and B. All three arrays were milled consecutively in the same corner of a Si₃N₄ diaphragm, yet sufficiently far from each other (3 μ m) to eliminate a potential interference of the milling of an array with the character of pores of a neighboring array. The pores were analyzed individually using the routine described in Chapter 3.2.2.3. The resulting diameters of the pore mouths and the annular elevations, as well as the height of the elevations, have been depicted in the form of column plots in sections D, E, and F of the figure, respectively. The peripheral pores are considered equivalent, thus a single mean value is presented for each set.

There is an obvious difference between the central pores of arrays A and B. The diameter of the pore milled in the center of an existing hexagonal sextet of pores is 1.3 \times larger than that of the central pore milled before the peripheral sextet (D). On the contrary, the elevated annulus around the pore opening is barely present in the former case, yet rather pronounced in the latter case (F). Pore mouth diameter and elevated annulus height of the single pore of array C falls between those

of the central pores of arrays A and B. The characteristics of the peripheral pores are homogeneous not only within a particular sextet, but also between the two sets (D). Only the annulus height seems to be slightly different for the two sets. The outer diameters of the annular elevations are uniform around all pores irrespective of when and where they were milled.

Apparently, pore mouth diameter shrinks and annulus height grows due to subsequent milling in the vicinity of a pore. The central pore of array A, milled last, is unambiguously the largest pore with the lowest annular elevation. On the other hand, the central pore of array B, milled before the peripheral sextet, shows a diameter evidently smaller and an annulus slightly higher than the surrounding pores. It appears that electrostatic build-up of volatile ionized carbonous material may be responsible for both pore shrinking and elevation growth. Based on the notion that accelerated ions interact with the bombarded solid matter via the ‘collision cascade’, it can be expected that the walls of the pores are positively charged due to Ga⁺ ions embedded in the matrix of Si₃N₄. If material is to accumulate selectively at the pore mouth and walls, it should do so based on electrostatic attraction. Redeposition of Si and N seems unlikely, as annulus formation would have to be a session-independent effect, which is not the case. Carbonous contamination, either volatile or adsorbed at the back side of the diaphragm, can both be considered.

The central pore of array A and the sole pore of array C were both milled as the ‘last’ pores of the respective arrays, yet the pore in array C has a smaller diameter and enhanced topography. Apparently, the pile-up of material induced by the milling of itself is sensitive to the presence of the surrounding six pores. It may be that less material was available for ionization when the 7th pore of array A was milled (this can be considered in the case of surface-confined contamination only), or the material ionized upon the milling of the last pore was distributed among all pores of the array.

If a conclusion is to be deduced based on the experiment just described, it follows that if homogeneous characteristics among all pores of an array are desired, the pores should not be milled one after another, but rather in a parallel fashion, and particularly so at short pore-to-pore distances.

4.3.6. Minimum attainable pore size

Painted BLMs have been shown to gain stability with decreasing aperture size.^{24,100} As the same is expected for npsLBs, it was motivating to try to identify the lowest pore diameter that could be attained reproducibly in 100-nm-thick Si₃N₄ diaphragms by the FEI Nova 600 FIB. An approach of milling a single pixel (i.e. static irradiation w/o rastering) by the i-beam for prolonged periods of time has been adopted. A series of pores was milled at 1 pA in time intervals ranging from a fraction of a second to 60 s (Figure 4-23). Unfortunately, this particular session had been impaired

by prominent growth of annular elevations. Hill-like elevations emerged at an irradiation dose of 2.5 pC and the first unambiguous break-through was detected at 4.5 pC. The usual plots of best-fit ellipse diameters and annular heights are included.

Lines of darker shade can be noticed in the SEM micrograph (Figure 4-23E) that propagate in the positive x direction relative to every pore. For an unknown reason, some undefined sputtering or deposition seems to have occurred in this direction. Whatever the process, all pores that had a pore milled to their left were affected. This is well noticeable in an AFM height image of the five pores of the array milled for the longest periods of time (Figure 4-23A). Pores ‘15’ and ‘30’ both had a pore milled to the left, whereas pores ‘20’, ‘40’, and ‘60’ did not. The former two pores are barely through and exhibit elevations far more evident than the latter three pores. Interestingly, the annular elevations of the latter three pores are lowest in the direction the process propagated in. A similar trend can be noticed at the pores milled in shorter intervals – ‘15’ is smaller than ‘9.5’, ‘8.5’ is smaller than ‘7.5’, etc. Despite the interfering effect, the characteristics of pores along the line parallel and further from the diaphragm edge could be evaluated (Figure 4-23F).

Reproducibility of fabricating a multitude of pores with constant specifications was verified by repeated milling of a pattern under the settings of pore ‘4.5’ of Figure 4-23C. The milling was done in the same corner of the same diaphragm at yet another session and two distinct locations. A high-magnification height scan of the original ‘4.5’ pore and of example pores corresponding to the two verification arrays are displayed in Figure 4-23G, H, and I, respectively. Obviously, elevations were less prone to form in verification array 1 and larger pores than the original were obtained therefore ($\varnothing_{\text{maj}} = 59 \pm 4 \text{ nm}$, $\varnothing_{\text{min}} = 52 \pm 3 \text{ nm}$, $n = 10$). Interestingly, pores of array 2 were noticeably smaller ($\varnothing_{\text{maj}} = 47 \pm 3 \text{ nm}$, $\varnothing_{\text{min}} = 37 \pm 3 \text{ nm}$, $n = 5$) and showed elevations comparable to that of the original ‘4.5’ pore ($\varnothing_{\text{maj}} = 102 \pm 8 \text{ nm}$, $\varnothing_{\text{min}} = 86 \pm 3 \text{ nm}$, height = $4.1 \pm 0.8 \text{ nm}$, $n = 5$).

In summary, the smallest pore diameter of $\sim 50 \pm 10 \text{ nm}$ in diameter could be obtained reproducibly in 100-nm-thick Si_3N_4 diaphragms by the FEI Nova 600 FIB. Hard-to-control factors (e.g. imperfect vacuum or long-term beam current drift) are suspected to be responsible for the variation of pore size and topography from session to session. More importantly, however, the variation of pore size and topography within a specific array was low, allowing one to assume uniform properties for all npsLBs formed on the array.

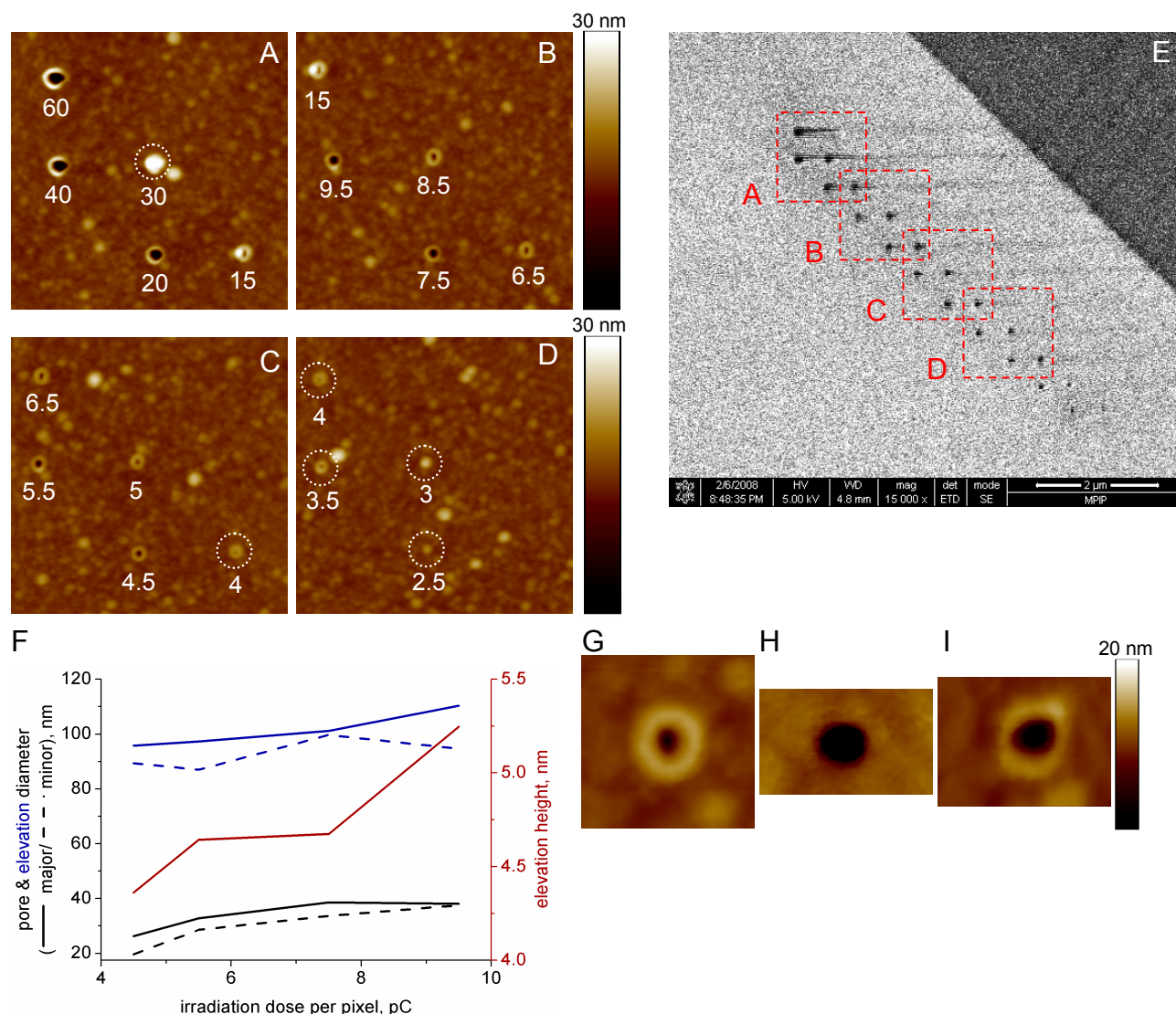


Figure 4-23. FIB milling of a single pixel through an Si₃N₄ diaphragm. A-D are topographical AFM close-ups of the flat side of parts of the test array. E – an SEM image of the pit side of the complete array. The value beneath a pore or a protuberance denotes the exposure dose in pC. Milling locations where pore lumen cannot be resolved clearly are emphasized by white dotted circles. F – a plot of pore and elevation diameters and elevation and height. G-I – high-magnification AFM images comparing three pores milled through the same Si₃N₄ diaphragm under the same milling parameters at 2 different sessions and 3 locations: G – session 1/original test array, H – session 2/verification array 1, I – session 2/verification array 2.

4.3.7. Arrays used for the formation of npsLBs

Arrays of pores that npsLBs were spun over comprised 1, 3, 7, or 12 pores in a hexagonal arrangement. Nominal pore diameters and pitch (shortest pore center-to-center distance) were varied in addition to the number of pores per array. ND and pitch were (meant to be) constant within a particular array. A single array per Si₃N₄ diaphragm was fabricated.

AFM and SEM images of an assortment of arrays used for the formation of npsLBs are displayed in Figure 4-24. Arrays with low pitch were patterned as a whole, whereas pores of arrays of a pitch of 1 μm and above were milled one-by-one using a single-circle pattern coupled to successive stage

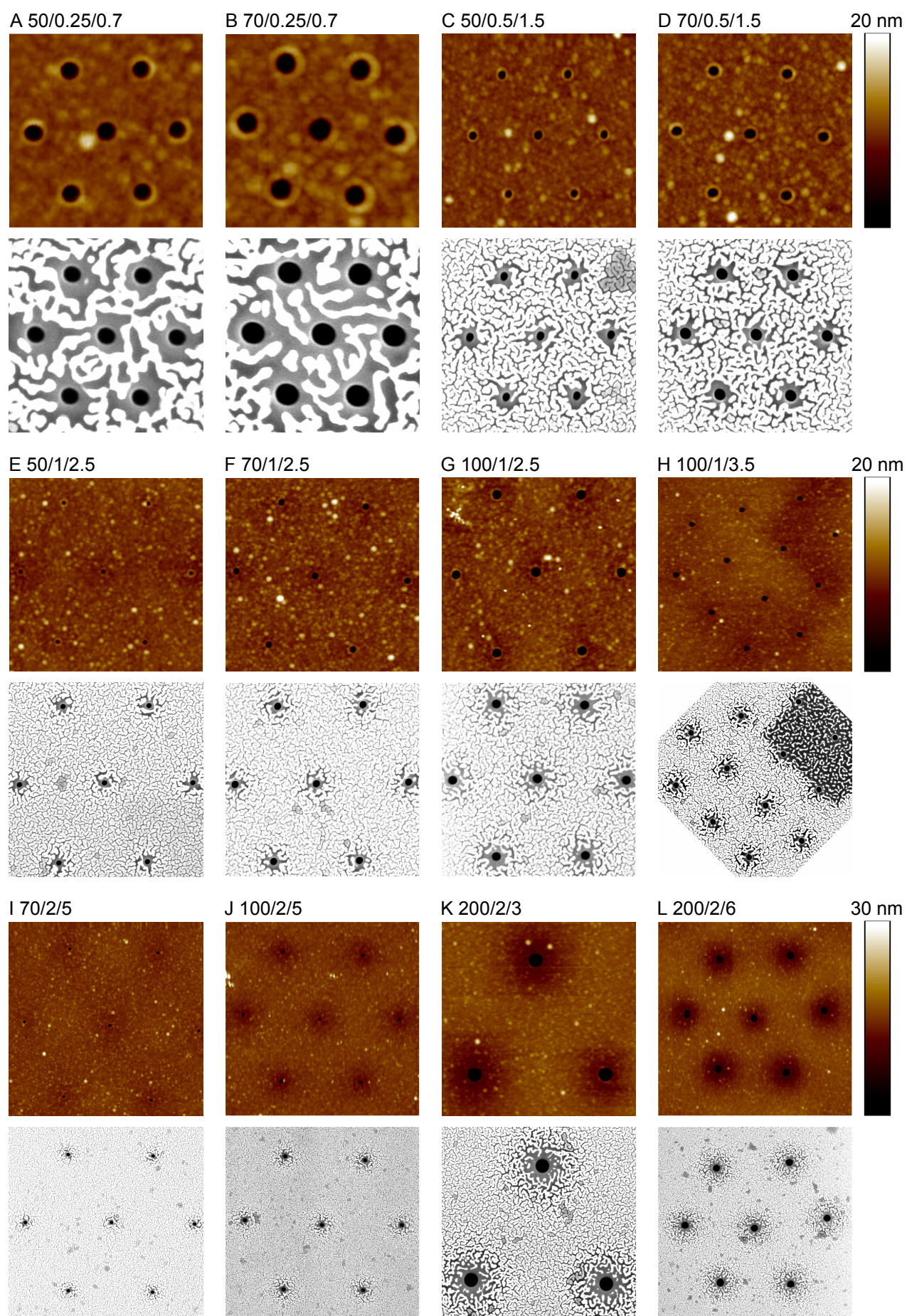


Figure 4-24 (previous page). Examples of pore arrays used for the formation of npsLBs. A square AFM topography image of the flat side and an SEM image of the pit side are shown for each array. The three values characterizing an array stand for the nominal pore diameter [nm], the pitch of the array [μm], and the size of imaged area [μm], respectively.

movements. The former approach gave rise to very regular pore distributions (A-D). On the contrary, deviations from the desired pore arrangement are apparent in some of the presented arrays that were milled by the latter approach (e.g. E, F, L). Obviously, the accuracy of lateral stage movement of the Nova 600 FIB was limited, or there was considerable lateral drift of the samples relative to the ion beam.

In addition to the pores that resolve as depressions relative to the diaphragm surface, some randomly distributed elevated spots are apparent in the AFM images. The elevations mostly show round shapes of 50-100 nm in diameter and up to 10 nm in height. The features could be detected on any Si₃N₄ diaphragm as received. Cleaning procedures aggressive against organics (hot piranha solution/oxygen plasma) did not alter the character of these features. It thus appears the elevations, evidently inorganic in composition, were intrinsic to the Si₃N₄ diaphragms. Presumably, such surface roughness is natural to thin films of Si₃N₄ CVD-deposited over Si.

4.3.8. Pore taper

Gradual increase of skill during the course of the study with respect to SEM imaging of FIB-milled pores eventually allowed for the acquisition of images of very high-quality. These images made it possible to directly see that the pores were conical, and to make an estimate of the taper angle.

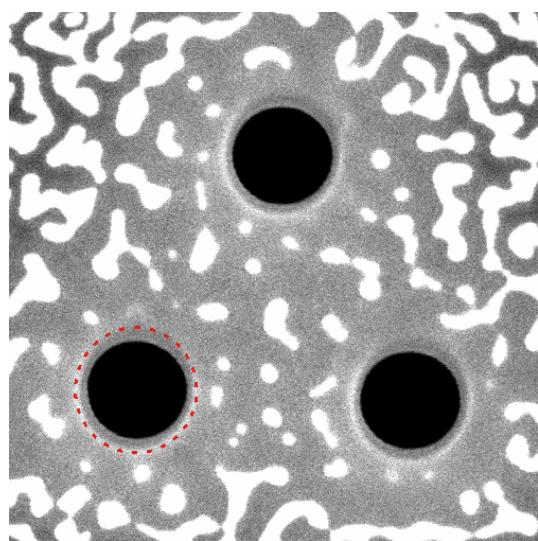


Figure 4-25. A high-quality SEM image of the front (pit) side of an array of 3 pores milled through a 100-nm-thick Si₃N₄ diaphragm. Nominal diameter and center-to-center distance of the pores were 200 nm and 500 nm, respectively. The back-side and the front-side pore openings can be discerned well: the former are defined by the black regions, whereas the latter resolve as circular contours of a lighter shade (overlaid by the red dotted trace at the left bottom pore).

An example of an SEM image that the degree of pore taper can be extracted from is shown in Figure 4-25. Upon a closer examination of the pores one can notice several distinct concentric features of varying signal intensity. First, every pore exhibits a black circular central region. Second, an annulus of a shade of gray intermediate to that of the pore centers and of the further surroundings can be observed around the central region. Third, sections of the outer edge of the annulus are lined by a noticeable bright contour (overlaid by a red dotted trace at one of the pores). It is known that due to the Gaussian intensity distribution of the focused i-beam and the redeposition of sputtered material during milling, the sidewalls of a feature milled through a continuous material always exhibit some degree of deviation from the beam direction.^{49,52} Circular features milled vertically through a free-standing silicon nitride film are thus expected to give rise to holes of the shape of truncated cones rather than cylinders. Based upon this assumption, the black central region of the pores in the figure can be associated with the edge of the pore opening at the back side of the diaphragm, the semi-dark annulus with the walls of the inverse truncated cone, and the outer edge of the annulus with the edge of the pore opening at the front side. Via particle analysis, diameters of the back-side openings evaluate to 175 ± 0.5 nm. Approximate circular overlay of the front-side openings yields diameters of ~ 220 nm. Based on these values, the angle of taper of the nominally 200-nm pores is $\sim 12^\circ$. As images of comparable resolution of pores of other sizes were not captured, assessment of pore taper with respect to pore size was not possible. A value near to that of the 200-nm pores was thus assumed for all pores.

4.3.9. Conductance of unobstructed pores in Si_3N_4 diaphragms

The resistance of a conical through pore filled and surrounded with electrolyte is given by the sum of the internal pore resistance, R_{internal} , and the external access resistances of the pore mouths on either side of the partition, R_{acc1} and R_{acc2} ¹⁰¹⁻¹⁰⁵:

$$R_p = (R_{\text{acc1}} + R_{\text{internal}} + R_{\text{acc2}}), \text{ where} \quad (\text{Eq. 4-1})$$

$$R_{\text{acc1}} = l / 4\kappa r_1 \quad (\text{Eq. 4-2})$$

$$R_{\text{internal}} = l_p / (\pi \kappa r_1 r_2), \quad (\text{Eq. 4-3})$$

$$R_{\text{acc2}} = l / 4\kappa r_2 \quad (\text{Eq. 4-4})$$

κ is the conductivity of electrolyte, r_1 and r_2 are the radii of the pore openings at the respective sides of the partition, and l_p is the length of the pore. Electrochemical impedance spectra were acquired for Si_3N_4 diaphragms with varying pore size and numbers. Based on these spectra, conductance of free unobstructed pores as well as the overall electrical parameters of the system could be evaluated accurately (see Chapter 4.5 for examples of impedance spectra and the modeling scheme). Figure

4-26 displays the obtained pore resistance, R_p , with respect to pore size for an assortment of Si₃N₄ windows bearing single or multiple pores. Experimental data presented as scattered points for 100 mM TMACl, 100 mM KCl and 1 M KCl (all of pH 7, buffered by 5 mM HEPES) are overlaid with theoretical pore resistance traces. In the theoretical calculations based on the equation above, l_p was 100 nm, as given by the thickness of the Si₃N₄ membrane, κ was 1.282 S/m and 10.86 S/m for 0.1 M and 1 M KCl¹⁰⁶, respectively, and 0.969 S/m for 0.1 M TMACl.¹⁰⁷ r_1 , the radius of the pore mouth at the flat side of the diaphragm, was substituted by nominal pore radius. r_2 was determined from r_1 by correcting for the truncated cone taper of 12° as obtained from SEM image analysis. Resistance values for TEM windows with pore arrays, R_p , were adjusted for the number of pores, n , via $R_p = nR_p$. Multiple-pore TEM windows with constant nominal pore size were included only. The experimental pore resistance data distribute well along the corresponding simulated curves for the given range of pore radii. Discrepancies might have been introduced by mismatch between nominal and actual pore size, which has not been accounted for in the figure. Moreover, assuming an electrolyte conductance temperature coefficient of ~2%, room temperature fluctuations might have given rise to ~10% scatter interval of the measured pore resistances.

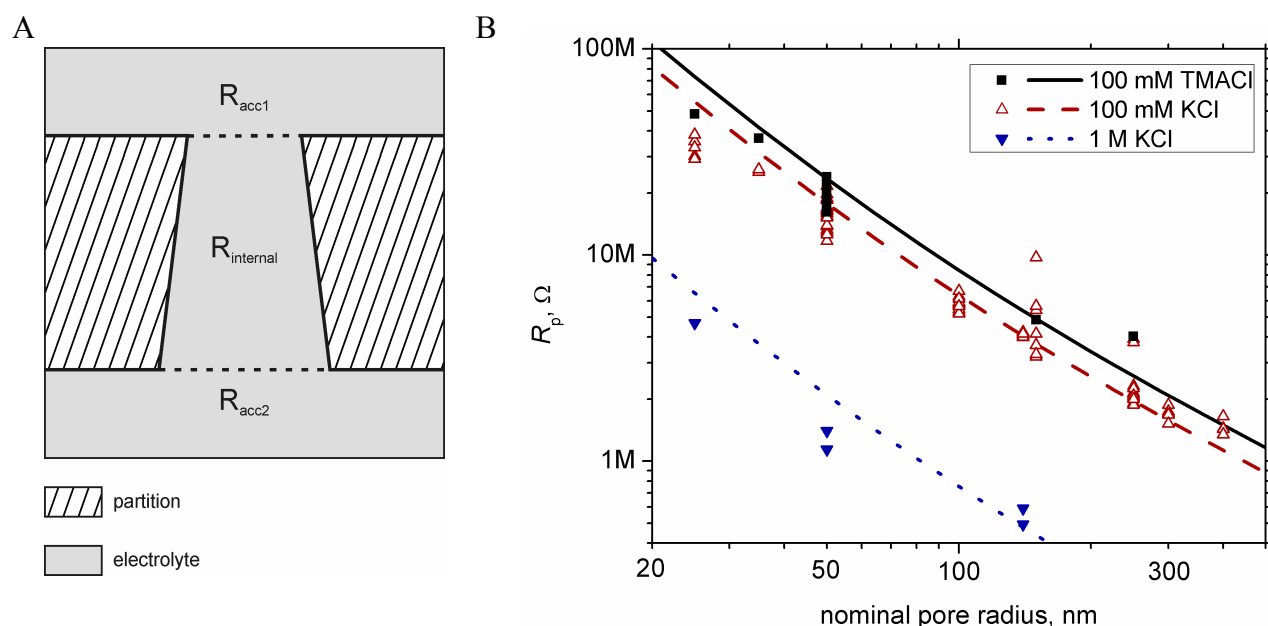


Figure 4-26. A - a cross-section schematic of a through pore of the shape of a truncated cone filled and surrounded with electrolyte. The three regions contributing to the total pore resistance are separated by dashed lines. B - experimental and theoretical resistance of unobstructed pores in Si₃N₄ diaphragms milled by FIB. Scattered points represent experimental data, solid lines are theoretical curves for single 100 nm long cylindrical pores. Data measured and calculated for 100 mM TMACl, 100 mM KCl and 1 M KCl are shown (see the legend). All electrolytes were buffered by 5 mM HEPES at pH 7.

4.3.10. Conclusion

Well-defined arrays of through pores could be milled through 100-nm-thick Si₃N₄ diaphragms by the FIB. Pore openings were imaged by the SEM on the pit (i.e. beam incident) side and by the

AFM on the flat (i.e. reverse) side of the diaphragms. The most determinant parameters of the FIB patterning process on final pore specifications were the nominal pore diameter and the apparent milling depth, whereas parameters such as magnification at milling, pixel dwell time, or scan direction did not have a significant impact on pore characteristics. Arrays of 1-12 pores with controlled pore size and pore-to-pore distance were produced. The smallest pore diameter of ~ 50 nm could be attained quite reproducibly. Taper angle of $\sim 12^\circ$ towards the flat side was estimated from high resolution SEM images of 200-nm-wide pores. Conductance of unobstructed pores filled with electrolyte correlated well with theoretical predictions based on pore geometry.

4.4. Reduction of Si₃N₄ window capacitance

This chapter begins with giving reasons for the necessity of capacitance reduction of Si₃N₄ windows with respect to DC current recordings through single channel proteins. It continues by analyzing the structure of a Si₃N₄ window and identifies the individual contributors to overall chip capacitance. Relationships between the contributors are established and conclusions with respect to possible capacitance reduction pathways are derived. Reasons for choosing a strategy based on a light-sensitive polymerizable organic coating are given. The results of employing this passivation strategy are assessed microscopically and by impedance spectroscopy.

4.4.1. The need of low capacitance

In order to obtain low-amplitude DC electrical recordings of high fidelity through channels or pores embedded in a lipid bilayer, it is crucial to minimize the overall capacitance of the system. Similarly, low capacitance is preferential for AC characterization of well-sealing lipid bilayers spanned over pores. The reasons behind these requirements are as follows:

- The electronics of amplifiers designed for high-bandwidth low-noise current recordings through protein channels is not compatible with capacitances beyond 1 nF. Capacitance below 100 pF is preferential for single-channel recordings at high gains.^{68,69}
- Noise of significant magnitudes is generated due to high capacitance.²³ Low noise is a key prerequisite for accurate single-channel recordings.
- A well-sealing lipid bilayer spanned over a through pore shows the characteristics of a parallel RC circuit, where C is the sum of bilayer and partition capacitance and R is in the 1 - 50 G Ω regime. The electrical response is dominated by C at high AC frequencies, whereas the low-frequency region of a corresponding impedance spectrum is governed by R . At constant R , the transition frequency between the R - and the C -dominated region of the spectrum scales inversely to C . If R , the most interesting attribute of a psLB, is to be determined by impedance spectroscopy, AC perturbations of frequencies at which R dominates must be probed. At $R = 10^{10} \Omega$ and C of 10^{-11} , 10^{-10} , and 10^{-9} F, the transition frequencies ($dZ''(f) = 0$) are ~ 1.6 , 0.16, and 0.016 Hz, respectively (see also Figure 3-13, green vs. red trace). Time needed to measure the impedance at a particular frequency is inversely proportional to the frequency. Obviously, the lower the transition frequency, the shorter the measurement time. Good accuracy in fitting an impedance spectrum is obtained if the spectral range spans an order of magnitude below the transition frequency. At high C , this may translate to very long measurement time if accuracy is to be maintained (e.g.

~45 min for a range of 1×10^{-3} - 1.6×10^4 Hz, 5 points/decade, integration time $1/f$ per point). Slow system dynamics may become significant and the usual assumption that an impedance spectrum relates to a steady state is likely not to hold true for lengthy experiments. If, on the other hand, measurement time is limited, fitting accuracy becomes deteriorated severely. Obviously, then, impedance measurements are faster and more accurate at low capacitance.

4.4.2. Capacitance of a Si_3N_4 window

The body of a Si_3N_4 window is made of silicon. Being a semiconductor, silicon exhibits poor dielectric properties. The capacitance of the window is therefore rather high. Although the Si_3N_4 film coating both sides of the window is an insulator, it is too thin to eliminate the high capacitance of the frame. Additional treatment is thus required to reduce the chip capacitance.

When a Si_3N_4 window is mounted as a partition between two compartments of electrolyte, four unique regions can be identified that make up the total chip capacitance (Figure 4-27). Overall, the chip capacitance, C_{chip} , is a sum of the capacitance of the frame and the free-standing Si_3N_4 diaphragm, which act in parallel:

$$C_{\text{chip}} = C_{\text{frame}} + C_{\text{fsSiN}} \quad (\text{Eq. 4-5})$$

Determination of the capacitance of the diaphragm is straight-forward:

$$C_{\text{fsSiN}} = \epsilon_0 \epsilon_{\text{SiN}} A / d, \quad (\text{Eq. 4-6})$$

where ϵ_0 is the permittivity of free space (8.85×10^{-12} F/m²), ϵ_{SiN} is the relative dielectric constant of silicon nitride (~7.5), A is the diaphragm area, and d is the diaphragm thickness. For the chip specifications used in this work ($A \approx 0.11$ mm², $d \approx 100$ nm) C_{fsSiN} evaluates to ~72 pF.

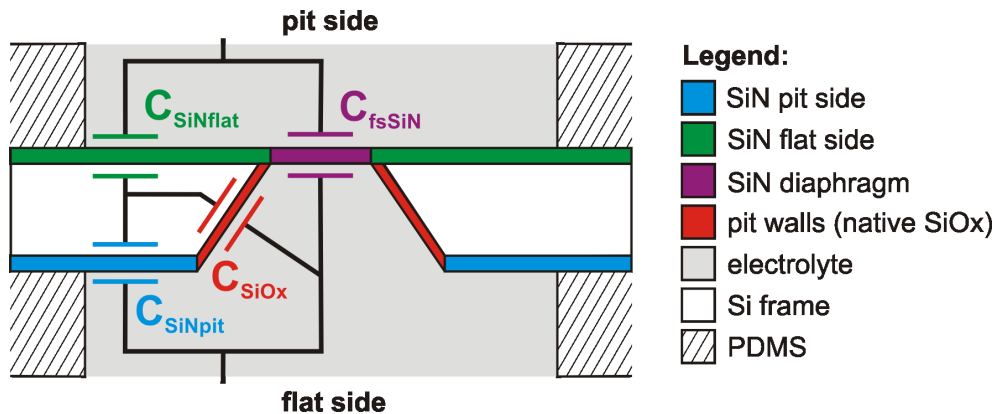


Figure 4-27. Schematic of an Si_3N_4 TEM window: capacitance of the individual regions that contribute to the total window capacitance.

The capacitances of the respective sides of the frame are linked in series via the conductive silicon bulk of negligible resistance. One thus obtains

$$1/C_{\text{frame}} = 1/C_{\text{pit-side}} + 1/C_{\text{flat-side}} \quad (\text{Eq. 4-7})$$

i.e.

$$C_{\text{frame}} = C_{\text{pit-side}} \times C_{\text{flat-side}} / C_{\text{pit-side}} + C_{\text{flat-side}} \quad (\text{Eq. 4-8})$$

$C_{\text{flat-side}}$ is given simply by the area of the Si₃N₄ film that is in contact with the electrolyte,

$$C_{\text{flat-side}} = C_{\text{SiNflat}}, \quad (\text{Eq. 4-9})$$

while $C_{\text{pit-side}}$ is the sum of the parallel capacitances of the Si₃N₄ film on the pit side and the pit walls coated with native silicon oxide¹⁰⁸:

$$C_{\text{pit-side}} = C_{\text{SiNpit}} + C_{\text{SiOx}} \quad (\text{Eq. 4-10})$$

Frame capacitance can hence be expanded into

$$C_{\text{frame}} = (C_{\text{SiNpit}} + C_{\text{SiOx}}) \times C_{\text{SiNflat}} / (C_{\text{SiNpit}} + C_{\text{SiOx}} + C_{\text{SiNflat}}) \quad (\text{Eq. 4-11})$$

C_{SiNflat} and C_{SiNpit} can be calculated in analogy to eq. 4-6 based on the areas of the respective surfaces wetted with electrolyte. A typical comfortable wetted area to work with would be ~5-7 mm², as given by a circular cut-out of 2.5-3 mm in diameter in a sealing PDMS pad. For the Si₃N₄ TEM windows specific for this work, C_{SiNflat} and C_{SiNpit} would be in the range of 3.3-4.6 nF and 2.7-4.0 nF*, respectively.

It is problematic to calculate C_{SiOx} accurately, since the thickness of the oxide layer is not well defined. Nevertheless, with a thickness estimate of ~2 nm¹⁰⁸ and a dielectric constant of ~4, it is clear that the specific capacitance of the pit walls is ~20-25 times higher than the specific capacitance of the 100-nm-thick nitride film. C_{SiOx} of ~30 nF is thus expected for the total pit wall area, 1.8 mm², of the windows used in this work. Apparently, the pit walls are the major contributor to the capacitance of the pit side ($C_{\text{pit-side}}$, eq. 4-10). This large capacitance does not affect the overall capacitance directly, however, as it acts in series with $C_{\text{flat-side}}$ (eq. 4-8).

4.4.3. Implications on capacitance reduction strategies

The above analysis of Si₃N₄ window capacitance generates some important implications for the possible passivation strategies:

1. The capacitive contributions of the frame and the diaphragm are additive. The frame is by far the dominant contributor ($C_{\text{frame}} \approx 3$ nF vs. $C_{\text{fsSiN}} \approx 72$ pF) at the specific chip parameters. The primary goal is thus to **target C_{frame}** . On the other hand, even after complete elimination of

* C_{SiNpit} has been corrected for the missing area of the base of the pyramidal pit

C_{frame} , the chip capacitance would remain equal to C_{fsSiN} and hence still rather high. Therefore, if possible, a passivation strategy should be sought that reduces C_{frame} and C_{fsSiN} jointly.

2. It follows from equations 4-7 and 4-8 that a substantial reduction of the capacitance of one side of the frame to a virtual value of C_x is effective in bringing down the total frame capacitance to just below C_x , no matter how large the capacitance of the other side. A reduction of the capacitance of both sides to C_x would result in an overall frame capacitance of $C_x/2$. The additional benefit of passivating the other side thus appears marginal. Proper **passivation of a single side of the chip should be sufficient** in reducing the total chip capacitance to an acceptable value.
3. A **sole passivation of the pit walls** (e.g. via thermal growth of SiO_2) **will not induce a sufficient decrease of chip capacitance**. At complete elimination of the capacitance of pit walls ($C_{\text{SiOx}} \approx 0$) the total frame capacitance simplifies to

$$C_{\text{frame}} = C_{\text{SiNpit}} \times C_{\text{SiNflat}} / (C_{\text{SiNpit}} + C_{\text{SiNflat}}), \quad (\text{Eq. 4-12})$$

which for the chips used in this work and 5 mm^2 wetted by electrolyte evaluates to $\sim 1.5 \text{ nF}$.

Given the above implications it appears that an additional coating layer applied to the complete surface of one side of the Si_3N_4 TEM window can bring about the desired reduction of window capacitance.

4.4.4. Requirements on coated chips

1. **Maximum final chip capacitance of 100 pF, capacitance below 50 pF preferred**
2. **Thickness of material at the pore area as low as possible**

The key point behind using thin Si_3N_4 diaphragms is the excellent pore aspect ratio, which avoids the limitations due to diffusion in confined geometries. If a coating strategy is considered that would apply to the complete surface of either side, a route must be designed to avoid or remove the coating locally at the pore-bearing area of the diaphragm.

3. **Smoothness of frame surface**

Our approach to obtain a sealing mount of the chips in a measurement cell relied heavily on the intrinsic adhesion of PDMS films to flat-surfaces. Substantial loss of flatness due to the passivation process would result in severe sealing difficulties.

4. **Opportunity for surface chemistry**

The opportunity for chemical modification and patterning of the surface with respect to enhancement of the pore-spanning bilayer properties should be preserved. In this sense, the

chemical inertness of Si₃N₄ is a great advantage. Since bilayers are spanned on the surface of the flat side of the chips, it would be beneficial to focus the passivation efforts at the pit side of the chips. Although the 3D character of the pit side might provide additional challenges with respect to the passivation procedure, the flat side would remain intact for chemical modification.

5. Robustness after passivation

Considerable effort is put into production and characterization of a single chip with a specific pore configuration. Once produced, it is favorable to try to reuse the chip and collect statistically relevant amounts of npsLB-related data (stability, resistance, etc.) for the particular pore configuration or surface modification. A possibility to ‘regenerate’ a chip, i.e. to bring it back to its original pre-experimental state, is preferred in this sense. Regeneration of non-passivated chips was found to be possible in the course of this work by means of wet (piranha solution) and dry (O₂-plasma, UV-ozone) oxidative treatments. In this context, the ability of the passivation layer to withstand such regeneration would be of great benefit.

4.4.5. Cross-linkable photoresist coating - the passivation strategy of choice

Schmidt et al. reported a successful reduction of the capacitance of analogous Si₃N₄ windows to below 35 pF by thermal growth of 1 μm of SiO₂, an inorganic insulator, over the complete back side (excluding the diaphragm).⁴⁴ Two key differences exist between the windows used in the above and in our study: 1) the back side of their windows was not coated with Si₃N₄, and 2) diaphragm size was in the order of ~50 μm only, which made C_{fsSiN} considerably smaller than in our case. The former attribute allowed the authors to grow thermal oxide over the complete back side of the windows. Unfortunately, adequate technology was not available in the scope of this thesis to follow such a passivation strategy. Moreover, the back side of our windows was coated with Si₃N₄. Removal of Si₃N₄ from the back side to expose the bulk Si of the frame - a requirement for thermal growth of SiO₂ - would introduce a high risk of damaging the unprotected Si₃N₄ diaphragm. The latter attribute, namely small diaphragm capacitance, spared Schmidt et al. the necessity to expand the passivation strategy to this region of the window.

Our approach to reduce the capacitance made use of an organic coating deposited over one side of a window. A primary advantage of this strategy dwelled in the fact that relatively simple ‘benchtop’ methods were sufficient to apply the coating. As the material was deposited over the complete side of a window *after* pore fabrication, however, the challenge of removing the coating from the pore-bearing region of the diaphragm had to be tackled. The MicroChemicals AZ[®] 5214E image reversal photoresist – a special sort of positive photosensitive resist – was found to be well suitable for this goal. A positive resist is a type of photoresist in which the portion of the photoresist that is

exposed to light becomes soluble, whereas the portion of the photoresist that is unexposed remains insoluble to the photoresist developer. The pores blocked by the resist could hence be released simply by localized exposure and dissolution of the coating from the pore-bearing region of the diaphragm. The additional benefit of using the image reversal resist was provided by the possibility to enhance the hardness and chemical robustness of the coating by light- and heat-induced polymerization. Unlike a coating based on an ordinary positive resist, a polymerized film of an image reversal resist is able to stand an exposure to some mild solvents (e.g. EtOH or IPA). This ability was crucial as such solvents were used routinely to rinse a window between successive experiments.

4.4.6. Deposition parameters

A significant effort was devoted to fine-tuning the parameters of the coating process:

1. Chemical robustness of AZ[®] 5214E vs. hardbake parameters

Robustness to EtOH, IPA, and acetone (5-min immersion) of films of the photoresist spin-coated on fragments of Si wafers was tested with respect to hard-bake temperature (150°-180°) and time (10-100 min). No dissolution of the films was apparent after hard-bakes of ~60 min at 170°.

2. Capacitance of AZ[®] 5214E films on Si

Suitability of AZ[®] 5214E for the projected capacitance reduction strategy was checked using films of the photoresist spin-coated and hard-baked on fragments of Si wafers.* Fragments coated with ~500-nm-thick films showed specific capacitance ~30 times lower than bare Si fragments.

3. Deposition strategy

a) *Spin-coat*

Applicability of spin-coating, the classical method of deposition of thin organic films on flat surfaces, to coating Si₃N₄ windows with films of AZ[®] 5214E was checked first. Spin-coating typically gives rise to homogeneous flat films that completely cover the coated surface.⁶¹ In addition, it allows for excellent control over film thickness by dilution of the deposited material and setting the rotation speed. Coating the pit side of the windows was preferred to coating the flat side, as stated above. Unfortunately, spin-coating has little effect on the distribution of material inside a deep cavity such as the pit of the Si₃N₄ windows. The cavity would thus remain filled with the resist at an amount absolutely excessive and incompatible with further processing (Figure 4-28B). A stream of gas directed inside the cavity normal to the window surface and applied either before or

* A fragment of an Si wafer was used as a working electrode in a setup analogous to that described in Chapter 3.2.7.

during the spin-coat helped to reduce the residual amount of the substance in the cavity to an acceptable amount (Figure 4-28C). Sadly, the surface of either side of a Si_3N_4 window spin-coated with the resist showed significant heterogeneity in terms of film thickness. Due to its small size, the resist accumulated at the edges of the chip (Figure 4-28A, B and C). Differences in film thickness of up to $10\text{ }\mu\text{m}$ were found between the central and the peripheral regions of the windows. As a consequence, sealing adhesion of PDMS films was impaired and severe difficulties with mounting the chips in the measurement cells had to be faced.

b) Brush-paint

Deposition of AZ[®] 5214E on the *flat side* of the Si_3N_4 windows using a fine painting brush was tested next. Homogeneity of film thickness was greatly improved by brush-painting as compared to spin-coating, and chips sealing well in the measurement cells were produced this way (Figure 4-28D). Crude control over film thickness was possible by resist dilution and the number of strokes applied. Regrettably, the mechanical contact between the brush and the fragile Si_3N_4 diaphragm damaged the diaphragms in some cases. Besides, coating the *pit side* with the resist by brush-painting was not possible. A few well-passivated chips were obtained by brush-painting nevertheless that helped to confirm the validity of the photoresist-based approach to reduction of window capacitance.

c) Spray-coat

Good resist coatings of the pit side were attained by depositing the resist by a static air-brush (Figure 4-28E). The following factors were evaluated: rate of air- and resist-flow into the mixing nozzle, dilution of the resist, and distance between the air-brush and the window (see Chapter 3.2.9 for the final parameters). A combination of higher rates of air-flow and lower rates of resist-flow tended to result in smooth and homogeneous films over the entire surface of the pit side including the pit walls. Presumably, the resist was deposited in smaller droplets and the drying of the film

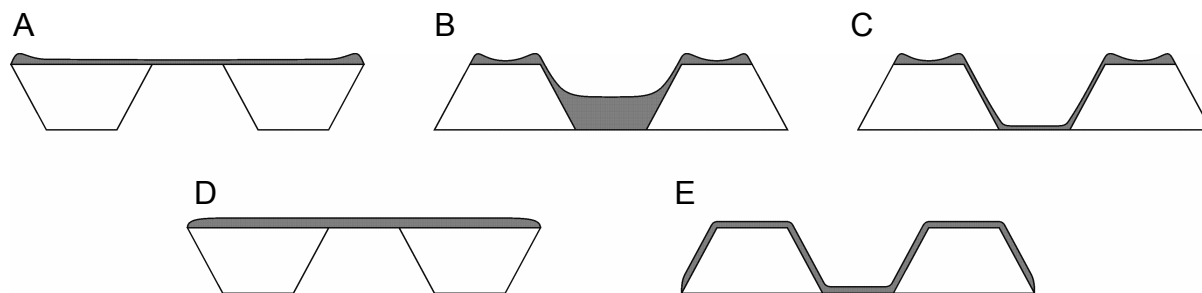


Figure 4-28. Cross-section views of an Si_3N_4 window showing profiles of photoresist deposited by simple spin coating on the flat side (A) and the pit side (B), spin-coating on the pit side assisted by stream of gas (C), brush-painting on the flat side (D), and spraying on the pit side (E). The illustrations are not drawn to scale.

was enhanced under such conditions. The flow of the resist down the walls of the pit was thus limited. Partial control over final film thickness was possible by adjusting the duration of spraying.

4.4.7. Assessment of coating and development quality

The photoresist strategy of capacitance reduction has been chosen primarily with the prospect of easy and selective removal of the resist from around and inside the pores. Quality of coating and effectiveness of resist removal from exposed areas was assessed using optical microscopy, AFM, and impedance spectroscopy.

4.4.7.1. Assessment by optical microscopy

Resist development from the pore-bearing region of a diaphragm after localized exposure was verified by bright-field optical microscopy. Figure 4-29A shows an image of a typical diaphragm of a window the pit side of which was spray-coated with resist. A single round spot was exposed and developed in the resist film. The developer was applied to the pit side only so as to avoid unnecessary contamination of the clean flat side. The spot is $\sim 70\ \mu\text{m}$ wide and well circular. A darker contour along the edges of the spot suggests that the walls of the feature are tapered. No features or heterogeneities are apparent in the developed area at the given resolution. The resist seems to have been removed completely from the entire exposed area.

A close-up of the developed corner of another diaphragm is shown in Figure 4-29B. This image comes from a real npsLB experiment, hence the adsorbed GUV over the array of pores. Here, the developed spot is twice as large ($\sim 100\ \mu\text{m}$) because a $50\times$ objective instead of the usual $100\times$ was used for exposure of the resist. As in the previous case, most of the exposed area is completely free

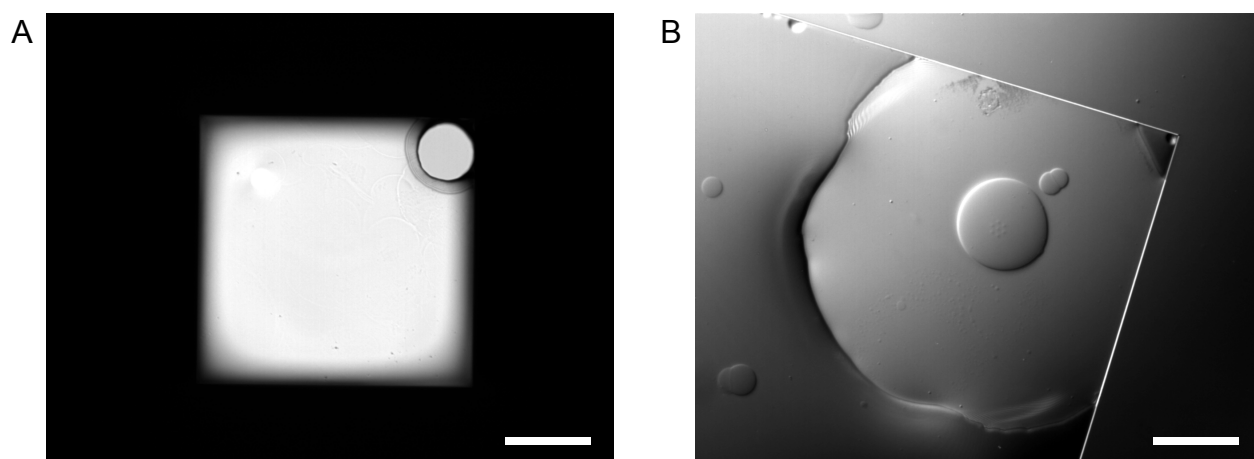


Figure 4-29. Optical micrographs of Si_3N_4 diaphragms with single developed spots in a photoresist film. The resist was sprayed over the entire area of the pit side of the windows. A – bright field in transmission mode, $10\times$ magnification, image taken in air, $100\ \mu\text{m}$ scalebar. B – DIC in reflected mode, taken in aqueous electrolyte in the course of spanning npsLBs over an array of seven pores. The array is located near to the center of the developed area under the adhered GUV. $40\times$ magnification, $25\ \mu\text{m}$ scalebar.

of resist residuals. Some remains are apparent at the edge of the diaphragm north of the array.

4.4.7.2. Assessment by AFM

Release of photoresist from the pores was examined on the nanoscale by AFM. AFM scans of the flat side of passivated porous diaphragms reveal that resist sprayed on the pit side penetrates into the pores and fills them right up to the rim (Figure 4-30E). As shown above, development of exposed resist whereby the developer is applied solely to the pit side appears to result in full removal of the resist from the diaphragm (Figure 4-29A). An AFM close-up at the pores after development from the pit side (Figure 4-30B) shows that the resist filling up the pores has been attacked by the developer, yet the pore mouths on the flat side remain considerably obstructed. Absolutely no signs of resist release have been detected on the flat side of pores that were not exposed to blue light, though (Figure 4-30E). A subsequent development step whereby the developer was applied to the flat side of the window proved to be effective in dissolving most of the exposed resist residues (Figure 4-30C). Although traces of attack by developer can be found on the resist filling up the unexposed pores, the extent of dissolution was negligible here (Figure 4-30F). In summary, nanoscale AFM analysis shows that development of exposed resist solely from the pit side may not release the pores completely, whereas bilateral development restores the original

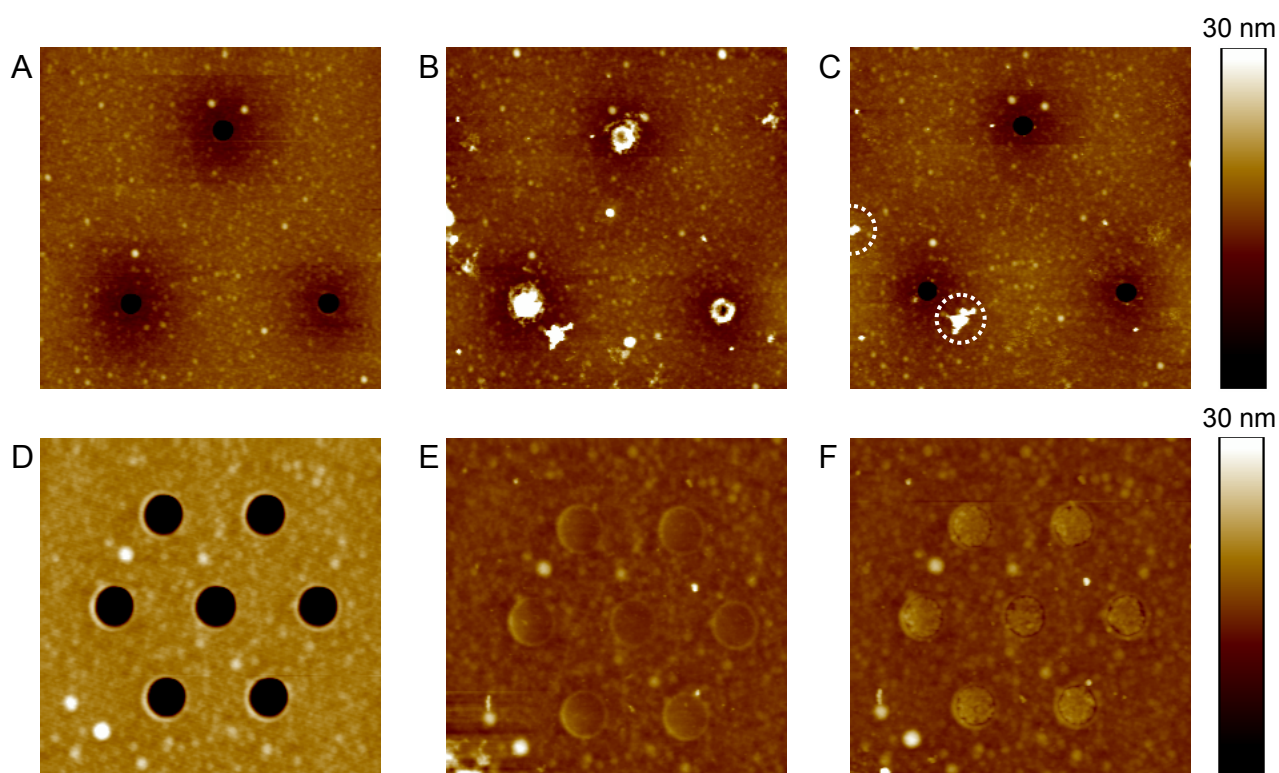


Figure 4-30. AFM topographs illustrating penetration of photoresist into nanopores and pore release by resist development. AFM topographs of two pore arrays (array 1: A-C, array 2: D-F) milled in different sections of the *same* Si₃N₄ diaphragm are shown. A, D – before passivation; B, E – after exposure of array 1 but not array 2 to blue light and development from the *pit side*; C, F – after additional development from the *flat side*. The white dashed contours in C mark dominant roughness spots that were not present on the surface before passivation (A).

condition almost perfectly (Figure 4-30A vs. C). Photoresist inside unexposed pores remains well resistant to the developer and the pores stay completely filled with the organic.

4.4.7.3. Assessment by EIS

Figure 4-31 depicts a series of impedance spectra acquired for a pore-bearing Si_3N_4 window before, during, and after the capacitance reduction process. A simple $R_S(R_P C_W)$ circuit was sufficient for the interpretation of the spectra in this case, where R_P , the pore resistance, and C_W , the total window capacitance, form a parallel loop in series to R_S , the series resistance of electrolyte and electrodes. Table 4-2 lists R_P and C_W values extracted from the spectra. Note that 7 pores of 50 nm in diameter were milled in a hexagonal array arrangement in *each* corner of the particular Si_3N_4 diaphragm, the total number of pores thus being 28. The impedance spectrum recorded for a clean chip without coating (*squares*) has yielded an R_P value of $1.37 \text{ M}\Omega$, which corresponds to $\sim 38 \text{ M}\Omega/\text{pore}$. After photoresist deposition (*circles*), the capacitance of the chip has fallen by a factor of 39 to an acceptable value of $\sim 50 \text{ pF}$, as reflected by a significant shift of the $|Z|$ vs. frequency trace upwards. Since the pores were blocked by the organic film, R_P approaching infinity has been measured and the trace has been dominated by C_W over most of the frequency range. In the final step, the pores

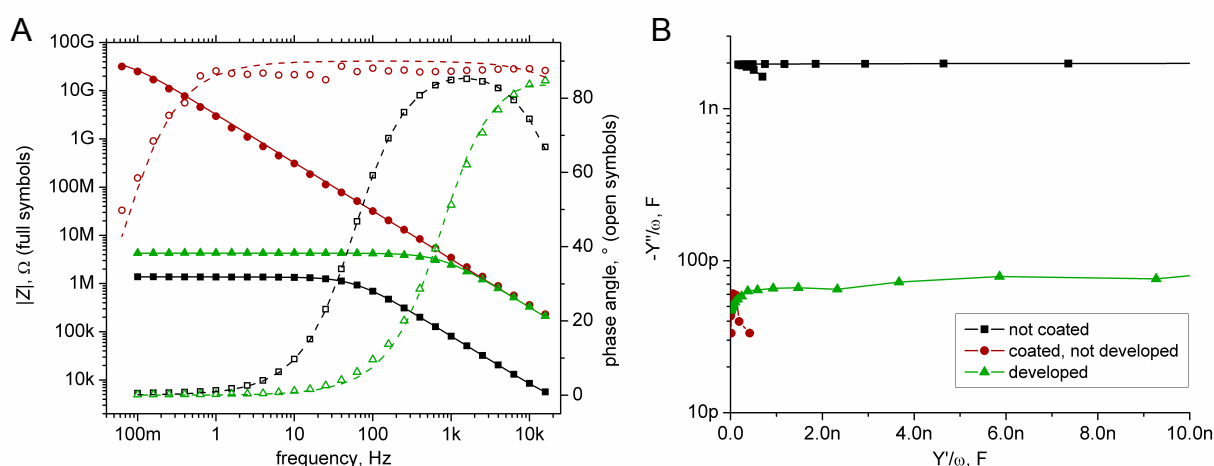


Figure 4-31. Impedance spectra illustrating TEM window capacitance reduction and pore release. A – Bode plot, B – $-Y''/\omega$ vs. Y'/ω . Experimental data in A are represented by scattered symbols (*full* – $|Z|$, *open* – phase angle), lines are the best-fit traces modeled using an equivalent $R_S(R_P C_W)$ circuit (*solid* – $|Z|$, *dashed* – phase angle). B displays the experimental data only. The shift along the y-axis is illustrative of the significant change of window capacitance upon photoresist deposition. The legend in B applies to A, too.

Table 4-2. Capacitance and resistance of a Si_3N_4 window with 4 arrays of $7 \times 50 \text{ nm}$ pores before, in the course of, and after photoresist coating and development.

	C_W , F	R_P , Ω
not coated	1.96×10^{-9}	1.37×10^6
coated	49.4×10^{-12}	47.2×10^9
developed	49.5×10^{-12}	4.25×10^6

have been released via dissolution of the organic material from the illuminated region. The new $|Z|$ trace (*triangles*) overlays the previous one in the high-frequency range, indicating a similar value of C_W . On the contrary, the trace exhibits purely resistive behavior below ~ 500 Hz, and levels-off at $R_P \sim 4.3$ M Ω . Since only one of the four 7-pore arrays was released, the value complies well with the expected resistance. After passivation, the chip exhibits a C_W of ~ 50 pF and an array of unobstructed pores, which meets the requirements for current measurements through transmembrane pores with single channel resolution. An additional noteworthy implication of our approach to minimization of Si₃N₄ window capacitance is that pores in a particular section of the Si₃N₄ diaphragm can be selectively released while pores in other sections remain blocked by the passivation layer. The layer may be completely dissolved without apparent distortion to the character of the pores and the Si₃N₄ window itself. Multiple equivalent arrays of pores can thus be milled through a single diaphragm and the best-looking array in terms of roughness or pore character can be chosen for spanning of npsLBs. Alternatively, several arrays of varying parameters can be milled and studied sequentially by repeated passivation and selective local development.

4.4.8. Conclusion

Plain Si₃N₄ windows based on Si frames showed dielectric properties incompatible with DC voltage clamp single-channel measurements. A passivating organic layer, a positive cross-linkable image-reversal photoresist, was thus deposited over the windows so as to reduce the stray capacitance. Release of pre-fabricated pores was possible by selective exposure to light and development of the resist in the pore-bearing regions. The resist allowed for chip passivation in a single deposition step and showed fair chemical robustness after thermal polymerization. Given the requirements on the passivating film, spraying turned out to be the best deposition strategy. Reduction of effective window capacitance from ~ 2 nF to below 50 pF was achieved this way.

4.5. Nanopore-spanning bilayer lipid membranes

Sedimentation of GUVs due to a density difference between the inside and the outside of the vesicles was exploited to form npsLBs over horizontally-mounted porous Si_3N_4 diaphragms. In the initial phases of the project GUVs were allowed to sink to the diaphragms in a random fashion. Although some reduction of pore conductance (indicative of blocking of pore mouths by lipid structures) could be achieved, giga-seals were rare. It has soon been realized that a giga-seal forms almost exclusively under the condition that the GUV adheres to the diaphragm at the pore-bearing location prior to rupture. The alternative notion of npsLB spanning, namely that of an advancing front of an SLB patch, turned out not to be functional. If one of the first GUVs did not unfold right over the pores, the surface of the diaphragm around the pores soon became ‘contaminated’ with a lipid bilayer due to other SLB patches expanding in the vicinity. Proper unfolding of GUVs over pre-formed SLBs did not occur under our experimental conditions. Further addition of vesicles resulted in SLBs of near-to-full surface coverage, yet sealing bilayers were never formed. In fact, over-saturated SLBs* often induced bizarre bilayer ‘creeping’ onto the other side of the diaphragm via the pore walls. These observations called for a way to guide the sedimenting GUVs to the pore-bearing spot of a diaphragm. A technique was devised of maneuvering GUVs by lateral movements of the tip of a patch-clamp pipette, which was directed under a microscope objective by a micromanipulator. Excellent success rates of spanning giga-seal npsLBs were achieved. The evolution of electrical properties of the assembly upon GUV adsorption, spreading, rupture, and unfolding over the pores determined by AC impedance spectroscopy is presented below.

4.5.1. npsLB formation sequence

An example of the maneuvering of a GUV to an array of pores is visualized in Figure 4-32. A large single GUV is clearly visible in the first image of the sequence. It is apparent in the following image that the GUV had descended *near to*, but not *over* the array (see figure caption). In the course of ~ 28 s after the capture of image A the GUV was pushed to and centered over the pore array by a micromanipulator. Between $t = 28.44$ and $t = 28.80$ the vesicle adhered, spread, and ruptured on the diaphragm. Spreading and flattening brought the contours of the vesicle into the microscope’s plane of focus (images F-H). The area covered by the vesicle in images G and H is virtually the same. This indicates that spreading of the GUV ceased by $t = 28.8$. The diminished intensity of the contours of the vesicle in image H compared to image G suggests the vesicle

* SLBs of near-to-full surface coverage with a few GUVs adsorbed on top of and fused to the SLB via stalks so that diffusional continuity existed between the vesicles and the SLB. The excess bilayer area constituted by the lamellae of such vesicles provided a driving force for the lateral expansion of the SLB onto uncovered areas of the support.

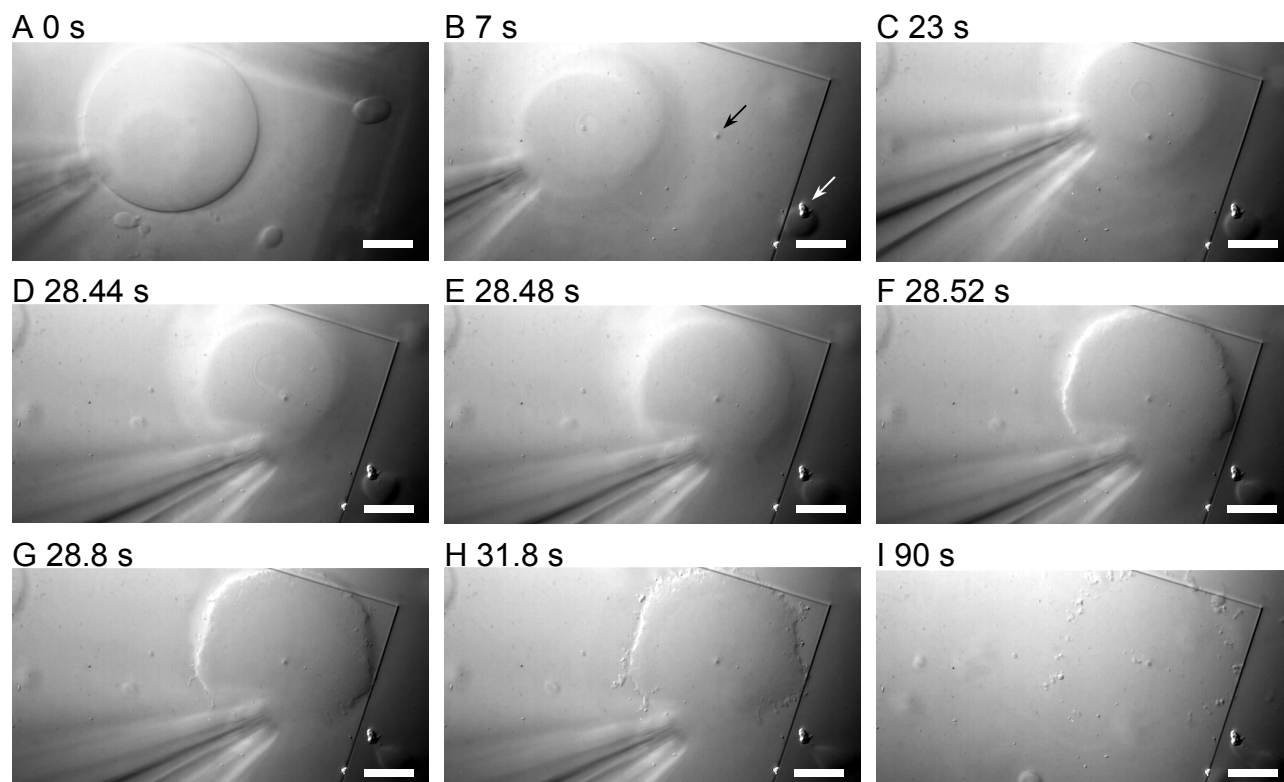


Figure 4-32 A sequence of DIC optical micrographs showing the formation of npsLBs from a GUV under opto-mechanical control. In the first image of the sequence the focal plane has been raised to above the surface to image the contours of the GUV sharply, while in the other images it is the surface of the Si_3N_4 diaphragm that is in focus. The corner of the diaphragm is well visible. Additionally, DIC helps to resolve the pore array (*black arrow* in image B) as well as some undefined microscopic debris (*white arrow* in image B). The manipulator tip appears blurred since it is located $\sim 10\ \mu\text{m}$ above the focal plane. The GUV appears blurred in images B-E for the same reason. Sharp vesicle contours can be seen in images F-H whereby the GUV adheres, spreads, and ruptures on the surface. The images are denoted by the time that elapsed since the capture of the 1st image. The scalebars are $20\ \mu\text{m}$ long.

flattened as the three seconds lapsed. Moreover, microscopic structures scattered beyond the contour of the vesicle are apparent in image H but not in image G. Obviously, rupture of the GUV had occurred and a planar lipid patch started spreading around the vesicle. No contours that would imply the existence of an adsorbed vesicular structure could be seen 60 s after the rupture (image I). Some microscopic structures line the former location of the GUV contour roughly. Based on our earlier observations of fluorescently labeled GUVs on Si_3N_4 surfaces, the GUV is presumed to have transitioned from a vesicular into a planar bilayer state.

4.5.2. Impedance changes upon npsLB formation

GUV adhesion to the surface of a Si_3N_4 membrane over a pore was detected as a fall of admittance of the Si_3N_4 TEM window to below 1 nS, as monitored in the continuous AC current vs. time mode at 0.2 Hz. Figure 4-33A displays a conductance trace with respect to time of an npsLB forming over a single 300-nm-wide pore in 100 mM TMAcI base electrolyte. The trace starts just below 250 nS, i.e. at a conductance level that complies well with what is expected for the particular pore parameters and electrolyte composition. After injection of $1\ \mu\text{l}$ of a GUV suspension, real

admittance exhibits a fall to ~ 140 nS followed by a logarithmic-like climb. The drop is attributed to the dense sucrose suspension sinking to the bottom of the compartment and locally changing the electrolyte composition. The subsequent climb is an effect of a slow diffusion-driven restoration of the original ion concentration at the Si_3N_4 -liquid interface. During this period a GUV has been maneuvered to above the pore by the micromanipulator tip. Its adhesion and rupture at $t = 150$ s is accompanied by a fall of pore conductance to below 1 nS (inset of Figure 4-33A). Bode plots of impedance spectra of the Si_3N_4 window with an open and npsLB-covered pore acquired before and after the Y' vs. time trace (Figure 4-33A), respectively, are shown in Figure 4-33B. Before GUV adhesion, the pore resistance of 4.9 M Ω clearly dominates the part of the spectrum at $f < 2$ Hz, with the phase angle converging all the way to 0° at $f = 100$ mHz. After npsLB formation over the pore, the resistance shoots up by 3 orders of magnitude to 7.6 G Ω , as clearly revealed by the capacitive dominance over the same part of the spectrum. The onset of resistive convergence of $|Z|$ barely becomes apparent before the lowest frequencies are reached.

As indicated by the existence of a double shoulder in the phase plot, two time constants had to be provided in the equivalent circuit to adequately model the experimental spectra. All impedance spectra, except those acquired for photoresist-coated Si_3N_4 windows, were interpreted in terms of the circuit depicted in Figure 4-33C. R_p and R_s correspond to the resistance of the pore, or array of

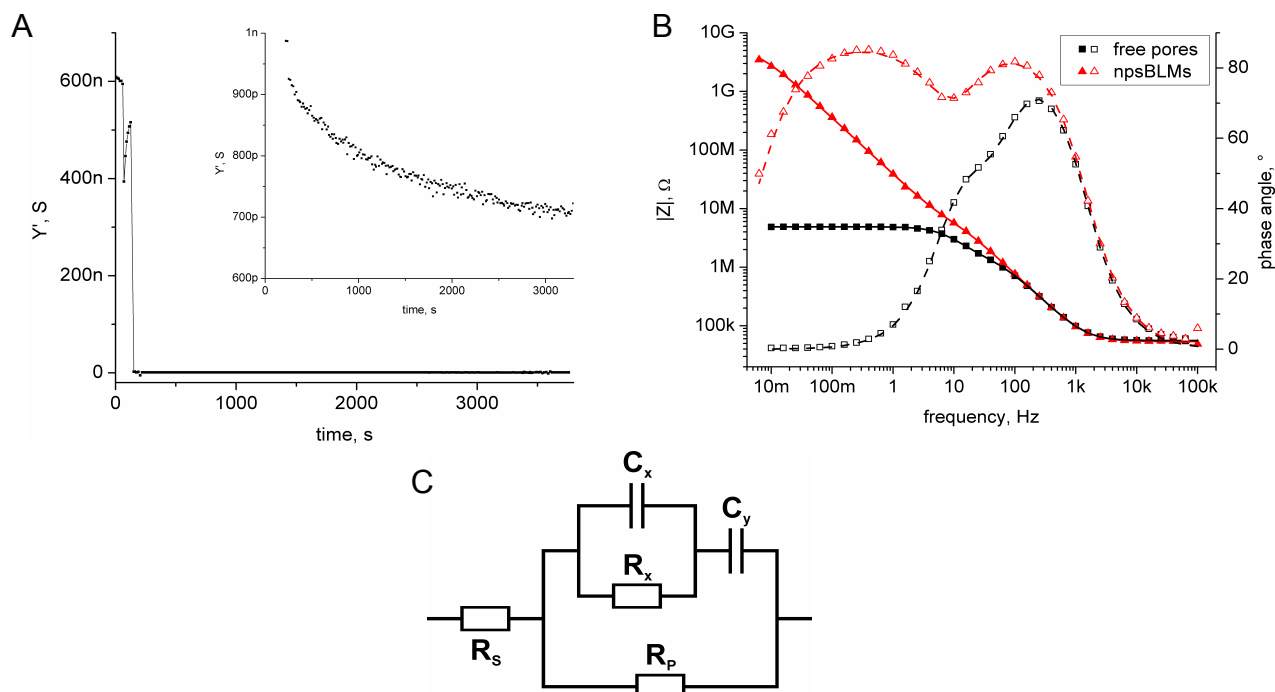


Figure 4-33 Formation of npsLBs monitored by impedance spectroscopy. A - real component of admittance vs. time trace derived from a continuous AC current recording (10 mV rms, 200 mHz). GUVs were injected 70 s and the npsLBs formed 125 s after the start of the recording, respectively. The inset displays the same trace at a finer scale. B - Bode plot of impedance spectra taken before and after npsLB formation. Scattered points represent experimental data ($|Z|$ - solid symbols, phase - open symbols), lines are the best-fit traces modeled using an equivalent circuit drawn in C.

pores, and the combined resistance of electrolyte and electrodes, respectively. After a lipid bilayer has been spanned over the pores, R_p reflects the resistance of the npsLBs. R_x , R_y , and C_x are circuit components without a straight-forward physical meaning. They account for the contribution to the impedance of the native silicon oxide and the space-charge region at the pit walls, as well as the layers of silicon nitride on both sides of the TEM window. The circuit used for routine modeling (Figure 4-33C) is a simplification of a fully-detailed circuit that takes every section of the TEM window into account individually.

Formation of npsLBs by directed fusion of GUVs was highly reproducible. With some manipulation practice, a success rate near to 100% has been attained. Overall, total seal resistances of hundreds of M Ω up to several tens of G Ω were obtained for npsLBs formed over single as well as multiple nanopores. These values are comparable to those reported earlier for single npsLBs formed by rupture of GUVs carrying a negative charge on their envelopes over pores in positively-charged SiO₂/Si₃N₄ diaphragms.⁴⁴ No apparent dependence of npsLB resistance on pore size or SLB patch size (estimated from the size of the GUV giving rise to the SLB patch) has been observed in this study. A similar variation of seal resistance has been found for BLMs spanned over single nanopores in glass.¹⁰³ Intriguingly, this variation of npsLB resistance was observed not only among samples, but also with respect to repeated tries using the same TEM window. In general, npsLBs formed over Si₃N₄ surfaces that were rinsed briefly with water and ethanol without cell disassembly showed lower seal resistances as opposed to npsLBs formed over surfaces treated with a fresh piranha solution. The npsLBs were able to withstand continuous bilateral perfusion. This provided a convenient pathway to change the composition of the bathing electrolyte or to insert pore-forming peptides. The need for stirring as well as errors and lags arising from uneven distribution of substances in the electrolyte compartment upon injection were thus avoided.

4.5.3. Electrochemistry of TEM Si₃N₄ Windows

4.5.3.1. Simple modeling approach

Figure 4-34A displays typical impedance spectra of a porous TEM window mounted as a partition between two electrolyte compartments. The two spectra were acquired successively with a 15-minute delay without alteration of the experimental conditions. Interestingly, an evident difference exists between the spectra in the 5-500 Hz frequency range, which suggests the electrical properties of the window changed in the course of the measurement.

In the first approximation, an electrical system consisting of two electrolyte chambers with Ag/AgCl electrodes separated from each other by a dielectric partition can be modeled by a resistor, R_s , combining the resistance of the electrolyte for the particular setup geometry and the faradaic

resistance of electrodes, in series with a capacitor, C_{part} , representing the capacitance of the partition (Figure 4-34B).^{*} Fabrication of one or more pores through the partition introduces a pathway for the electrolyte ions to traverse between the two electrolyte compartments that can effectively be represented by an element of finite resistance, R_p , in parallel to the partition capacitance^{21, 32}.

Best-fit curves to the experimental data based on an equivalent circuit described above are also shown in Figure 4-34A. The calculated curves overlay the experimental data poorly, indicating the model does not describe our system in a satisfactory manner. In addition, there is only a negligible difference between the two theoretical curves, contrary to the obvious difference between the experimental traces. Apparently, the model fails to detect the changes that occurred in the system in the course of the measurement. Since ‘spontaneous’ changes of impedance spectra shape were observed commonly during prolonged experiments, however, an appropriate modeling scheme was desired that would account for such changes. The appearance of two shoulders in the peak of the phase plot of the experimental data suggests that an additional time constant needs to be introduced in the model circuit. In addition, an estimate of capacitance of the Si frame, if treated as a dielectric, points to 1-2 pF, whereas C_{part} extracted from the fits is 3 orders of magnitude higher. These facts imply that the presented simple modeling scheme is not applicable to a Si_3N_4 window in the ‘partition’ configuration, and an alternative model should be sought.

4.5.3.2. Elaborate modeling approach

In the above analysis, a partition made of a dielectric material has been considered. This assumption is hardly valid for a Si_3N_4 window of the configuration used in this study, however. The Si_3N_4 film that coats the frame of the window and spans the central gap as a free-standing diaphragm indeed is an insulator. The material of the frame, on the other hand, is ordinarily available silicon. Due to the requirements of the semiconductor industry, silicon is typically doped to resistivities in the order of 0.001 – 100 Ωcm . Even if not doped deliberately, thermal treatment of Si wafers (as, for example, during chemical-vapor deposition of Si_3N_4) is known to introduce impurities in the silicon crystal matrix that increase its conductivity. The supplier of our TEM windows specified a maximum resistivity value of 30 Ωcm for the supporting Si wafers. In other words, even at the maximum specified Si resistivity, the window frames are very conductive. Obviously, the contribution arising from the semiconductor character of the silicon frame must be taken into account in the modeling.

^{*} Due to surface inhomogeneity and time constant distribution phenomena it is oftentimes unavoidable to use a constant phase capacitive element (CPE_{part}) instead of C_{part} to model the capacitance of the partition.(ref) electrochem book

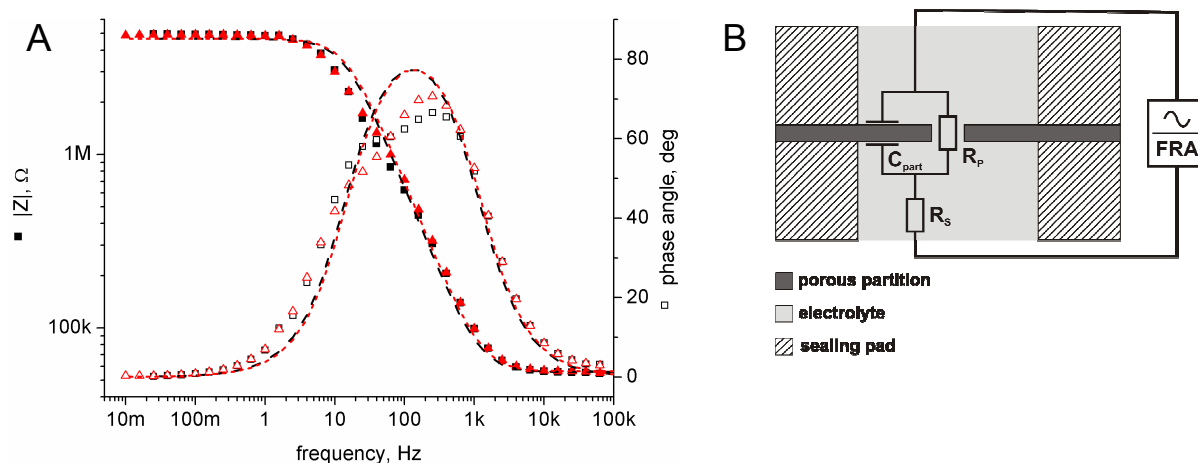


Figure 4-34. A - Bode plot of impedance spectra acquired for a TEM window with a single 100 nm wide pore in 100 mM TMAH, 5 mM HEPES, pH 7. Experimental data (*scattered points*) are overlaid with best-fit curves (*lines*) calculated using an equivalent circuit displayed in (b). The 2nd spectrum ($\blacktriangle, \triangle$) was measured immediately after the 1st one (\blacksquare, \square). Time delay between the respective points of the two spectra is ~15 minutes.

A. 'Partition' configuration

Figure 4-35A shows a schematic of a pore-bearing TEM Si_3N_4 window based on a *conductive Si frame* that is used as a partition between two electrolyte compartments. The electrical circuit representation of the different subsections of the window, electrolyte and electrodes is superimposed over the schematic. R_{Sflat} and R_{Spit} represent the ohmic resistance of the electrolyte and the Ag/AgCl electrode on each side of the window. R_p is the pore resistance introduced previously. C_{fsSiN} is the capacitance of the thin free-standing Si_3N_4 diaphragm. The heterogeneous frame of the window is further subdivided into the following homogeneous subsections and interfaces: the Si_3N_4 film covering both sides of the frame, represented in capacitive terms by C_{SiNflat} and C_{SiNpit} , and in hypothetical conductive terms by R_{SiNflat} and R_{SiNpit} , respectively; the silicon bulk, the resistance of which is accounted for by R_{Si} ; and the pit walls, represented in Figure 4-35A by the rhomboid region. Figure 4-35B depicts the scheme of the pit wall sub-circuit, a double RC loop - ($R_{\text{SiOx}}C_{\text{SiOx}}$) and ($R_{\text{sc}}C_{\text{sc}}$) - in full detail. The circuit depicted in Figure 4-35 exhibits a substantially higher complexity relative to the one considered initially, and direct NLLS modeling of such a number of unknown parameters might yield results lacking any physical meaning. Note, however, that at this point the scheme is theoretical, and some of the phenomena accounted for (elements of dotted contours: R_{SiNpit} , R_{SiNflat} , R_{SiOx} , R_{sc} , and C_{sc}) might not be applicable to our particular case. In the following, a simpler scheme will be derived by eliminating some elements whose effective contribution is negligible, combining some of the other ones, and estimating/calculating several of the parameter values. It should be noted that linearity of the

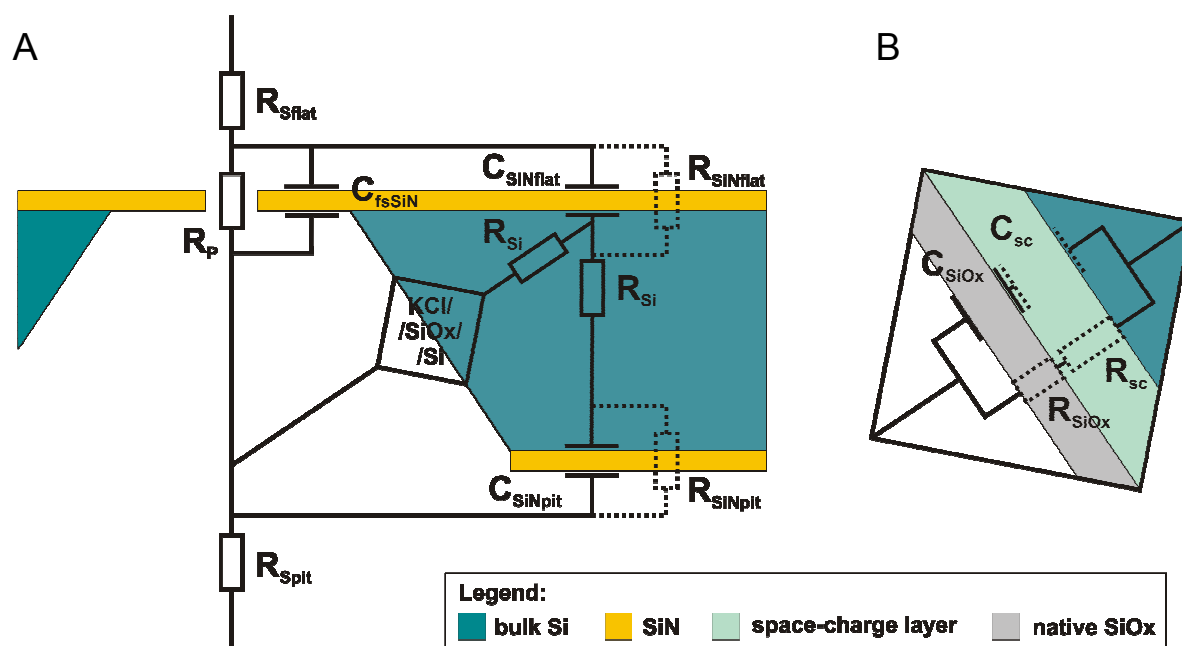


Figure 4-35. Cross-section schematic of a pore-bearing TEM Si_3N_4 window. The window is divided into electrically homogeneous subsections. A circuit scheme comprising resistive and capacitive elements that correspond to the respective subsections is overlaid over the schematic. The electrolyte/native-SiOx/Si interface at the pit walls is represented by a rhombus in (a) and illustrated in full detail in (b). Circuit elements the relevance of which is questioned (see text) are outlined in a dotted line style.

system is assumed due to the low amplitude of AC perturbations used throughout the impedance spectroscopy measurements.

R_{Sflat} and R_{Spit} add up to form the combined electrode/electrolyte resistance, R_{S} , as described above (Figure 4-34B). The values of R_{S} fall typically in the range of 10^3 - $10^5 \Omega$ depending on electrolyte resistivity and chamber geometry. If not covered up by a very low series capacitance, R_{S} dominates the highest frequency region of an impedance spectrum.

Similarly to R_{S} , the value of R_{P} , the pore resistance, is given by pore geometry and number, as well as the specific electrolyte resistivity (Chapter 4.3.9). For the requirements of this section it is sufficient to note that R_{P} dominates the low frequency region of an impedance spectrum. In the scope of this study it ranges from about 1 to 40 M Ω .

The capacitance of the square-shaped free-standing Si_3N_4 membrane bearing the pore, C_{fsSiN} , can be estimated directly via the $C = \epsilon_0 \epsilon_r A / d$ plane capacitor relationship, where ϵ_0 is the permittivity of free space, ϵ_r is the relative dielectric permittivity of the material, and A and d are the area of and the distance between the capacitor planes, respectively. Taking $\epsilon_r \approx 7$ and $d \approx 100 \text{ nm}$, the specific capacitance of the Si_3N_4 diaphragm is 62 nF/cm^2 . With an area of $A \approx (330 \mu\text{m})^2$, the estimate of C_{fsSiN} points to about 70 pF.

R_{Si} , the resistance of the silicon frame bulk, can be estimated via the $R = \rho l/A$ relationship, where ρ is the specific resistivity of the material, and l and A are the length and the area of the volume considered. The contact area of the electrolyte and the TEM window was defined by 3 mm wide circular cut-outs in a PDMS sealing sheet. Assuming the circular regions wetted by electrolyte are centered and overlapping each other perfectly, we consider a cylindrical shape for the resistive geometry. We neglect here the fact that a tetrahedral segment had been etched out of the Si frame for it does not introduce a significant error in R_{Si} estimation. Thus, substituting ρ by the maximum wafer resistivity value specified by the manufacturer, 30 Ωcm , l by 525 μm , and A by $\sim 7 \text{ mm}^2$, we obtain an R_{Si} estimate of $\sim 20 \Omega$. For this reason, R_{Si} will be neglected in the further considerations and infinite conductance of the Si frame will be assumed.

C_{SiNpit} and C_{SiNflat} represent the capacitance of the interface between the bulk silicon of the frame and the electrolyte, separated by a thin layer of insulator, Si_3N_4 , on the pit and the flat side of the Si_3N_4 window. We employ again the simple plane capacitor model used for the estimation of C_{fsSiN} . Whether free-standing or supported, the specific capacitance of the Si_3N_4 film is the same. Again, the contact area of the electrolyte on the flat side is $\sim 7 \text{ mm}^2$, thus C_{SiNflat} should be about 4.3 nF. On the pit side the area is reduced by the missing base of the etched tetrahedron and C_{SiNpit} evaluates to about 3.6 nF.

The surface of silicon nitride films is known to undergo a relatively slow conversion to a hydrated SiO_2 layer or an oxynitride during contact with an aqueous solution.¹⁰⁹ It has been hypothesized that further chemical modification of the insulator can proceed due to dispersive transport of reactive species across the previously formed oxygen-rich surface layer. A requirement might thus exist to model possible charge transfer at the Si_3N_4 /electrolyte interface on either side by R_{SiNpit} and R_{SiNflat} , respectively.

Perhaps the most interesting components of the electrical scheme of a Si_3N_4 window are those associated with the pit walls (Figure 4-35B). It is known that a thin layer of ‘native’ oxide grows on a bare silicon surface in ambient atmosphere or water.^{108,110} Since exposure of the Si_3N_4 diaphragm by etching a tetrahedral pit through the silicon bulk was the last step in the window manufacture process, we presume the walls of the pit are covered by a thin native oxide layer. A typical thickness of native oxide on silicon is 1–2 nm. SiO_x is known for its insulating properties that are explored extensively by the semiconductor industry. The oxide layer is thus expected to show distinct capacitive properties, described by C_{SiOx} . On the other hand, tunneling currents through an oxide layer are common at low oxide thickness between a metal film and a bulk semiconductor.¹¹¹ As native SiO_x comprises a few atomic layers only, charge transfer between electrolyte and bulk

silicon cannot be ruled out *a priori*. Possible charge transfer currents through native SiO_x are accounted for by R_{SiO_x} of a finite value.

A famous interfacial phenomenon of semiconductors is the existence of the so-called ‘space-charge layer’. Briefly, the space charge layer is a region at an interface where the density of mobile charge carriers can oscillate. At mobile charge carrier density equal to that of the semiconductor bulk the space-charge layer is in an ‘accumulation’ regime, at a reduced mobile charge carrier density a ‘depletion’ regime develops. The transition between accumulation and depletion is potential-dependent. At depletion, the space-charge layer can be associated with a distinctly low capacitance, C_{sc} , given roughly by its thickness (10^{-8} - 10^{-7} m) and the dielectric constant of the semiconductor. Similarly, the limited conductance of the region due to reduced mobile charge carrier density is described by R_{sc} , which at full depletion becomes several orders of magnitude higher than at accumulation.

In total, three hypothetical sources for the occurrence of an additional time constant in the Si_3N_4 window impedance spectra have been identified above: i) conductance associated with dispersive transport of reactive species at the electrolyte/ Si_3N_4 interface (R_{SiNpit} and R_{SiNflat}), ii) charge transfer between electrolyte and bulk silicon through the native oxide layer (R_{SiO_x}), and iii) elevated resistance of the space-charge layer (R_{sc}) upon depletion. Unfortunately, impedance spectroscopy of the TEM window mounted as a partition between two electrolyte compartments does not reveal the magnitude of contribution of the respective elements. Therefore, a TEM Si_3N_4 window was used as a working electrode in a classical three-electrode electrochemical setup in order to gain a better understanding of the impedance phenomena. The electrochemical measurements so performed allowed us to separate the impedance behavior of the two sides. In the following, the respective single-side mounts are referred to as the ‘flat’ and the ‘pit’ configuration (Figure 4-36).

B. EIS in the ‘flat’ configuration

In the ‘flat’ configuration (Figure 4-36A), the flat side of the TEM window was used as a working electrode. The surface of the flat side is entirely constituted by a continuous Si_3N_4 film, therefore a completely capacitive behavior was expected. Figure 4-38A shows an example of an impedance spectrum taken in the flat configuration at $E = 0$ mV. The spectrum exhibits the characteristics of a pure capacitor in series with a resistor. The capacitance can be attributed to the insulating Si_3N_4 film, whereas the resistance is the ever-present R_{S} . A remarkable uniformity was observed among spectra acquired at holding potentials between -500 and 500 mV. The spectra were interpreted in terms of a simple R_{S} -in-series-to- C_{SiNflat} model circuit. Figure 4-38B depicts the results obtained for C_{SiNflat} with respect to holding potential. The capacitance of the Si/ Si_3N_4 /electrolyte interface

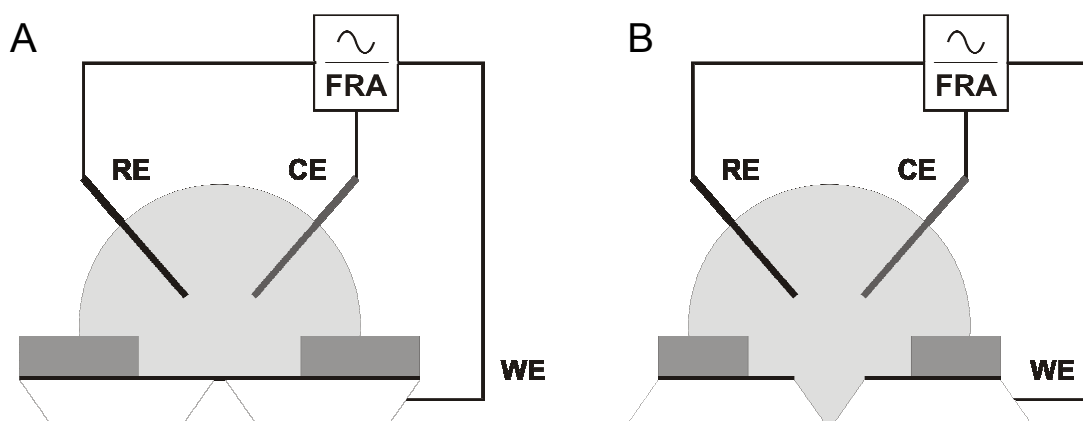


Figure 4-36. Schematic of the setup used for electrochemical impedance spectroscopy measurements with a TEM Si_3N_4 window as a working electrode: ‘flat’ (a) and ‘pit’ (b) configuration. An Ag/AgCl wire and a Pt wire were used as a reference and an auxiliary electrode, respectively. Access to the window/electrolyte interface was attained via fastening an alligator clamp from the sides against the silicon window frame. The wetted area between a drop of electrolyte and the window surface was defined by a circular cut-out in a PDMS sealing sheet.

remains almost constant over the entire range of holding potentials investigated. The mean value, 2.20 nF, yields after correction for the Si_3N_4 diaphragm area, which is not in electrical contact with the silicon bulk, a specific capacitance for a 100 nm thick Si_3N_4 film, $C_{\text{Si}(\text{SiN})}$, of 73.0 nF/cm². This result is 18% higher compared to the theoretical value derived above, possibly due to a different relative permittivity constant of the Si_3N_4 film and a minor discrepancy between the nominal and the actual film thickness. A further analysis of the discrepancy is not needed for the purpose of this study, however, and the value obtained experimentally will be used from this point on. In addition to the real value of $C_{\text{Si}(\text{SiN})}$, the measurements in the ‘flat’ configuration revealed no currents that could be associated with a chemical reaction at the Si_3N_4 /electrolyte interface, as reported by Kataoka-Hamai et al.¹¹² and Jamasb et al.¹⁰⁹. R_{SiNflat} and R_{SiNpit} can be considered infinite and thus left out of the electrical scheme considerations.

C. EIS in the ‘pit’ configuration

As apparent from Figure 4-35A, the electrical scheme of the portion of the TEM window accessed if the ‘pit’ side is used as a working electrode (Figure 4-36B) is significantly more complex than that resolved in the ‘flat’ configuration. The value of C_{SiNpit} can be calculated at least, based on $C_{\text{Si}(\text{SiN})}$ and the dimensions of the pit base (1.05 mm). For a 2-mm-wide circular wetting area, as defined by the cut-out in the PDMS sheet, C_{SiNpit} becomes 1.47 nF. The hypothetical equivalent circuit of the ‘pit’ configuration then adopts the form illustrated in Figure 4-37. Reliable identification of the five missing parameters of the scheme is feasible via NLLS fitting, as long as the spectra span a sufficiently broad range of frequencies and the two time constants of the circuit differ significantly.

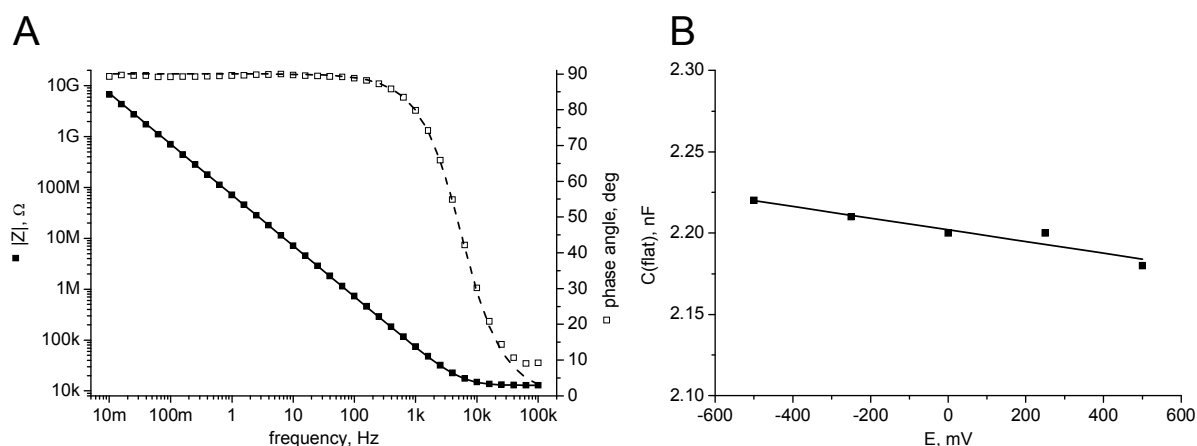


Figure 4-38. A - Bode plot of an impedance spectrum acquired in the ‘flat’ configuration at $E = 0$ mV vs. Ag/AgCl. A purely capacitive behavior is noteworthy. B - capacitance of the flat side of a TEM Si_3N_4 window plotted against holding potential. The capacitance was derived based on fitting the parameters of an R in series to C circuit to the experimental data. All spectra were acquired in 100 mM KCl, 5 mM HEPES, pH 7.

Impedance of the Si/native- SiO_x /electrolyte interface at varying bias potentials was studied previously. A minor C_{sc} change with and a pronounced dependence of R_{SiO_x} on substrate potential has been observed for highly-doped silicon (ionized donor concentration $> 10^{18} \text{ cm}^{-3}$).^{85, 86} At moderate dopant densities, development of the depletion region was manifested clearly by C_{sc} falling as low as 40-80 nF/cm² and R_{sc} reaching the 10^5 - $10^6 \Omega\text{cm}^2$ regime.¹¹³⁻¹¹⁵

Figure 4-39 displays a set of impedance spectra acquired in the ‘pit’ configuration at varying working potentials. The spectrum measured at -500 mV is one of a simple RC loop in series with R_s . The absence of the second RC loop suggests the space charge region is in the accumulated state. At -250 mV and above, the conductive inflection of $|Z|$ at low frequencies becomes almost absent, presumably due to reduction of charge transfer through the native oxide layer. Moreover, an additional time constant emerges at the higher boundary of the frequency range. The appearance of this second time constant signalizes the onset of depletion of the space-charge region. The trough in the phase plot associated with the second RC loop shifts towards lower frequencies as the holding potential rises to 0 mV, which is indicative of a growing resistance due to continuing depletion.

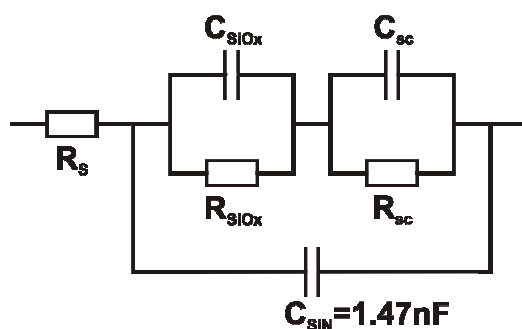


Figure 4-37. ‘Pit’ configuration equivalent circuit. R_s represents the series of solution, electrode and contact resistances. C_{SiO_x} , R_{SiO_x} , C_{sc} and R_{sc} correspond to capacitance and resistance of the electrolyte/ SiO_x /Si interface and the space-charge layer, respectively. C_{SiN} is the capacitance of the electrolyte/ Si_3N_4 /Si interface.

The spectrum characteristics do not change significantly as the bias potential is raised stepwise up to 500 mV. A distinct potential-dependent contribution of both RC loops associated with the electrolyte/native SiO_x /bulk Si interface to the impedance spectra could be observed. The fact that the depletion region develops with growing bias potential indicates that the window frame is based on n -type silicon and the dopant density is moderate.

Circuit parameters obtained from modeling a series of impedance spectra of the ‘pit’ side using the equivalent circuit of Figure 4-37 are depicted against bias potential in Figure 4-40 (R_s not shown). The plot of R_{SiO_x} (Figure 4-40A, *black full squares*) exhibits a broad maximum at about -100 mV. The values exceed $120 \text{ k}\Omega\text{cm}^2$ in the range from about -200 to 100 mV. This translates to an actual measured value of $\sim 10 \text{ G}\Omega$. Because C_{SiO_x} is relatively large, too, the onset of ohmic dominance in the impedance behavior is shifted to very low frequencies. Since AC periods at low frequencies become increasingly long, a precise determination of R_{SiO_x} would only be possible at the expense of very long measurement times. Values of R_{SiO_x} above $100 \text{ k}\Omega\text{cm}^2$ are thus burdened by a considerable error. The key point is, however, that in the given interval of potentials R_{SiO_x} is large enough not to interfere with R_p or R_{npSLB} . At both boundaries of the potential range R_{SiO_x} drops by several orders of magnitude. In a preceding study the phenomenon has been attributed to electron tunneling, ohmic and ionic conduction through the oxide layer.¹¹⁵

Native C_{SiO_x} (Figure 4-40A, *red empty squares*) follows an interesting curve with a major minimum at about -150 mV, a minor minimum between 300 and 400 mV, and a local maximum at +150 mV. An analogous C_{SiO_x} vs. E curve, although flipped along the y-axis since it was obtained on p -type silicon, was presented previously.¹¹⁴ Thickness of $\sim 1.5 \text{ nm}$ for the native oxide layer was calculated

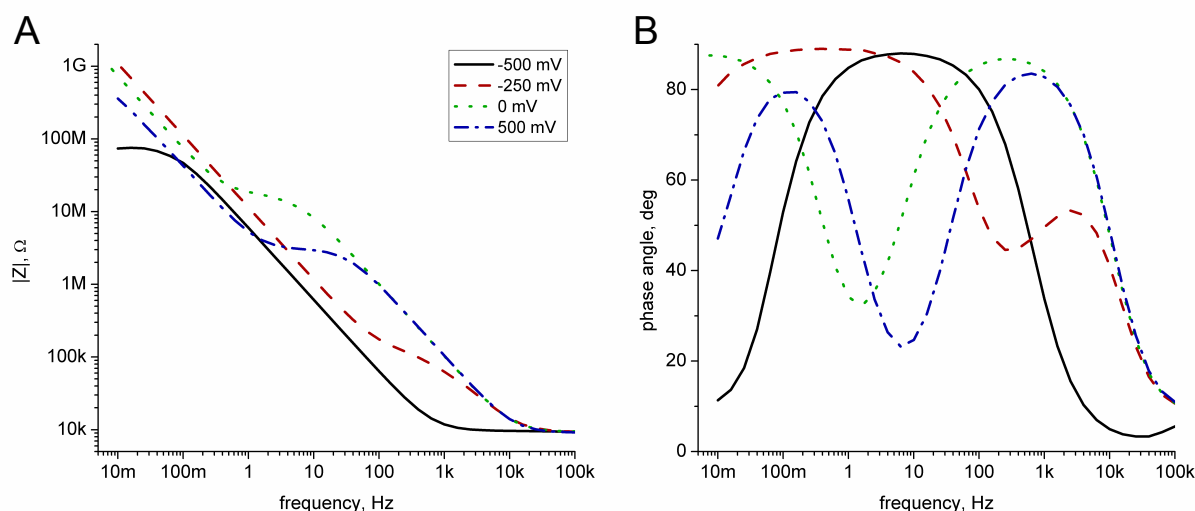


Figure 4-39. Bode plots of impedance spectra ((a) – $|Z|$, (b) – phase angle) of a Si_3N_4 window acquired in the ‘pit’ configuration at varying bias potential. Measurements were performed in 100 mM KCl, 5 mM HEPES, pH 7.

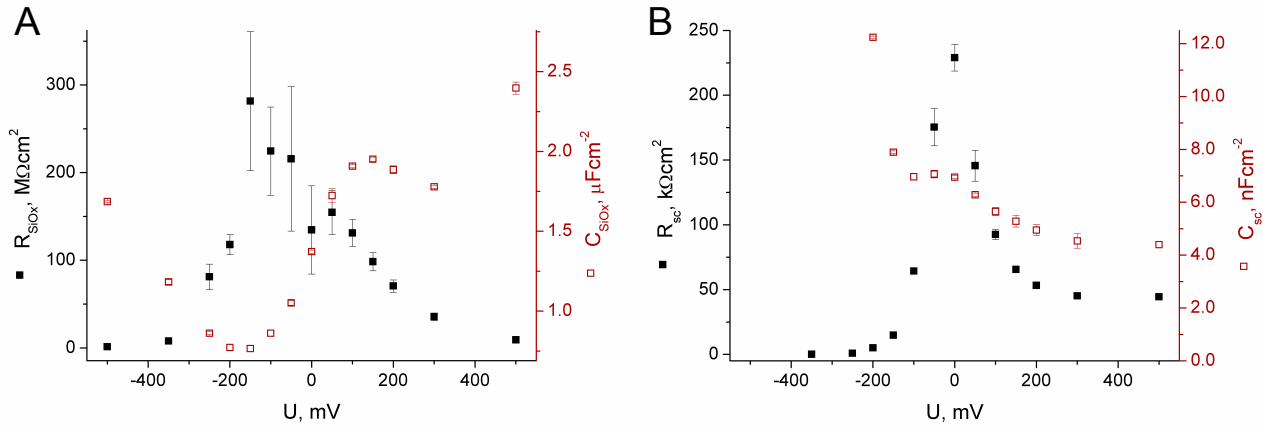


Figure 4-40. Normalized equivalent circuit parameters associated with the pit walls plotted with respect to bias potential: A – ($R_{SiOx}C_{SiOx}$), B – ($R_{sc}C_{sc}$). The parameters were obtained by modeling EIS spectra acquired for the ‘pit’ side of a TEM Si_3N_4 window in 100 mM KCl, 5 mM HEPES, pH 7.

using the parallel-plate capacitor approach with $\epsilon_r(SiOx) = 4.5$, which is in good agreement with the values reported elsewhere.¹¹⁵⁻¹¹⁷

Similar to R_{SiOx} , R_{sc} shows a maximum at just below 0 mV (Figure 4-40B, *black full squares*). Here the peak is slimmer, however, and the values of R_{sc} converge to $\sim 3 M\Omega$ at higher positive potentials. The absence of R_{sc} at negative bias potentials is associated with the accumulation state of the space charge layer. A substantial rise of R_{sc} upon depletion has been documented in the preceding works, too.¹¹³⁻¹¹⁵ Unfortunately, none of the works investigated R_{sc} at potentials beyond the onset of depletion. The interesting convergent decrease of R_{sc} at higher potentials could possibly be attributed to a transition of the space charge layer to the inversion state.

C_{sc} follows a rise as E descends from 500 mV, passes a minor inflection at about -50 mV and grows steeply to infinity below -200 mV (Figure 4-40B, *red empty squares*). The same dependence of C_{sc} on bias potential for moderately-doped n -type silicon was reported by Lin et al.¹¹³ Analogous to R_{sc} , the exponential growth of C_{sc} at bias potentials below -150 mV is associated with the depleted-to-accumulated state transition. At 500 mV, i.e. at full depletion, C_{sc} converges to $\sim 4.5 nF/cm^2$. Minimum specific C_{sc} of ~ 30 and $40 nF/cm^2$ has been reported for depleted silicon/electrolyte interfaces at donor densities of $5.5 \times 10^{15} cm^{-3}$ and $1 \times 10^{17} cm^{-3}$, respectively^{113,115}. Since via the Mott-Schottky relation C_{sc} is proportional to the square root of doping density^{36, 40}, it can be deduced that the donor density in the frame of our Si_3N_4 windows is in the $10^{14} - 10^{15} cm^{-3}$ range.

D. TEM window OCP

EIS results plotted in Figure 4-40 demonstrate that the electrical parameters of the ‘pit’ sub-circuit are greatly dependent on bias potential of the window frame. Unlike in the ‘pit’ or ‘flat’ configuration, no direct electrical access to the silicon bulk exists in our setup if the Si_3N_4 window

is mounted as a partition between two electrolyte compartments. The bias potential of the window thus cannot be monitored or controlled. It can be expected, however, that in the ‘partition’ configuration the bias potential of the window with respect to the Ag/AgCl electrodes is defined by the open circuit potential (OCP). We therefore investigated the OCP behavior of either side of the window with respect to time (Figure 4-41). A continuous steep drift of potential was observed over time under zero current conditions in the ‘flat’ configuration. OCP measured for the ‘pit’ side showed distinctly convergent behavior, on the contrary. In most of the independent measurements OCP grew initially in a logarithmic fashion starting at values between -300 and 0 mV. In some cases the logarithmic rise changed to a slow linear increase after ~1000 s that continued at a constant rate until the end of the measurement. The final values that the OCP either converged to or reached after 3000 s are in the interval of -90 to +50 mV. It is notable that the OCP value obtained in repeated measurements on the same sample varied significantly.

Since in the ‘flat’ configuration a well-isolating Si_3N_4 film separates Si bulk from the electrolyte, little or no interaction between the two conductive media takes place. The drift observed during the OCP measurement is typical for a ‘disconnected’ working electrode. The contribution of the electrolyte/ Si_3N_4 /Si interface to the window OCP is thus supposed to be insignificant. Most OCP traces obtained for the ‘pit’ side are convergent in a consistent pattern. The temporal evolution is rather slow and the range of potentials attained after prolonged monitoring is ~150 mV broad. It is therefore assumed that in the ‘partition’ configuration the bias potential of the window is determined primarily by the OCP of the ‘pit’ side. The electrical characteristics of the pit walls

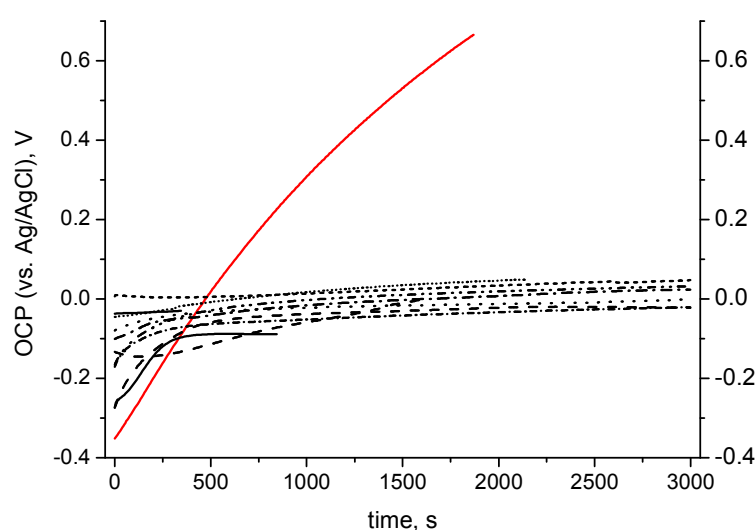


Figure 4-41. Open circuit potential of a Si_3N_4 window. Traces obtained in the ‘flat’ and ‘pit’ configuration are plotted in red and black, respectively. All measurements were performed using the same Si_3N_4 window in a 3-electrode setup (Ag/AgCl as reference, Pt as auxiliary) in 100 mM KCl, 5 mM HEPES, pH 7.

have been shown to vary significantly in the range of bias potentials the ‘pit’ side OCP evolves to, however (Figure 4-40). Apparently, impedance spectra acquired in the ‘partition’ configuration are affected by the linkage between the OCP of the window and the electrical properties of the pit wall. Based on the OCP measurements, we conclude that the variation of impedance characteristics observed experimentally in the ‘partition’ configuration can be attributed to the temporal drift of the window bias potential.

E. ‘Flat’ and ‘pit’ configurations combined

Results of the single-side impedance and OCP measurements have several important implications on the ‘partition’ configuration modeling scheme presented in Figure 4-35. First, no conductive behavior was observed at the Si/Si₃N₄/electrolyte interface. The values of R_{SiNflat} and R_{SiNpit} can hence be assumed to be near to infinity and the elements omitted from further considerations. Second, R_{SiOx} was found to be higher than 10 GΩ in the potential range given by the OCP. A conductive contribution of R_{SiOx} to overall impedance thus needs to be considered at very low frequencies only. Third, specific capacitance of the 100 nm thick Si₃N₄ film, $C_{\text{S(SiN)}}$, was determined. Accurate values of C_{SiNflat} , C_{SiNpit} , and C_{fsSiN} can be derived from $C_{\text{S(SiN)}}$, window geometry, and size of the wetted areas on each side of the window. In this manner, the number of free parameters in the modeling scheme is greatly reduced. The missing values of the model can be obtained unambiguously via NLLS fitting to experimental data.

The full ‘partition’ configuration modeling scheme is depicted in Figure 4-42A. As reasoned above, R_{Si} , R_{SiNflat} and R_{SiNpit} have been left out. The subsections of the scheme targeted by the single-side configurations are outlined in color. The ‘partition’ impedance spectra presented in Figure 4-34A were modeled again, this time in terms of the elaborate scheme. Experimental data and resulting model curves are plotted in Figure 4-42B. The new model curves overlay the experimental data points noticeably better than those derived from the single-time-constant equivalent circuit (Figure 4-34B). For illustration, the χ^2 goodness-of-fit test coefficient improved from 0.14 to 0.00094 and the weighted sum-of-squares coefficient improved from 8.61 to 0.057 for the first (*black*) spectrum model curve.

Table 4-3 lists both the fixed and the fitted circuit element values. C_{fsSiN} has been calculated using $C_{\text{S(SiN)}}$ and the area of the free-standing Si₃N₄ membrane. In analogy, $C_{\text{S(SiN)}}$ and electrolyte-wetted areas, defined by circular cut-outs in sealing PDMS sheets of 3 and 2.5 mm in diameter, were used to calculate C_{SiNflat} and C_{SiNpit} , respectively. R_{SiOx} has been set to 10 GΩ based on the R_{SiOx} vs. E curve (Figure 4-40A) and the effective OCP range of -90 to +50 mV. R_{p} , R_{S} , C_{SiOx} , C_{sc} , and R_{sc} were free parameters of the fitting routine. Negligible difference has been observed for R_{p} values

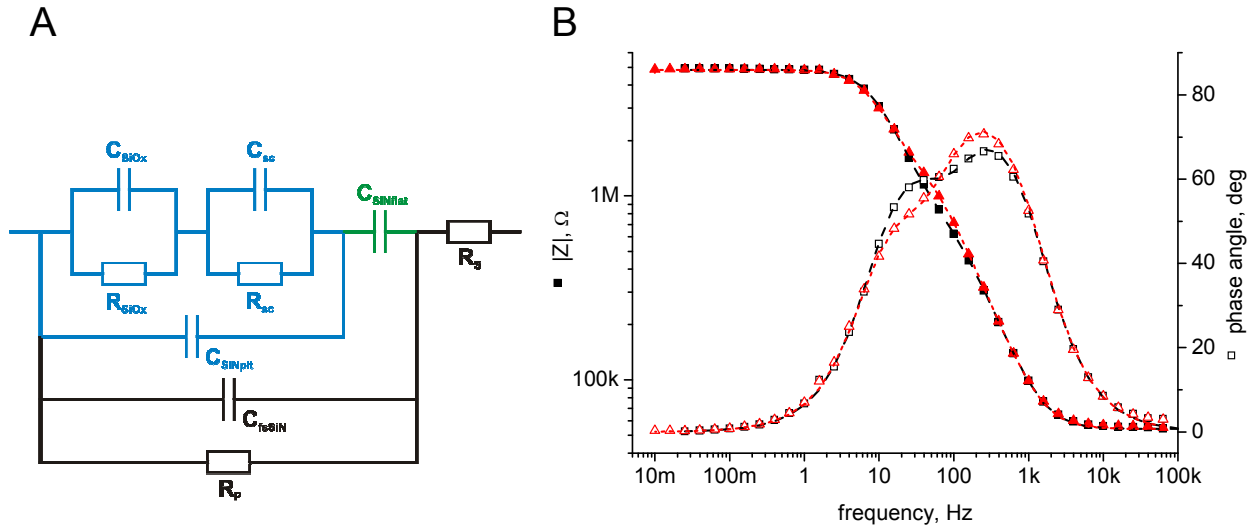


Figure 4-42. A - full electrical circuit corresponding to a Si_3N_4 TEM window in the ‘partition’ configuration. Elements accessed in the single-side ‘flat’ and ‘pit’ configuration are outlined in *green* and *blue*, respectively. Elements outlined in *black* are accessed in the ‘partition’ configuration only. B - re-plot of impedance spectra displayed in Figure 4-34A. Experimental data (*scattered points*) are overlaid with best-fit curves (*lines*), calculated using an equivalent circuit displayed in A. Circuit parameters are listed in Table 4-3.

Table 4-3. Equivalent circuit parameters corresponding to model impedance spectra plotted in Figure 4-42B. Parameters in **bold** were fitted, the rest were fixed based on the results presented above (see text).

spectrum	R_p , $\text{M}\Omega$	R_s , $\text{k}\Omega$	C_{fsiN} , pF	C_{SiNflat} , nF	C_{SiNpit} , nF	C_{SiOx} , nF	R_{SiOx} , $\text{G}\Omega$	C_{sc} , pF	R_{sc} , $\text{M}\Omega$
1	4.83	55.4	79.0	2.78	5.16	10.2	20.0	116	0.640
2	4.84	56.1	79.0	2.78	5.16	12.2	20.0	96.4	1.25

corresponding to the two spectra. Apparently, pore conductance has been stable over the given period of time. Similarly, R_s has remained relatively unchanged. The values of C_{SiOx} , C_{sc} , and R_{sc} have all undergone a change, however, indicative of the window’s bias potential drift. C_{sc} has decreased and C_{SiOx} has increased moderately, while R_{sc} has doubled. Given the upward trend in window OCP evolution over time and the dependence of C_{SiOx} , C_{sc} , and R_{sc} on bias potential (Figure 4-40), the difference of the second (*red*) spectrum relative to the first one implies an OCP rise by about +50 mV. Taking absolute values of C_{SiOx} , C_{sc} , and R_{sc} in regard, the applicable range of window OCP can be estimated as -200 – -150 mV for the former and -150 – -100 mV for the latter spectrum.

F. Final model simplification

In this chapter, detailed understanding of the TEM window electrical properties has been gained. Throughout the rest of the study, precise determination of R_p , be it of a free pore or a pore suspending a lipid bilayer, is of primary importance. On the contrary, exact knowledge of the remaining circuit element parameters is not required for npsLB characterization. Since differently-sized cut-outs were used in the sealing PDMS sheets in the course of this work, exact values of C_{SiNflat} and C_{SiNpit} are not available for most of the spectra. This means that only more or less broad

intervals that the parameters of the full-detail circuit of the ‘partition’ configuration (Figure 4-42) can fall into are known. Modeling all of the capacitance parameters at once is likely to produce results with little physical meaning. For this reason, using the full-detail model circuit of the Si_3N_4 window for routine extraction of R_p from ‘partition’ EIS spectra is useless. A circuit that simplifies the window frame impedance contribution will suffice as long as the value of R_p obtained via modeling by either circuit is the same. Although composed of a number of elements, the full circuit exhibits two time constants only. Figure 4-43 depicts three simplest-form circuits that possess two time constants. Fit quality to experimental ‘partition’ spectra using any of the three simpler circuits and the full circuit is the same, albeit with different parameters. Circuit A is not physically applicable to the real setup, however, since it is impossible to directly associate R_p with either R_x or R_y . The two remaining circuits both account for R_p correctly. We choose B as the default model because it produces an R_x parameter closer to the actual value of R_{sc} , as obtained from the full circuit. In this context, C_x and C_y are capacitance values without straightforward physical meaning.

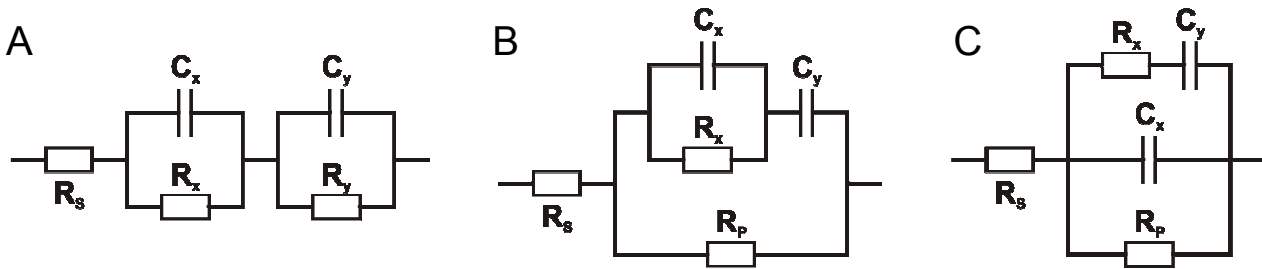


Figure 4-43. All simplest-form equivalent circuits exhibiting 2 time constants. Only B and C comply with a porous TEM Si_3N_4 window in the ‘partition’ configuration.

4.5.4. npsLB breakdown voltage

An important criterion of stability of an npsLB is the temporal breakdown of its resistivity due to the application of defined potentials. Characteristic breakdown voltages of classical BLMs are in the range of 150 - 200 mV.¹¹⁸ Breakdown voltages of npsLBs formed by controlled fusion of GUVs were tested by sweeping DC potential across npsLB arrays at low scan rates. This approach allowed for isolation of individual bilayer breakdown events. The system exhibits ohmic behavior, i.e. upon a linear potential sweep the slope of the current trace is equal to the total conductance, G_{total} . The total current through an array of unobstructed pores is given by the sum of currents through the individual pores: $I_{\text{total}} = \sum I_{\text{IP}i}$, where $I_{\text{IP}i} = V/R_{\text{IP}i}$ and $R_{\text{IP}i}$ is the resistance of the i^{th} individual pore. If the pores composing an array exhibit constant length and width, every unobstructed pore contributes an equal share to the total current: $I_{\text{total}} = nI_{\text{IP}} = nV/R_{\text{IP}}$, where n is the number of unobstructed pores. A single npsLB collapse, i.e. a pore-opening event, increases the current by $I_{\text{IP}} = V/R_{\text{IP}}$, and the total conductance becomes $G_{\text{total}} = n/R_{\text{IP}} + 1/R_{\text{IP}} = (n+1)/R_{\text{IP}}$.

Individual opening events of pores of equal dimensions thus manifest themselves by discrete conductance leaps, $\Delta G = 1/R_{IP}$.

4.5.4.1. Successive collapse of npsLBs

An instance of current traces recorded in response to linear DC potential sweeps across an array of npsLBs is displayed in Figure 4-44a. The measurement was performed in a TMAcI electrolyte using a 12-pore array of 100 nm nominal pore diameter and 1 μm least center-to-center distance. A unit cylindrical pore conductance of about 43 nS is predicted by theory (Chapter 4.3.9). A single npsLB collapsed before the measurement began, thus the current slope between 0 and 290 mV of the first sweep reflects the conductance of a single open pore. At 290 mV a single npsLB collapse occurs accompanied by an instantaneous current leap to about a double of the previous magnitude. The new conductance level corresponds to two unblocked pores. For the rest of the sweep, i.e. up to the reversal potential of 300 mV and back to 0 mV, the current trace follows the doubled system conductance. The ascending current trace of the next sweep overlays the descending trace of the former sweep, indicating the number of conductive pores has not changed. At 260 mV the current leaps to yet another level due to the opening of a third pore. The successive current traces portray the breaking of the rest of the npsLBs in the same fashion. Note that the collapse of the 4th & 5th, 8th & 9th, and 10th & 11th npsLB occurred shortly one after another in the scope of the same respective potential sweeps. The ‘skipped’ conductance levels (4, 8, and 10 open pores) could hence not be resolved.

Conductance (extracted by modeling of impedance spectra) with respect to the number of open pores is plotted as scattered points in Figure 4-44b. A fit of a linear equation (*solid line*) to the experimental data generates a unit pore conductance of 51.9 ± 0.6 nS. Only a negligible discrepancy exists between the final resistance after all 12 npsLBs were broken (1.66 M Ω) and the initial resistance measured before the npsLBs were formed (1.69 M Ω , represented by an *open triangle* in Figure 4-44b). Apparently, the residues of the npsLBs after collapse that might possibly be covering sections of pore walls did not make an impact on free pore resistance.

Figure 4-44c displays a plot of breakdown voltage against the breaking event sequence number. A general rising trend can be noted which indicates that either a variation in robustness exists among the individual npsLBs irrespective of the state of the neighboring suspended bilayers, or the effect of the electric field on the remaining npsLBs weakens as their number decreases. A simple cause of the former alternative might be the presence of heterogeneous topographical features in the vicinity of the pores. The scattered round elevations intrinsic to the Si₃N₄ diaphragms (e.g. Figure 4-24) could be involved, for example. Given the fact that breaking events 3 and 6 occurred at potentials

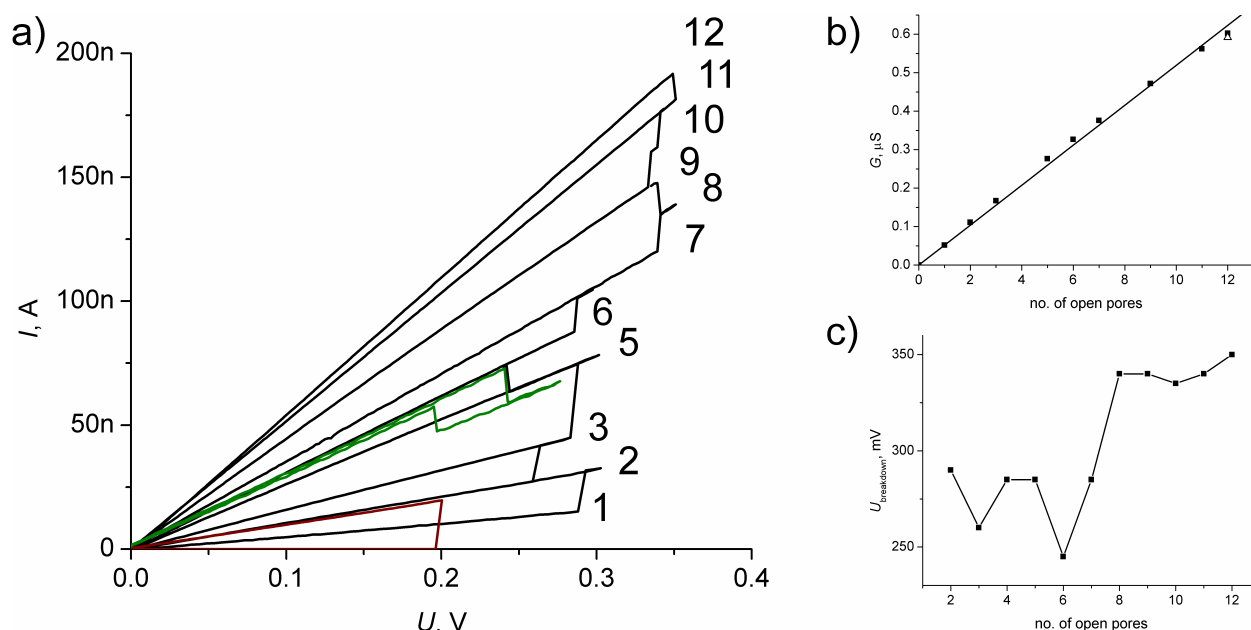


Figure 4-44. npsLB breakdown at elevated dc potentials. Potential across the TEM window was swept linearly between 0 mV and a variable positive reversal value at a rate of 10 mV/s. (a) Current traces corresponding to successive potential sweeps. Conductance of the partition is defined by the steady-state current gradient. Events of npsLB breakdown appear as rapid transitions to higher conductance levels. *Black lines* – 12-pore array, nominal pore diameter 100 nm, pitch 1 μm . Single and double npsLB breakdown events were observed. The values to the right denote the number of open pores per particular conductance level. *Red line* – 7-pore array, nominal pore diameter 50 nm, pitch 250 nm. All npsLBs collapsed in a single breakdown event. *Green line* – an example of a single pore reseal (258 mV, upward sweep) followed by a single npsLB collapse (212 mV, downward sweep). (b) Conductance versus number of open pores (*scattered points*) and a linear fit thereof (*solid line*). Slope of the fitted line, i.e. the unit pore conductance, evaluates to 51.9 ± 0.6 nS. Conductance of the TEM window prior to npsLB formation is represented by an *open triangle*. (c) Breakdown potential with respect to sequence number of the breaking event.

significantly lower than the preceding events, it appears that a breakdown of an npsLB might in some cases have a negative influence on the stability of some of the remaining ones. This is in contrary to the general validity of the latter alternative. Our data did not allow for a decisive characterization of the relationship.

Mayer et al.²⁴ observed breakdown voltages higher than 300 mV for about a half of their BLMs spanned by the Montal-Mueller technique¹⁷ over 50- μm -wide apertures in Teflon sheets. In addition, the authors reported successful experiments of up to 460 mV using a 2 μm aperture. Ability to stand dc voltages of up to 780 mV has been reported for painted BLMs spanning nanopores in hydrophobized glass membranes¹⁰⁰. The interaction of phospholipid molecules with the support in these studies has a hydrophobic character, whereas in our case the interaction is hydrophilic. One might speculate that higher lateral stress develops in a BLM spanning a hydrophilic surface, possibly due to a relatively lower mobility of the phospholipids in direct contact with the support, were the contrary not concluded from a study of mechanical breakdown of pore-spanning bilayers induced by AFM tips.¹¹⁹ Fine-tuning the support-phospholipid interactions

via surface chemistry may shift the breakdown voltages of hydrophilic npsLBs nearer to those observed by White et al. Besides, breakdown voltages for single pores are reported in these studies, whereas our values refer to pore arrays. The existence of a multitude of pores at low interpore separation may have a destabilizing effect on the npsLBs of the array, as discussed below.

4.5.4.2. Simultaneous collapse of npsLBs

It has been observed that the ‘sensitivity’ of some npsLBs to the collapse of other npsLBs in the array seems to get pronounced as the pitch of the array decreases. The *red line* in Figure 4-44a shows an example of a breakdown event of npsLBs suspended over an array of seven pores of 50 nm in diameter and 250 nm least center-to-center distance. As all pores were initially blocked by npsLBs ($R_p \approx 30 \text{ G}\Omega$), negligible current was detected at the onset of the sweep. An obvious breakdown event occurred at $U = 196 \text{ mV}$. The slope of the current trace after the event yields $G \approx 96 \text{ nS}$, which is very near to the conductance measured before the npsLBs were spanned. Conductance of $\sim 14 \text{ nS}$ per pore is predicted by theory for the particular electrolyte and cylindrical pore size. Given these facts, it seems that (almost) all of the seven npsLBs of the array collapsed very shortly one after another, i.e. within the 0.4 s interval between two data points. This is significantly different to arrays of a pitch of $1 \mu\text{m}$ whereby simultaneous breakdowns of two npsLB at most were seen. As suggested above, interpore distance may play a key role in determining whether breakdown of a single npsLB can induce a destabilizing effect on the neighboring npsLBs.

4.5.4.3. Pore resealing

Interestingly, downward discrete conductance transitions complying in magnitude with $1/R_{\text{IP}}$ were observed in multiple cases, too. Such drops of conductance can be associated with pore resealing events. The *green* current trace of Figure 4-44a shows an example of a pore reseal followed by a pore-opening, both in the scope of a single potential cycle. Conductance of the array upon the upward sweep corresponds to five unblocked pores. A reseal of a pore accompanied by an instantaneous conductance drop to a level characteristic of four open pores occurred at $U = 258 \text{ mV}$. U was further swept to 280 mV whereby the direction of the scan was reversed. The state of four unblocked pores was preserved until $U = 212 \text{ mV}$ was reached. At this potential, a sharp current increase was detected reminiscent of the collapse of a single npsLB. A conductance level slightly lower than that of five open pores at the beginning of the sweep was attained after the collapse. This could be due to the freeing of a pore other than the one that was resealed during the upward scan. This other pore could exhibit a smaller cross-sectional area and hence a lower conductance. Alternatively, partial residual obstruction of a pore by lipid could be a plausible cause, too.

Schmitt et al.⁴⁷ observed a gradual loss of resistance of their multiporous alumina substrates covered with LUV-derived npsLBs. The effect was attributed to successive breakdown of individual npsLBs. The resistance could be regained partially upon reintroduction of LUVs in the bathing medium, supposedly due to a reseal of some of the pores where npsLBs had collapsed previously. It is unlikely, however, that in our case the resealing was due to involvement of lipid structures from the bathing medium, for these had been washed away previously. It appears that the phenomenon is rather related to the dynamics of the SLB patch itself. The factors that determine the possibility of a pore reseal are unclear. In accordance with an instinctive expectation that an inverse dependence should exist between reseal probability and pore size, reseals of 50- and 100-nm-wide pores were rather common. On the other hand, reseals of pores as large as 300 nm were observed occasionally as well.

It must be emphasized that the technological potential of spontaneous reseal of collapsed npsLBs is tremendous. The platform is functional only as long as the background conductance of all the pores that are accessed electrically at once remains low. One way to secure this is to establish conditions whereby npsLBs do not collapse at all. Should this turn out unachievable, however, it may be comparably effective to induce a reseal of the freed pores.

A better understanding of the mechanisms underlying the observed npsLB collapse/re-seal phenomena will be gained if the status of a particular pore of an array can be resolved. Even a bulk conductance method such as involving two static redox electrodes is capable of providing this information for an array whereby each pore has a unique size. The difference in size between any two pores should be such that the change of total conductance due to a single opening or a reseal can unambiguously be attributed to a specific pore. Unfortunately, the contribution of pore size to npsLB robustness would be difficult to analyze thereby. A technically demanding yet very elegant approach would make use of an ion-conductance SPM (SICM).^{120,121} This method would not pose any requirements on pore size. On the other hand, the ability of the SICM to resolve single open pores could fail at small pore diameters and low pitch values. The design of the probe tips would play a key role here.

4.5.5. Electrical manifestation of the GUV – SLB transition

Spanning of npsLBs over (arrays of) nanopores proceeded in a sequence of three steps: 1) sinking of a GUV to the pore-bearing location, 2) adhesion and spreading of the GUV on the surface and over the pores, and 3) transition into an SLB patch by rupture and unfolding of the adhered vesicle. Interestingly, the dynamics of the process was rather variable. It would usually take the GUV a few seconds to spread, rupture and form a planar SLB patch. On the other hand, intervals as short as

few hundreds of milliseconds or as long as tens of minutes were needed for the complete process in some cases. No obvious correlation between transition dynamics and experimental parameters was identified, although variation of affinity of the lipid headgroups for the surface due to its momentary physico-chemical character is suspected.

Simultaneous optical and electrical monitoring of the process in real time showed that typically a giga-seal was formed as soon as a GUV adhered to the diaphragm over the pores. Occasional prolonged periods between adhesion and rupture of the vesicle made it possible to assess the change of npsLB resistance upon the transition from an adhered spread vesicle to a planar SLB. An example of an impedance trace reflecting the changes upon pore obstruction by a GUV whereby vesicle rupture occurred ~ 25 min after adhesion is presented in Figure 4-45. GUVs were injected at $t \approx 200$ s and a GUV adhered to the diaphragm at $t \approx 500$ s. The event of GUV rupture and unfolding at $t \approx 2000$ s had no obvious impact on the impedance. The objective was withdrawn, the cell was sealed from above, and shielding was replaced in the course of ~ 400 s following GUV rupture. The minor increase of impedance that occurred while these actions were taken can be attributed to the withdrawal of the microscope objective from the top compartment (reduced noise/change of hydrostatic pressure). The seal resistance of the npsLBs, as derived from a subsequent impedance spectrum, evaluated to ~ 40 G Ω .

An analogous scenario of probing a pore array by impedance before and after vesicle rupture is presented in Figure 4-46. In this case, npsLB formation was not followed in real time, but impedance spectra as well as microscope images have been taken instead. A large GUV adhered to the Si₃N₄ diaphragm over the pores is clearly apparent in image A, whereas the contrast of the vesicular structure is completely absent in image B. Instead, faint contours of an SLB patch can be resolved. The impedance spectra taken before and after the transition overlay almost perfectly, indicating that rupture and unfolding of the adhered GUV had little effect on the resistance of the npsLBs. Equivalent circuit modeling yielded resistance values of 8.6 and 7.8 G Ω , respectively.

The major implication of this result, namely that electrical means were not sufficient to distinguish whether the lipid structure occluding the pores was a closed adsorbed vesicle or a planar SLB patch,

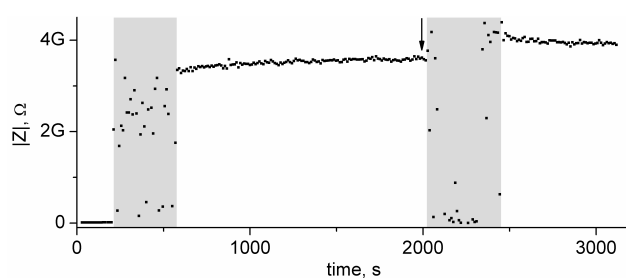


Figure 4-45. Transition of a GUV adsorbed to an Si₃N₄ diaphragm over an array of pores into an SLB patch monitored in real time via AC impedance at 0.2 Hz. Gray background denotes intervals of elevated noise due to removed shielding and manipulation. The instant of transition of the GUV from closed vesicular to unfolded planar form is indicated by an arrow. Array specifications: 7 pores, nominal pore diameter 50 nm, pitch 250 nm.

should be emphasized. Obviously, efforts to assess the behavior of protein reconstituted in the npsLBs without direct access from above, as would be the case if the structure occluding the pores is a continuous vesicle, may be completely vain. The possibility to state undoubtedly by microscopic observation that the vesicle has ruptured and unfolded turned out to be crucial in this context.

White et al. investigated the ionic conductance of the aqueous layer separating a lipid bilayer membrane and a glass support using glass diaphragms with single nanopores.¹⁰³ The resistance of the aqueous layer has been associated with the radial migration of ions between the pore orifice and the edge of the lipid bilayer film. The resistance of this layer has been modeled as $R_d = \ln(r_2/r_1)/(2\pi\kappa_d d)$, where r_1 is the radius of the pore orifice beneath the bilayer, r_2 is the radius of the bilayer film concentric with the pore, and d and κ_d are the thickness and ionic conductivity,

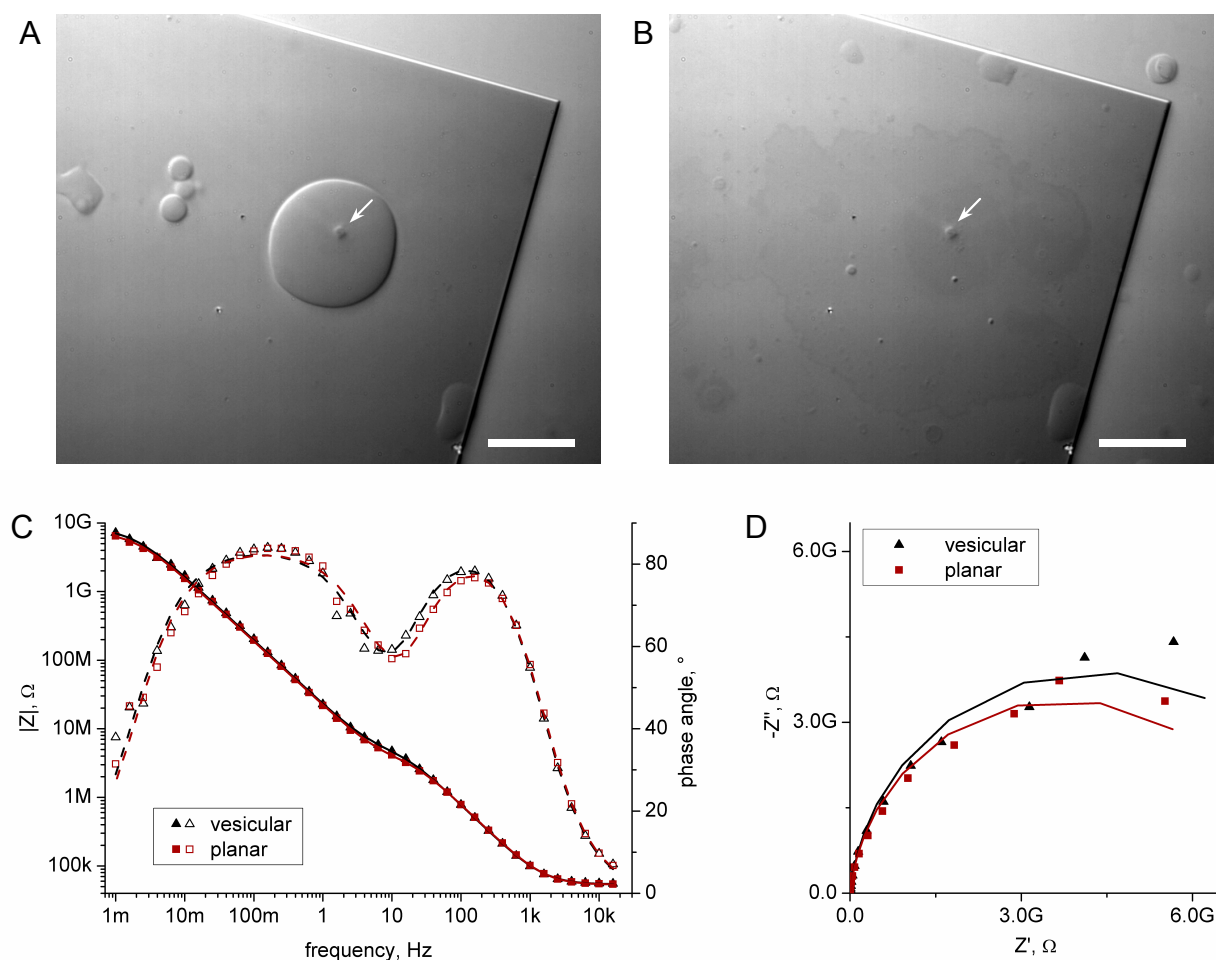


Figure 4-46. Transition of a GUV blocking an array of pores into an SLB patch. A, B – DIC microscope images of a corner of an Si_3N_4 diaphragm before (A) and after (B) the rupture and unfolding of a single GUV adsorbed to the diaphragm over the array of pores. The scalebars are 20 μm long. The location of the array is indicated by the *white arrow*. Faint contours of the SLB patch (darker against the background) can be noticed in B. C, D – impedance of the Si_3N_4 diaphragm before (*black*) and after (*red*) the transition. Bode (C) and Nyquist (D) plots of the spectra are shown. Scattered points represent experimental data ($|Z|$ – *solid symbols*, phase angle – *open symbols*), lines are spectra corresponding to equivalent circuits of best-fit parameters.

respectively, of the aqueous layer between the lipid bilayer and the glass support (Figure 4-47A). A set of resistance measurements ($r_1 \approx 50\text{-}500\text{ nm}$, $r_2 \approx 200\text{ }\mu\text{m}$, $d \approx 1\text{ nm}$, POPC bilayers) allowed the authors to estimate for κ_d a value of $0.26 \pm 0.06\text{ }\Omega^{-1}\text{cm}^{-1}$. The conductivity was found to be constant between 1 and 10^{-2} M KCl. Resistance curves calculated using the above equation (the internal resistance of our short pores has been neglected) for pore and SLB patch radii relevant to our conditions are plotted in Figure 4-47B. Based on this simulation, maximum resistance in the range of $\sim 2.5\text{-}4\text{ G}\Omega$ can be expected for SLB patches of $20\text{-}40\text{ }\mu\text{m}$ in diameter spanning pores $50\text{-}200\text{ nm}$ wide. Contrary to the theory, seals of a few tens of $\text{G}\Omega$ were obtained routinely in the course of this work with analogous SLB patches and pore sizes. The discrepancy suggests that a lower κ_d is applicable to our experimental conditions. This could be due to, for example, a different (electrostatic) character of the Si_3N_4 surface compared to glass, lower roughness, fewer defects in the SLB, etc. More important than the actual value of κ_d is the fact that the anticipated change of resistance upon GUV unfolding is rather low. As shown in Chapter 4.1.2, the transition from a fully-spread vesicle to a planar SLB patch roughly doubles the area of the support covered by lipid. Based on the value of κ_d provided by White et al., the unfolding of a $20\text{-}\mu\text{m}$ -wide GUV into a circular SLB patch whereby both are centered over the pore should induce a resistance increase by as little as 7%. At a smaller κ_d the predicted resistance increase is even lower. Changes of such insignificant magnitudes may easily be obscured by noise or additional factors that influence npsLB resistance.

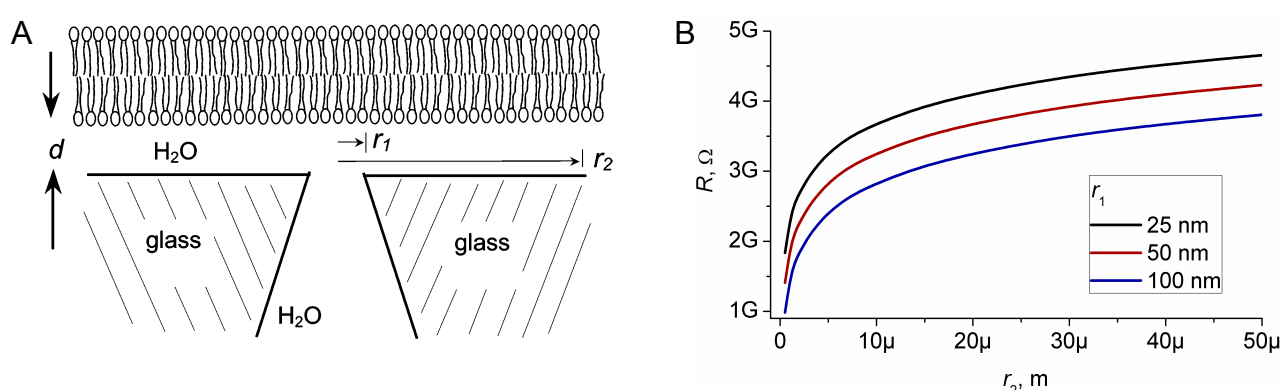


Figure 4-47. Ionic conductance of the aqueous layer between a lipid bilayer membrane and a hydrophilic support. A - cross-sectional view of the nanopore/lipid bilayer membrane illustrating the geometry used to analyze the measured resistance. r_1 , r_2 , and d are the nanopore radius, the radial distance from the pore center, and the water layer thickness, respectively (adopted from ref. [103]). B - plot of resistance, R , as a function of distance from the center of the pore (r_2) for $r_1 = 25, 50$, and 100 nm .

4.5.6. Conclusion

npsLBs were spanned over nanopores by maneuvering sedimenting GUVs with a micromanipulator to pore-bearing locations of horizontally-mounted Si_3N_4 diaphragms. The transition from a non-

adsorbed vesicular state to a planar SLB state of the lipid bilayer typically proceeded in the course of a few seconds after contact of a GUV with the support. The process was monitored in real time by AC impedance measurements across the porous windows at a fixed frequency. Abrupt falls of conductance to levels well below 1 nS were observed upon GUV adsorption and unfolding. Impedance spectra of porous Si_3N_4 windows showed an unexpected drifting time constant in the system. Impedance characteristics of the windows in a non-redox electrolyte were hence analyzed carefully. The drifting time constant could be associated with the dynamic space charge layer affecting the impedance behavior of the window pit walls. A relevant equivalent circuit was deduced for the Si_3N_4 windows and used to interpret impedance spectra acquired before and after npsLB formation. npsLB resistance could thus be determined accurately. Breakdown of individual npsLBs of an array due to growing transmembrane DC potential was observed. Frequency of simultaneous breakdown of multiple npsLBs seemed to increase at shorter pore-to-pore distances, suggesting that destabilizing effects may propagate between neighboring npsLBs. Infrequent yet unambiguous events of pore resealing were observed, too.

4.6. Pore-forming peptides in npsLBs

The final goals of this work were to demonstrate that TM channels can be detected in the npsLBs by electrical means, and to establish platform parameters allowing for recordings of ionic currents with single-channel resolution. Macroscopic changes of npsLB impedance were observed due to assembly of a multitude of gramicidin pores in the bilayers. After the setup was adjusted to meet the necessary parameters (see Table 4-4 for the prerequisites and implementation), DC voltage clamp resolution was achieved that allowed for the observation of opening and closing of single α -hemolysin and alamethicin channels.

Table 4-4. Prerequisites for successful protein single-channel measurements and the specific respective solutions.

Requirement	Implementation
low noise	on-stage Faraday cage chip capacitance reduced to ~50pF (Chapter 4.4)
high-gain amplification high sampling rate good resolution at A/D conversion	HEKA EPC10 patch-clamp amplifier
low-impedance electrodes suitable for steady-state dc monitoring	Ag/AgCl wires
low background conductance	below 0.1 nS – an intrinsic property of the npsLBs (Chapter 4.5.2)

4.6.1. Gramicidin D

4.6.1.1. Background

Gramicidin D (gD) is a well characterized antibiotic, which forms channels that selectively transport monovalent cations of less than 200 pm unhydrated radius.¹²² The channel is impermeable to divalent cations, anions, and larger cations.¹²³ Gramicidin D from *Bacillus brevis* is a natural mixture of 85% gramicidin A (gA), 10% gramicidin C and 5% gramicidin B, which differ only in one amino acid in position 11.¹²⁴ The small dimeric peptide-based ionophore is one of the best characterized and most extensively studied pore-forming compounds.^{125,126} Its β -helical dimer structure is shown in Figure 4-48A and B. The linear pentadecapeptide forms a continuous channel consisting of two antiparallel oriented monomers, bound to each other by six hydrogen bonds. The resulting length of the dimer is about 2.5 nm,¹²⁷ which is sufficient to span the hydrophobic part of a lipid bilayer. Conducting dimers and non-conducting monomers are in equilibrium in the bilayer membrane as schematically depicted in Figure 4-48C. The van-der-Waals size of the pore is about 4 Å in diameter.¹²⁷ The cation selectivity determined by conductivity measurements in BLMs is small but significant and follows: $H^+ > NH_4^+ > Cs^+ > Rb^+ > K^+ > Na^+ > Li^+$.¹²⁸ The increasing

conductivity of the larger alkali ions arises from the decrease in hydration enthalpy with the size of the cation.¹²⁹

Early experiments with gramicidin in BLMs date back to the 1970s, where the single channel conductance of gramicidin A, B and C,¹³⁰ the ion selectivity,¹²⁸ and the blocking with divalent ions were investigated.¹²³ The dimeric single stranded structure already proposed by Urry in 1971¹³¹ was still highly discussed in the late 1990s, due to the fact that double stranded dimers were crystallized from organic solvents and taken to be the active form of the channel.¹²⁴ The identity of the channel structure was established by 1980 through mutation experiments, determining the single stranded head-to-head dimers as the conductive channel form in lipid bilayers, as this conformation is energetically favored over the double stranded structure, at least in a lipid environment.¹³²

The conductive TM gramicidin single-helix head-to-head dimer exhibits a single conductance state. The permeability of the channel depends on the composition and concentration of the electrolyte. In addition, gA single-channel conductance is sensitive to lipid headgroup characteristics (e.g. charge or extent of methylation). The length of the acyl chains of the surrounding lipid molecules, on the other hand, affects the open channel lifetimes.¹³³ Single-channel conductance of gramicidin A in glyceryl-monooleate membranes is ~90 pS and ~50 pS for 1 M CsCl and 1 M KCl, respectively.¹³⁰ In DPhPC membranes, the conductance is lower: 46 pS for 1 M CsCl, 15 pS for 0.1 M CsCl, 25 pS for 1 M KCl,¹³⁴ 10 pS for 0.1 KCl.¹³⁵ Mean open channel lifetimes of ~1 s were reported for gA in painted DPhPC/*n*-decane BLMs.¹³⁶ Effect of pH on gA conductance is small.¹³⁴

4.6.1.2. gD in npsLBs – multi-channel conductance

An example of the dynamics of formation of conductive gramicidin dimers in an npsLB is shown in Figure 4-49A. Conductance of the initially well-resistive (~5 GΩ) single npsLB was monitored by

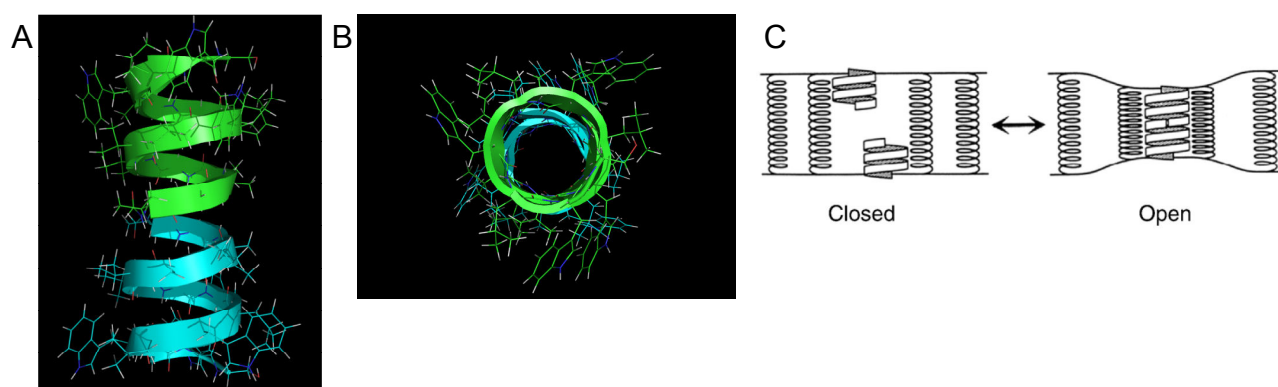


Figure 4-48. Gramicidin channel - structure and assembly. Top (A) and side (B) view of the gramicidin channel (PDB code 1MAG, visualized by PyMOL (<http://www.pymol.org>)) C – schematic of the transmembrane dimer formation (image adopted from ref. [126]). Gramicidin monomers residing and diffusing within the contiguous monolayers of the lipid bilayer meet and form temporary conducting head-to-head TM dimers.

AC impedance in real time. Incubation of a single side of the npsLB with 10- μ M gramicidin D induced no change of conductance (event 1), whereas subsequent perfusion along the other side of the bilayer by the base electrolyte plus 10 μ M of gramicidin D resulted in a significant logarithmic increase of conductance (event 2). The former complies with a previous finding that gramicidin monomers permeate poorly across lipid bilayers and assembly of conductive transmembrane dimers upon single-sided peptide administration is hence limited.¹³⁷ The rate of change of conductance was strongly dependent on the rate of electrolyte perfusion through the bottom compartment (events 3 and 4). Presumably, convection of the aqueous medium enhances the rate of peptide insertion into the npsLB. Conductance of more than 200 nS has been attained in the course of \sim 5000 s.

Gramicidin has been reported to be almost completely impermeable to $\text{N}(\text{CH}_3)_4^+$.¹²⁸ To rule out the possibility that the observed increase of conductance was simply an effect of npsLB seal deterioration, the base electrolyte (100 mM KCl, 5 mM HEPES, pH 7) bathing the npsLB loaded with gramicidin was exchanged for 100 mM TMAcI, 5 mM HEPES, pH 7 (Figure 4-49B). Exchange of electrolyte in the first of the two compartments (event 1) brought the conductance to about half the previous steady-state level, in accordance with the expectations. Subsequent exchange of electrolyte in the other compartment (event 2) reduced the conductance to \sim 0.4 nS, implying that the observed conductance truly was due to ionic flow through gramicidin channels.

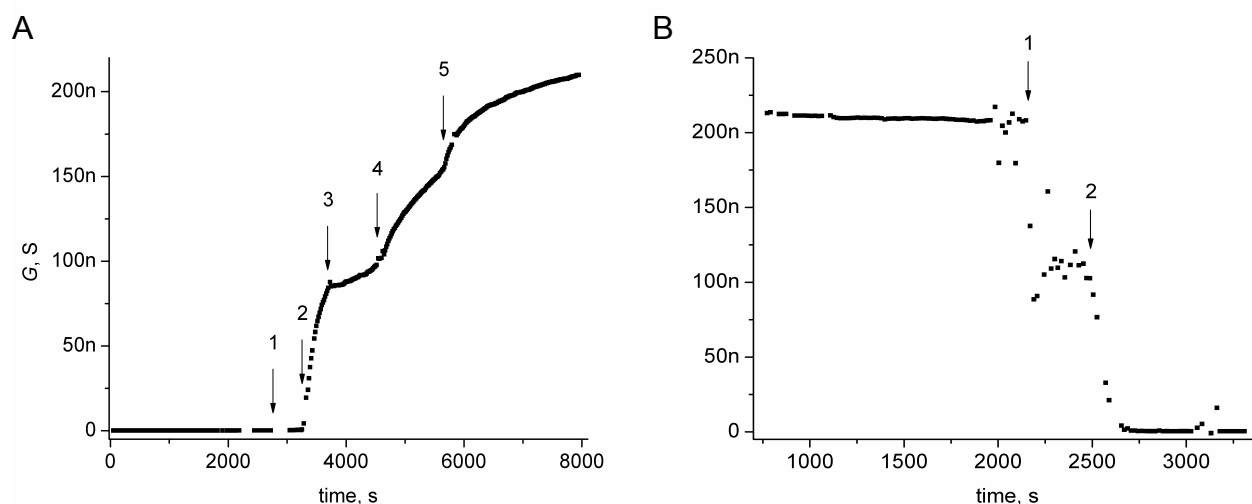


Figure 4-49. Changes of conductance in time of an npsLB upon administration of gramicidin D (A) and exchange of electrolyte from KCl to TMAcI (B). AC impedance was measured at a fixed frequency of 0.2 Hz in 100 mM KCl, 5 mM HEPES, pH 7 (base electrolyte, BE). Bottom compartment was perfused using a peristaltic pump, top compartment was perfused manually. A: 1 – BE + 10 μ M gramicidin D in the top compartment; 2 – start of perfusion of bottom compartment with BE + 10 μ M gramicidin D; 3 – perfusion of bottom compartment paused; 4 – perfusion of bottom compartment resumed; 5 – increase of conductance change rate w/o an external stimulus. B (20 min after A): before 1 – BE w/o gramicidin D in both compartments; 1 – exchange of BE for 100 mM TMAcI, 5 mM HEPES, pH 7 (TE) in top compartment; 2 – exchange of BE for TE in bottom compartment. Gaps in the traces are phases of removed shielding and manipulation whereby the measured conductance values showed no relevance to the physical state of the system.

Figure 4-50 shows a sequence of impedance spectra acquired for an npsLB suspended over a single 280 nm wide pore at varying concentrations of gramicidin in the electrolyte. The trace lined with open squares reflects the status of the npsLB before gramicidin had been introduced, with $R_p \approx 15\text{ G}\Omega$. The other traces were acquired after stepwise increases of gramicidin concentration in both electrolyte compartments to 320 nM, 1 μM , 3.2 μM and 10 μM , always one hour after a concentration step was made. The respective npsLB resistances (R_p) extracted via modeling of the spectra are 133, 91, 61, and 47 M Ω . At 10 μM of gramicidin, an extra spectrum was acquired after 12 hours of incubation, revealing a further decrease of resistance to 34 M Ω . Apparently, a higher density of conductive gramicidin dimers in the npsLB had been attained during the additional incubation time. Yet another spectrum was acquired after bilateral exchange of KCl for TMAcI of the same concentration. npsLB resistance increased to 8.7 G Ω . The specific conductivity ratio of the two electrolytes was 1.32. Therefore, if some of the conductance could be attributed to a leaky seal, the resistance measured in 100 mM KCl in the absence of gramicidin would not have been restored. Exchange of KCl for TMAcI led to a 260-fold increase of resistance, however, to a level near to that before gramicidin addition. This result suggests that the seal deteriorated negligibly in the course of the experiment and the observed increase of npsLB conductance was indeed due to the presence of gramicidin channels in the bilayer.

Because the attained conductance is rather high respective to the area of the npsLB, an interesting question arises as to how much gD was actually present in the bilayer. gD was dissolved in ethanol, diluted in base electrolyte at the desired concentration, and delivered to both sides of the npsLB by perfusion. gD forms primarily non-conductive double-helical dimers when dissolved in ethanol at

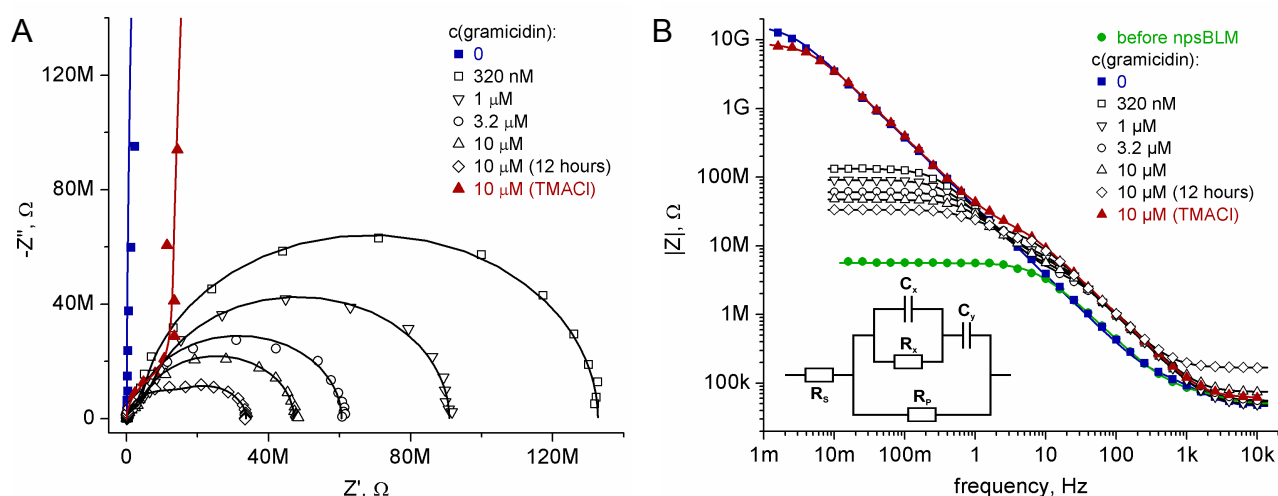


Figure 4-50. Nyquist (A) and Bode (B) plot of impedance spectra acquired for a single npsLB at varying concentrations of gramicidin D. Scattered points represent experimental data (see legend), lines are the best-fit traces modeled using an equivalent circuit inset in B (see Chapter 4.5.3 for circuit rationale). The spectrum of a clean chip with a free pore before npsLB formation has been included in (B) for comparison (green circles).

high concentrations.⁷⁸ These are, however, known to rapidly unwind and break into monomers if the polarity of the solvent is increased (e.g. by addition of water in fractional amounts).¹³⁸ As the stock solutions of gD in ethanol were mixed with base electrolyte hours prior to administration of the mixture to the bilayer, gD reaching the lipid bilayer was predominantly monomeric. Double-helical dimers are also known to slowly unwind and break into monomers in a lipid bilayer environment.⁷⁸ Any residual double-helices that did not break apart before having reached the bilayer must have unwound in the course of the lengthy experiment. Therefore, gD is assumed to have resided in the npsLB in the monomeric or conductive head-to-head dimeric form, but not in the double-helical dimeric form.

White et al. found for the conductivity of an aqueous layer between an sBLM and a glass support a value as small as $0.0026 \Omega^{-1}\text{cm}^{-1}$.¹⁰³ The access resistance of a hypotetic conductive channel in an sBLM would be increased severely due to the proximity of the support to the channel mouth. Based on these facts, we assume that all conductive dimers that are electrically accessible and contribute to the measured conductance are located in the pore-spanning region of the bilayer. We further assume 1) 250 \AA^2 per gramicidin monomer as well as conductive dimer,¹³⁹ 2) unitary conductance of 10 pS of a gD channel in a DPhPC bilayer in 100 mM KCl,¹³⁵ and 3) 76 \AA^2 per DPhPC molecule.¹⁴⁰ The minimum measured resistance of 34 M Ω then corresponds to ~ 3000 gD channels open simultaneously in the membrane, which translates to a molar gD-to-lipid ratio of 1:24. The highest available value of the dimerization constant for gramicidin in PC bilayers is $\sim 5 \times 10^{-14} \text{ mol/cm}^2$.¹⁴¹ $K = [M]^2/[D]$, where $[M]$ and $[D]$ are the monomer and dimer surface densities, respectively. In our case, $[D]$ is $\sim 8.5 \times 10^{-12} \text{ mol/cm}^2$, hence $[M] \approx 6.5 \times 10^{-13} \text{ mol/cm}^2$ per bilayer and $3.3 \times 10^{-13} \text{ mol/cm}^2$ monomers per monolayer leaflet. Only $\sim 4\%$ of the gD molecules are monomeric at this very high surface density, whereas the rest are agglomerated in conductive dimers. Please note that a smaller K would generate a proportion of free monomers even lower than 4%. The estimate of the molar gD-to-lipid ratio corrected for monomeric gD evaluates to $\sim 1:23$. The channel density attained here is considerably higher than that of $\sim 5 \times 10^{-14} \text{ mol/cm}^2$, which was identified previously as limiting for accurate conductance measurements in a standard painted BLM setup.¹⁴¹ An electrical measurement at comparably high channel surface densities has not been reported before. Reduction of the bilayer area to below $0.1 \mu\text{m}^2$ without the penalty of a high aperture aspect ratio, as presented here, shifts the window of accessible channel densities towards considerably higher values. A possibility thus emerges to probe lipid-protein and protein-protein interactions at saturating protein densities directly by electrical means. Given the fact that the intra-membraneous perimeter of a gD monomer is expected to accommodate 7 to 8 diacyl lipids,¹⁴² the

calculated peptide/lipid ratio suggests a peptide density has been reached where such phenomena might be coming into play.

4.6.1.3. psLBs compared to tBLMs

As mentioned above, gramicidin is a 15-amino-acid peptide that forms simple helices in a lipid bilayer environment. We have shown above that gD does incorporate into npsLBs and can do so up to very high densities. In our previous work we looked at the incorporation of a similarly simple peptide, a 28-amino-acid hydrophobic helix with charged termini, into tBLMs derived from DPTL by the method of electrostriction.¹⁶ The electrostriction method makes use of AC current harmonics due to oscillatory nano-compressions of a lipid bilayer in an AC potential field. Physical characteristics of the lipid membrane, such as electrical capacitance, C , elasticity modulus normal to membrane plane, E_{\perp} , and transmembrane potential, Φ_m , can be deduced from the amplitude of the harmonics. A decrease of E_{\perp} with growing peptide concentration indicated a disordering effect of the peptide on the bilayer. An accompanying pronounced growth of Φ_m suggested solely a unilateral interaction of the peptide with the tBLM. Apparently, adhesion of the peptide to bilayer surface yet little or no penetration into bilayer interior occurred. In agreement with the results of other groups^{13,15,144}, we have thus shown that transmembrane incorporation of even very simple peptides into a tightly-packed tBLM may be impossible.

Based on these findings, further developments of tBLMs focused on dilution of the tethering moiety on the surface.¹³ Reduction of surface density of the linker generated a submembrane region of looser packing and higher water content and a lipid bilayer of higher fluidity. Incorporation from the bathing solution and electrical detection of gramicidin and melittin has been reported for such diluted tBLMs.¹⁴³ Unfortunately, lower tether density that increases tBLM compatibility with complex TM proteins usually comes in the expense of lower electrical resistance of the membrane.¹³ Electrical signal due to charge translocation through TM protein thus becomes obscured by large (nonspecific) background currents.¹⁴³

A well-sealing tBLM can only be constructed on a smooth and stable conductive surface. Materials that are ‘inert’ to the working electrolyte must be used therefore. By design, the electrical interaction of such electrodes with the electrolyte may only be of the capacitive high-impedance type, and not of the faradaic low-impedance yet surface-reactive type. Low-impedance access is required for standard DC voltage clamp SChM, however. Attempts to construct a high-resistance tBLM tethered to a low-impedance electrode have been failing thus far.¹³ Although the tBLM is an excellent model membrane system for surface-analytical and spectroscopic techniques, its design does not seem to allow for single-channel current recordings.

4.6.2. α -hemolysin

4.6.2.1. Background

The exotoxin α -hemolysin (α HL) is secreted by *Staphylococcus aureus* as a water soluble, monomeric, 293-residue polypeptide that forms heptameric pores in lipid bilayers.¹⁴⁵⁻¹⁴⁷ The overall shape of the pore resembles a mushroom with the stem penetrating the membrane bilayer and the cap extending into the extracellular space.¹⁴⁸ Each subunit has 16 antiparallel β -strands and four short α -helices. The crystal structure of the pore (Figure 4-51A and B) reveals a mushroom-shaped object in which the lower half of the stem forms a transmembrane channel made up of residues from the seven central glycine-rich regions of the polypeptide chains. The N- and C-terminal thirds of the polypeptides, which are rich in β -structure, form the cap of the mushroom and reside outside the target cell.¹⁴⁹ In solution, the central domain of the monomer is loosely organized and exposed to solvent. Incorporated into cell membranes, α HL leads to lysis of the cells by formation of large pores within the membrane. The α HL monomers bind to the cell membrane, and pore assembly occurs upon subsequent collision during lateral diffusion in the bilayer (Figure 4-51C).^{150,151}

The α HL pore typically exhibits a well-characterized dominant high-conductance state with low ionic selectivity (Figure 4-51D).¹⁵² In addition, some poorly-characterized partially-closed states of lower conductance have been reported¹⁵²⁻¹⁵⁴. The conductance of the dominant state is slightly pH-dependent^{153,155} and falls between 0.7 - 0.75 nS in 1 M NaCl^{21,153,155,156} and ~0.9-1 nS in 1 M

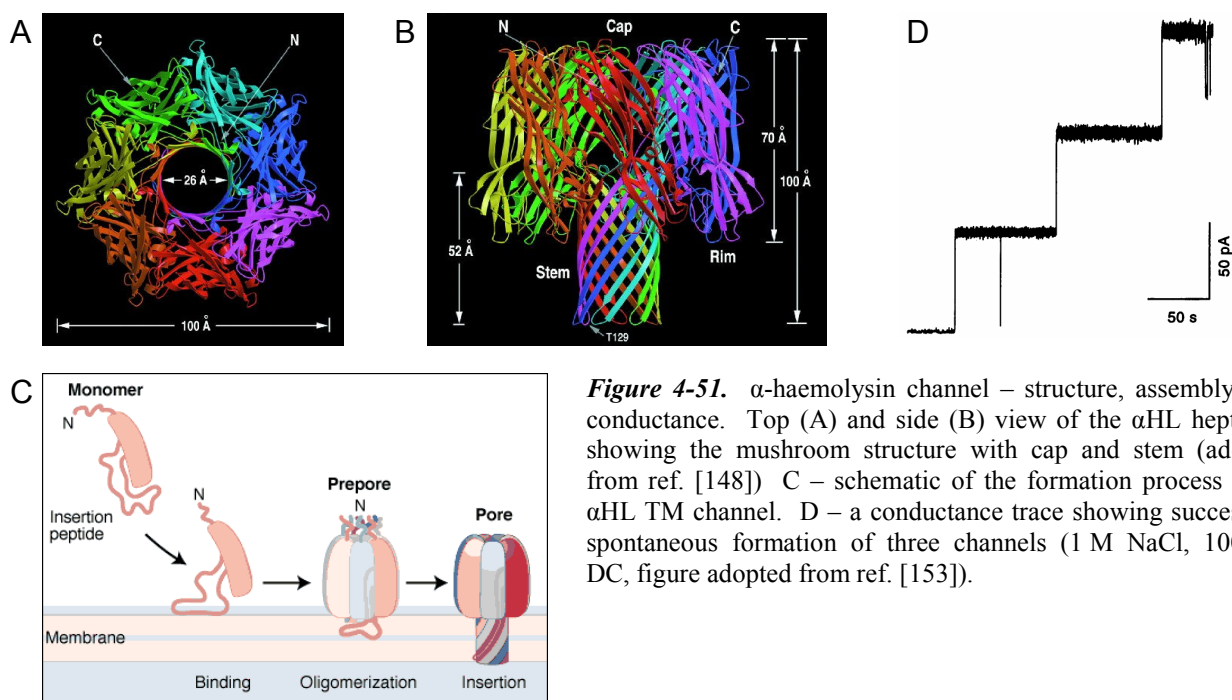


Figure 4-51. α -haemolysin channel – structure, assembly, and conductance. Top (A) and side (B) view of the α HL heptamer showing the mushroom structure with cap and stem (adopted from ref. [148]) C – schematic of the formation process of an α HL TM channel. D – a conductance trace showing successive, spontaneous formation of three channels (1 M NaCl, 100 mV DC, figure adopted from ref. [153]).

KCl^{100,157-159} of neutral pH. The channel shows quasi-ohmic behavior at DC potentials between -100 and +100 mV. Mean open state lifetime is in the range of minutes and is modulated by pH^{153,160} (longer at higher pH) and TM potential^{152,153,160} (longer at lower absolute potential). Once a low-conductance state has been attained, the state of high conductance can be restored by eliminating the TM potential.¹⁵⁴

4.6.2.2. α HL single-channel conductance

A. α HL in npsLBs

Voltage-clamp recordings of ionic currents through α HL channels in npsLBs were acquired in 1 M KCl at ± 100 mV DC. A minor 50 Hz AC current component, most likely arising due to imperfect shielding of the measurement setup, was superimposed over the recorded DC current traces. A simple subtraction of the AC component was not possible because of the variation of its amplitude in time. A significant part of the AC component was removed by applying a digital reverse FFT band-block filter between 40 and 60 Hz. Some residuals of the AC signal superimposed over the DC current are still evident in the presented data, however. Nevertheless, histogram analysis of current amplitudes over extended periods of time (at least 100ms) coupled to fitting of simple Gaussian functions to the amplitude distributions allows one to extract the average DC current levels fairly accurately. Unless stated otherwise, the time interval of a current recording trace corresponding to a particular histogram is outlined in gray in the following figures. Mean and s.d. values of current magnitudes were derived via fitting of Gaussian distribution functions to the amplitude histograms. The current magnitudes were not corrected for background leakage and are presented as acquired. Noteworthy current levels are denoted by horizontal lines in the *I*-vs.-time traces and vertical lines in the amplitude histograms.

Figure 4-52 depicts a series of current recordings acquired in the course of a single npsLB/ α HL experiment at a DC potential of -100 mV. Section 1 of the figure illustrates the condition of the npsLB prior to addition of α HL: an example of a trace acquired at -100 mV (A) and an ohmic dependence of current on applied potential (B). The reciprocal of slope of a linear fit to the measured *I*-vs.-*E* data points reveals for the particular npsLB a resistance value of 28.5 G Ω . Data capture was continued some seconds after the opening of the first channel(s) in the npsLB, hence the non-zero initial current amplitude in Figure 4-52-2A. At *t* = 2.3 s, a transition from -24.4 ± 3.5 pA (level 1) to -9.2 ± 2.8 pA (level 2) occurred, followed after 200 ms by a return to the

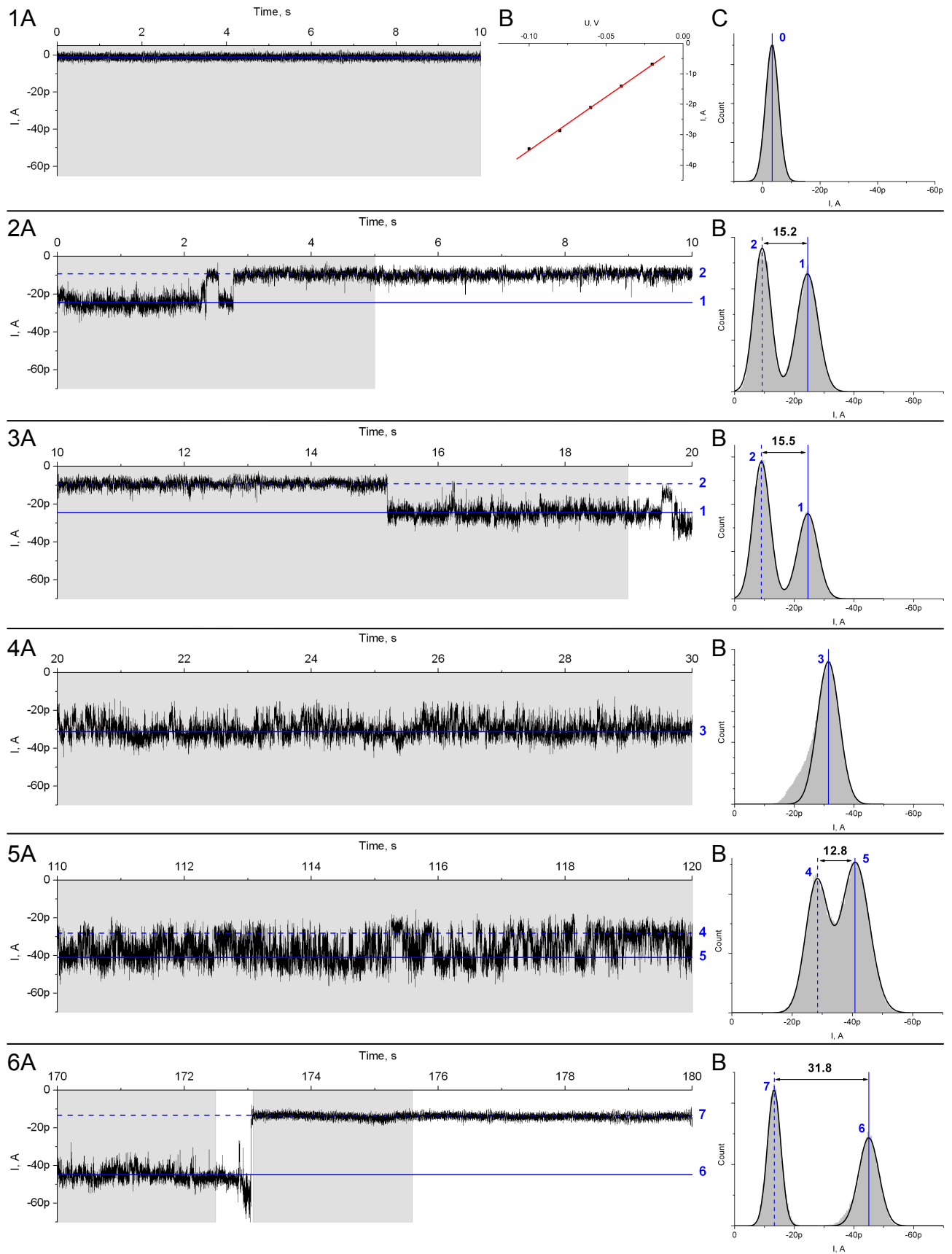


Figure 4-52. An example of a series of current recordings through an array of npsLBs before (section 1) and after (sections 2-5) administration of monomeric α HL in the bathing medium. -100 mV DC, unbuffered 1 M KCl in both compartments.

original level lasting another 200 ms, and a persistent switch to level 2. After 12.5 s, the DC current stepped back to level 1. A brief drop to -14.0 ± 2.5 pA at $t = 19.5$ s was followed by a switch to a new state of frequent low-amplitude fluctuations around a mean current level of -31.4 ± 3.7 pA (level 3, Figure 4-52-4). The mean current level was observed to rise slowly in the subsequent sweeps. If discrete steps were responsible for the increase, they must have been of amplitudes low enough to be obscured by the noise. The fluctuations seemed to have become more pronounced in the course of time, as exemplified in section 5 of the figure. It is evident in the amplitude histogram that two conductance levels, -28.2 ± 3.7 pA (level 4) and -41.0 ± 4.7 pA (level 5), of virtually equal occupancy were prevalent. About a minute later, the fluctuations were less apparent, yet still clearly present (section 6, initial part of the current recording), and the mean current level moved to -45.0 ± 3.4 pA (level 6). At $t = 173$ s, a transient increase to about -55 pA was followed by a fast significant drop to -13.2 ± 2.2 pA (level 7). A similar current was recorded briefly at $t = 19.5$ s, i.e. right before the onset of the marked evanescent fluctuations. It is noteworthy that no fluctuations were apparent at the new current level. As the mean current level dropped and the fluctuations disappeared in one instant, it seems probable that both phenomena were related to the same single α HL channel. It is unclear whether the observed drop of current was a consequence of (partial) channel closing, breakdown, or escape. A linkage might exist between the slight increase of conductance right before the drop and the closing or breakdown of the channel.

Interesting bursts of recurrent transient current steps were observed in the presence of α HL in npsLBs, too (Figure 4-53-1). The spikes were downward-oriented and exhibited a mean step magnitude of 40.8 pA. The current amplitude distribution at the target level, 72.1 ± 14.4 pA, was fairly broad. The I-vs.-t trace depicted in Figure 4-53-2 was recorded ~5 min later. Recurrent switching between two conductance levels with comparable dwell times at each level was observed. Two seconds after the beginning of the current recording a relatively permanent transition by ~41 pA occurred. The mean magnitude of the frequent short-lived steps before (34.5 pA) and after (34.7 pA) the transition was very similar. Interestingly, the mean magnitude of the recurrent transient current steps in Figure 4-53-1 and the permanent transition in Figure 4-53-2 are almost identical.

In analogy to Figure 4-52, Figure 4-54 depicts a chronological series of recordings acquired in a single experiment. A single α HL channel of conductivity of ~0.75 nS seems to have opened at $t = 0.4$ s and closed at $t = 4.1$ s of recording A. The ground level of 36 ± 3.5 pA (level A1) in the initial phase of the displayed trace indicates the presence in the npsLB of either a single α HL channel of conductance of ~0.3 nS, possibly in the hexameric form,^{153,161,162} or a few α HL channels

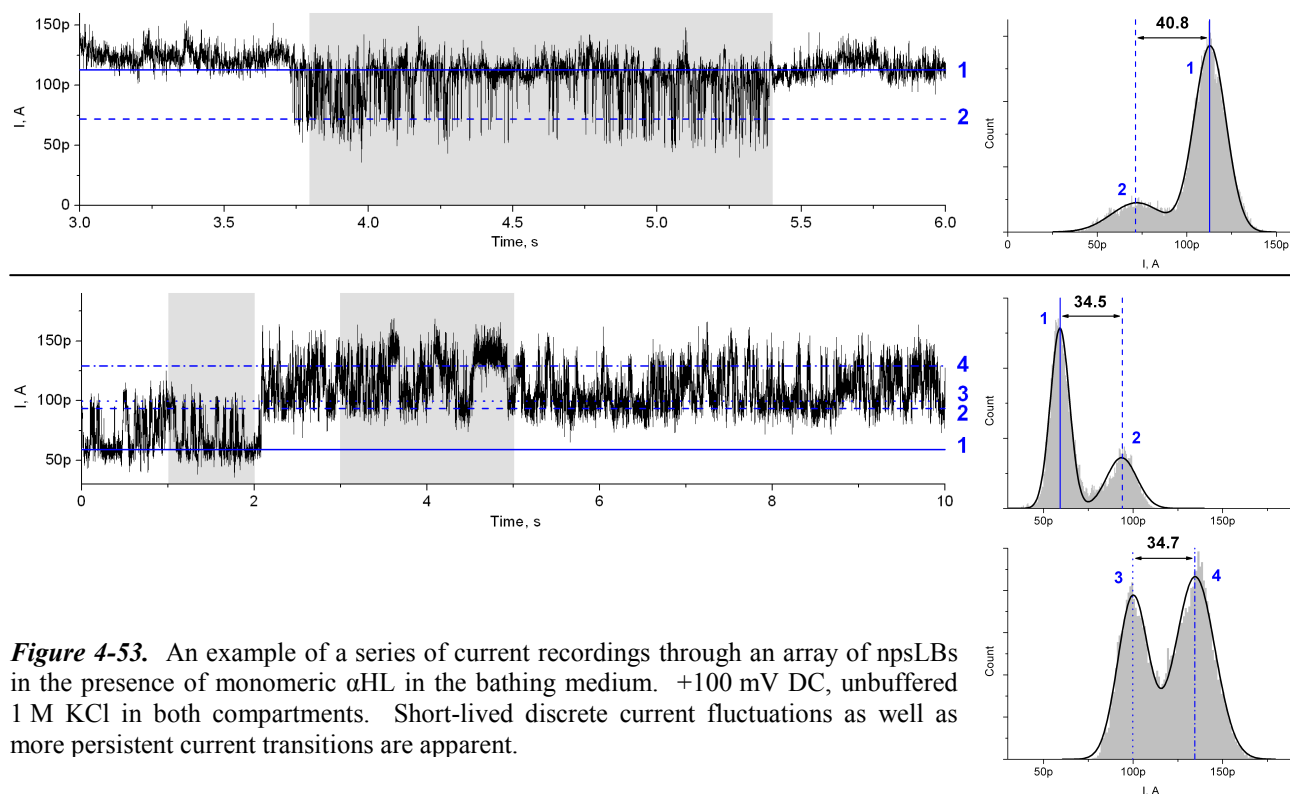


Figure 4-53. An example of a series of current recordings through an array of npsLBs in the presence of monomeric α HL in the bathing medium. +100 mV DC, unbuffered 1 M KCl in both compartments. Short-lived discrete current fluctuations as well as more persistent current transitions are apparent.

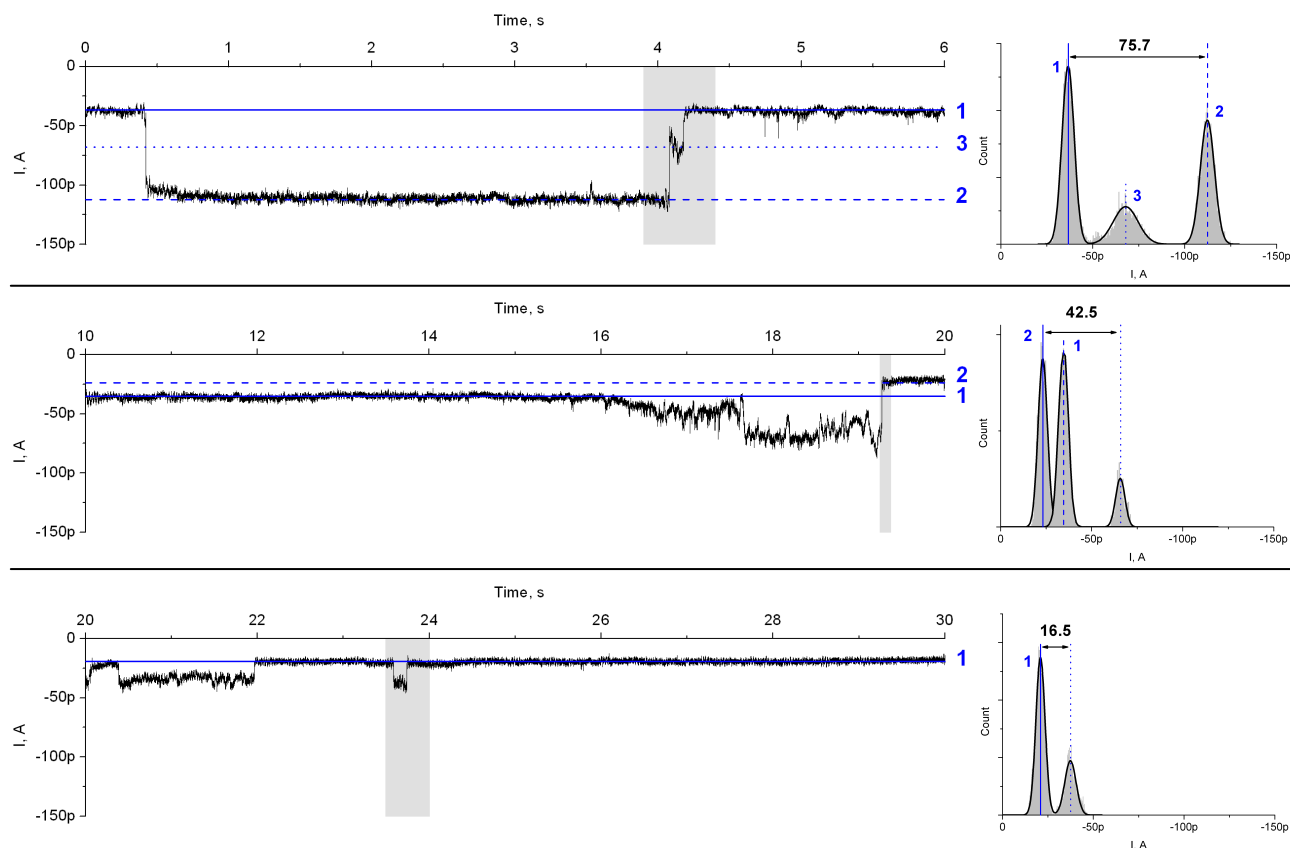


Figure 4-54. An example of a series of current recordings through an array of npsLBs in the presence of monomeric α HL in the bathing medium. -100 mV DC, unbuffered 1 M KCl in both compartments. A discrete high-conductance event is followed by interesting a continuous conductance transition and discrete events of lower magnitudes.

occupying a low-conductance state.¹⁵⁴ The initial current step is rapid and of considerable magnitude, yet it reaches down to about -100 pA only. An additional minor step to a steady current level of -111 ± 4 pA (level A2) seems to have occurred at $t = 0.65$ s. The transition back to the original current level proceeded in two distinct steps. A rather variable current, -67.9 ± 6.7 pA (level A3), was recorded during the fraction of a second that the system remained in the inter-state. The ground level stayed occupied for the following 12 s. After this time, an interesting rise of current, appearing more continuous than discrete, was observed (B). Some stochastic transient fluctuations were superimposed over the signal since $t = 16.7$ s. The chaotic-looking behavior was terminated abruptly at $t = 19.25$ s by a drop to -20.8 ± 2.2 pA (level B2), which implies that both the continuous change and the fluctuations could be attributed to a single entity. Interestingly, level B2 is by 13.7 pA lower than level A1. During the following 11 s, the system remained at a relatively stable state, performing only a few quasi-persistent steps by ~ 20 pA ($t = 20.2, 23.6$). These phenomena could perhaps be attributed to the specific way an α HL channel can become or cease being electrically accessible in an npsLB. An assembled α HL channel exhibits a mushroom-shaped structure: a bulky cap forms at the side of contact with the bilayer, and a hollow β -barrel, the stem domain, spans the bilayer.¹⁴⁸ No extramembrane (EM) domain exists at the base of the stem. It thus appears that there is no restriction for complete transmembrane (TM) α HL channels to assemble in an sBLM. A lateral diffusion rate of $6 - 7 \times 10^{-3} \mu\text{m}^2/\text{s}$ has been reported for a single TM peptide helix without EM domains that was embedded in an sBLM on glass.¹⁶³ Since the external diameter of the TM α HL stem domain is not substantially larger than that of the TM helix, a similar lateral mobility in an sBLM can be expected for the channel. npsLBs of the design presented here are presumed to retain diffusibility among the supported and the pore-spanning regions of the sBLM patch formed via GUV collapse at the surface. This should hold true for both leaflets of the bilayer. α HL channels embedded in the sBLM should thus be able to diffuse freely from the supported to the pore-spanning regions, and vice versa. Such lateral entries and exits of assembled channels to and from an npsLB are expected to induce electrical effects comparable to those associated with channel opening and closing, respectively. Traversing of an open channel the boundary between the supported and the pore-spanning BLM might give rise to additional current modulation at transition events that has not been observed previously (e.g. the ‘continuous-like’ change of current magnitude in Figure 4-54-A).

Summary. The above figures demonstrate a variety of changes of npsLB conductance that were detected after addition of α HL into the medium bathing the bilayers. As only steady-state currents of low magnitudes were observed for purely lipidic npsLBs in the absence of the toxin (e.g. Figure

4-52-1A,B), the observed changes of conductance can unambiguously be attributed to α HL adsorption and agglomeration in the npsLBs. The magnitude of the current transitions entails that single-channel level resolution has been attained in the recordings. Interestingly, the nature of the observed effects was far more heterogeneous than reported previously. Besides the ‘usual’ conductance transitions for the particular electrolyte concentration and TM potential (Figure 4-54-1), conductance steps of lower magnitudes with both short and long dwell times were seen. Comparative experiments in classical painted BLMs were hence performed to better understand the grounds of this motley behavior.

B. α HL in painted BLMs

In former studies, conductance behavior of α HL channels has been investigated almost exclusively using painted BLMs.^{152,153,160,161} We pursued analogous experiments in painted BLMs to relate to the previous findings and to establish a reference for the α HL recordings in the novel architecture of npsLBs presented above. Voltage-clamp measurements on painted BLMs in the presence of α HL were performed under equivalent conditions and using the same α HL sample as in the case of npsLBs. The following figures display examples of recordings of ionic currents through α HL channels across painted DPhPC/*n*-decane BLMs. The ‘A’ sections of the figures show *I*-vs.-time traces, whereas the ‘B’, ‘C’, and ‘D’ sections show respective current amplitude histograms. As in the preceding figures of this chapter, sections of the *I*-vs.-time traces used to construct the amplitude histograms exhibit a gray background.

An example of α HL behavior in a painted BLM comparable to that reported previously is shown in Figure 4-55. The initial steady current of -5.1 ± 1.1 pA (level 1) at a TM holding potential of 100 mV is the same as that before toxin addition. At $t = 5.4$ s, an instantaneous current magnitude increase by a single 60.1 pA step to a new steady-state level of 65.6 ± 2.1 pA (level 2) occurred.

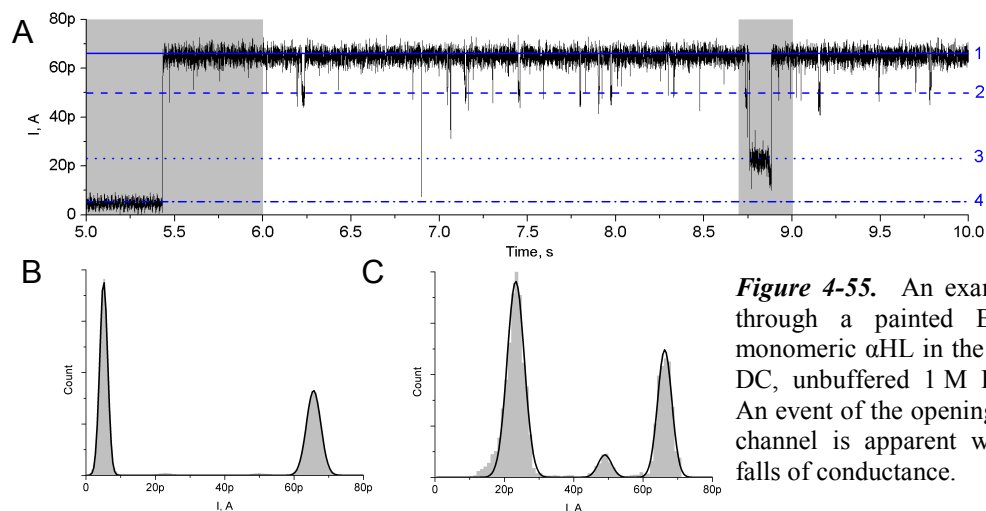


Figure 4-55. An example of a current recording through a painted BLM in the presence of monomeric α HL in the bathing medium. +100 mV DC, unbuffered 1 M KCl in both compartments. An event of the opening of a typical persistent α HL channel is apparent with some unusual transient falls of conductance.

The system remained in the newly-acquired state for the following 70 s, when the measurement was terminated (not shown). Brief stochastic current drops from level 2 to at least two additional current levels (levels 3 and 4, 49.0 ± 1.9 pA and 23.3 ± 2.5 pA, respectively) are evident. Correlating these observations to previous findings on the properties of painted BLMs in the presence of α -hemolysin makes it possible to attribute current level 2 to the presence of a single α -hemolysin channel in the BLM. The momentary drops of current to levels 3 and 4 can be associated with transient conductance alterations of the channel. These stochastic alterations can possibly be due to: 1) changes in the inner pore conductance due to ionization of pore walls¹⁵³ while the oligomer remains assembled, 2) transitions of the oligomer as a whole towards the non-inserted pre-pore^{150,151}, 3) some of the monomer subunits falling out of the aggregate comprising the pore (but variation after formation not usually seem¹⁶¹, and pre-pore assumed to be irreversible¹⁶⁴, and/or 4) failures of the pore to span the BLM in the peripheral regions of the BLM where the bilayer thickens to and becomes the torus.

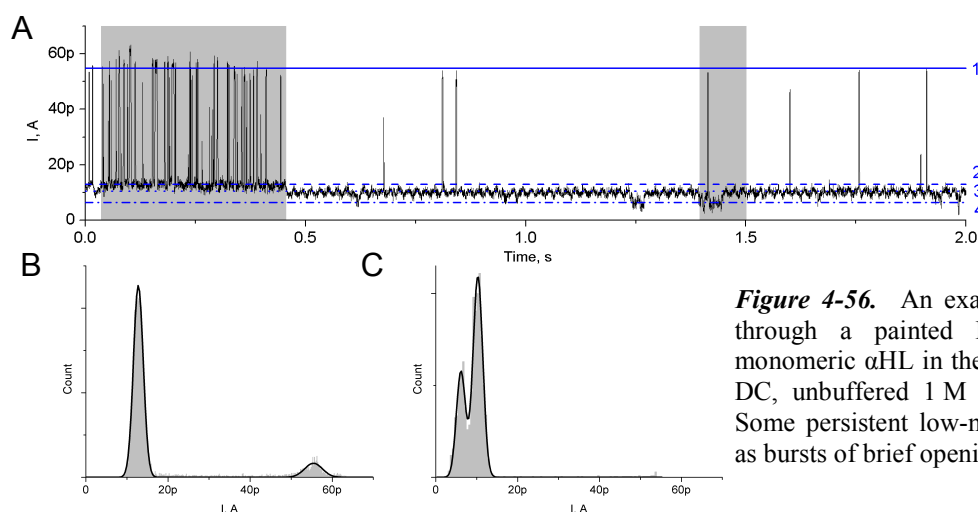


Figure 4-56. An example of a current recording through a painted BLM in the presence of monomeric α HL in the bathing medium. +100 mV DC, unbuffered 1 M KCl in both compartments. Some persistent low-magnitude transitions as well as bursts of brief opening events can be seen.

Alternative channel behavior observed under the same experimental conditions is illustrated in Figure 4-56. Unlike in the former example, the channel, or channels, for the simultaneous involvement of several units cannot be ruled out *a priori*, now remain(s) in a primarily closed or low-conductance state. Low-magnitude transitions from the dominant current level of 10.3 ± 1.2 pA (level 1) either downwards to 6.1 ± 1.1 pA (level 2) or upwards to 12.8 ± 1.2 pA (level 3) are apparent. Moreover, rapid transient steps to 55.5 ± 2.2 pA (level 4) occurred in a few moments from level 1 and very frequently from level 3.

Figure 4-57 gives evidence for yet another sort of ionic current transitions across a BLM in the presence of the toxin. Here, the brief closing or opening transitions presented in the preceding examples are completely absent. The specific current levels, once attained, remain occupied for

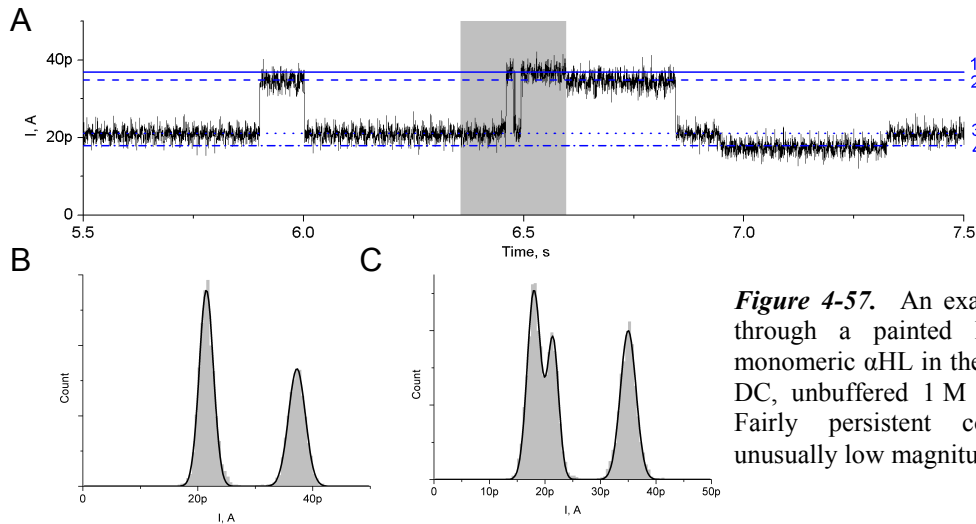


Figure 4-57. An example of a current recording through a painted BLM in the presence of monomeric α HL in the bathing medium. +100 mV DC, unbuffered 1 M KCl in both compartments. Fairly persistent conductance transitions of unusually low magnitudes.

periods in the order of hundreds of milliseconds. It is noteworthy that direct transitions among levels 1, 2 and 3 are possible. As for level 4, transitions to and from level 3 were observed only.

In contrary to the previous three current trace examples, the next figures present current recordings of magnitudes that are above the maximum unitary α HL conductance reported for 1 M KCl. Partial deterioration of the seal resistance of painted BLMs on single apertures does not occur. It is thus justified to presume that more than one open channel are present in the BLM in any moment of the recordings shown below. A current recording is illustrated in Figure 4-58 that exhibits evident persistent transitions from 231 ± 5 pA (level 4) to two other current levels: 262 ± 5 pA (level 3, step magnitude 31 pA) and 309 ± 4 pA (level 2, step magnitude 78 pA). Transitions to level 3 were rare and coupled exclusively to level 4. Level 1 (327 ± 4 pA) seemed to be reachable from level 2 only (step magnitude 18 pA) and such transitions were abundant. The dwell times at level 1 were longer than those at level 2. In addition, very frequent short-lived current drops in the order of about -20 pA can be noticed at any of the four conductance levels. These fluctuations are responsible for the significant asymmetry of the amplitude histogram peak distributions of Figure 4-58B and C. Overall, the figure captures an interesting but complex transitory behavior of several α HL channels. At least two sorts of phenomena seem to be happening at the same time: relatively persistent transitions of both high ($4 \leftrightarrow 2$) and low ($2 \leftrightarrow 1$) magnitudes, and recurrent transient downward pulses of ~ 20 pA. Given the fact that a transition from level 4 by +18 pA was not observed, the former can most likely be related to opening and closing of a particular single α HL channel with at least two distinct conductance sub-states. The fact that the characteristics of the latter effect do not change upon the high-magnitude transitions implies that at least one independent α HL aggregate exists in the BLM that exhibits a completely different transitory behavior.

4. Results and discussion

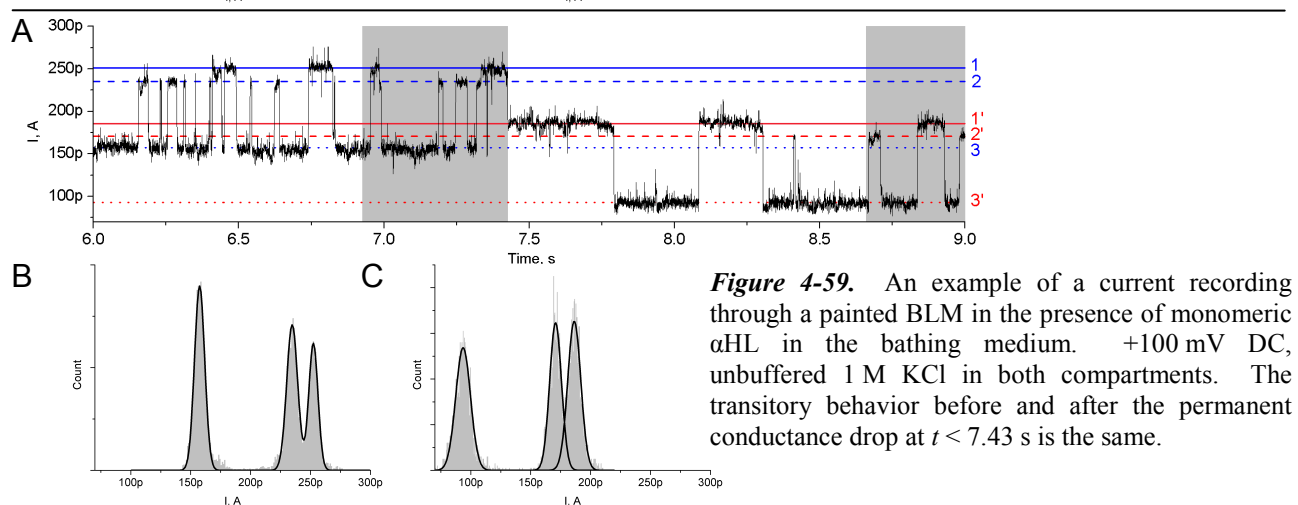
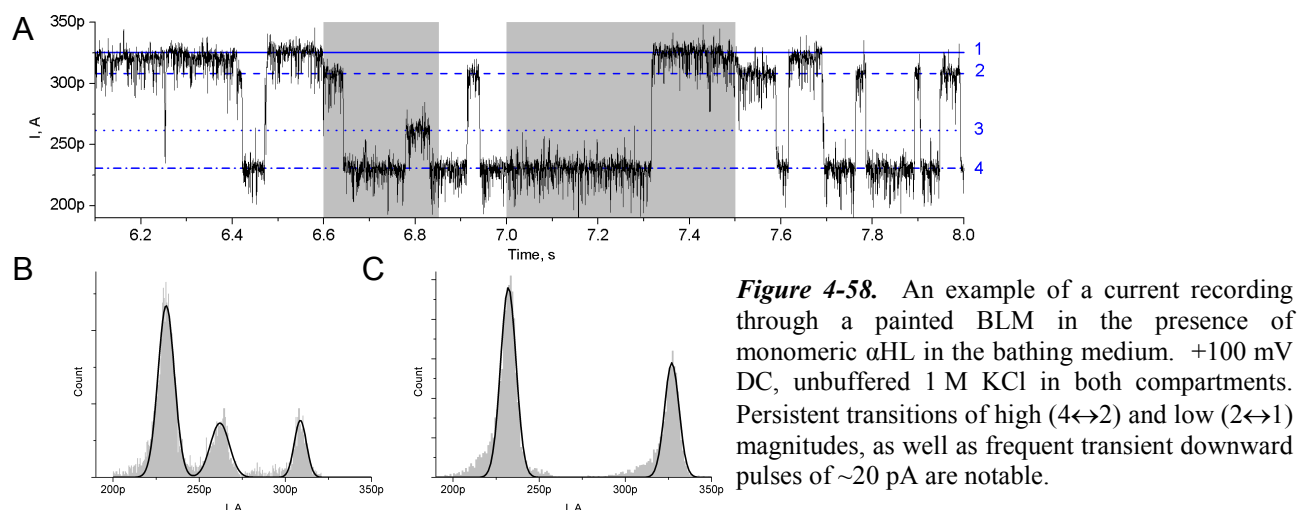


Figure 4-59 captures a scenario similar to that displayed in Figure 4-58. At $t < 7.43$ s, transient openings of intermediate duration, $3 \leftrightarrow 2$ ($\Delta G \approx 78$ pA) and $2 \leftrightarrow 1$ ($\Delta G \approx 17$ pA), were recorded. Unlike in the preceding case, however, the $3 \leftrightarrow 1$ ($\Delta G \approx 95$ pA) transition seems to be possible here. At $t = 7.43$ s, a shift of the complete pattern by about -65 pA occurred. The new current levels, denoted as 3', 2', and 1', were 93 ± 6 pA, 171 ± 5 pA, and 186 ± 5 pA, respectively. The intervals between the conductance levels remained virtually the same as before the drop (histograms B and C). Such a shift of the pattern is indicative of a persistent closure of a single α HL channel with conductivity of ~ 0.65 nS. As the pattern of current transitions appears to be the same before and after the shift, one can draw the conclusion that the channel, the closing of which induced the shift, was not involved in the transient switching. A shift analogous to the one just described is presented in Figure 4-60, too. Again, repeated current steps from 166 ± 5 pA (level 3) to either 243 ± 4 pA (level 2) or 261 ± 4 pA (level 1) can be observed initially. A solitary brief drop by -85 pA from level 3 and a step upwards by 83 pA from level 2 occurred at $t = 0.76$ s and $t = 2.32$ s, respectively. At $t = 2.45$ s, the latter step was followed by a brief drop to 227 ± 3 pA, which in the further course

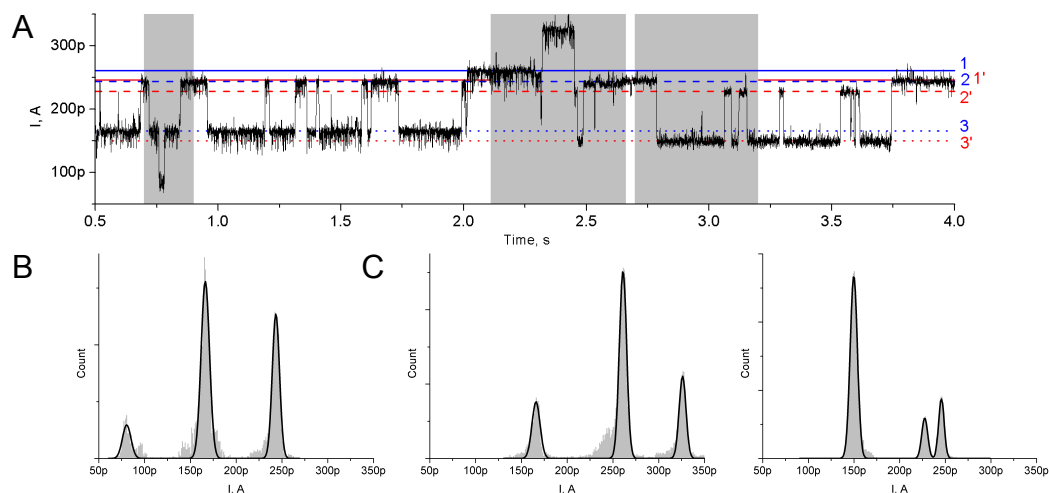


Figure 4-60. An example of a current recording through a painted BLM in the presence of monomeric α HL in the bathing medium. +100 mV DC, unbuffered 1 M KCl in both compartments. Conductance levels 1-3 are shifted by -16 pA and the recurrent transient downward pulses disappear at $t = 2.45$ s.

of the recording turns out to be level 2', then a full decline to 150 ± 4 pA (level 3'), and a rise to 246 ± 3 pA (level 1'). As in the previous case, current levels 1, 2 and 3 were all shifted downwards, this time, however, by about -16 pA only. In contrast to the previous case, an additional change is apparent in the trace here: the extent of low-magnitude current fluctuations is significantly reduced after the instant of the shift. Numerous brief drops in the order of ~ 20 pA, reminiscent of those captured in Figure 4-59, can be noted at any conductance level before $t = 2.45$. Again, their occurrence is clearly noticeable in the histograms B and C, but not D, as uneven (leftward) lateral spreading of the otherwise strictly Gaussian distributions. The magnitude and dwell time of the pulses are comparable to those presented in Figure 4-59. Intriguingly, the fluctuations disappear right at the shift at $t = 2.45$. It seems that a permanent closure of a particular transiently-closing channel with low conductance was captured. Although happening subsequently, it remains unknown whether the closure of the channel was induced by the transition to 326 pA at $t = 2.32$. As before, though, it appears that the transitions among levels 1, 2, and 3, or 1', 2', and 3', were not affected by the closure of this channel. As suggested before, independent units seem to be responsible for the recurrent transient low-magnitude falls and the relatively persistent current transitions.

A different form of a quasi-regular stepping pattern among current levels is illustrated in Figure 4-61. Initially, the system switches among two persistent (1 and 2) and one relatively transient (3) levels of conductance, with infrequent momentary drops of higher amplitude. The difference between the neighboring main levels is 16 and 29 pA. All transitions involved level 2, i.e. no direct switching between levels 1 and 3 was observed. No transitions to a hypothetical level 2_x that would be located at 29 pA above level 3 and 16 pA below level 1 were detected. This fact implies that the

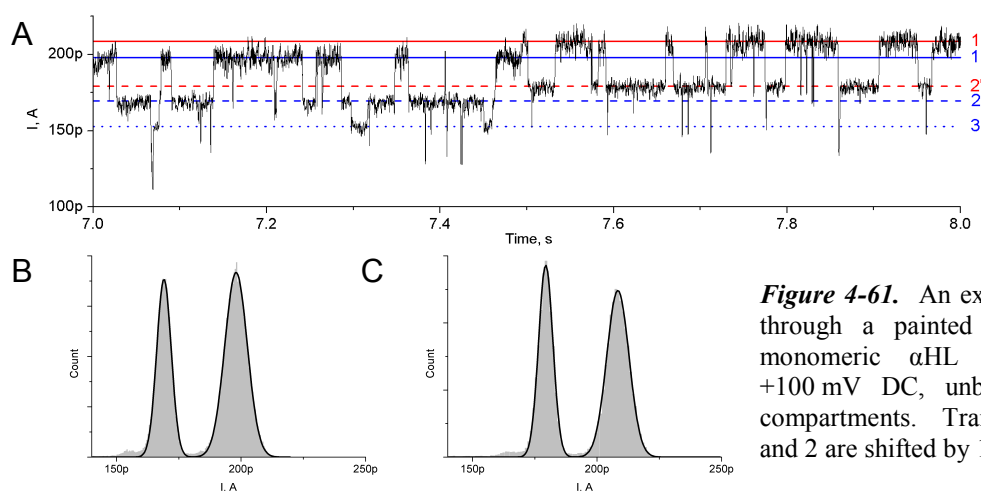


Figure 4-61. An example of a current recording through a painted BLM in the presence of monomeric α HL in the bathing medium. +100 mV DC, unbuffered 1 M KCl in both compartments. Transitory conductance levels 1 and 2 are shifted by 10.5 pA at $t = 7.49$ s.

two transitions are not independent, and that they are most likely related to the same channel. Besides, there is a marked increase of width of the peak of level 1 as compared to level 2 in the amplitude histograms. Although unspecific noise originating from independent pores is cumulative, for a 10% increase of current magnitude, as is the case upon a step from level 2 to level 1, the increase of amplitude dispersion purely due to unspecific noise is inadequate. Apparently, an additional mode of rapid low-magnitude conductance oscillations is attained at level 1. At $t = 7.49$ s, a step by +10.5 pA from level 1 shifts the pattern upwards. Although the remaining 450 ms of the figure do not capture a transition to level 3', this level has been attained repeatedly in the following moments of the recording. Thus, again, either a persistent opening of a new low-conductance α HL channel, or an increase of conductance of an existing one was observed. The undisturbed continuation of the transitory conductance pattern implies that the two phenomena are independent. Figure 4-62 depicts a recording of the same BLM about a minute later. Again, the least probable transition $1 \leftrightarrow 3$, or $1' \leftrightarrow 3'$, was not captured in the presented 700 ms. The frequency and magnitude of transitions between levels 1 and 2 remained unchanged. At $t = 0.25$ s, the two levels are shifted upwards again, this time by +60 pA, however.

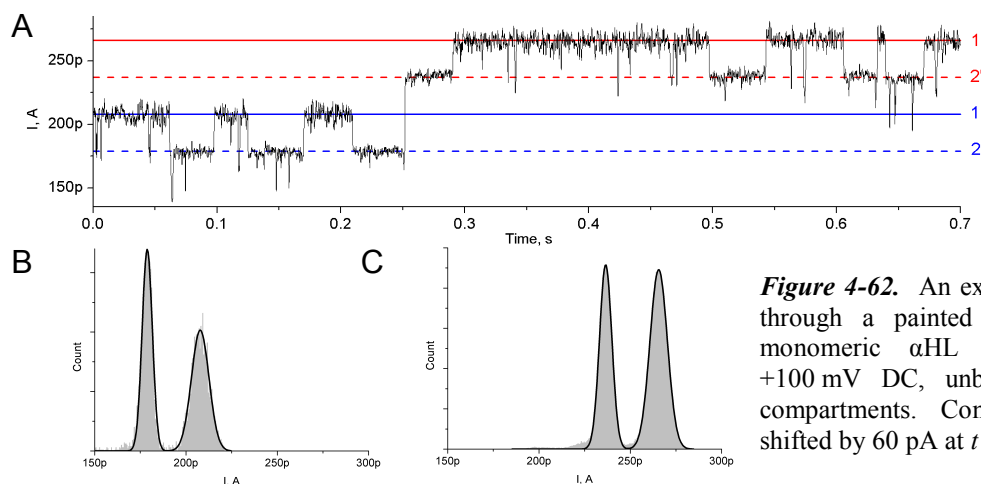


Figure 4-62. An example of a current recording through a painted BLM in the presence of monomeric α HL in the bathing medium. +100 mV DC, unbuffered 1 M KCl in both compartments. Conductance levels 1 and 2 are shifted by 60 pA at $t = 0.25$ s.

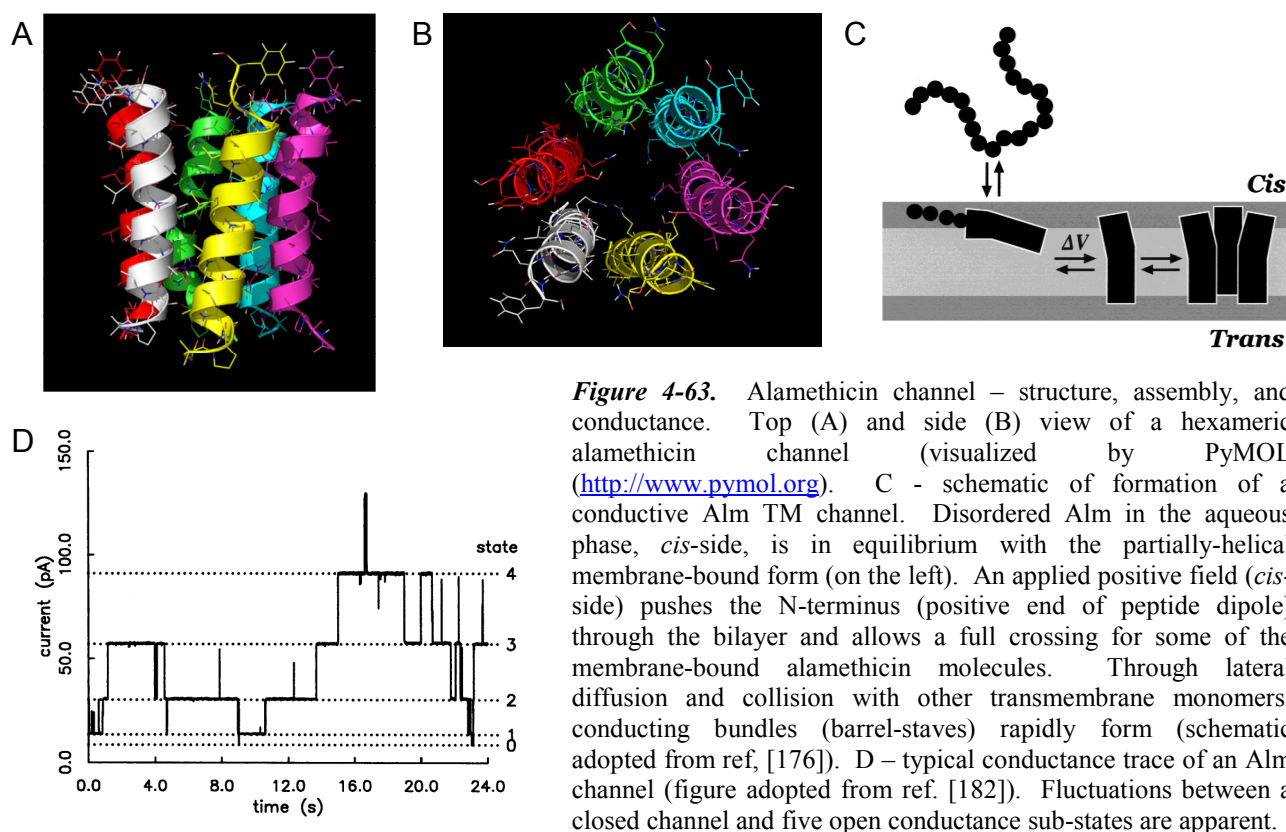
Summary. Similar to the case of npsLBs, voltage-clamp recordings of ionic currents through painted BLMs in the presence of α HL revealed an unexpectedly motley behavior of the toxin-induced channels. Apart from transitions between current levels of magnitudes characteristic of the ‘typical’ high-conductance state of the channel, a plethora of low-scale transitions, some of them as low as ~ 3 pA, were observed. This finding implies that the unusual conductance behavior of npsLBs in the presence of α HL was not induced by the npsLB platform. Although non-typical conductance states of wild-type α HL channels have been reported previously, they are badly characterized and believed to, once attained, be reversible only by elimination of the clamping voltage. Here, on the other hand, countless reversible current steps of various magnitudes were detected. It thus appears that instead of the npsLB platform, the origin of the unusual conductance effects can be attributed to the sample of α HL available for this study. Contamination or degradation of the sample might have affected the monomeric peptides in a way that resulted in altered channel assembly and/or functionality. Unfortunately, a biochemical analysis of the toxin sample was out of the scope of this study. Regardless of the grounds of the non-typical conductance, the α HL experiments gave an unmistakably positive answer to the principal question whether DC voltage-clamp recordings with single-channel resolution could be achieved with our npsLBs setup. Further investigations were pursued using an alternative microbial channel-forming peptide, alamethicin.

4.6.3. Alamethicin

4.6.3.1. Background

Alamethicin (Alm), an antibiotic peptide produced by the fungus *Trichoderma viride*, spontaneously inserts into lipid membranes producing voltage-gated channels.¹⁶⁵ Alm is a relatively small linear molecule (~ 2000 g/mol) consisting of 19 amino acids and 1 amino alcohol.¹²⁵ The name of the peptide is derived from the prevalence of the rather unusual α -methylalanine in the primary structure. The secondary structure of the Alm monomer determined by crystallography is largely α -helical with a bend in the helix axis at an internal proline residue. The helix structure is highly amphipathic as most of the solvent-accessible polar groups lie on a narrow strip of surface parallel to the helix axis.¹⁶⁶

Under an applied transmembrane potential of the correct polarity, alamethicin readily forms well-defined channels with multiple conductance states¹⁶⁷ in a wide range of artificial lipid bilayers¹⁶⁸ and natural cell membranes¹⁶⁹ (Figure 4-63D). The channels have long open durations¹⁷⁰, especially in phospholipid bilayers at low temperatures¹⁶⁸. The size of a single Alm molecule is too small to form a conducting pore¹²⁵. This, together with the kinetics of Alm channel



formation^{168,171,172}, indicates that an Alm channel is an aggregate of a number of monomers. Individual Alm monomers in the channel aggregate have mainly helical conformations and span the lipid bilayer with the axes of the helices normal to the plane of the bilayer^{173,174} (Figure 4-63A and B). Channels are formed by bundles of such helices surrounding aqueous pores through which ions can pass across the lipid bilayer. This so-called ‘barrel-stave’ model further assumes continuous dynamic uptake and release of individual transmembrane monomers within the conducting bundle (Figure 4-63C). The characteristic Alm conductance substates are explained by a change in the channel cross-section due to the fluctuation in the number of monomer units in the oligomer. Up to eight different sub-conductance states of a single Alm channel were identified that are presumed to correspond to 4-11 monomers composing the conducting aggregate. The voltage-gating effect arises by alignment of peptide monomers adsorbed flat at the surface of a lipid bilayer to a membrane-spanning orientation by a TM electric field via coupling to the molecular dipole.

4.6.3.2. Alm single-channel recordings

Further DC current recordings through single polypeptide channels inserted in npsLBs were conducted with the fungal peptide antibiotic alamethicin (Alm). Discrete current steps typical of transitions between individual conductance states of the transmembrane permeable bundle formed by Alm monomers were observed after administration of Alm in the bathing medium (see Figure

4-65 and Figure 4-66 for typical current traces).^{125,175,176} Lifetimes of the individual substates were in the millisecond range, while a channel as a whole would remain assembled for seconds, as reported before.¹²⁵ For comparison, recordings of ionic currents through Alm channels were

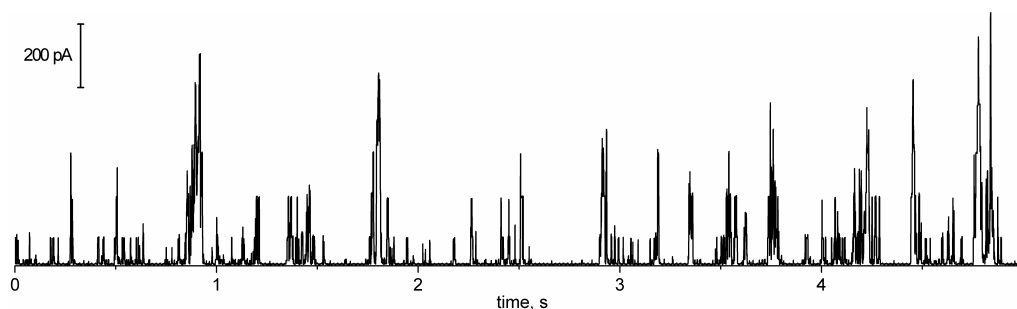


Figure 4-64. Recording of an ionic current through Alm channels in a classical BLM painted over an aperture in a Teflon septum. Most of the bursts are due to a single channel, although two channels act simultaneously at a few moments. The current was measured at 105 mV DC with the side of Alm administration being positive. The BLM was bathed by 1 M KCl, 5 mM HEPES, pH 7.

additionally done in classical painted BLMs. At Alm concentrations whereby a sole Alm channel was active in the bilayer, current bursts of significantly shorter duration (i.e. channel mean open time) and lower preferred conductance states were observed in painted BLMs as compared to npsLBs (Figure 4-64 vs. Figure 4-65 and Figure 4-66). Six discrete conductance levels per single channel were found at most, contrary to maximum of eight conductance substates detected in npsLBs (Figure 4-67). Moreover, assembly of multiple channels was far more frequent in BLMs than in npsLBs (e.g. Figure 4-67B). Membrane properties such as thickness, tension, and fluidity have been shown to alter the dynamics and stability of Alm helix bundles.^{168,169,175} The differences described above in Alm behavior in the *n*-decane-containing painted BLMs and the solvent-free npsLBs can be well related to the fact that the former are thicker and tenser than the latter^{177,178}.

4.6.3.3. Transmembrane voltage effects

Induction of channel assembly by transmembrane potential characteristic of Alm channels was observed in npsLBs, in agreement with previous studies using Muller-Rudin,^{64,68,69} Montal-Mueller,¹⁷⁹⁻¹⁸¹ and other lipid bilayer systems.^{45,182} Higher transmembrane potentials gave rise to current bursts of higher frequency of appearance (Figure 4-65). Moreover, it is apparent in the figure that channel mean open time increased significantly upon potential step from 60 mV to 80 mV, but remained roughly the same at 100 mV as compared to 80 mV. Quasi-ohmic (supra-linear) behavior has been reported for the respective conductance substates of an Alm channel.^{125,182} For the traces of Figure 4-65, conductance of substates 3-5 increased by a mean factor of 1.65 and 1.36, respectively, upon potential increase from 60 mV to 80 mV and 80 mV to 100 mV.

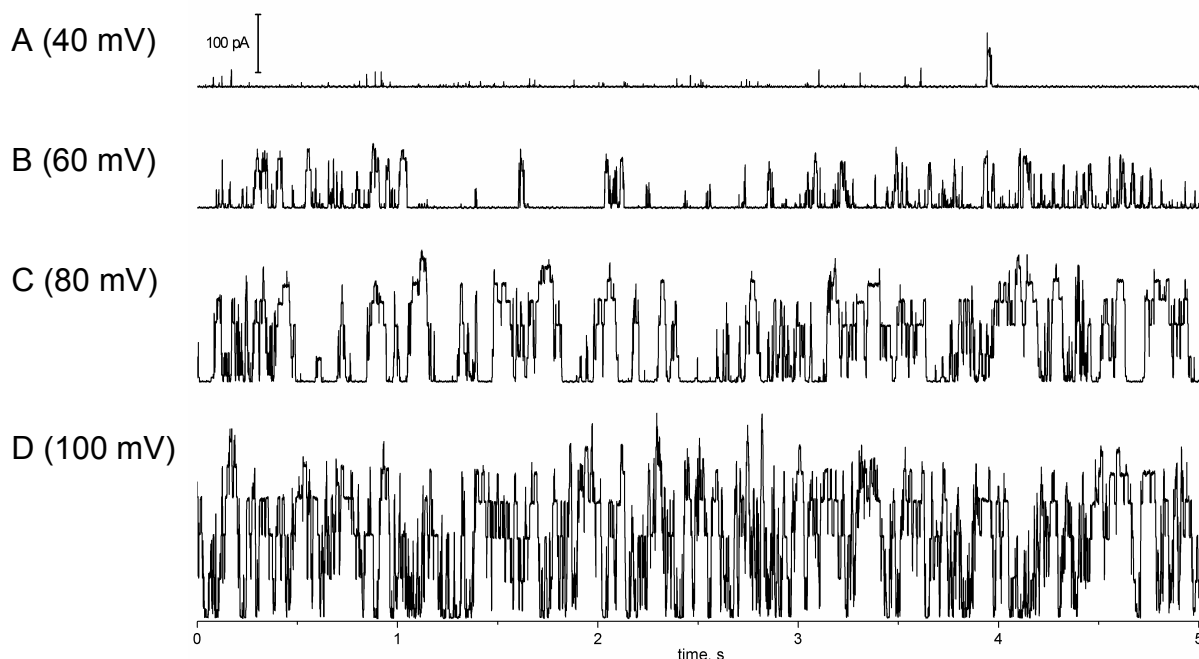


Figure 4-65. The effect of varied DC potential on ionic currents through a single Alm channel in an npsLB (A – 40 mV, B – 60 mV, C – 80 mV, D – 100 mV). The traces were recorded one after another without delay starting at 40 mV. The npsLB was bathed by 1 M KCl, 5 mM HEPES, pH 7. All traces are scaled equally.

4.6.3.4. Alamethicin concentration effects

In accordance with previous findings¹⁷¹, higher concentration of Alm in the bathing medium increased the frequency of burst appearance (Figure 4-66A and B). Pause of convection of electrolyte (perfusion) was found to result in a gradual decrease of frequency of current bursts (C). It appears that the density of the peptide in the npsLB was falling in time. Similar to what has been suggested for gramicidin, this could be due to equilibration of the concentration between the bilayer and the bathing medium according to a steady-state partitioning coefficient after convection had ceased. If Alm could traverse the bilayer, diffusion into the upper compartment completely free of the peptide would make the decay even more pronounced. Unlike in the case of gramicidin, however, Alm had only been administered from the pit side through the pores. Obviously, the npsLB was the only point of entry for every Alm monomer into the SLB patch. The ratio of concentration of the peptide in the npsLB relative to the rest of the SLB patch is thus expected to be very high. As fluidic continuity is assumed between the free-standing and the supported regions of the SLB, it may be that the polypeptide also diffused within the bilayer into regions of the SLB patch not electrically accessible.

Current traces recorded after further perfusion with electrolyte containing still more Alm per unit volume showed higher overall magnitudes and lacked the clearly discernible conductance substates (Figure 4-66D). The corresponding histogram reveals numerous discrete conductance levels.

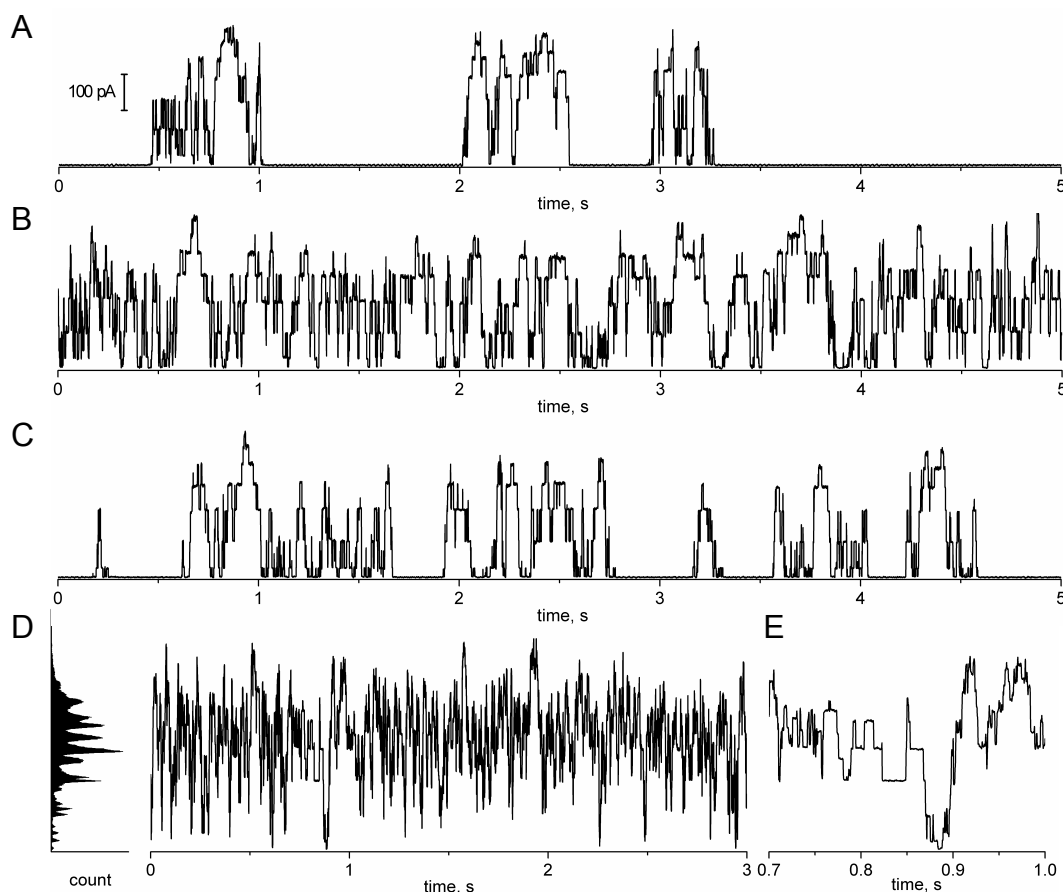


Figure 4-66. The effect of perfusion on ionic currents through Alm channels in an npsLB. Before the recordings, the pit side of the Si_3N_4 window was perfused continuously for ~ 60 s with base electrolyte containing Alm. B – immediately after perfusion, C – 150 s after B, D – after further perfusion, E – a section of D at finer temporal resolution. The currents were measured at 130 mV DC with the side of Alm administration being positive. The npsLB was bathed by 1 M KCl, 5 mM HEPES, pH 7. All traces are scaled equally.

Apparently, simultaneous opening of multiple channels has been induced at higher polypeptide concentrations, as reported previously.¹⁷⁵ A rare moment of idleness of all but one channel is shown in trace E of the figure ($t = 0.79 - 0.88$ s). Subsequent reduction of transmembrane potential had an impairing effect on channel activity, resulting again in current traces with predominantly a single active channel (not shown).

4.6.3.5. Unique alamethicin behavior in npsLBs

A. Conductance of respective channel substates

Comparison of Alm single channel conductance in npsLBs and classical BLMs. Unlike any other bilayer system that Alm has been studied in thus far, the magnitude of conductance of the respective substates of the channel in npsLBs did not obey a quasi-geometric progression. Instead, $\Delta G_n = G_n - G_{n-1}$ was found to grow for $n < 3$ only, and decline for $n > 3$.

Figure 4-67 compares the levels of conductance of the respective substates of the Alm channel in an npsLB and a painted BLM. Sections A and B of the figure are traces of ionic currents (converted to

G) flowing through Alm channels in an npsLB and a painted BLM, respectively. A clear difference is apparent between the distributions of peaks in the histogram plots of the conductance traces. Except for substates O_1 and O_2 , conductance of every substate was lower in the npsLB than in the painted BLM (Figure 4-67C). The conductance differed by as much as a factor of 2 for substate O_6 . In a painted BLM, ΔG grows continuously with substate sequence number, whereas in an npsLB ΔG declines steadily above substate O_3 . The BLM traces of C and D are plots of mean values of 9 bursts whereby O_6 had been attained. As in npsLBs the conductance of a particular substate has also been observed to drift in time (*vide infra*), the npsLB traces in C and D are derived from a single burst. An event of highest overall conductance has been chosen for the plots.

Schmidt et al. reported successful recordings of ionic currents through single Alm channels using a platform based on Si_3N_4 diaphragms similar to ours⁴⁴. Although the authors do not discuss any

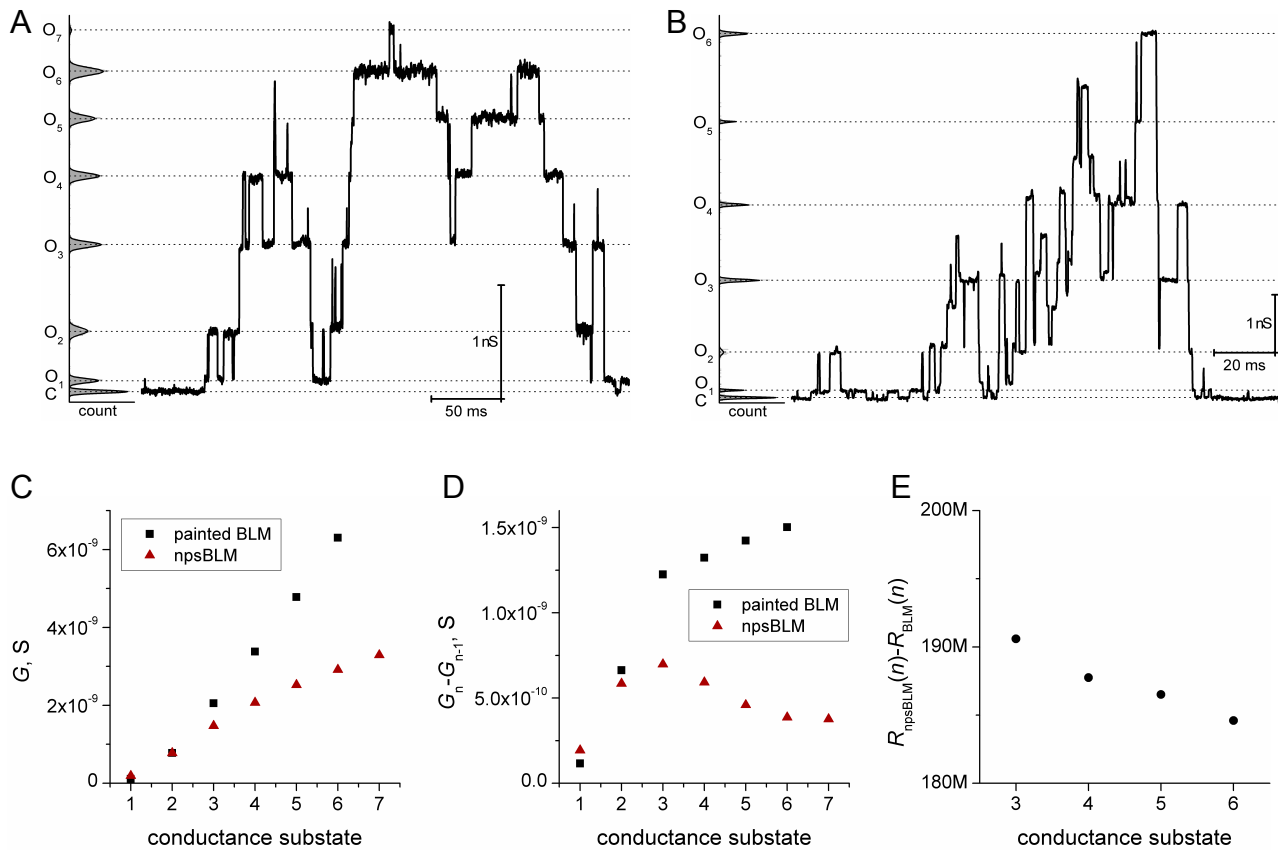


Figure 4-67. Comparison of Alm single-channel conductance in an npsLB and a classical painted BLM. A, B – recordings of ionic currents (converted to G by $G = I/U$) through Alm channels in an npsLB and a classical BLM, respectively. Fluctuations between conductance substates of two Alm channels are apparent in the initial phase of B, whereas only a single channel remains active in the final phase of the recording. Current amplitude histograms are plotted to the left of the respective current traces, mean conductance levels are indicated by horizontal dashed lines (in B the histogram corresponds to the single-channel part of the recording only). Note the different scaling (both X and Y) for A and B. C and D are plots of total (G_n) and differential ($\Delta G_n = G_n - G_{n-1}$) conductance vs. conductance substate of a single Alm channel in an npsLB and a classical BLM. E is a plot of the additional resistance ($R_{\text{add}}(n) = R_{\text{npsLB}}(n) - R_{\text{BLM}}(n)$) associated with the npsLB but not the classical BLM. All data were acquired in 1 M KCl, 5 mM HEPES, pH 7.

peculiarities in the detected channel behavior, a careful examination of the current amplitude histogram presented in the paper reveals that in their case, too, ΔG was not strictly monotonous, but showed a maximum at $n = 3$. The conductance was not as attenuated as in our case, however. Sondermann et al., on the other hand, obtained the typical distributions of Alm substate conductance in GUV-derived psLBs over apertures in thin glass slides.⁴⁵ In all three cases including ours, the bilayers were suspended over the pores via hydrophilic interactions of the lipid molecules with the surface around the pores. Schmidt et al. enhanced the electrostatic interaction between the support and the lipid by a charged coating and inclusion of charged lipid species in the vesicle envelope. Similar to our approach, Sondermann et al. let their PC GUVs spread and rupture on clean glass without additional functionalization. It appears it is the character of the pores or the surface of the support that induces the attenuation of Alm conductance. Several possibilities as to the grounds for this interesting behavior will be discussed below.

Improper channel assembly. Primarily, improper channel assembly in the free-standing npsLB could be considered: a property might exist in the lipid bilayer that would impair the formation of channels with lumen as wide as in other bilayer platforms. Obviously, narrow channel lumen could account well for the lower conductance of the channels. Except for the (unnoticed) altered behavior in the npsLBs of Schmidt et al., though, only the typical Alm conductance patterns have been reported consistently for a wide variety of bilayer systems. It is unlikely, therefore, that our solvent-free free-standing npsLB would prevent proper channel assembly so exclusively.

Additional resistance. If proper channel assembly is assumed, an additional (constant) resistance in series with the channel resistance seems to have the potential to qualitatively explain the observed effects: the higher the conductance substate of the channel, the lower the channel resistance, and thus the more prominent the contribution of the additional resistance to the total resistance. As normal distribution of conductance levels was observed in the painted BLM, it seems that the additional resistive contribution must somehow arise from the porous Si_3N_4 diaphragm. The additional resistance, $R_{\text{add}}(n)$, due to the npsLB relative to the painted BLM can be expressed as

$$R_{\text{add}}(n) = R_{\text{npsLB}}(n) - R_{\text{BLM}}(n), \quad (\text{Eq. 4-13})$$

where n is the sequence number of the channel conductance substate and $R_{\text{npsLB}}(n)$ and $R_{\text{BLM}}(n)$ are the resistances of the n^{th} substate in the npsLB and the painted BLM, respectively. $R_{\text{add}}(n)$ derived

from the curves of Figure 4-67C has been plotted in Figure 4-67E for $3 \leq n \leq 6$.^{*} The resistance is surprisingly consistent for the four substates and evaluates to $187 \pm 2 \text{ M}\Omega$. Can a reasonable source of $R_{\text{add}}(n)$ of such magnitude be identified? Two options will be discussed subsequently in the following: R_{add} due to the porous support 1) without, and 2) with interaction between the channel and the diaphragm.

Planar npsLB. Let us first consider the system as pictured in Figure 4-68A, i.e. a channel incorporated in a planar npsLB with no interaction between the channel and the Si_3N_4 support. The assumption that the npsLB spans flat over the pore is based on AFM reports on analogous bilayers.^{41,46,183} The resistance of a pore in a Si_3N_4 diaphragm and of an Alm channel in a painted BLM can be described similarly as

$$R_{\text{P}} = 2R_{\text{Pacc}} + R_{\text{Pint}} \quad (\text{Eq. 4-14})$$

and

$$R_{\text{CH}}(n) = R_{\text{BLM}}(n) = 2R_{\text{CHacc}}(n) + R_{\text{CHint}}(n), \quad (\text{Eq. 4-15})$$

respectively, where the subscript ‘P’ stands for ‘pore’, ‘CH’ for ‘channel’, ‘acc’ for ‘access’, and ‘int’ for ‘internal’. It thus holds for the resistance of an Alm channel in an npsLB spanning a pore that

$$R_{\text{npsLB}}(n) = R_{\text{CHacc}}(n) + R_{\text{CHint}}(n) + R_{\text{Pacc}} + R_{\text{P/CH}}(n), \quad (\text{Eq. 4-16})$$

where $R_{\text{P/CH}}(n)$ accounts for the resistance of pore lumen and access to channel through the pore. Can $R_{\text{P/CH}}(n)$ attain the required magnitude of $R_{\text{add}}(n)$? Unfortunately, an attempt to evaluate this resistance using eq. 4-16 relies on the quantification of $R_{\text{CHacc}}(n)$ and $R_{\text{CHint}}(n)$. $R_{\text{CHacc}}(n)$ can be calculated fairly accurately for O_3 and O_4 by correcting the values reported by Bezrukov and Vodyanoy¹⁸⁰ for 1 M KCl: $G(3) \approx 24 \text{ M}\Omega$, $G(4) \approx 22 \text{ M}\Omega$. Estimation of $R_{\text{CHint}}(n)$ via the simple approach of a conductive cylinder builds on three ambiguous assumptions: known channel length, ‘bulk’ conductivity of electrolyte within the channel, and no deviations in the structure of the channel from assumed cylindrical geometry.¹⁸⁰ The need to estimate $R_{\text{CHint}}(n)$ can be avoided by substituting eq. 4-15 and eq. 4-16 into eq. 4-13, which yields

$$R_{\text{add}}(n) = R_{\text{P/CH}}(n) + R_{\text{Pacc}} - R_{\text{CHacc}}(n). \quad (\text{Eq. 4-17})$$

^{*} As $R_{\text{npsLB}}(n) \approx R_{\text{BLM}}(n)$ for $n < 3$ and the currents associated with these conductance substates are relatively low, evaluation of $R_{\text{add}}(n)$ under this condition is considerably inaccurate.

A value of $\sim 210 \text{ M}\Omega$ is required of $R_{\text{P/CH}}$ for both O_3 and O_4 to make it fully account for the additional resistance (R_{Pacc} in the given pore geometry is negligible compared to the other terms). Two possibilities to model $R_{\text{P/CH}}$ are considered: 1) $R_{\text{P/CH}} = R_{\text{Pint}} + R_{\text{CHacc}}(n)$, and 2) $R_{\text{P/CH}} = R_{\text{cone}}(n)$, where $R_{\text{cone}}(n)$ is calculated from eq. 4-1 using the radius of the channel and the radius and length of the pore. Option 1 generates $\sim 25 \text{ M}\Omega$ and option 2 generates $\sim 35 \text{ M}\Omega$ for the given pore geometry, electrolyte conductivity, and substates O_3 and O_4 . These values fall far below the $\sim 210 \text{ M}\Omega$ needed to account for the observed effect of diminished G simply by pore geometry. Some improvement in the produced resistance values can be expected if the location of the channel near to the edge of the pore rather than the center of the npsLB is considered. This should induce a further constraint on the access of the channel through the pore. Nevertheless, roughly a 2-fold increase of $R_{\text{P/CH}}$ due to limiting the access to about a half of the former space still does not come anywhere near to the required value of resistance. Hence it appears that the notion of a flat npsLB with an active Alm channel whereby the channel does not interfere with the support is not able to explain the diminished conductance.

Curved npsLB. Let us next consider an Alm channel, still without interaction with the support, in an npsLB that does not span flat over the pore. The scenario is not much different from the above case for an npsLB protruding outward of the pore in a dome-like structure (Figure 4-68B). As above, the access to the channel through the pore should again depend on the location of the channel relative to the diaphragm surface, yet even in the near vicinity of the surface the inner channel access resistance is not expected to exceed $50 \text{ M}\Omega$ for substates O_3 or O_4 . The access resistance to the pore from the space between the bilayer and the diaphragm should not be substantially higher than the access resistance in an unrestricted space. The situation may become more interesting if an npsLB is considered that extends into the pore (Figure 4-68C). No difference to the above cases is presumed if the channel is located in the central part of the free-standing bilayer. At the periphery, however, the space occupied by electrolyte between the bilayer and the wall of the pore may be rather constrained. The inner access resistance of a channel located at the periphery of the npsLB can thus be significantly higher than in unrestricted space. It seems plausible for C to attain the magnitude of R_{add} this way. Unfortunately, there is an experimental observation, or rather a lack thereof, that flaws the scheme in part. As free diffusion of the polypeptide, be it monomeric or oligomeric, is assumed within the npsLB, a channel should assemble at or diffuse to the central region of the bilayer from time to time. It follows from the above analysis that the conductance of the channel should then be hindered by a series resistance of up to $\sim 10 \text{ M}\Omega$ only. In other words, $G_{\text{npsLB}}(n)$ of a channel located near the center of a flat or a

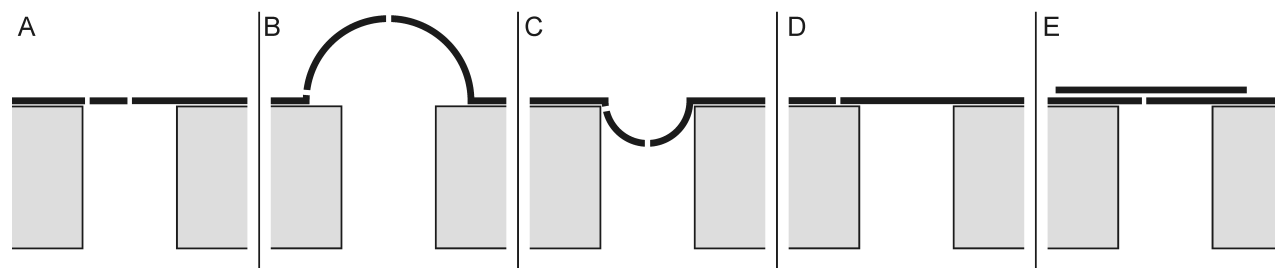


Figure 4-68. Possible scenarios of npsLB character and Alm channel location relative to the pore. A – npsLB spanning flat over the pore, B – outward-protruding npsLB, C – inward-protruding npsLB, D – Alm channel located in the SLB rather than the npsLB section of the BLM patch, E - additional lipid structure on top of the npsLB. Central and peripheral locations of the channel are indicated in A-C, as discussed in the text.

protruding npsLB should be virtually indiscernible from $G_{\text{BLM}}(n)$. Intriguingly, such conductance has not been observed. Reasons justifying why a channel, or Alm in general, in an inward-protruding npsLB would prefer the periphery to the center of the bilayer are unclear. It could be that the polypeptide is responsive to the character of curvature of the lipid bilayer and abounds predominantly at the peripheral regions of the npsLB where the curvature may be most favorable.¹⁸⁴

Alm channel in the SLB section. Yet another scenario to be discussed is that of the channel being located in the lipid bilayer supported by the Si_3N_4 diaphragm around the pore rather than in the free-standing npsLB itself. The series resistance, $R_{\text{P/CH}}$, would in this case be comprised by the aqueous layer between the lipid bilayer and the support, its magnitude being a function of the distance of the channel from the pore. White et al.¹⁰³ evaluated the ionic conductivity of the aqueous layer between a lipid bilayer and a glass support to $\sim 0.3 \Omega^{-1}\text{m}^{-1}$. Obviously, a distance must exist between the channel and the pore at which $R_{\text{P/CH}} \approx 210 \text{ M}\Omega$ regardless of actual channel conductance. Note that proper channel assembly, although still possible, should no longer be assumed if a channel in an SLB is considered. Presence of the channel in the SLB rather than the npsLB and the series resistance induced thereby seems to be able to credibly account for the unusual channel conductance. Besides, this notion is valid for any npsLB shape, be it flat, outward-, or inward-bent. As the previous hypothesis, though, it does not explain satisfactorily the absence of the ordinary conductance of Alm channels. The peptide had been administered from the pit side through the pore. As mentioned above, the npsLB was the only site of entry of Alm into the bilayer, hence the density of the peptide must have been higher there than in the surrounding SLB. Alm is known to primarily adsorb to the bilayer parallel to the surface plane. Distribution of the adsorbed peptide into the SLB by diffusion along the bilayer surface facing the pore should be constrained by the proximity of the support.¹⁶³ The rate of diffusion of Alm monomers that span the bilayer or are adsorbed at its outer surface from the npsLB into the SLB may proceed relatively unhindered. Alm monomers spanning the bilayer should readily assemble into channels. Monomers can be adsorbed

to the outer surface of the bilayer only after having spanned the bilayer previously. It is unclear, then, why channel assembly and the corresponding usual conductance had not been observed *before* the channels burdened by series resistances of $>190\text{ M}\Omega$ appeared.

Channel blocked by an additional lipid structure. A final possibility to consider is an additional lipid structure, perhaps a bilayer, on top of the npsLB partially blocking access to the channels. Judging by the magnitude of R_{add} , the structure would not extend too far around the channel in a continuous manner. Although our fluorescence observations of GUVs unfolding into SLB patches on Si_3N_4 surfaces indicated that regions of single bilayer leaflets prevail, multi-layered or otherwise altered structures cannot be disregarded completely. Obviously, an AFM study of the npsLB profile simultaneous or at least successive to the DC current measurements could help associate the altered conductance with one of the proposed hypotheses.

B. Continuous change of conductance of a specific substate

The mean conductance of a specific channel substate at a fixed DC potential remained fairly constant in painted BLMs. In npsLBs, on the other hand, continuous drifts of conductance levels such as the one depicted in Figure 4-69C were often observed for multiple substates that a channel

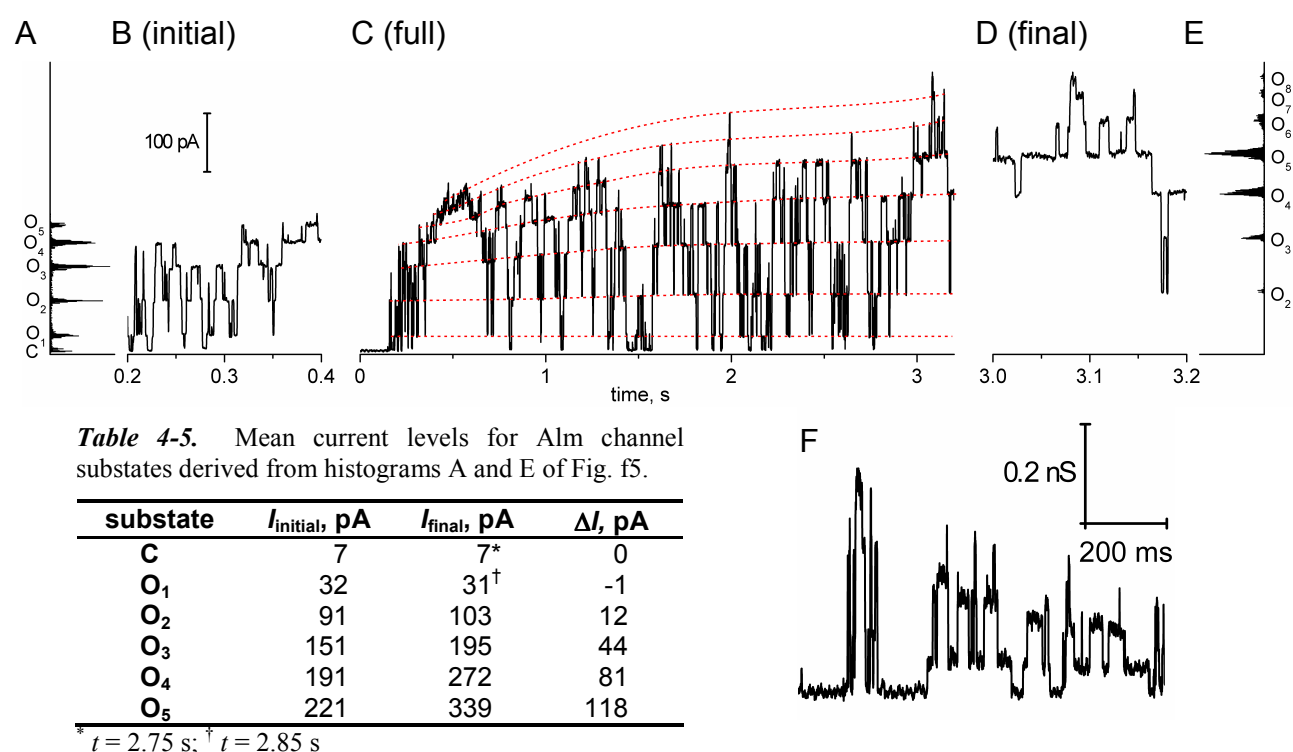


Figure 4-69. Continuous change of conductance of a single Alm channel in time. C – recording of an ionic current at 130 mV DC through a single Alm channel in an npsLB bathed by 1 M KCl, 5 mM HEPES, pH 7. The red traces approximate the continuous change of conductance of the respective seven substates. B, D – initial and final section of C at finer temporal resolution, respectively. A, E – current amplitude histograms corresponding to B and D, respectively. F – another example of a recording showing a continuous change of conductance of a single Alm channel. A substantial decline of conductance of O₂ and O₃ in time is obvious.

was fluctuating among. The increase of G of the individual substates is approximated by the dashed lines. Current amplitude histograms (A, E) have been extracted from 200-ms-sections of the initial and the final portions of the trace (B, D) and listed in Table 4-5. The change of mean current level per individual substate scales progressively with substate sequence number. No increase of conductance was detected for O_1 , whereas conductance at O_5 rose by 55%, and $\Delta G_{4 \leftrightarrow 5}$ increased by as much as a factor of 2.2. Section F of the figure is an example of a current recording analogous to that in C. Here, the conductance decreases, however, and substates as low as O_3 and O_2 are evidently affected. G_3 and G_2 seem to have changed by a factor of 2 in the course of the 200 ms. If an average value of ~ 0.3 nS is estimated for G_3 of the channel recorded in Figure 4-69F, then $R_{\text{add}}(3)$ for the particular recording calculated using eq. 4-13 evaluates to ~ 2.5 G Ω . Apparently, the interval of values that R_{add} can adopt seems to span more than an order of magnitude.

The suggestions presented above for reasons behind the unusual steady-state conductance of Alm channels in npsLBs all build on the concept of a series resistance related to the npsLB platform. In all of the proposals, the magnitude of the series resistance is a function of the location of the channel relative to the pore center. Fluidity of the bilayer and random diffusibility of the polypeptide monomers as well as oligomers therein is assumed. It seems feasible, then, that continuous change of G_n should occur due to spontaneous channel translocation by diffusion if the translocation is down or up a resistance gradient. In the case of an inward-protruding npsLB (Figure 4-68C), dynamics related to the shape of the bilayer itself (e.g. extent of protrusion or local distance between the bilayer and the pore walls) may induce the observed continuous changes of G_n without the necessity of channel translocation.

C. Spikes

An additional unique feature of Alm channels assembled in our npsLBs was a transient state of conductance about twice the G of substates O_7 or O_8^* (Figure 4-70). Such spikes occurred infrequently (once per ~ 150 s), yet they showed fairly consistent characteristics. In the majority of occurrences the spike marked the end of an ongoing burst. The rise and the decline of the current were typically very fast. Successive brief dwells at the lowest substates (O_1 - O_3) could usually be resolved at the decline. The duration of the transient measured at half-peak magnitude was in the order of ~ 1 ms. The basis of this interesting effect is currently not understood. It can be speculated that a number of monomers composing the channel can be attained that renders the agglomerate

* Typically it was not clearly discernible from the current trace whether the spike had been preceded by O_7 , O_8 , or still a higher ‘reversible’ substate.

unstable. It may be that before the assembly breaks down, a pre-breakdown channel state of very high conductance is attained briefly. The magnitude of the current at the maximum of the spike implies an instantaneous total circuit resistance in the order of 200 M Ω , which is near to the minimum value of R_{add} observed. If R_{add} is assumed not to have changed at the occurrence of the spike, it appears that an instantaneous resistance in the order of only 10 M Ω could be associated with the Alm channel. This translates into a transient pre-breakdown Alm channel of a diameter in the order of 10 nm, which is very large. The contrary scenario – no change to channel functionality, but rather a temporary fall of R_{add} – can be considered, too. It is difficult to imagine, however, how R_{add} , whatever its grounds are, could undergo such a rapid and significant change with no apparent external stimulus, and how the breakdown of the channel could be induced at the same time.

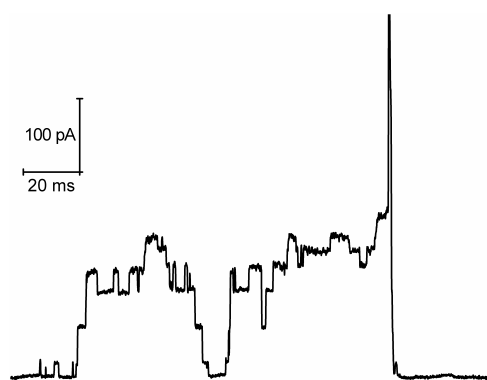


Figure 4-70. DC current trace of a single Alm channel in an npsLB showing a burst terminated by a transient current spike of high magnitude. The trace was recorded in 1 M KCl, 5 mM HEPES, pH 7 and filtered at 3 kHz.

4.6.4. Conclusion

A variety of microbial peptides forming TM channels could be inserted and detected electrically in the npsLBs. Assembly of conductive gramicidin channels was investigated by AC impedance using non-passivated Si₃N₄ windows. npsLB conductance increased respective to concentration of gramicidin in the bathing electrolyte, indicating that a multitude of TM channels was forming in the bilayers. At high gramicidin concentrations, a molar ratio of conductive gramicidin dimers to phospholipid molecules as high as ~1:40 was estimated based on npsLB conductance. Resistance of npsLBs with incorporated gramicidin could be restored to levels very near to those measured in the absence of gramicidin upon substituting small monovalent cations (K⁺) with large ones (TMA⁺). This proved that the observed rise of npsLB conductance was due to TM gramicidin channels. Formation of TM channels of α HL and Alm was followed at the level of a single channel by DC voltage clamp in npsLBs on passivated Si₃N₄ windows, as well as in classical painted BLMs. α HL showed rather non-typical behavior in both npsLBs and painted BLMs, most likely due to a degraded and/or contaminated sample of the peptide. Alm behaved normally in BLMs and quasi-normally in npsLBs. The characteristic effects of Alm concentration and TM voltage on the

assembly of Alm channels were observed with npsLBs. Fluctuations of Alm channels over up to eight conductance sub-states were detected. A comparison of resistances of the individual sub-states in npsLBs to those in classical BLMs points to the existence of an additional resistance of $200\text{ M}\Omega$ - $2\text{ G}\Omega$ in series to the resistance of the channels. Several possible sources of such resistance were considered, the most likely one being a protrusion of the bilayers into the pores. Further unique features of Alm behavior in npsLBs were the continuous change of conductance of a particular sub-state in time, probably related to the additional series resistance and lateral diffusion of the assembled channel in the npsLB, and transient sub-states of very high conductance.

5. Conclusion and outlook

The principal goal of the thesis, i.e. *solvent-free* bilayer lipid membranes spanning over *arrays* of through nanopores (npsLBs) allowing for recordings of currents via *single* channel proteins, has been accomplished.¹⁸⁵ The sub-objectives, as listed in Chapter 2, have been fulfilled in the following manner:

1. Septa of thickness in the sub-micrometer range afford the possibility of custom fabrication of closely-packed arrays of through nanopores. Therefore, TEM windows with 100-nm-thin Si₃N₄ diaphragms became the substrates of choice to meet the goals of this project. Continuous diaphragm windows of specifications compatible with this work's requirements (e.g. diaphragm robustness, frame size and thickness, etc.) are commercially available. This spared us the need to fabricate the diaphragms ourselves and allowed us to dedicate more effort to the electrochemical and biophysical objectives of the thesis. A measurement cell tailored to the particular substrate has been developed and redesigned in several stages of the project to accommodate for the expanding requirements (in the order of chronology: bilateral low-impedance electrical access, bilateral perfusion access, horizontal mount for sedimenting GUVs, optical and mechanical access for GUV maneuvering).
2. Optical microscopy revealed a high affinity of DPhPC GUVs (in ~100 mM electrolyte of common salts) for clean hydrophilic Si₃N₄ surfaces, where they adsorbed, spread, ruptured, and unfolded into planar SLB patches. Low pH and the presence of cations enhanced the rate, at which the transition from vesicular to planar form occurred. Unfolding of multiple GUVs next to each other gave rise to mutually interconnected supra-patches with full fluidic continuity.
3. Arrays of through pores were milled in the Si₃N₄ diaphragms by an FIB. It has been shown by AFM and SEM that the pores were very well defined both in terms of size and location. The benefit due to the low thickness of the diaphragms was dual: not only was the FIB milling of pores fast and precise, but also the pore aspect ratio was low, and thus the chemical and electrical access to the npsLBs through the pores remained unhindered. A single array comprising 1-12 pores of 50-800 nm in diameter was milled per diaphragm to be used for psLB formation.
4. npsLBs were formed by spontaneous adhesion, rupture and unfolding of GUVs on porous Si₃N₄ diaphragms. A need to counter the stochastics of having a GUV descend to over an array of pores has been identified. Mechanical maneuvering of sedimenting GUVs before adhesion was thus instrumental to, for the first time, reliably span all pores of an array with npsLBs. In

conjunction with the intrinsically high affinity of PC lipids for clean Si-derived surfaces, the smooth regular pores yielded npsLBs of high stability and electrical resistance in the GΩ regime. Furthermore, the spontaneous unfolding of PC lipid vesicles into planar SLB patches on clean Si₃N₄ spared us the need to functionalize the surface so as to enhance the lipid-surface interaction and induce vesicle rupture. Unlike suspending a lipid bilayer over a pore using hydrophobic interactions with the support, the ‘hydrophilic’ approach maintains full structural continuity of the fluidic bilayer between the pore-spanning and the supported regions. Hospitality of the platform to transmembrane protein should be enhanced thereby. Moreover, diffusion of the reconstituted protein between the supported and free-standing portions of the SLB without loss of functional folding may be possible. The contribution of size of the GUVs to the success was significant. First, the vesicles were well visible under an optical microscope, be it in the fluorescence or the DIC mode. Second, they could be (easily) maneuvered and were large enough not to pose too demanding a requirement on the size of the manipulator tip. Last and most important, they unfolded into planar SLBs with vast lateral continuity, which is believed to be the key reason behind the reliable spanning of all pores of an array with npsLBs with very high overall seal resistance.

5. A variety of microbial channel-forming peptides could be delivered and inserted in the npsLBs from the bathing solution. Assembly of conductive gramicidin channels was followed by AC impedance using non-passivated Si₃N₄ windows. npsLB conductance increased respective to concentration of gramicidin in the bathing electrolyte, indicating that a multitude of TM channels was forming in the bilayers. Unprecedented peptide-to-lipid ratios (~1:25) have been reached and the possibility of probing protein-protein interactions electrically via npsLBs has been indicated thereby. Breakdown DC voltages of individual npsLBs (>200 mV) in an array are well in the range compatible with standard electrophysiological DC voltage clamp experiments. Modification of porous substrates by an organic coating has been shown to provide for chip dielectric properties consistent with protein single-channel recordings. Quality single-channel recordings of ionic currents through α-hemolysin and, more particularly, alamethicin channels have been achieved.

Low membrane and stray capacitances are crucial for high-fidelity DC recordings of ionic currents through protein channels with single channel resolution. Stray capacitance reduction of the Si₃N₄ windows has been accomplished by means of a polymerized photoresist coating. Window capacitances as low as 50 pA have been achieved by this method. The so-passivated windows have been used successfully to record single-unit currents through α-hemolysin and alamethicin

channels. Nevertheless, a refinement of the strategy of Si_3N_4 window passivation for capacitance reduction would be beneficial in future endeavors. Although there are a number of undisputable benefits to the current approach (e.g. bench-top implementation, reversibility, selective pore release), the process is rather elaborate and, more importantly, the resulting coating does not exhibit sufficient chemical robustness. To resolve the latter, a material must be found for the passivation layer more rugged than the AZ 5214E resist. If simplicity of the process – application of a single layer and maskless exposure using a microscope – is to be retained, a positive resist must be used. A positive polyimide-based resist may provide the desired sturdiness, yet requires processing at temperatures that may prove incompatible with the fragile Si_3N_4 diaphragms. If the maskless requirement is abandoned, negative resists (e.g. the well-known SU-8) that, in general, polymerize better than the positive ones can be utilized. Custom fabrication of ‘negative’ masks and precise alignment of the blocking feature over the spot to be released prior to irradiation would be unavoidable. Alternatively, if application of multiple organic layers during the passivation process is put up with, very robust fluoropolymers (Teflon AFTTM, CytopTM) can be cast from solution to form the passivating layer. Because photosensitive varieties of these materials are not available, the spot(s) of choice on the Si_3N_4 diaphragm would have to be etch-released through a structured film, either organic or metallic (step d of Figure 3-7).

Another interesting effect to address is the one of hydrostatic pressure on the npsLBs. The prospective application of the npsLB platform – the membrane protein drug screening assay – will likely involve bilateral (micro)fluidic delivery of substances to the targeted entity. Such pressurized conveyance may easily introduce destabilizing pressure gradients across the bilayer. Our preliminary results^{*} on single sub-micrometer pores in glass chips drilled by laser ablation indicate that subtle differences in hydrostatic pressure may induce pronounced, yet reversible, changes in bilayer seal resistance. The dynamics of the effect seem to depend on the direction of the pressure gradient. Parameters underlying the occurrence and the character of the phenomenon are currently unclear.

We have shown that the design of the platform allows for facile bilateral chemical, electrical, and optical access to the bilayers. The npsLBs presented here hence have the potential to make a strong impact on membrane protein research and inspire the design of functional screening assays for drug candidates targeting membrane proteins. Doubts may perhaps emerge with respect to the apparent

^{*} The scope of this work had been restricted to npsLBs on pores in Si_3N_4 diaphragms. Results obtained on other types of substrates (glass and porous AlO_x) have not been presented here in order not to extend the scale of the thesis inadequately.

discrepancy between the sophisticated technology (FIB, SEM, AFM) required to accomplish the results presented here and the prospected wide applicability of the platform in membrane protein research and pharmacology. The need of a motorized micromanipulator, a DIC microscope, and an operator for the formation of npsLBs may possibly induce further objections as to the feasibility of a smooth transfer towards the projected applications. It must be emphasized therefore that the platform is currently at a prototyping phase. A plethora of unknowns still exist with respect to vesicle-derived npsLBs over arrays of nanopores that must be investigated before the technology is ported to real-world use. For example, the impact of pore array parameters (e.g. pore size, topography, quantity per array, pore-to-pore distance, etc.), surface functionalization (hydrophilic, hydrophobic, intermediate), or lipid composition (surface charge, fluidity, intrinsic curvature), to name a few, on the stability and properties of the npsLBs must be understood. The FIB and the analogous e-beam lithography, both of which might be argued against as expensive and slow, are the only processes capable of generating nanoscopic pores at the required precision at present. Similarly, there is hardly a substitute for the SEM and the AFM in terms of the informative detail on the nanostructures these techniques deliver, detail, without which the above relationships cannot be determined. Obviously, the use of this (complex) technology is unavoidable in the development phase of the platform. Cheaper and faster approaches, such as the novel colloidal lithography process¹⁸⁶, can be employed to fabricate nanoporous Si₃N₄ diaphragms at large scale once the optimum array parameters had been identified. After a reproducible large-scale process of pore fabrication has been established, nanoscopic inspection of the features on every diaphragm will not be required any more. This work has provided a guideline to reach that stage. It is the ambition of ASMENA, a joint multi-partner academic-industrial project funded by the EU's 7th Framework Program, to follow this guideline and reach the goals presented above. We believe that the approach presented here can provide a deeper insight into the biophysics of npsLBs, and that this understanding will pave the way towards npsLBs forming spontaneously from sub-micrometer (proteo)lipid vesicles and sealing multitudes of pores perfectly, as craved for by many a drug designer or electrophysiologist.

References*

- 1 B. Alberts, A. Johnson, J. Lewis, M. Raff, K. Roberts and P. Walter, *Molecular Biology of the Cell*, Garland Science, New York, 2002.
- 2 D. Voet, C. W. Pratt and J. G. Voet, *Fundamentals of Biochemistry: Life at the Molecular Level*, John Wiley & Sons, 2005.
- 3 S. J. Singer and G. L. Nicolson, Fluid Mosaic Model of Structure of Cell-Membranes, *Science*, 1972, vol. 175, pp. 720-&.
- 4 S. Munro, Lipid rafts: Elusive or illusive?, *Cell*, 2003, vol. 115, pp. 377-388.
- 5 T. P. W. McMullen, R. N. A. H. Lewis and R. N. McElhaney, Cholesterol-phospholipid interactions, the liquid-ordered phase and lipid rafts in model and biological membranes, *Current Opinion in Colloid & Interface Science*, 2004, vol. 8, pp. 459-468.
- 6 P. Somerharju, J. A. Virtanen, K. H. Cheng and M. Hermansson, The superlattice model of lateral organization of membranes and its implications on membrane lipid homeostasis, *Biochimica Et Biophysica Acta-Biomembranes*, 2009, vol. 1788, pp. 12-23.
- 7 J. E. Johnson and R. B. Cornell, Amphitropic proteins: regulation by reversible membrane interactions (review), *Molecular Membrane Biology*, 1999, vol. 16, pp. 217-235.
- 8 E. Wallin and G. von Heijne, Genome-wide analysis of integral membrane proteins from eubacterial, archaean, and eukaryotic organisms, *Protein Science*, 1998, vol. 7, pp. 1029-1038.
- 9 C. I. o. H. Research, CIHR Training Program: Structural Biology of Membrane Proteins Linked to Disease, 2007, http://biochemistry.utoronto.ca/CIHR_membrane/program1.html, Accessed May 03, 2009.
- 10 P. Mueller, D. O. Rudin, H. T. Tien and W. C. Wescott, Reconstitution of Cell Membrane Structure in Vitro and Its Transformation into an Excitable System, *Nature*, 1962, vol. 194, pp. 979-&.
- 11 E. Neher and B. Sakmann, Single-Channel Currents Recorded from Membrane of Denervated Frog Muscle-Fibers, *Nature*, 1976, vol. 260, pp. 799-802.
- 12 H. T. Tien, Self-Assembled Lipid Bilayers for Biosensors and Molecular Electronic Devices, *Advanced Materials*, 1990, vol. 2, pp. 316-318.
- 13 I. Koper, Insulating tethered bilayer lipid membranes to study membrane proteins, *Molecular Biosystems*, 2007, vol. 3, pp. 651-657.
- 14 **C. M. A. Brett, S. Kresak, T. Hianik and A. M. O. Brett, Studies on self-assembled alkanethiol monolayers formed at applied potential on polycrystalline gold electrodes, *Electroanalysis*, 2003, vol. 15, pp. 557-565.**
- 15 J. Kunze, J. Leitch, A. L. Schwan, R. J. Faragher, R. Naumann, S. Schiller, W. Knoll, J. R. Dutcher and J. Lipkowski, New method to measure packing densities of self-assembled thiolipid monolayers, *Langmuir*, 2006, vol. 22, pp. 5509-5519.
- 16 **P. Vitovic, S. Kresak, R. Naumann, S. M. Schiller, R. N. A. H. Lewis, R. N. McElhaney and T. Hianik, The study of the interaction of a model at-helical peptide with lipid bilayers and monolayers, *Bioelectrochemistry*, 2004, vol. 63, pp. 169-176.**
- 17 M. Montal and P. Mueller, Formation of Bimolecular Membranes from Lipid Monolayers and a Study of Their Electrical Properties, *Proceedings of the National Academy of Sciences of the United States of America*, 1972, vol. 69, pp. 3561-3566.
- 18 H. Schindler, Formation of Planar Membranes from Natural Liposomes and from Lipid-Protein Vesicles, *Experientia*, 1980, vol. 36, pp. 758-758.
- 19 D. J. Woodbury and C. Miller, Nystatin-Induced Liposome Fusion - a Versatile Approach to Ion Channel Reconstitution into Planar Bilayers, *Biophysical Journal*, 1990, vol. 58, pp. 833-839.

* the author's publications relevant to this dissertation are highlighted in bold letters

- 20 H. Suzuki, K. V. Tabata, H. Noji and S. Takeuchi, Highly reproducible method of planar lipid bilayer reconstitution in polymethyl methacrylate microfluidic chip, *Langmuir*, 2006, vol. 22, pp. 1937-1942.
- 21 X. F. Kang, S. Cheley, A. C. Rice-Ficht and H. Bayley, A storable encapsulated bilayer chip containing a single protein nanopore, *Journal of the American Chemical Society*, 2007, vol. 129, pp. 4701-4705.
- 22 P. C. Gufler, D. Pum, U. B. Sleytr and B. Schuster, Highly robust lipid membranes on crystalline S-layer supports investigated by electrochemical impedance spectroscopy, *Biochimica Et Biophysica Acta-Biomembranes*, 2004, vol. 1661, pp. 154-165.
- 23 W. F. Wonderlin, A. Finkel and R. J. French, Optimizing Planar Lipid Bilayer Single-Channel Recordings for High-Resolution with Rapid Voltage Steps, *Biophysical Journal*, 1990, vol. 58, pp. 289-297.
- 24 M. Mayer, J. K. Kriebel, M. T. Tosteson and G. M. Whitesides, Microfabricated teflon membranes for low-noise recordings of ion channels in planar lipid bilayers, *Biophysical Journal*, 2003, vol. 85, pp. 2684-2695.
- 25 N. Fertig, C. Meyer, R. H. Blick, C. Trautmann and J. C. Behrends, Microstructured glass chip for ion-channel electrophysiology, *Physical Review E*, 2001, vol. 64, pp. 040901:040901-040904.
- 26 W. Romer, Y. H. Lam, D. Fischer, A. Watts, W. B. Fischer, P. Goring, R. B. Wehrspohn, U. Gosele and C. Steinem, Channel activity of a viral transmembrane peptide in micro-BLMs: Vpu(1-32) from HIV-1, *Journal of the American Chemical Society*, 2004, vol. 126, pp. 16267-16274.
- 27 D. Weiskopf, E. K. Schmitt, M. H. Kluhr, S. K. Dertinger and C. Steinem, Micro-BLMs on highly ordered porous silicon substrates: Rupture process and lateral mobility, *Langmuir*, 2007, vol. 23, pp. 9134-9139.
- 28 W. Romer and C. Steinem, Impedance analysis and single-channel recordings on nano-black lipid membranes based on porous alumina, *Biophysical Journal*, 2004, vol. 86, pp. 955-965.
- 29 E. K. Schmitt, M. Vrouenraets and C. Steinem, Channel activity of OmpF monitored in nano-BLMs, *Biophysical Journal*, 2006, vol. 91, pp. 2163-2171.
- 30 X. J. Han, A. Studer, H. Sehr, I. Geissbuhler, M. Di Berardino, F. K. Winkler and L. X. Tiefenauer, Nanopore arrays for stable and functional free-standing lipid bilayers, *Advanced Materials*, 2007, vol. 19, pp. 4466-4470.
- 31 G. Baaken, M. Sondermann, C. Schlemmer, J. Ruhe and J. C. Behrends, Planar microelectrode-cavity array for high-resolution and parallel electrical recording of membrane ionic currents, *Lab on a Chip*, 2008, vol. 8, pp. 938-944.
- 32 N. Fertig, M. Klau, M. George, R. H. Blick and J. C. Behrends, Activity of single ion channel proteins detected with a planar microstructure, *Applied Physics Letters*, 2002, vol. 81, pp. 4865-4867.
- 33 N. Fertig, R. H. Blick and J. C. Behrends, Whole cell patch clamp recording performed on a planar glass chip, *Biophysical Journal*, 2002, vol. 82, pp. 3056-3062.
- 34 R. Pantoja, J. M. Nagarah, D. M. Starace, N. A. Melosh, R. Blunck, F. Bezanilla and J. R. Heath, Silicon chip-based patch-clamp electrodes integrated with PDMS microfluidics, *Biosensors & Bioelectronics*, 2004, vol. 20, pp. 509-517.
- 35 K. G. Klemic, J. F. Klemic, M. A. Reed and F. J. Sigworth, Micromolded PDMS planar electrode allows patch clamp electrical recordings from cells, *Biosensors & Bioelectronics*, 2002, vol. 17, pp. 597-604.
- 36 A. Bruggemann, S. Stoelzle, M. George, J. C. Behrends and N. Fertig, Microchip technology for automated and parallel patch-clamp recording, *Small*, 2006, vol. 2, pp. 840-846.
- 37 C. Miller, Ion Channels in Liposomes, *Annual Review of Physiology*, 1984, vol. 46, pp. 549-558.
- 38 A. A. Seddon, P. Curnow and P. J. Booth, Membrane proteins, lipids and detergents: not just a soap opera, *Biochimica Et Biophysica Acta, Biomembranes*, 2004, vol. 1666, pp. 105-117.
- 39 C. Hennessal, J. Drexler and C. Steinem, Membrane-suspended nanocompartments based on ordered pores in alumina, *Chemphyschem*, 2002, vol. 3, pp. 885-889.
- 40 J. Drexler and C. Steinem, Pore-suspending lipid bilayers on porous alumina investigated by electrical impedance spectroscopy, *Journal of Physical Chemistry B*, 2003, vol. 107, pp. 11245-11254.
- 41 S. Steltenkamp, M. M. Muller, M. Deserno, C. Hennessal, C. Steinem and A. Janshoff, Mechanical properties of pore-spanning lipid bilayers probed by atomic force microscopy, *Biophysical Journal*, 2006, vol. 91, pp. 217-226.

-
- 42 O. Worsfold, N. H. Voelcker and T. Nishiya, Biosensing using lipid bilayers suspended on porous silicon, *Langmuir*, 2006, vol. 22, pp. 7078-7083.
- 43 C. Danelon, J. B. Perez, C. Santschi, J. Brugger and H. Vogel, Cell membranes suspended across nanoaperture arrays, *Langmuir*, 2006, vol. 22, pp. 22-25.
- 44 C. Schmidt, M. Mayer and H. Vogel, A chip-based biosensor for the functional analysis of single ion channels, *Angewandte Chemie-International Edition*, 2000, vol. 39, pp. 3137-3140.
- 45 M. Sondermann, M. George, N. Fertig and J. C. Behrends, High-resolution electrophysiology on a chip: Transient dynamics of alamethicin channel formation, *Biochimica Et Biophysica Acta-Biomembranes*, 2006, vol. 1758, pp. 545-551.
- 46 A. P. Quist, A. Chand, S. Ramachandran, C. Daraio, S. Jin and R. Lal, Atomic force microscopy imaging and electrical recording of lipid bilayers supported over microfabricated silicon chip nanopores: Lab-on-a-chip system for lipid membranes and ion channels, *Langmuir*, 2007, vol. 23, pp. 1375-1380.
- 47 E. K. Schmitt, M. Nurnabi, R. J. Bushby and C. Steinem, Electrically insulating pore-suspending membranes on highly ordered porous alumina obtained from vesicle spreading, *Soft Matter*, 2008, vol. 4, pp. 250-253.
- 48 FEI-Company, Focused Ion Beam Technology, Capabilities, and Applications, 2004.
- 49 L. A. Giannuzzi, B. I. Prenzler and B. W. Kempshall, in *Introduction to Focused Ion Beams: Instrumentation, Theory, Techniques and Practice*, Springer, New York, 2005, pp. 13-52.
- 50 R. M. Langford, P. M. Nellen, J. Gierak and Y. Q. Fu, Focused ion beam micro- and nanoengineering, *Mrs Bulletin*, 2007, vol. 32, pp. 417-423.
- 51 SII-NanoTechnology, Focused Ion Beam (FIB), http://www.sint.com/en/products/fib/tec_descriptions/descriptions_e.html, Accessed 11.1., 2009.
- 52 C. A. Volkert and A. M. Minor, Focused ion beam microscopy and micromachining, *Mrs Bulletin*, 2007, vol. 32, pp. 389-395.
- 53 L. Reimer, *Scanning electron microscopy - Physics of Image Formation and Microanalysis*, Springer, Berlin, 1998.
- 54 JEOL, A Guide to Scanning Microscope Observation, http://www.jeol.com/sem/docs/sem_guide/guide.pdf, Accessed 20.1., 2009.
- 55 Veeco, SPM Training Notebook, 2003, www.veeco.com.
- 56 P. West and A. Ross, An introduction to Atomic Force Microscopy Modes, 2006, <http://www.pacificnanotech.com/afm-modes.html>, Accessed 20.5., 2009.
- 57 Veeco, A Practical Guide to SPM (Scanning Probe Microscopy), 2005, www.veeco.com.
- 58 G. Drenkow, What is an atomic force microscope?, 2007, <http://nano.tm.agilent.com/blog/2007/06/21/what-is-an-atomic-force-microscope/>, Accessed 12.1.2009, 2009.
- 59 S. Morita, R. Wiesendanger and E. Meyer, *Noncontact Atomic Force Microscopy*, Springer, 2002.
- 60 S. Kalinin, *Scanning probe microscopy*, Springer, New York, 2007.
- 61 MicroChemicals, *Lithography*, MicroChemicals, 2006.
- 62 H. G. Kapitza, *Microscopy from the very beginning*, Carl Zeiss GmbH., Jena, 1997.
- 63 B. Valeur, *Molecular fluorescence: principles and applications*, Wiley-VCH, Weinheim, 2002.
- 64 M. Pluta, *Advanced light microscopy*, Elsevier, Amsterdam, 1988.
- 65 A. J. Bard and L. R. Faulkner, *Electrochemical Methods: Fundamentals and Applications*, John Wiley & Sons, 2001.
- 66 C. M. A. Brett and A. M. O. Brett, *Electrochemistry: Principles, Methods, and Applications*, Oxford University Press, New York, 1993.
- 67 C. H. Hamann, A. Hamnett and W. Vielstich, *Electrochemistry*, Wiley, 2007.
-

-
- 68 Axon-Instruments, *Axopatch 200B Patch Clamp - Theory and Operation*, 1999.
 - 69 HEKA-Elektronik, *EPC 10 Patch Clamp Amplifier User's Manual*, 2004.
 - 70 Molecular-Devices, *The Axon CNS Guide to Electrophysiology & Biophysics Laboratory Techniques*, 2006.
 - 71 B. G. Kornreich, The patch clamp technique: principles and technical considerations, *J Vet Cardiol*, 2007, vol. 9, pp. 25-37.
 - 72 A. L. Hodgkin and A. F. Huxley, A Quantitative Description of Membrane Current and Its Application to Conduction and Excitation in Nerve, *Journal of Physiology-London*, 1952, vol. 117, pp. 500-544.
 - 73 A. Huxley, From overshoot to voltage clamp, *Trends in Neurosciences*, 2002, vol. 25, pp. 553-558.
 - 74 N. Patterson, D. P. Adams, V. C. Hodges, M. J. Vasile, J. R. Michael and P. G. Kotula, Controlled fabrication of nanopores using a direct focused ion beam approach with back face particle detection, *Nanotechnology*, 2008, vol. 19, pp. -.
 - 75 R. Dimova, S. Aranda, N. Bezlyepkina, V. Nikolov, K. A. Riske and R. Lipowsky, A practical guide to giant vesicles. Probing the membrane nanoregime via optical microscopy, *Journal of Physics: Condensed Matter*, 2006, vol. 18, pp. S1151-S1176.
 - 76 S. L. Veatch, in *Lipid Rafts*, ed. T. J. McIntosh, Humana Press, 2007, pp. 59-72.
 - 77 H. Lindsey, N. O. Petersen and S. I. Chan, Physicochemical Characterization of 1,2-Diphytanoyl-Sn-Glycero-3-Phosphocholine in Model Membrane Systems, *Biochimica Et Biophysica Acta*, 1979, vol. 555, pp. 147-167.
 - 78 J. A. Killian, Gramicidin and gramicidin-lipid Interactions, *Biochimica Et Biophysica Acta*, 1992, vol. 1113, pp. 391-425.
 - 79 R. P. Richter, R. Berat and A. R. Brisson, Formation of solid-supported lipid bilayers: An integrated view, *Langmuir*, 2006, vol. 22, pp. 3497-3505.
 - 80 A. L. Bernard, M. A. Guedeau-Boudeville, L. Jullien and J. M. di Meglio, Strong adhesion of giant vesicles on surfaces: Dynamics and permeability, *Langmuir*, 2000, vol. 16, pp. 6809-6820.
 - 81 A. L. Bernard, M. A. Guedeau-Boudeville, O. Sandre, S. Palacin, J. M. di Meglio and L. Jullien, Permeation through lipid bilayers by adhesion of giant vesicles on decorated surfaces, *Langmuir*, 2000, vol. 16, pp. 6801-6808.
 - 82 C. Hamai, P. S. Cremer and S. M. Musser, Single giant vesicle rupture events reveal multiple mechanisms of glass-supported bilayer formation, *Biophysical Journal*, 2007, vol. 92, pp. 1988-1999.
 - 83 A. Priel, Z. Gil, V. T. Moy, K. L. Magleby and S. D. Silberberg, Ionic requirements for membrane-glass adhesion and giga seal formation in patch-clamp recording, *Biophysical Journal*, 2007, vol. 92, pp. 3893-3900.
 - 84 C. Dietrich, R. Merkel and R. Tampe, Diffusion measurement of fluorescence-labeled amphiphilic molecules with a standard fluorescence microscope, *Biophysical Journal*, 1997, vol. 72, pp. 1701-1710.
 - 85 K. H. Drexhage, Monomolecular Layers and Light, *Scientific American*, 1970, vol. 222, pp. 108-&.
 - 86 A. Lambacher and P. Fromherz, Fluorescence interference-contrast microscopy on oxidized silicon using a monomolecular dye layer, *Applied Physics a-Materials Science & Processing*, 1996, vol. 63, pp. 207-216.
 - 87 A. Lambacher and P. Fromherz, Orientation of hemicyanine dye in lipid membrane measured by fluorescence interferometry on a silicon chip, *Journal of Physical Chemistry B*, 2001, vol. 105, pp. 343-346.
 - 88 A. Lambacher and P. Fromherz, Luminescence of dye molecules on oxidized silicon and fluorescence interference contrast microscopy of biomembranes, *Journal of the Optical Society of America B-Optical Physics*, 2002, vol. 19, pp. 1435-1453.
 - 89 M. Bras, V. Dugas, F. Bessueille, J. P. Cloarec, J. R. Martin, M. Cabrera, J. P. Chauvet, E. Souteyard and M. Garrigues, Optimisation of a silicon/silicon dioxide substrate for a fluorescence DNA microarray, *Biosensors & Bioelectronics*, 2004, vol. 20, pp. 797-806.
 - 90 B. Rousset, L. Furgal, P. Fadel, A. Fulop, D. Pujos and P. Temple-Boyer, Development of SiNx LPCVD processes for microtechnological applications, *Journal De Physique Iv*, 2001, vol. 11, pp. 937-944.
-

- 91 N. L. Thompson, H. M. McConnell and T. P. Burghardt, Order in Supported Phospholipid Monolayers Detected by the Dichroism of Fluorescence Excited with Polarized Evanescent Illumination, *Biophysical Journal*, 1984, vol. 46, pp. 739-747.
- 92 V. Kiessling, C. Wan and L. K. Tamm, Domain coupling in asymmetric lipid bilayers, *Biochimica Et Biophysica Acta-Biomembranes*, 2009, vol. 1788, pp. 64-71.
- 93 J. H. Wittke, Electron Interaction with Matter: Volume, 2006, <http://www4.nau.edu/microanalysis/Microprobe/Interact-Volume.html>, Accessed 14.5., 2009.
- 94 E. Sackmann, Supported membranes: Scientific and practical applications, *Science*, 1996, vol. 271, pp. 43-48.
- 95 H. Pagnia, Carbonaceous Thin-Films, *Vacuum*, 1989, vol. 39, pp. 3-5.
- 96 D. C. Joy and C. S. Joy, Low voltage scanning electron microscopy, *Micron*, 1996, vol. 27, pp. 247-263.
- 97 J. Vancea, G. Reiss, F. Schneider, K. Bauer and H. Hoffmann, Substrate Effects on the Surface-Topography of Evaporated Gold-Films - a Scanning Tunnelling Microscopy Investigation, *Surface Science*, 1989, vol. 218, pp. 108-126.
- 98 W. M. Zhang, Y. G. Wang, J. Li, J. M. Xue, H. Ji, Q. Ouyang, J. Xu and Y. Zhang, Controllable shrinking and shaping of silicon nitride nanopores under electron irradiation, *Applied Physics Letters*, 2007, vol. 90, pp. -.
- 99 T. Schenkel, V. Radmilovic, E. A. Stach, S. J. Park and A. Persaud, Formation of a few nanometer wide holes in membranes with a dual beam focused ion beam system, *Journal of Vacuum Science & Technology B*, 2003, vol. 21, pp. 2720-2723.
- 100 R. J. White, E. N. Ervin, T. Yang, X. Chen, S. Daniel, P. S. Cremer and H. S. White, Single ion-channel recordings using glass nanopore membranes, *Journal of the American Chemical Society*, 2007, vol. 129, pp. 11766-11775.
- 101 N. C. Li, S. F. Yu, C. C. Harrell and C. R. Martin, Conical nanopore membranes. Preparation and transport properties, *Analytical Chemistry*, 2004, vol. 76, pp. 2025-2030.
- 102 E. N. Ervin, H. S. White, L. A. Baker and C. R. Martin, Alternating current impedance imaging of high-resistance membrane pores using a scanning electrochemical microscope. Application of membrane electrical shunts to increase measurement sensitivity and image contrast, *Analytical Chemistry*, 2006, vol. 78, pp. 6535-6541.
- 103 R. J. White, B. Zhang, S. Daniel, J. M. Tang, E. N. Ervin, P. S. Cremer and H. S. White, Ionic conductivity of the aqueous layer separating a lipid bilayer membrane and a glass support, *Langmuir*, 2006, vol. 22, pp. 10777-10783.
- 104 P. Scopece, L. A. Baker, P. Ugo and C. R. Martin, Conical nanopore membranes: solvent shaping of nanopores, *Nanotechnology*, 2006, vol. 17, pp. 3951-3956.
- 105 W. Desorbo, Ultraviolet Effects and Aging Effects on Etching Characteristics of Fission Tracks in Polycarbonate Film, *Nuclear Tracks and Radiation Measurements*, 1979, vol. 3, pp. 13-32.
- 106 K. W. Pratt, W. F. Koch, Y. C. Wu and P. A. Berezansky, Molality-based primary standards of electrolytic conductivity - (IUPAC technical report), *Pure and Applied Chemistry*, 2001, vol. 73, pp. 1783-1793.
- 107 R. A. Horne and R. P. Young, Electrical Conductivity of Aqueous Tetraalkylammonium Halide Solutions under Hydrostatic Pressure, *Journal of Physical Chemistry*, 1968, vol. 72, pp. 1763-1767.
- 108 M. Morita, T. Ohmi, E. Hasegawa, M. Kawakami and M. Ohwada, Growth of Native Oxide on a Silicon Surface, *Journal of Applied Physics*, 1990, vol. 68, pp. 1272-1281.
- 109 S. Jamasb, S. Collins and R. L. Smith, A physical model for drift in pH ISFETs, *Sensors and Actuators B-Chemical*, 1998, vol. 49, pp. 146-155.
- 110 Y. Y. Chen and G. Jin, Refractive index and thickness analysis of natural silicon dioxide film growing on silicon with variable-angle spectroscopic ellipsometry, *Spectroscopy*, 2006, vol. 21, pp. 26-+.
- 111 T. Hirokane, N. Yoshii, T. Okazaki, S. Urabe, K. Nishimura, S. Morita, K. Arima, J. Uchikoshi and M. Morita, Characterization of Tunneling Current through Ultrathin Silicon Dioxide Films by Different-Metal Gates Method, *Japanese Journal of Applied Physics*, 2008, vol. 47, pp. 8317-8320.
- 112 C. Kataoka-Hamai, H. Inoue and Y. Miyahara, Detection of supported lipid bilayers using their electric charge, *Langmuir*, 2008, vol. 24, pp. 9916-9920.

-
- 113 J. Lin, M. Merzlyakov, K. Hristova and P. C. Searson, Impedance spectroscopy of bilayer membranes on single crystal silicon, *Biointerphases*, 2008, vol. 3, pp. FA33-FA40.
 - 114 M. Chemla, V. Bertagna, R. Erre, F. Rouelle, S. Petitdidier and D. Levy, Thickness of surface thin oxide layers determined by impedance spectroscopy using silicon/oxide/electrolyte (SOE) structures, *Applied Surface Science*, 2004, vol. 227, pp. 193-204.
 - 115 O. Purucker, H. Hillebrandt, K. Adlkofer and M. Tanaka, Deposition of highly resistive lipid bilayer on silicon-silicon dioxide electrode and incorporation of gramicidin studied by ac impedance spectroscopy, *Electrochimica Acta*, 2001, vol. 47, pp. 791-798.
 - 116 A. Abdelghani, C. Jacquin, M. Huber, R. Deutschmann and E. Sackmann, Supported lipid membrane on semiconductor electrode, *Materials Chemistry and Physics*, 2001, vol. 70, pp. 187-190.
 - 117 V. Atanasov, N. Knorr, R. S. Duran, S. Ingebrandt, A. Offenhausser, W. Knoll and I. Koper, Membrane on a chip: A functional tethered lipid bilayer membrane on silicon oxide surfaces, *Biophysical Journal*, 2005, vol. 89, pp. 1780-1788.
 - 118 J. C. Weaver and Y. A. Chizmadzhev, Theory of electroporation: A review, *Bioelectrochemistry and Bioenergetics*, 1996, vol. 41, pp. 135-160.
 - 119 I. Mey, M. Stephan, E. K. Schmitt, M. M. Müller, M. Ben Amar, C. Steinem and A. Janshoff, Local Membrane Mechanics of Pore-Spanning Bilayers, *Journal of the American Chemical Society*, 2009, vol. 131, pp. 7031-7039.
 - 120 P. K. Hansma, B. Drake, O. Marti, S. A. C. Gould and C. B. Prater, The Scanning Ion-Conductance Microscope, *Science*, 1989, vol. 243, pp. 641-643.
 - 121 M. Bocker, B. Anczykowski, J. Wegener and T. E. Schaffer, Scanning ion conductance microscopy with distance-modulated shear force control, *Nanotechnology*, 2007, vol. 18, pp. -.
 - 122 B. W. Urban, S. B. Hladky and D. A. Haydon, Ion Movements in Gramicidin Pores - an Example of Single-File Transport, *Biochimica Et Biophysica Acta*, 1980, vol. 602, pp. 331-354.
 - 123 E. Bamberg and P. Lauger, Blocking of Gramicidin Channel by Divalent-Cations, *Journal of Membrane Biology*, 1977, vol. 35, pp. 351-375.
 - 124 B. M. Burkhart, N. Li, D. A. Langs, W. A. Pangborn and W. L. Duax, The conducting form of gramicidin A is a right handed double-stranded double helix, *Proceedings of the National Academy of Sciences of the United States of America*, 1998, vol. 95, pp. 12950-12955.
 - 125 G. A. Woolley and B. A. Wallace, Model Ion Channels - Gramicidin and Alamethicin, *Journal of Membrane Biology*, 1992, vol. 129, pp. 109-136.
 - 126 D. A. Kelkar and A. Chattopadhyay, The gramicidin ion channel: A model membrane protein, *Biochimica Et Biophysica Acta-Biomembranes*, 2007, vol. 1768, pp. 2011-2025.
 - 127 O. S. Smart, J. M. Goodfellow and B. A. Wallace, The Pore Dimensions of Gramicidin-A, *Biophysical Journal*, 1993, vol. 65, pp. 2455-2460.
 - 128 V. B. Myers and D. A. Haydon, Ion Transfer across Lipid-Membranes in Presence of Gramicidin-A .2. Ion Selectivity, *Biochimica Et Biophysica Acta*, 1972, vol. 274, pp. 313-322.
 - 129 B. A. Wallace, Gramicidin Channels and Pores, *Annual Review of Biophysics and Biophysical Chemistry*, 1990, vol. 19, pp. 127-157.
 - 130 E. Bamberg, K. Noda, E. Gross and P. Lauger, Single-Channel Parameters of Gramicidin-a, Gramicidin-B and Gramicidin-C, *Biochimica Et Biophysica Acta*, 1976, vol. 419, pp. 223-228.
 - 131 D. W. Urry, M. C. Goodall, J. D. Glickson and D. F. Mayers, Gramicidin a Transmembrane Channel - Characteristics of Head-to-Head Dimerized Pi(L,D) Helices, *Proceedings of the National Academy of Sciences of the United States of America*, 1971, vol. 68, pp. 1907-&.
 - 132 O. S. Andersen, H. J. Apell, E. Bamberg, D. D. Busath, R. E. Koeppe, F. J. Sigworth, G. Szabo, D. W. Urry and A. Woolley, Gramicidin channel controversy - the structure in a lipid environment, *Nature Structural Biology*, 1999, vol. 6, pp. 609-609.
 - 133 O. S. Andersen, Gramicidin Channels, *Annual Review of Physiology*, 1984, vol. 46, pp. 531-548.
-

- 134 H. J. Apell, E. Bamberg and P. Lauger, Effects of Surface-Charge on the Conductance of the Gramicidin Channel, *Biochimica Et Biophysica Acta*, 1979, vol. 552, pp. 369-378.
- 135 A. Schatz, A. LinkeHommes and J. Neubert, Gravity dependency of the gramicidin A channel conductivity - A model for gravity perception on the cellular level, *European Biophysics Journal with Biophysics Letters*, 1996, vol. 25, pp. 37-41.
- 136 D. B. Sawyer, R. E. Koeppe and O. S. Andersen, Gramicidin Single-Channel Properties Show No Solvent-History Dependence, *Biophysical Journal*, 1990, vol. 57, pp. 515-523.
- 137 A. M. O'Connell, R. E. Koeppe and O. S. Andersen, Kinetics of Gramicidin Channel Formation in Lipid Bilayers - Transmembrane Monomer Association, *Science*, 1990, vol. 250, pp. 1256-1259.
- 138 R. K. Chitta and M. L. Gross, Electrospray ionization-mass spectrometry and tandem mass spectrometry reveal self-association and metal-ion binding of hydrophobic peptides: A study of the gramicidin dimer, *Biophysical Journal*, 2004, vol. 86, pp. 473-479.
- 139 R. R. Ketchum, B. Roux and T. A. Cross, High-resolution polypeptide structure in a lamellar phase lipid environment from solid state NMR derived orientational constraints, *Structure*, 1997, vol. 5, pp. 1655-1669.
- 140 Y. L. Wu, K. He, S. J. Ludtke and H. W. Huang, X-Ray-Diffraction Study of Lipid Bilayer-Membranes Interacting with Amphiphilic Helical Peptides - Diphytanoyl Phosphatidylcholine with Alamethicin at Low Concentrations, *Biophysical Journal*, 1995, vol. 68, pp. 2361-2369.
- 141 W. R. Veatch, R. Mathies, M. Eisenberg and L. Stryer, Simultaneous Fluorescence and Conductance Studies of Planar Bilayer Membranes Containing a Highly Active and Fluorescent Analog of Gramicidin-A, *Journal of Molecular Biology*, 1975, vol. 99, pp. 75-92.
- 142 Z. Kota, T. Pali and D. Marsh, Orientation and lipid-peptide interactions of gramicidin A in lipid membranes: Polarized attenuated total reflection infrared spectroscopy and spin-label electron spin resonance, *Biophysical Journal*, 2004, vol. 86, pp. 1521-1531.
- 143 L. H. He, J. W. F. Robertson, J. Li, I. Karcher, S. M. Schiller, W. Knoll and R. Naumann, Tethered bilayer lipid membranes based on monolayers of thiolipids mixed with a complementary dilution molecule. 1. Incorporation of channel peptides, *Langmuir*, 2005, vol. 21, pp. 11666-11672.
- 144 M. A. Deverall, E. Gindl, E. K. Sinner, H. Besir, J. Ruehe, M. J. Saxton and C. A. Naumann, Membrane lateral mobility obstructed by polymer-tethered lipids studied at the single molecule level, *Biophysical Journal*, 2005, vol. 88, pp. 1875-1886.
- 145 S. Bhakdi and J. Tranumjensen, Alpha-Toxin of Staphylococcus-Aureus, *Microbiological Reviews*, 1991, vol. 55, pp. 733-751.
- 146 S. Bhakdi, H. Bayley, A. Valeva, I. Walev, B. Walker, U. Weller, M. Kehoe and M. Palmer, Staphylococcal alpha-toxin, streptolysin-O, and Escherichia coli hemolysin: Prototypes of pore-forming bacterial cytolysins, *Archives of Microbiology*, 1996, vol. 165, pp. 73-79.
- 147 J. E. Gouaux, O. Braha, M. R. Hobaugh, L. Z. Song, S. Cheley, C. Shustak and H. Bayley, Subunit Stoichiometry of Staphylococcal Alpha-Hemolysin in Crystals and on Membranes - a Heptameric Transmembrane Pore, *Proceedings of the National Academy of Sciences of the United States of America*, 1994, vol. 91, pp. 12828-12831.
- 148 L. Z. Song, M. R. Hobaugh, C. Shustak, S. Cheley, H. Bayley and J. E. Gouaux, Structure of staphylococcal alpha-hemolysin, a heptameric transmembrane pore, *Science*, 1996, vol. 274, pp. 1859-1866.
- 149 E. Gouaux, alpha-hemolysin from Staphylococcus aureus: An archetype of beta-barrel, channel-forming toxins, *Journal of Structural Biology*, 1998, vol. 121, pp. 110-122.
- 150 B. Walker, O. Braha, S. Cheley and H. Bayley, An Intermediate in the Assembly of a Pore-Forming Protein Trapped with a Genetically-Engineered Switch, *Chemistry & Biology*, 1995, vol. 2, pp. 99-105.
- 151 Y. Fang, S. Cheley, H. Bayley and J. Yang, The heptameric prepore of a Staphylococcal alpha-hemolysin mutant in lipid bilayers imaged by atomic force microscopy, *Biochemistry*, 1997, vol. 36, pp. 9518-9522.
- 152 G. Menestrina, Ionic Channels Formed by Staphylococcus-Aureus Alpha-Toxin - Voltage-Dependent Inhibition by Divalent and Trivalent Cations, *Journal of Membrane Biology*, 1986, vol. 90, pp. 177-190.

- 153 J. J. Kasianowicz and S. M. Bezrukov, Protonation Dynamics of the Alpha-Toxin Ion-Channel from Spectral-Analysis of Ph-Dependent Current Fluctuations, *Biophysical Journal*, 1995, vol. 69, pp. 94-105.
- 154 Y. E. Korchey, C. L. Bashford, G. M. Alder, J. J. Kasianowicz and C. A. Pasternak, Low-Conductance States of a Single-Ion Channel Are Not Closed, *Journal of Membrane Biology*, 1995, vol. 147, pp. 233-239.
- 155 L. Q. Gu and H. Bayley, Interaction of the noncovalent molecular adapter, beta-cyclodextrin, with the staphylococcal alpha-hemolysin pore, *Biophysical Journal*, 2000, vol. 79, pp. 1967-1975.
- 156 L. Q. Gu, O. Braha, S. Conlan, S. Cheley and H. Bayley, Stochastic sensing of organic analytes by a pore-forming protein containing a molecular adapter, *Nature*, 1999, vol. 398, pp. 686-690.
- 157 M. Akeson, D. Branton, J. J. Kasianowicz, E. Brandin and D. W. Deamer, Microsecond time-scale discrimination among polycytidylic acid, polyadenylic acid, and polyuridylic acid as homopolymers or as segments within single RNA molecules, *Biophysical Journal*, 1999, vol. 77, pp. 3227-3233.
- 158 M. A. Holden and H. Bayley, Direct introduction of single protein channels and pores into lipid bilayers, *Journal of the American Chemical Society*, 2005, vol. 127, pp. 6502-6503.
- 159 E. N. Ervin, R. Kawano, R. J. White and H. S. White, Simultaneous alternating and direct current readout of protein ion channel blocking events using glass nanopore membranes, *Analytical Chemistry*, 2008, vol. 80, pp. 2069-2076.
- 160 Y. E. Korchey, G. M. Alder, A. Bakhramov, C. L. Bashford, B. S. Joomun, E. V. Sviderskaya, P. N. R. Usherwood and C. A. Pasternak, Staphylococcus-Aureus Alpha-Toxin-Induced Pores - Channel-Like Behavior in Lipid Bilayers and Patch Clamped Cells, *Journal of Membrane Biology*, 1995, vol. 143, pp. 143-151.
- 161 G. Belmonte, L. Cescatti, B. Ferrari, T. Nicolussi, M. Ropele and G. Menestrina, Pore Formation by Staphylococcus-Aureus Alpha-Toxin in Lipid Bilayers - Dependence Upon Temperature and Toxin Concentration, *European Biophysics Journal with Biophysics Letters*, 1987, vol. 14, pp. 349-358.
- 162 S. Furini, C. Domene, M. Rossi, M. Tartagni and S. Cavalcanti, Model-based prediction of the alpha-hemolysin structure in the hexameric state, *Biophysical Journal*, 2008, vol. 95, pp. 2265-2274.
- 163 M. Merzlyakov, E. Li and K. Hristova, Directed assembly of surface-supported bilayers with transmembrane helices, *Langmuir*, 2006, vol. 22, pp. 1247-1253.
- 164 B. Walker and H. Bayley, Key Residues for Membrane-Binding, Oligomerization, and Pore-Forming Activity of Staphylococcal Alpha-Hemolysin Identified by Cysteine Scanning Mutagenesis and Targeted Chemical Modification, *Journal of Biological Chemistry*, 1995, vol. 270, pp. 23065-23071.
- 165 P. Mueller and D. O. Rudin, Action Potentials Induced in Biomolecular Lipid Membranes, *Nature*, 1968, vol. 217, pp. 713-719.
- 166 R. O. Fox and F. M. Richards, A Voltage-Gated Ion Channel Model Inferred from the Crystal-Structure of Alamethicin at 1.5-Å Resolution, *Nature*, 1982, vol. 300, pp. 325-330.
- 167 L. G. M. Gordon and D. A. Haydon, Unit Conductance Channel of Alamethicin, *Biochimica Et Biophysica Acta*, 1972, vol. 255, pp. 1014-&.
- 168 L. G. M. Gordon and D. A. Haydon, Kinetics and Stability of Alamethicin Conducting Channels in Lipid Bilayers, *Biochimica Et Biophysica Acta*, 1976, vol. 436, pp. 541-556.
- 169 B. Sakmann and G. Boheim, Alamethicin-Induced Single Channel Conductance Fluctuations in Biological-Membranes, *Nature*, 1979, vol. 282, pp. 336-339.
- 170 G. Boheim, Statistical-Analysis of Alamethicin Channels in Black Lipid-Membranes, *Journal of Membrane Biology*, 1974, vol. 19, pp. 277-303.
- 171 M. Eisenberg, J. E. Hall and C. A. Mead, Nature of Voltage-Dependent Conductance Induced by Alamethicin in Black Lipid-Membranes, *Journal of Membrane Biology*, 1973, vol. 14, pp. 143-176.
- 172 J. E. Hall, I. Vodyanoy, T. M. Balasubramanian and G. R. Marshall, Alamethicin - a Rich Model for Channel Behavior, *Biophysical Journal*, 1984, vol. 45, pp. 233-247.
- 173 M. K. Mathew and P. Balaram, A Helix Dipole Model for Alamethicin and Related Transmembrane Channels, *Febs Letters*, 1983, vol. 157, pp. 1-5.

-
- 174 G. Spach, H. Duclohier, G. Molle and J. M. Valleton, Structure and Supramolecular Architecture of Membrane Channel-Forming Peptides, *Biochimie*, 1989, vol. 71, pp. 11-21.
 - 175 R. Latorre and O. Alvarez, Voltage-Dependent Channels in Planar Lipid Bilayer-Membranes, *Physiological Reviews*, 1981, vol. 61, pp. 77-150.
 - 176 H. Duclohier and H. Wroblewski, Voltage-dependent pore formation and antimicrobial activity by alamethicin and analogues, *Journal of Membrane Biology*, 2001, vol. 184, pp. 1-12.
 - 177 D. Needham and D. A. Haydon, Tensions and Free-Energies of Formation of Solventless Lipid Bilayers - Measurement of High Contact Angles, *Biophysical Journal*, 1983, vol. 41, pp. 251-257.
 - 178 D. Uhrikova, N. Kucerka, A. Islamov, A. Kuklin, V. Gordeliy and P. Balgavy, Small-angle neutron scattering study of the lipid bilayer thickness in unilamellar dioleoylphosphatidylcholine vesicles prepared by the cholate dilution method: n-decane effect, *Biochimica Et Biophysica Acta-Biomembranes*, 2003, vol. 1611, pp. 31-34.
 - 179 J. J. Donovan and R. Latorre, Inactivation of the Alamethicin-Induced Conductance Caused by Quaternary Ammonium-Ions and Local-Anesthetics, *Journal of General Physiology*, 1979, vol. 73, pp. 425-451.
 - 180 S. M. Bezrukov and I. Vodyanoy, Probing Alamethicin Channels with Water-Soluble Polymers - Effect on Conductance of Channel States, *Biophysical Journal*, 1993, vol. 64, pp. 16-25.
 - 181 I. Vodyanoy, S. M. Bezrukov and V. A. Parsegian, Probing Alamethicin Channels with Water-Soluble Polymers - Size-Modulated Osmotic Action, *Biophysical Journal*, 1993, vol. 65, pp. 2097-2105.
 - 182 D. O. D. Mak and W. W. Webb, Two classes of alamethicin transmembrane channels: Molecular models from single-channel properties, *Biophysical Journal*, 1995, vol. 69, pp. 2323-2336.
 - 183 A. Simon, A. Girard-Egrot, F. Sauter, C. Pudda, N. P. D'Hahan, L. Blum, F. Chatelain and A. Fuchs, Formation and stability of a suspended biomimetic lipid bilayer on silicon submicrometer-sized pores, *Journal of Colloid and Interface Science*, 2007, vol. 308, pp. 337-343.
 - 184 C. L. Pocanschi, G. J. Patel, D. Marsh and J. H. Kleinschmidt, Curvature elasticity and refolding of OmpA in large unilamellar vesicles, *Biophysical Journal*, 2006, vol. 91, pp. L75-L77.
 - 185 S. Kresák, T. Hianik and R. Naumann, Giga-seal solvent-free bilayer lipid membranes: from single nanopores to nanopore arrays, *Soft Matter*, 2009, DOI:10.1039/B907661A, in press.**
 - 186 E. Reimhult, K. Kumar and W. Knoll, Fabrication of nanoporous silicon nitride and silicon oxide films of controlled size and porosity for combined electrochemical and waveguide measurements, *Nanotechnology*, 2007, vol. 18, pp. 275303.
-